Study of the Bulk Properties of Liquid Transition Metals

A dissertation presented

by

Mohammad Riazuddin Molla

to

The Department of Theoretical Physics

in partial fulfillment of the requirements

for the Degree of

Doctor of Philosophy

in the subject of

Theoretical Physics

University of Dhaka

Dhaka-1000

November 2016

Professor G. M. Bhuiyan
Ph. D.
Phone:+880-2-9661920-73, Ext. 7022
Cell:+8801911305306
E-mail:gbhuiyan@du.ac.bd

Department of Theoretical Physics
University of Dhaka
Dhaka-1000, Bangladesh
Phone:+880-2-9661920-73, Ext. 7051
Fax: +880-2-9667222
E-mail: theor_phys@du.ac.bd

Approval Sheet

This is to certify that a thesis entitled "Study of the Bulk Properties of Liquid Transition Metals" has been written by Mohammad Riazuddin Molla who has successfully carried out these basic researches under my supervision and guidance. He can now submit this thesis to the concerned authority for evaluation for his degree of Ph. D.

Dated, Dhaka

November 28, 2016

Dr. Golam Mohammed Bhuiyan

তাত্ত্বিক পদার্থবিজ্ঞান বিভাগ, ঢাকা বিশ্ববিদ্যালয়, ঢাকা - ১০০০, বাংলাদেশ।
ফোন ঃ +৮৮০-২-৯৬৬১৯২০-৭৩, এক্স- ৭০৫১, ফ্যাক্স ঃ +৮৮০-২-৯৬৬৭২২২, ই-মেইল ঃ theor_phys@du.ac.bd

ISBN: 978-984-34-1448-9

Thesis supervisor

Dr. Golam Mohammed Bhuiyan

Author

Mohammad Riazuddin Molla

Study of the Bulk Properties of Liquid Transition Metals

Abstract

Due to versatile applications of transition metals it is always interesting to study the properties of these metals and their alloys theoretically. The properties of transition metals largely depend on the electronic configuration of the outermost shell or next-to-outer most shell. We have studied some static and dynamic properties for liquid transition metals by using the orbital free *ab initio* molecular dynamics (OF-AIMD) simulation technique at thermodynamic states near their respective melting temperatures. The systems studied are the $3d$ (Cr, Mn, Fe, Co, Ni, Zn), $4d$ (Pd, Cd) and $5d$ (Pt, Hg) liquid transition metals. Due to the availability of experimental data for static structure factor we have also performed simulation at several thermodynamic states for some systems, namely for liquid Fe (l-Fe), l-Zn, l-Hg, and l-Co.

The OF-AIMD simulation technique is related to the density functional theory (DFT) of Hohenberg and Kohn. The exchange correlation energy is described by the local density approximation. To describe electron-ion interaction, we have used a model local pseudopotential proposed by Bhuiyan *et al.*, which has proven to be the successful to generate the structural and dynamical properties of some liquid transition metals. The calculated results are presented here for a range of static structural magnitudes, such as static structure factor, isothermal compressibility, pair distribution function and coordination number. A comparison with the available X-ray and neutron diffraction data shows that the OF-AIMD method can provide a reasonable description of the static structure.

As for the dynamic properties, results are reported for both single and collective dynamics. The calculated dynamic structure factors show side peaks which point to the existence of collective density excitations, from where the adiabatic sound velocities are calculated. Finally, we have performed calculation of some transport coefficients and obtained results are compared with the corresponding experimental data. Calculated results for static and dynamic properties are found to be good in agreement with available experimental data. We also have observed through the present work that a heavy computational demand of Kohn-Sham orbital representation of DFT used in AIMD can be partly overcomed by the OF-AIMD simulation method.

Contents

List of Figures

List of Tables

List of Published and Unpublished Papers

The content of the following published paper, submitted and completed manuscripts are appeared in this thesis.

I. **Static and dynamic properties of liquid Zn, Cd and Hg divalent metals: An orbital free ab initio molecular dynamics study**; Mohammad Riazuddin Molla, A. Z. Ziauddin Ahmed, Horipada Sarker, G. M. Bhuiyan, M. R. Amin, L. E. González and D. J. González; Journal of Non-Crystalline Solids **406**, 45, (2014).

II. **Static and dynamic properties of liquid Cr, Mn, Fe and Co transition metals near their melting points: An OF-AIMD study**; Mohammad Riazuddin Molla, A. Z. Ziauddin Ahmed, G. M. Bhuiyan, M. Rahmman, L. E. González and D. J. González, (Manuscript ready for submission).

III. **Static and dynamic properties of liquid Ni, Pd and Pt transition metals near their melting points: An orbital free ab initio molecular dynamics study**; Mohammad Riazuddin Molla, A. Z. Ziauddin Ahmed, G.M. Bhuiyan, L. E. González and D. J. González, (Manuscript ready for submission).

IV. **Orbital free ab initio study of static and dynamic properties of some liquid transition metals**; G. M. Bhuiyan, Mohammad Riazuddin Molla, A. Z. Ziauddin Ahmed, L. E. González and D. J. González, (Manuscript submitted in Euro Phys. J. Web of Conferences).

Acknowledgments

First of all, I pay my gratitude to the almighty Allah for keeping me fit both physically and mentally upto the completion of this research work.

I would like to express my deep gratitude and thanks to Professor Dr. Golam Mohammed Bhuiyan for his excellent supervision, encouragement, unforgettable continuous support during the whole period of my Ph.D research work. His invaluable guidance, insightful discussions, analysis of the problem and scientific advice keep me in track towards the fulfilment of my Ph.D degree. The trust and freedom he offered lead me towards the successful completion of all the project on time. I found him the most enthusiastic, energetic and active researcher in the entire faculty of science.

I am highly encouraged and motivated to work in cordial and collaborative environment of the condensed matter physics group at the Department of Theoretical Physics, Unversity of Dhaka. Specially I would like to mention the collaburation with Departamento de Física Teórica, Universidad de Valladolid, Valladolid, Spain. The journey of the rough path to pursue my Ph.D has been made easy and possible by the continuous support, contribution, collaboration and encouragement from my colleagues and friends around.

My profound gratitude goes to Prof. Dr. D. J. González and Prof. Dr. L. E. González, Departamento de Física Teórica, Universidad de Valladolid, Valladolid, Spain for providing us the orbital free *ab initio* molecular dynamics (OF-AIMD) simulation code. Their support and collaboration enriched my dissertation.

I would also like to thank Professor Dr. Mohammed Arshad Momen, Chairman, Department of Theoretical Physics, Univesity of Dhaka, Bangladesh for the facility he has provided me during the entire period of my Ph.D study and also for all of his administrative suports. I would like to express my appreciation to all the faculty members and stuffs of the Department of Theoretical Physics, University of Dhaka for their warm cooperation.

I am most thankful to Dr. A. Z. Ziauddin Ahmed for making me be familiar with the simulation program and also for giving me continuous unforgettable support from the very beginning to the end of my Ph.D work. I am also thankful to Mr. Ziauddin for his patience reading of the dissertation and his fruitful suggestion for improvement of the manuscript. I am very thankful to Dr. Abu M. Khan, Associate Professor, Department of Mathematics and Physics, North South University, Bangladesh for his patience reading a few chapters of this dissertation and also for his invaluable suggestions to develop the construction of the language of those chapters. I am also thankful to Mohammad Saiful Alam regarding his help to prepare some figures and the cover by using illustrator.

I am greatly indebted to my wife, Farjana Akter and my daughter, Wadia Fatema Bimbita because they form the backbone and origin of my happiness. Their constant support any complaint or regret and unparallel love has enabled me to complete write

up this thesis. I owe my every achievement to both of them.

My most sincere thanks goes to Prof. Sajeda Banu for enabled to learn how to think for writing a good research article when I was writing my first research article. My sincere thanks also goes to Prof. Dr. Md. Abdul Matin, Prof. Dr. Ainul Islam, Prof. Dr. Muklesur Rahman, Prof. Dr. Md. Anwar Hossain, Prof. Dr. Md. Tazibar Rahman, Prof. Dr. Amulya Chandra Mandal, Prof. Dr. Amal Krishna Halder, Prof. Dr. Selina Parvin, Prof. Dr. Razina Ferdausi, Prof. Dr. Mezbahuddin Ahmed, Prof. Dr. Md. Shahidul Islam and Prof. Shapla Shirin for giving me inspiration all the time during my research work.

I would like to thank my friend Golam Dastegir Al-Quaderi for his advice of doing Ph.D under the supervision of Prof. Dr. G. M. Bhuiyan and also to introducing me with Dr. A. Z. Ziauddin Ahmed.

I acknowledge the financial support of the Ministry of Science and Technology, Bangladesh under the project of Bangabandhu Fellowship on science and ICT to carry out my PhD study.

Mohammad Riazuddin Molla, November 28, 2016

This dissertation is dedicated to
my late father Mohammad Nannu Molla
and
my late mother Fatema Begum.

Chapter 1

Introduction

A system is a part in this universe on which we focus our attention for analysis. The system is composed of any number of similar or dissimilar objects and the conditions of those objects identify the state of the system [1]. We can explain a physical system either by a theory or by analysing a collection of data obtained from experiment. Theoretically we can describe a physical system through mathematical model. But sometimes it gets extremely difficult to solve a particular problem either analytically or numerically, and even it may become imposible to solve at all. This is due to the lack of our proper understanding of the complexity of a system and also due to lack of knowledge in developing the appropriate mathematical tools. On the other hand, experiments to collect data are expensive, difficult to set up the necessary instruments, and sometimes it is also risky and hazardous. Even we can not perform any experiment for some specific situations. In these circumstances, simulation techniques play an important role to study a physical system. One may treat simulation as a computer experiment which acts as a bridge between theory and experiment.

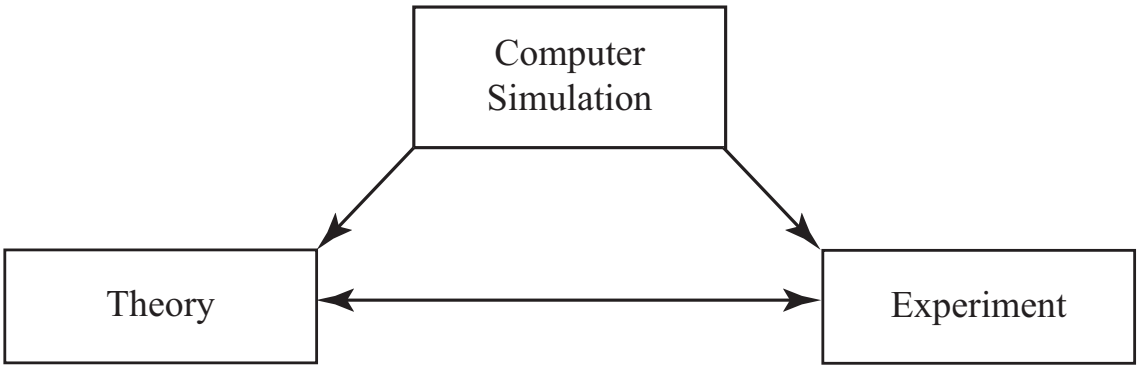

Figure 1.1: Conventional representation of the interplay among theory, experiment and computer simulation.

Simulation often leads to important advancement of a mathematical model where there is a lack of agreement between experimental data and the proposed mathematical model. Therefore the computer simulation becomes one of the most efficient and effective alternative tool for studying the properties of physical systems. Efficient algorithms for computer simulation have been highly developed over the period of time. Already a large number of experimental observations are verified successfully by using simulation technique. This technique is also capable of bringing new insights and interpretations of the experimental findings at the atomic level. Now-a-days simulation is considered essential before performing the experiment in reality and hence became a separate field of study. The huge improvement in computational power together with more efficient algorithms provides us a vast scope to perform simulations with high accuracy to answer the questions, like what are the structure of liquid metals. Moreover accessing extreme physical conditions computationally is much more easier and safer rather than obtaining in real experiments.

The achievement of the computer simulations of materials relies on the accuracy

of model how atoms interact with each other. Furthermore, some pre-parameterized empirical potentials have been applied with considerable success for some cases in the past and in modern days this has become the state-of-the-art method to model a large system. The parameters of a potential are usually obtained by data fitting to reproduce some liquid state properties at some ambient conditions. Applications of empirical potentials are very much limited to obtain the properties of systems for which they are parameterized and in most cases they fail to reproduce the properties of other systems [2]. On the contrary, there are techniques that are based on quantum mechanical description of the atoms, which are computationally much more demanding but more rigorous than empirical potentials. These methods do not require any input from experiments and are known as the *ab initio* methods. At the present, the parameters for the empirical potentials are often obtained from the *ab initio* methods.

The term *ab initio* usually refers to first-principle calculations. A calculation is called *ab initio* if it starts directly from establised laws and does not make any assumptions such as fitting the parameters of empirical models. An *ab initio* calculation gives the absolute energy of a system of fixed nuclei and moving electrons. The major disadvantage of the *ab initio* method is its dependence on heavy computational power. The main objective of the *ab initio* method is to solve the Schrödinger equation. The solutions of the Schrödinger equation describe the quantum states. From the ground state energy of a system in *ab initio* simulation other physical properties can be obtained. In practice, the Schrödinger equation can not be solved analytically for systems containing more than one electron. For this reason, different approximation methods have been introduced in the theory with high level of accuracy and

satisfaction. All these methods have their own advantages and disadvantages. These approximation methods are often classified into two groups: the wave function based approach and the density functional based approach.

In this dissertation, the method based on density functional theory (DFT) within the framework of Hohenberg and Kohn theory [3] is used to study the bulk properties of liquid transition metals. The DFT is the most convenient technique to solve the Schrödinger equation for the ground state energy of a system. This is because the DFT method is capable of dealing with systems consisting of hundreds or thousands or even more particles. Whereas for coupled cluster and other wave function based methods, the computational cost increases severely with the system size. One faces gridlock just for working with a few tens of paricles using the largest supercomputers and most efficient algorithms. Definitely DFT has already occupied the position of the most popular *ab initio* method recently for condensed phase simulations. The DFT can be categorized into either orbital based or orbital free method. Explicit density dependent total energy functional of the DFT proposed by Hohenberg and Kohn [3] is known as the orbital free DFT (OF-DFT). On the other hand, if the kinetic energy (KE) functional, $T_s[\{\psi_i\}]$, depends explicitly on the orbitals and all other terms including the exchange correlation (XC) term, $E_{xc}[\rho(\mathbf{r})]$, depend implicitly only on the orbitals in the total energy functional, it is named as Kohn and Sham DFT (KS-DFT) or orbital based DFT [4]. The KS-DFT method is time consuming and only been used for systems of small size (up to ≈ 100 particles), whereas OF-DFT can handle a system having hundreds or thousands or even more particles without considerable time consumption. By construction the OF-DFT techniqe is less accurate than the

KS-DFT because the former method does not take care of actual orbitals. We have employed OF-DFT in this dissertation for a number of systems, each having 500 particles in a cell and obtained the results with the accuracy [5] comparable to that of the KS-DFT.

Like all other electronic structure calculation methods, DFT has its own limitations. In principle, the DFT is exact calculation, but in practice it requires an appoximation to take care of the so-called electron exchange correlation interactions. Although the contribution of the exchange correlation (XC) energy is small, only a fraction of the total energy of a system, it can not be ignored and rather turns out to be extremely crucial for accurate description. The success of DFT depends on the accuracy of the approximations made for the exchange correlation functional. Among different methods two excellent ways to calculate the XC energy are mostly used. These are: (i) the local-density approximation (LDA) [4] and (ii) the generalized gradient approximation (GGA) method [6–9]. These two approximations for exchange correlation energy have been extremely successful in various fields but they often seems to be fail to treat the weakly bound systems. Here we have used the local density approximation which is the oldest approximation of DFT and was originally proposed by Kohn and Sham [4]. It is a key contribution to the work of Kohn and Sham and works effectively while the density variations are slow. But it turns out that the LDA works surprisingly well for the calculation of many energetic and structural properties for a wide range of materials. The key assumption of LDA is to grip the known result for a uniform electron gas (UEG) and apply it locally to a non-homogeneous system.

In the LDA, $\varepsilon_{xc}^{LDA}[\rho(\mathbf{r})] = \varepsilon_{x}^{LDA}[\rho(\mathbf{r})] + \varepsilon_{c}^{LDA}[\rho(\mathbf{r})]$ is the exchange correlation energy per particle of the uniform electron gas with density $\rho(\mathbf{r})$, where $\varepsilon_{x}^{LDA}[\rho(\mathbf{r})]$ has the analytic form given by the Dirac energy functional [10] and the correlation contribution $\varepsilon_{c}^{LDA}[\rho(\mathbf{r})]$ is determined from the Quantum Monte Carlo (QMC) simulations [11] along with some fitting procecedures [12, 13]. We also have used the Perdew-Zunger approximation [13] for the correlation energy functional, $\varepsilon_{c}^{LDA}[\rho(\mathbf{r})]$. The LDA fails in situations where the density changes rapidly. To overcome this problem the idea of LDA is further improved by constructing XC functionals which depend not only on the local density itself but also on its gradients [6–9] and this newly developed technique is known as the generalized gradient appoximation (GGA). The kinetic energy (KE) functional is one of the key ingredient in DFT calculations. The KE functional for Thomas-Fermi (TF) model [14] is based on the homogeneous electron gas. Thus, the KE functional of TF model is not very accurate for most of the physical systems. So, more accurate and transferable kinetic energy density functional is needed for the orbital free *ab initio* molecular dynamics (OF-AIMD) simulation. In particular, a reliable KE functional, $T_s[\rho]$ has been used in our present work which is proposed by González *et al.* [15, 16]. This KE functional includes the von Weizsäcker term plus further terms chosen in order to reproduce some exactly known limits correctly. By incorporating this modification we have found favorable results [5]. The external field in the energy functional of DFT contains electron-ion interaction, $V_{ext}(\mathbf{r})=\sum_i v(\mathbf{r}-\mathbf{R}_i)$. We have used the local model pseudopotential of Bhuiyan *et al.* [17] in the OF-DFT to describe the electron-ion interaction. This model local pseudopotential in conjunction with the OF-AIMD simulation provides

a good description of several static and dynamic properties of various liquid metals near melting points and above [5, 17, 18].

The molecular dynamics (MD) simulation techniqe provides detailed information about the positions and velocities of atoms in the liquid state. Molecular dynamics (MD) simulation techniques along with the first principle calculation have become a powerful tool in the study of liquid systems. During the last three decades we have witnessed huge applications of *ab initio* molecular dynamics (AIMD) simulation methods in various research purposes. Most of the first principle calculations are based on the density functional theory (DFT) [3, 4]. Since density functional theory is very simple to handle computationally, DFT has become a common tool in first principles calculations to describe the properties of the molecular and condensed systems. This theory allows us to calculate the ground state electronic energy of a collection of atoms for a given nuclear position and also yields the force on the nuclei via the Hellmann-Feynman theorem. Since the microscopic details of the orbitals are involved in the formulation of the KS density functional theory (KS-DFT) [4], most of the calculations are computationally very expensive, and this limits the size of the system under consideration to be small, only about hundred particles. This also limits the simulation time. However, our observation shows that some of these constraints may be reduced drastically if we use the orbital free *ab initio* molecular dynamics (OF-AIMD) simulation method [5, 15]. The fundamental varibale of the OF-AIMD simulation is the total valence electronic density instead of the electronic orbitals that is used in the the KS-AIMD formulation. The OF-AIMD method substantially reduces the number of variables needed to describe the electronic states and hence

allows us to study the larger systems (thousands of particles) for longer simulation times. However, this improvement is achieved at the cost of resorting to an approximate description of the electronic kinetic energy. This means that the OF-AIMD approach is, in principle, less accurate than the KS-AIMD method. Nevertheless despite of this caveat, the OF-AIMD method has provided good descriptions for several static and dynamic properties of a variety of bulk liquid metals [5, 15, 16, 19–21], binary alloys [22, 23] and free liquid surfaces [24–26].

The main purpose of this dissertation is to perform simulations to study some physical properties, namely the static and dynamic properties of liquid metals lying in the $3d$, $4d$ and $5d$ transition series and these metals are very difficult to handle theoretically. The objective here is two-folds: firstly to examine systems which have incompletely filled d-bands and bonding and antibonding states play an important role in addition to the hybridization effects in determining physical properties, and secondly to investigate the systems for which d-band is completely filled by electrons but there are evidences that they exhibit sd-hybridization effect. We believe that this study will provide us more clear understanding about different liquid metals in the transition series. Ten metals from the transition series under study are classified into three different groups. The first group consists of incompletely filled d-bands but lies near the middle of the series (*e.g.* Cr, Mn, Fe, Co). For these elements the interplay between bonding and antibonding states are found to be strong. In the second group we put metals with nearly filled d-band elements such as Ni, Pt, Pd. Finally the completely filled d-bands (viz. Zn, Cd, Hg) are placed in the third group.

The physical properties of liquid Cr, Mn, Fe, Co, Ni, Pd, Pt, Zn, Cd and Hg are

of considerable interest to physicists, chemists, material scientists and even to geophysists. These elements lie in the $3d$, $4d$ and $5d$-transition series. The static structure of the $3d$, $4d$ and $5d$ liquid transition metals has been studied experimentally by Waseda [27] using the X-ray diffraction experiment. For some systems understudy (*e.g.* for Fe, Co, Zn and Hg), measurements are done for several different temperatures. The structure determined by the neutron diffraction method is also available for some transition metal systems [28]. The knowledge of static structure factor, $S(q)$, or its real space counterpart, the pair distribution function, $g(r)$, is absolutely a necessary prerequisite for a complete description of static, thermodynamic and even transport properties. Most theoretical studies for liquid transition metals and their alloys focus on the structural and thermodynamic properties at temperatures near melting points [29–35]. In those works, the interionic interactions are accounted for by using the pseudopotential theory [29–31, 36–40], semi-empirical embadded atom methods [32, 33], tight binding theory [41, 42], and empirical methods [43]. Some simulation studies are also available in literature for liquid transition metals. Most of them are based on classical molecular dynamics (CMD) [33, 44]. Only a few *ab initio* MD simulation studies are available for liquid transition metals [45, 46]. Most importantly, nearly all *ab initio* simulation studies are performed for the late transition metals lying at the end of the $3d$, $4d$ and $5d$ transition series and close to the noble metals [5,18,47–51]. But the AIMD simulation study for liquid metals lying in the middle of the transition series is very scarce because the interplay between the bonding and anti-bonding states for the elements in the middle of the series significantly change the physical properties. Despite these difficulties, a few *ab initio* studies for liquid iron

are performed [45,52,53]. Vočadlo *et al.* [45] were the first to perfom *ab initio* MD for l-Fe, where they focused on the studies of the static structure and viscosity of iron in the inner core of the earth at high pressure and temperature. Very recently, Marques *et al.* [52] performed an *ab initio* study for l-Fe near the triple point, and showed that the inclusion of spin polarization, *i.e.* magnetic effect, describes the static and some dynamic properties well. But the magnitudes they have found from the non-magnetic AIMD method are far-off. For example, the values of isothermal compressibility in their study, with and without magnetic effect are: $\chi_T = 1.24 \pm 0.02$ and 10.3 ± 0.2 (in 10^{-12}cm^2 dyne^{-1} units), respectively. In the case of self-diffusion coefficent, they found $D_{\text{AIMD}} = 0.37 \pm 0.2\,\text{Å}^2$ ps^{-1} and $D_{\text{NM-AIMD}} = 0.82 \pm 0.03\,\text{Å}^2$ ps^{-1}. For shear viscosity, they found that $\eta_{\text{AIMD}} = 5.0 \pm 0.3$ GPa ps and $\eta_{\text{NM-AIMD}} = 1.8 \pm 0.2$ GPa ps. From the large discrepancy between AIMD and NM-AIMD results, it is very clear that the magnetic effect of ions of Fe in the liquid state is significantly important and needs to be considered. This new and interesting finding requires further examination to see wheather other version of AIMD without consideration of spin polarization yields the results with similar large magnitudes or not. To this end the current OF-AIMD study for l-Fe is very interesting. On the other hand, to the best of our knowledge, physical properties of liquid Cr, Mn, and Co have not been studied yet using any version of *ab initio* simulation methods. From this point of view, this study carries more importance.

The systems (Ni, Pd and Pt) are *d*-band transition metals located in the right-most column of group VIIIA of the periodic table. Several studies have already been carried out on bulk l-Ni, l-Pd and l-Pt by using MD simulation. Among all

the available research works, the classical MD simulation study of Alemany *et al.* [54] have performed theoretical calculations for the transport properties (viscosity and diffusivity) of some liquid transition metals using a semiempirical many-body potential based on the second-moment approximation to the tight-binding method (TBM-SMA) [55,56]. Alemany *et al.* [57] also have calculated the transport properties of some liquid transition metals using classical MD simulation along with the Voter and Chen version of the embedded atom model potential [58]. The classical MD simulation study of Kart *et al.* [59] have computed the transport properties of l-Pd, l-Ni using the Sutton-Chen (SC) potential with a new potential parameter set, namely the quantum Sutton-Chen potential (Q-SC) developed by Çağin *et al.* [60]. The transport properties are important for metallurgical processes as well as for understanding the dynamics of liquids. However, experimental data for the self-diffusivities of liquid metals are relatively scarce, mainly due to a lack of specific radio-isotopes. Experimental diffusion data are available only for about a dozen liquid metals [61]. However, there are variations between the different experimental viscosity data [62]. The accurate measurment of these quantities is a difficult task due to critical experimental conditions at high temperatures and pressures. One of the most basic transport properties is the velocity of sound. However, only a few studies have been found on this. Theoretical and semi-empirical equations for the velocity of sound in liquid metals as well as purely empirical methods are well reviewed by Iida and Guthrie [62, 63]. For these reasons, we have become interested to study the transport properties. Bermejo *et al.* [64] have computed the sound velocity of l-Ni at $T = 1763$ K with well-defined microscopic collective excitations by means of

inelastic neutron scattering (INS) method. Yokoyama [65] has computed the sound velocity for some $3d$ transition metals near the melting point by using hard-sphere model immersed in the uniform background potential. Using the AIMD simulations, Jakse *et al.* [66] have studied the transport properties of l-Ni at $T = 1850$ K. S. Blairs [67] has examined the inter-relationship between surface tension, σ, density, ρ and sound velocity, c_s, given by the equation $\log c_s = 0.5526 \log(\frac{\sigma}{\rho}) + 5.4364$ from the available experimental sound velocity of 41 metallic elemental systems at the melting point. By using this inter-relationship equation he estimated sound velocity of other 24 elements at the melting point from the experimental σ and ρ. Thakor *et al.* [68] have calculated the transport properties of $3d$ liquid transition metals using the scaling law proposed by Dzugutov [69], which represents the relationship between the excess entropy and transport properties of liquid. From the consideration of hard sphere model, Yokoyama [70] has studied transport properties for some liquid metals near the melting point by using the scaling law. In this calculation only the parameter, packing fraction, ξ, is calculated from excess entropy. Yokoyama *et al.* [71] have studied transport properties of liquid Ni near and above melting by using the Dzugutov [69] scaling law and the diffraction data of Waseda [27]. Moreover, they have also used the same diffraction data for evaluting excess entropy. Korkmaz *et al.* [72] have studied the transport properties for transition metal Ni near and above melting by using the scaling laws proposed by Li *et al.* [73, 74], Rosenfeld [75] and Dzugutov [69]. Protopapas *et al.* [61] have computed the self-diffusion coefficient by extending the Enskog theory [76] assuming that the self-diffusion coefficient of a dense metallic fluid is the same as that of an appropriate hard sphere fluid. Gosh *et al.* [77]

have studied the transport properties of transition metals by using the scaling laws proposed by Dzugutov [69] and Rosenfeld [75]. To the best of our knowledge no OF-AIMD simulation has been done before us for liquid Ni, Pd and Pt and no published results are available for any kind of *ab initio* simulation for l-Pd and l-Pt. Hence to study the liquid Ni, Pd, and Pt by applying the OF-AIMD simulation method will be an important contribution. Moreover, the OF-AIMD method describes the liquid systems much better than the classical method and gives better insight to understand the properties of a physical system.

Metals with incompletely filled d-bands exhibit strong d-character through the sp-d hybridization effects. This effect is accounted for either by changing s, p, d band occupancy number as in the case of the *ab initio* pseudopotential calculations or by changing the chemical valence with an effective value [29, 34, 36–40]. A study using the density functional based generalized pseudopotential theory [78, 79] shows that the hybridization effect alters the integral value of the chemical valence to have an effective non-integral value of Z. This effective value of Z lies in the range from 1.1 to 1.7 for transition metal elements. Even systems like Zn, Cd and Hg have completely filled d-bands, but interestingly the number of these d-band electrons are affected [43, 80, 81] via the so-called sd mixing, known as sd-hybridization. This is the reason, why the IIB metals have been put in the transition series in some cases. In the present work we do not consider sd-hybridization for the group IIB metals Zn, Cd and Hg which are considered as divalent metals. The liquids Zn and Cd have some anomalous surface properties that are characterized by the positive temperature coefficient of surface tension. Moreover, at thermodynamic states around

their respective triple point both l-Zn and l-Cd display the same type of "anomalous" liquid state structure factor, $S(q)$, namely, the main peak has an asymmetric shape which gradually becomes more symmetric with increasing temperature. Among the three systems Hg and Zn have the largest and smallest packing respectively whereas that of Cd lies in between their values. On the other hand their resistivities (ρ) follow a different order $\rho_{Hg} > \rho_{Zn} > \rho_{Cd}$. The occurrence of considerable changes in the physical properties of Hg, such as metal-non metal transitions, together with a relatively low critical temperature and concerns about its toxicity, made it interesting to study.

Several studies have already been carried out on bulk l-Zn, l-Cd and l-Hg by using either semiempirical or more fundamental approaches. Among the semiempirical works, we highlight references [82,83] which are basically resorted to the hard spheres (HS) model in order to analyze some structural and thermodynamical properties. Thus, Umar and Young [82] used the HS model with a packing fraction calculated within the framework of a variational theory to obtain a qualitative estimate of the $S(q)$ near melting. The HS model was also used by Ascarelli [83] to provide qualitative estimates of the isothermal compressibility and the velocity of sound of l-Zn, l-Cd and l-Hg near their triple points. Subsequently, several elaborate studies have been performed relying on more realistic descriptions of the interatomic interactions, which have mostly been derived within the framework of the pseudopotential theory. Thus, Jank and Hafner and coworkers [84, 85] have used the pseudopotential theory in order to obtain effective interatomic potentials which were combined with either liquid state theories [84] or with classical molecular dynamics (CMD) simulations [85]

in order to calculate several static structural properties of l-Zn, l-Cd and l-Hg. Also Lai *et al.* [86] have studied the "anomalous" S(q) of l-Zn and l-Cd near their triple point and its variation with temperature; this was performed by using interatomic potentials derived from non-local pseudopotentials along with several liquid state theories. More recently, Belashchenko [87–89] has used the embedded atom model (EAM) to obtain effective interatomic potentials which were used in conjunction with CMD simulations to evaluate the static structure of l-Zn and l-Hg at several thermodynamic states. Calderin *et al.* [90–93] have performed KS-AIMD simulations for l-Cd and l-Hg at thermodynamic states near their respective triple points. Both calculations used 90 particles, the local density approximation (LDA) for the electronic exchange correlation energy and ultrasoft non-local pseudopotentials [94]. Due to the high computational demands of the KS-AIMD method only a few thousand of configurations (5000 for l-Cd and 2200 for l-Hg) were generated. For both systems, the calculated static structure compared well with the experiments. As for the dynamic structural magnitudes, comparison with experiment could only be carried out for l-Hg (no experimental data are available for l-Cd yet) and the calculated dynamic structure factors showed a fair agreement with experimental data. We have found, no KS-AIMD type calculation carried out for l-Zn, so far. On the experimental side, we mention that the static structure of l-Zn, l-Cd and l-Hg have already been measured, at several temperatures, by both neutron scattering (NS) [95–97] and X-ray (XR) diffraction [27, 96] methods. As for the dynamic properties only the microscopic dynamics of l-Hg has been studied by both inelastic neutron scattering (INS) [98–100] and inelastic X-ray scattering (IXS) [101, 102] techniques. Those measurements have

unveiled the existence of propagating collective excitations along with an associated mode velocity which suggests an important positive dispersion.

This dissertation is organized as follows: Chapter 1 is the introduction. Most importantly we have tried to give an clear overview of the whole work in this chapter.

Since we mostly worked with transition metal elements, a brief introduction about transition metals and their fundamental properties are given in Chapter 2. We also have discussed how properties varies like crystal structure, electronic structure and their relative position in periodic table.

Chapter 3 is devoted to explore and understand the molecular dynamics simulation. Here we have presented a comprehensive description of *ab initio* molecular dynamics simulation technique. Description of Car-Parrinello MD simulation along with Verlet Leap-frog algorithm and periodic boundary conditions appear in this Chapter as a natural consequence.

In Chapter 4 we have concentrated to discuss about the development of the necessary theoretical background for first principle calculations. Starting from Schrödinger equation we have discussed up to DFT, which is very essential for computational purposes. All the necessary ingradients for OF-DFT are explained in this chapter concisely. A brief description of KS-DFT, the local density approximation (LDA) and the generalized gradient approximation (GGA) have also been presented here.

Chapter 5 describes the liquid state theories for equilibrium properties. Theoretical description of all properties which are studied in this work also appear in this Chapter.

Chapter 6 deals with elaborate discussion and analysis of the main results ob-

tained. In this Chapter we have presented the results for static, single particle dynamics and collective dynamics in property-wise sequence.

Finally, a summary and concluding remarks of the whole work and future perspectives in research are outlined in Chapter 7.

Chapter 2

General Features of The Transition Metals

The transition metals are found in the center of the modern periodic table (see figure 2.1). Many scientists [103–106] consider noble metals Cu, Ag, Au and divalent metals Zn, Cd, Hg as elements of transition series even their *d*-bands are completely filled. For these reasons, scientists of the present days use following prescription for the definition of transition metals.

(i). Any element in the *d*-block of the period table, which includes groups IIIA through IIB, *i.e.* all *d*-block elements are transition metals.

(ii). An element whose atom has an incomplete *d* sub-shell, or which can give rise to cations with an incomplete *d* sub-shell is called a transition metal.

Therefore, the transition metals lie in the three well defined periods in the periodic table. On the basis of the two definitions outlined above we may count 30 transi-

tion metal elements from $3d$, $4d$ and $5d$ series in total. The periods are generally characterised as $3d$, $4d$ and $5d$ series according to the filling of the $3d$, $4d$ and $5d$ bands. The transition metals belong to the first group are Sc, Y, and La, which have the electronic configurations $1s^2 2s^2 2p^6 3s^2 3p^6 3d^1 4s^2$, $1s^2 2s^2 2p^6 3s^2 3p^6 3d^{10} 4s^2 4p^6 4d^1 5s^2$ and $1s^2 2s^2 2p^6 3s^2 3p^6 3d^{10} 4s^2 4p^6 4d^{10} 5s^2 5p^6 5d^1 6s^2$, respectively. While the transition metals of the last group are Zn, Cd and Hg whose electronic configurations are $1s^2 2s^2 2p^6 3s^2 3p^6 3d^{10} 4s^2$, $1s^2 2s^2 2p^6 3s^2 3p^6 3d^{10} 4s^2 4p^6 4d^{10} 5s^2$ and $1s^2 2s^2 2p^6 3s^2 3p^6 3d^{10} 4s^2 4p^6 4d^{10} 4f^{14} 5s^2 5p^6 5d^{10} 6s^2$, respectively. The properties of transition metals largely rely on the electronic configuration of the outer-most shell and next-to-outer most shell.

The transition metals are interesting because they can have several oxidation states, unlike the most other metals. This happens because the transition metals can lose their d electrons in addition to their s electrons when forming ions. Elements within the same group contained the same number of electrons in their outer shell. For this reason, the elements lying in a same group shows the similar chemical behaviour. Paramagnetism in the transition metal elements is caused due to the presence of unpaired electrons in the d sub-orbital as a result a pronounced influence of a magnetic field is observed.

Sometimes the IIB metals Zn, Cd and Hg are called post transition metals. But still these divalent metals exhibit some of the characteristics of the transition elements. The common properties of the transition metals are as follows

(i). They form coloured compounds apart from Sc and Zn. There are variations in colour for compounds of the same valency and with different valency (oxidation)

Table 2.1: Position of simple, less simple and transition metals in the periodic table and their electronic configurations.

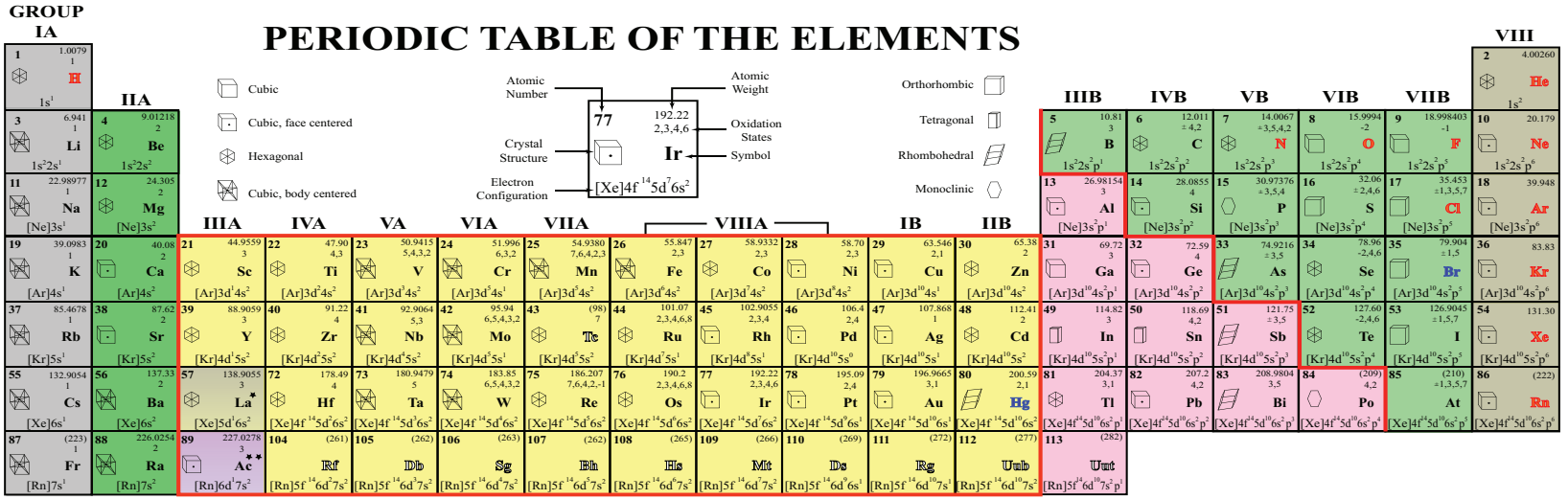

*Lanthanides	58 Ce 140.12 3,4 [Xe]4f 2 5d 0 6s 2	59 Pr 140.9077 3,4 [Xe]4f 3 5d 0 6s 2	60 Nd 144.24 3 [Xe]4f 4 5d 0 6s 2	61 Pm (145) 3 [Xe]4f 5 5d 0 6s 2	62 Sm 150.4 3,2 [Xe]4f 6 5d 0 6s 2	63 Eu 151.96 3,2 [Xe]4f 7 5d 0 6s 2	64 Gd 157.25 3 [Xe]4f 7 5d 1 6s 2	65 Tb 158.9254 3,4 [Xe]4f 9 5d 0 6s 2	66 Dy 162.50 3 [Xe]4f 10 5d 0 6s 2	67 Ho 164.9304 3 [Xe]4f 11 5d 0 6s 2	68 Er 167.26 3 [Xe]4f 12 5d 0 6s 2	69 Tm 168.9342 3,2 [Xe]4f 13 5d 0 6s 2	70 Yb 173.04 3,2 [Xe]4f 14 5d 0 6s 2	71 Lu 174.967 3 [Xe]4f 14 5d 1 6s 2
**Actinides	90 Th 232.0381 4 [Rn]5f 0 6d 2 7s 2	91 Pa 231.0359 5,4 [Rn]5f 2 6d 1 7s 2	92 U 238.029 6,5,4,3 [Rn]5f 3 6d 1 7s 2	93 Np 237.0482 6,5,4,3 [Rn]5f 4 6d 1 7s 2	94 Pu (244) 6,5,4,3 [Rn]5f 6 6d 0 7s 2	95 Am (243) 6,5,4,3 [Rn]5f 7 6d 0 7s 2	96 Cm (247) 3 [Rn]5f 7 6d 1 7s 2	97 Bk (247) 4,3 [Rn]5f 8 6d 1 7s 2	98 Cf (251) 3 [Rn]5f 10 6d 0 7s 2	99 Es (252) - [Rn]5f 11 6d 0 7s 2	100 Fm (257) - [Rn]5f 12 6d 0 7s 2	101 Md (258) - [Rn]5f 13 6d 0 7s 2	102 No (259) - [Rn]5f 14 6d 0 7s 2	103 Lr (260) - [Rn]5f 14 6d 1 7s 2

states.

(ii). They are good conductors of heat and electricity.

(iii). They can be hammered or bent into prefered shape easily.

(iv). They are less reactive than alkali metals such as sodium.

(v). They have high melting points and high densities.

High melting points and densities of transition metals suggest that the electrons which enter the *d*-orbitals are being used to bind the atoms together in the crystal lattice. But the divalent transition metals Zn, Cd and Hg are metals with low melting points. This is due to their stable electron configuration. Hg is so poor to forming metallic bonds that's why it remains in liquid state at room temperature.

Transition metals are distinguished from simple metals due to their peculiar thermodynamic properties. The cohesive energy of the transition metals of incompletely filled *d*-band is higher than that of the divalent transition metals Zn, Cd and Hg. From the experimental evidence, it is seen that the cohesive energies, atomic volumes, melting points, and bulk moduli roughly varies parabolically across the three series [107]. The peculiar properties of the transition metals correspond to the strong *d*-character in their valence states which arises from two factors [108]. These are namely:

(i). Their orbits are fairly small, compared with the other (*s,p*) valence states of comparable energy and the *d*-states are fairly localized; they are not strongly purturbed by the lattice potential and can not overlap very strongly with the atomic states of other atoms.

(ii). Due to their parabolic increase with distance near the origin, the *d*-electrons screen the nuclear charge within an atom badly.

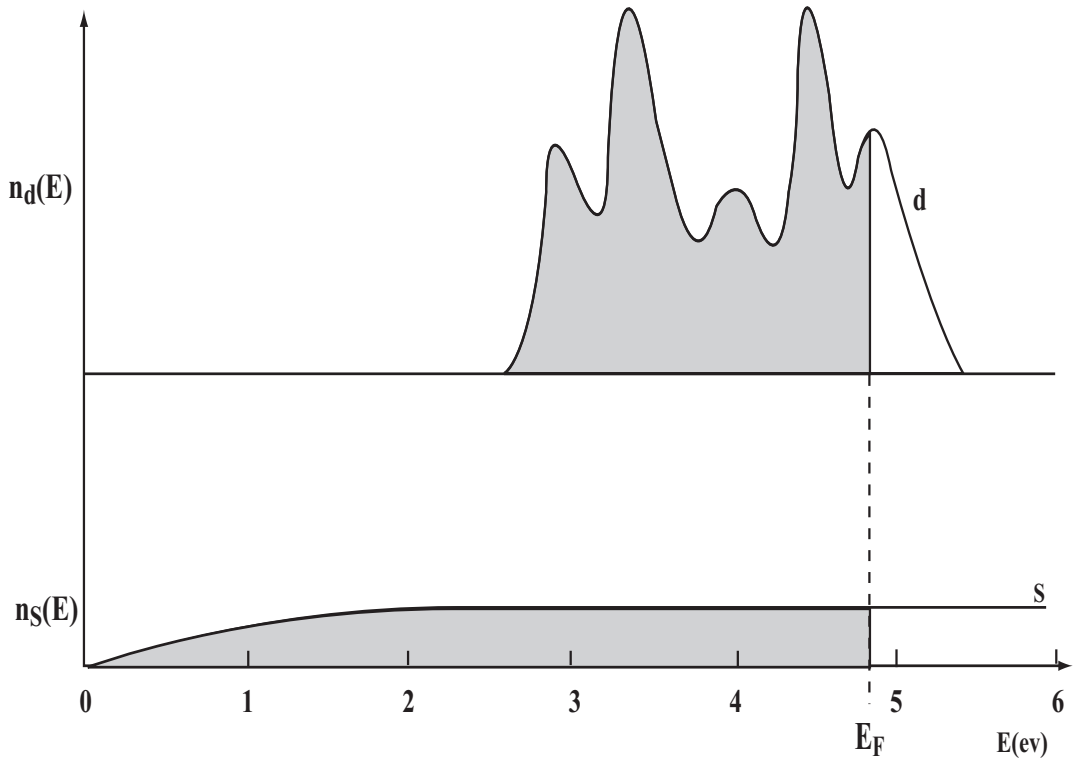

Figure 2.1: Narrow *d*-bands and free electron like *s*-band contribution to the density of level in transition metals [104].

The electronic structure of the *d*-band is exhibited in Figure 2.1. It is seen from the figure that the band structure made up of five narrow bands crossing and hybridizing with the nearly free electron's band of pseudoplane waves [109] formed from atomic *s* and *p* states. As the *d*-bands are narrower than the typical free electron conduction bands and hold enough levels to accommodate ten electrons the density of levels is substantially higher than that of free energy levels throughout the energy region where the *d*-band lies. Since the specific heat is proportional to the density of states at the Fermi energy, the effect of high density is seen in the electronic contribution

to the specific heat at low temperature. It is to be mentioned that the Fermi level in an incompletely filled d-band metals lie within the d-band.

For an incompletely filled d-band transition metals, there are more bonding states than antibonding states occupied. The maximum effect occurs when all the bonding states are occupied and all the antibonding states empty. This happens for the metals in the middle of the transition series. This is the main source of the regular variation of cohesion and related thermodynamic prperties with the filling of the d-band, peaking to a maximum for the refractory metals in the middle of the transition metal series [107].

The electrons in a metal move in a more or less constant potential from atomic centre to centre, where it is then scattered in a way characteristic of the atom. The point is that the scattering becomes strong and highly energy dependent, passing through a resonance around the energy of the d-band. The scattering phase-shift that stands in place of the resonance can be expressed by [109]

$$\eta_2(E) \simeq tan^{-1}\frac{\frac{1}{2}\Gamma}{E_d - E}\,, \tag{2.1}$$

where, Γ is the resonance width, which dominates the width of the d-band. The atomic d-state energy is symbolized by E_d. Actually when a d-electron escape into a plane wave of the same energy it has to pass through a barrier, which is the centrifugal term $\frac{l(l+1)}{r^2}$, in the radial wave equation [110]. It is the classic situation of a virtual bound state or a resonance of an incoming plane wave with the atomic d-state, which leads to a resonance in the $l = 2$ phase shift. In Eqn.(2.1), Γ is related to the life time $\frac{\hbar}{\Gamma}$ of the virtual bound state by the uncertanity principle. Therefore, the values of Γ and E_d for various metals can be estimated from first principles calculations.

The band width for the $3d$ series lies within 5 to 10 electron volts, which is slightly larger for the $4d$ and $5d$ series. The knowledge about the nature of their short range order is limited. For this reason, it is imposible to compute the density of states, $n(\varepsilon)$, accurately. But the bonding and antibonding limits are not much different from those of close packed crystalline structures. As a consequence the thermodynamic properties in the liquid state near melting follow similar trends in the solid phase across the three transition metal series. Nonetheless the d-band widths of liquid transition metals are smaller but of the same order of magnitude that found in the crystalline solids [108].

Chromium (Cr) is an important trace element that humans require in very small amounts. Cr is used in producing stainless steel and other alloys. Most stainless steel contains about 18 percent chromium. Chromium in superalloys (high-performance alloys) permits jet engines to operate in a high-temperature, high-stress, chemically oxidizing environment. It is also extensively used for plating automobile trim, bumpers, and other items to produce a hard beautiful surface and to prevent corrosion. This metal is also widely used as a catalyst. The transition metal Cr is found as a major element in several minerals. Chromium is used for improving blood sugar level in human body with prediabetes, type-I and type-II diabetes, and high blood sugar level caused due to intake of steroids. Some people may experience skin irritation, headaches, dizziness, nausea, mood changes and impaired thinking, judgment, and coordination etc. side effects due to taking Cr as supplements. High doses have been linked to more serious side effects including blood disorders, liver or kidney damage, and other problems. It has maximum number of unpaired d-electrons and therefore

Cr is very hard. Soild Cr has face centered cubic (fcc) structure.

Another trace element important for human health is manganese (Mn). It is necessary for the development of connective tissue, carbohydrate metabolism, calcium absorption, blood sugar regulation, normal brain and nerve functioning. Manganese is one of the component of antioxidant enzyme superoxide dismutase which neutralize the free radicals which occurs naturally in the body and causes cell damage. It has bcc structure in solid phase. Manganese has no alternate where it is needed, particularly in metallurgical alloys [111] and very importantly also used in iron, steel, low-cost stainless steel formulations [112].

A plentiful amount of elemental iron (Fe) found on earth's crust. In solid phase it has body centered cubic (bcc) structure. Iron is the fourth most abundant element in the Earth. We are passing the age of iron. The use of iron in modern era is so versatile due to its outstanding properties, it is almost impossible to tabulate its all uses and importance. From a large number of different uses of iron, we will discuss here a few of them as a representative one. Fe is needed for transporting oxygen and carbon dioxide in the human body. Iron deficiency causes anemia in human body, *i.e.* one has to take iron supplements for preventing and treating anemia. People often feel very tired due to iron deficiency. Pure iron is quite soft and therefore it is rarely used in industry in pure form. The iron alloys known to be steel are mostly used in industry. There are 27 grades of such steel. Steels are used for manufacturing automobile components, machineries, tools and building structure. Corrosion resistance stainless steel are made by alloying iron with carbon, chromium, silicon, molybdenum, nickel etc. are used for manufacturing cutlery, cookware, hardware, surgical appliances, aerospace

components and many more. The iron alloy with niobium is extremely strong and therefore it is being used for constructing nuclear reactors container vessel.

The transition metal cobalt (Co) has the hexagonal closed packed (hcp) structure in solid phase. It has several important uses in the form of alloys. Co alloys are used to manufacture for aircraft engine parts and few other applications for corrosion or wear resistant purposes. Cobalt salts are used to impart blue and green colors in glass and ceramics industry. Cobalt is also widely used in batteries and in electroplating. After nickel and chromium, cobalt is a major element causes of contact dermatitis [113].

The fcc structure metal nickel (Ni) is used as an ingredient in many industrial and consumer products, including stainless steel and other metallic alloys, coins, rechargeable batteries, and electroplating. Nickel is an important trace element in ultramafic and mafic rocks. A small quantity of nickel is essential for human body, but when the uptake level is too high it could be harmful for human body.

The major uses of divalent hcp transition metal zinc (Zn) are namely electroplating, metallic alloys, pigment in paint, agricultural fertilizers, pesticides and galvanized roofing material and all. It is known as an essential trace element which is important for immune system and also for the brain. Zinc is necessary for natural growth and proper maintenance of the human body. Several studies show that Zn has a relation with eye vision because high level of this mineral is found in macula, the part of the retina. Zinc deficiency can alter vision, the retina shape, retardation of child growth, infection susceptibility, diarrhea and all. Zinc might also have effects against viruses. In addition, there is some evidence that zinc has some antiviral activity against the herpes virus.

The divalent transition metal cadmium (Cd) is primarily used in Ni-Cd batteries, metallic alloys, electroplating, pigment in paint, and electronic components. The crystal structure of Cd is hcp.

Palladium (Pd) is a very important material both for technologically and for various scientific purposes. Palladium is a monomorphic metal, with fcc structure. Palladium, like all of the platinum group noble elements, has comparatively low electrical resistivity and high temperature coefficent of resistance. Both of these characteristics are extremely sensitive to metal purity [114]. Palladium is an important transition metal because of its wide usage in medicine, nano-technology, electronic, semiconductor, energy and chemical technologies, plating and jewllery, automotive, surgical instruments and space industry.

Platinum (Pt) is the least reactive metal with a fcc structure. It has remarkable corrosion resistance, even at high temperatures, and is therefore considered a noble metal. Platinum is used in catalytic converters, laboratory equipment, electrical contacts and electrodes, platinum resistance thermometers, dentistry equipment, and jewellery.

The divalent metal mercury (Hg) is used in thermometers and other scientific apparatus, amalgam for dental restoration, Hg vapor lamps, cosmetics, and liquid mirror telescopes. It has rhombohedral lattice structure in solid phase. Historically, Hg has been widely used in gold mining operations. Mercury has no positive role in the human body.

From the above discussions, it is clear that some of the transition metals under study are very useful for us such as Fe, Mn, Zn, Pt, Co, Ni and Cr. Some other

transition metals like Pd, Cd and Hg under study may causes serious harm on us. So they are key elements in life and evolution. We can conclude that the transition metals have great impact on us due to their versatile applications both in industry and medical purposes. It, therefore draws our attention to study their properties elaborately. A summary of the physical properties of the transition metals under study are presented in Table 2.2.

Table 2.2: Molar mass (g mol^{-1}), melting temperature (K), electronic configuration and crystal structure.

Systems	Molar mass	Melting temperature	Electronic configuration	Crystal structure
Cr	051.9960	2180.00	$[Ar]3d^5 4s^1$	bcc
Mn	054.9380	1519.00	$[Ar]3d^5 4s^2$	bcc
Fe	055.8450	1811.00	$[Ar]3d^6 4s^2$	bcc
Co	058.9332	1768.00	$[Ar]3d^7 4s^2$	hcp
Ni	058.7000	1782.00	$[Ar]3d^8 4s^2$	fcc
Pd	106.4000	1828.05	$[Kr]4d^{10} 5s^0$	fcc
Pt	195.0900	2041.40	$[Xe]5d^9 6s^1$	fcc
Zn	065.3800	0692.68	$[Ar]3d^{10} 4s^2$	hcp
Cd	112.4100	0594.22	$[Kr]4d^{10} 5s^2$	hcp
Hg	200.5900	0234.32	$[Xe]5d^{10} 6s^2$	rhombohedral

Chapter 3

Molecular Dynamics Simulation Method

3.1 Computer Simulation

Simulation can mimic real situation like experiment of a system by using a computer, so it is known as computer experiment. Computer simulation is an established tool and an effective way to study the deeper insight behaviour of complex systems. Besides, simulation can be performed in such situation where experiments are quite difficult, expensive and risky. In this modern days, both Monte Carlo (MC) and molecular dynamics (MD) methods are widely used to study the properties of materials, device fabrication and designing new functional materials. In the present case our main focus is on MD simulations. The core of the molecular dynamics simulation is to solve the Newtonian equations of motion for the system with a limited number of particles. MD method allows us to study the materials in molecular scale. The key

idea here is to see how the positions, velocities and orientatios of particles of the system change with time by solving the Newton's equations of motion of the molecules. For classical systems

$$\mathbf{F}_i(t) = M_i \frac{d^2\mathbf{R}_i}{dt^2}, i = 1, 2, \ldots, N, \tag{3.1}$$

where $\mathbf{F}_i$ denotes the force on the i-th particle caused by the other N-1 particles, M_i is the mass and $\mathbf{R}_i$ is the position of the i-th particle. In effect, molecular dynamics constitutes a motion picture that follows molecules as they moving to and fro, twisting, turning, colliding with one another. At first, a system of N particles is given an initial condition, that is, the coordinates and momenta of each particle. Then at each time step the equations of motion are used to calculate the coordinates and momenta of each particle for the next sequence. In this way, the system evolves dynamically in time and then we can take the time average of phase variables. MD simulation can be used to obtain time-dependent properties of the system as it follows the time evolution. MD method allows us to study both equilibrium thermodynamics and dynamical properties of a system at finite temperature. The output of any such simulation is simply the positions and velocities of the particles of the system in 'equilibrium', that is, at every time step of the simulation. By using these information, many physically interesting properties can be evaluated. The accuracy of a MD calculation largely depends on the method by which the forces are calculated. In the current work we have used *ab initio* molecular dynamics simulations which will be described in brief in the next coming section.

3.1.1 *Ab initio* Molecular Dynamics Simulation

An *ab initio* molecular dynamics simulation method uses force obtained from electronic structure theory using typically at the density functional level of theory in order to evolve the dynamics of the system in time. On the other hand, classical molecular dynamics (CMD) uses force obtained from (semi) empirical force fields. *Ab initio* is a latin term and litterally means "from the beginning". A calculation is said to be an *ab initio* or first principles if it depends on microscopic and establised laws of nature without any additional assumptions or special models. The simulation method that combines classical molecular dynamics of nuclei with electronic structure theory is called *ab initio* molecular dynamics (AIMD). AIMD is a rapidly evolving and growing technique that constitutes one of the most important theoretical tools developed in the last couple of decades. In an AIMD calculation, finite-temperature dynamical trajectories are generated by using forces obtained directly from electronic structure calculations performed "on the fly" as the simulation proceeds. Thus, AIMD permits the breaking and forming the chemical bond to occur and accounts for electronic polarization effects [115, 116]. AIMD has been successfully applied to a wide variety of physically significant problems in Physics and Chemistry and, recently, it is being also used to study the problem related to the biological systems as well. In numerous studies, new physical phenomena have been revealed and microscopic mechanisms elucidated that could not have been uncovered yet by using empirical methods. Therefore, it leads to the new interpretations of experimental data and in some cases even suggesting new experiments to perform. In its most ideal form, an AIMD calculation assumes only that the system is composed of M nuclei and N

electrons, that the Born-Oppenheimer approximation is valid, and the dynamics of the nuclei can be treated classically on the ground state electronic surface [117]. We have performed *ab initio* MD simulation in the present work within the scope of the famous Car-Parrinello approach.

3.1.2 The Car-Parrinello Method

The Car-Parrinello method is often referred to as an *ab initio* molecular dynamics because it does not require an interatomic potential to be supplied as an input. Instead, it calculates the forces and potential directly from the electronic structure as the simulation proceeds. This method stands out as a new and more efficient method for calculating the properties of materials. To surve this purpose the electronic equations are solved by employing appropriate boundary conditions, planewave basis sets and also from the approach of density functional theory (DFT). The Car-Parrinello method can also be used in the orbital free (OF) version of the density functional theory [118]. The approach by Car-Parrinello [119, 120] combines MD and DFT into one unified algorithm for the electronic states, self-consistency and nuclear movement. In this method of proceeding, nuclear and electronic dynamics are considered together so that the ionic and electronic degrees of freedom are relaxed simultaneously. On the whole, there are four apparent advances of the Car-Parrinello method used in the electronic structure calculation. These are as follows [121]:

(i) Optimization methods instead of variational equations.

(ii) Equations of motion instead of matrix diagonalization.

(iii) Fast Fourier transforms (FFT) instead of matrix operations.

(iv) A trace of occupied subspace instead of eigenvector operation.

It is to be noted that the AIMD method with an orbital free density functional theory (OF-DFT) approach, the total energy is a functional of charge density only. So we may also apply the Car-Parrinello technique for this energy functional [118]. The pseudo-Lagrangian for OF-DFT approach can be defined as

$$\mathcal{L}_{CP} = T_e + T_n - E[\rho, \{\mathbf{R}_i\}] + \mu\Big(\int \rho \, d\mathbf{r} - N\Big), \tag{3.2}$$

where, N is the total number of the electrons, $\mathbf{R}_i$ denote the coordinates of the i-th nucleus and $E[\rho, \{\mathbf{R}_i\}]$ is the total potential energy of a system [see Eqn. (4.61)]. The first term representing the fictitious kinetic energy associated with the electronic degrees of freedom defined as

$$T_e = \frac{1}{2} M_e \int \dot{\psi}^2 d\mathbf{r}, \tag{3.3}$$

where $\dot{\psi} = \frac{d\psi}{dt}$ and $\rho = \mid \psi \mid^2$, and the fictitious mass M_e appears as a parameter in the model of classical motion of charge density which is analogous to the orbital motion of electrons. The fictitious mass of the electrons must be small enough to keep the trajectory adiabatic, avoiding the transfer of energy from the ionic to the electronic degrees of freedom. This also requires that the time step is smaller than the usual values used in other MD methods. The second term in the Lagrangian is the kinetic energy of nuclei

$$T_n = \frac{1}{2} \sum_i M_i \mid \dot{\mathbf{R}}_i \mid^2, \tag{3.4}$$

where, M_i is the mass of the i-th nucleus and the dot denotes time derivative. The third term in Eqn. (3.2) is the total electronic energy of the combined system of electrons and ions. The above Lagrangian leads to the following Car-Parrinello equations of motion

$$M_i\ddot{\mathbf{R}}_i(t) = -\nabla_{\mathbf{R}_i} E_g \tag{3.5}$$

$$M_e\ddot{\psi}(\mathbf{r},t) = -\frac{\partial E_g}{\partial \psi(\mathbf{r},t)} + \mu\psi(\mathbf{r},t), \tag{3.6}$$

for both classical ionic degrees of freedom, $\{\mathbf{R}_i\}$ and electronic degrees of freedom, $\psi(\mathbf{r},t)$ respectively, subject to the constraint

$$\int \mid \psi \mid^2 d\mathbf{r} = N, \tag{3.7}$$

and E_g is the ground state energy of the system. The force on the i-th ion is given by

$$\mathbf{F}_i = -\nabla_{\mathbf{R}_i} E_g \tag{3.8}$$

and so Eqn. (3.5) becomes

$$\mathbf{F}_i(t) = M_i\ddot{\mathbf{R}}_i(t) \tag{3.9}$$

In Eqn. (3.9), the force on the i-th ion at time t, $\mathbf{F}_i(t)$, depends on the positions of all of the other ions of the system at that time. After specifying the initial positions and velocities of each of the N particles, the basic MD procedure follows, for which it repeats for the desired number of iterations according to the following steps:

(i) The force on each particle is calculated according to Eqn. (3.8).

(ii) The positions of the particles of the system are updated gradually in time according to Eqn. (3.9).

To solve the integration involved in step (ii) we have used the Verlet Leap-frog algorithm with time step Δt for each atomic movement. Similarly, the motion of electronic degrees of freedom Eqn. (3.6) is sloved numerically using the Verlet Leap-frog algorithm with electronic time step Δt_e. The choice of a time step Δt is also important. Large time step causes atoms to move too far along a given trajectory, which yields a poor simulation of the motion. For a time step that is too small requires more iterations, thus taking longer time to run the simulation. Therefore, the time step should be one order of magnitude less than the time scale of the vibrational period or the time between collisions. This gives time step on the order of femtoseconds for simulating a liquid of rigid molecules and tenths of a femtosecond for simulating vibrating molecules [122].

The time steps for evolving the ionic and electronic positions are not similar in evey detail. The time step Δt_e and the fake mass M_e should be chosen carefully such that the dynamics of electrons remains adiabatic. This means that the system should remain in its electronic ground state during the motion. The small fictitious mass M_e in turn requires that the electronic equations of motion are integrated using a smaller time step Δt_e than one which uses 1-10 fs in common practice for classical molecular dynamics [123].

3.1.3 The Verlet Leap-frog Algorithm

It is obvious that an efficient molecular dynamics program requires a good algorithm to integrate Newton's equations of motion. In the present work we have used the Verlet Leap-frog algorithm [124] to integrate Newton's equations of motion for ions

and electrons. The Verlet Leap-frog algorithm is a modified version of the orginal Verlet algorithm for use in molecular dynamics simulations. The Verlet algorithm uses the positions and forces at the time t and the positions at the time $t - \Delta t$ to predict the positions at the time $t + \Delta t$, where Δt is the integration time step in molecular dynamics scheme. The Verlet algorithm is a combination of two Taylor expansions. Using Taylor expansion for position from time t forward to $t + \Delta t$ and backward to $t - \Delta t$ up to the 3rd order, one obtains

$$\mathbf{R}_i(t + \Delta t) = 2\mathbf{R}_i(t) - \mathbf{R}_i(t - \Delta t) + \frac{\mathbf{F}_i(t)}{M_i}\Delta t^2 + O(\Delta t^4). \tag{3.10}$$

The estimate of the new ionic positions contain an error that is of the order Δt^4. The velocities are obtained from the basic definition of differentiation

$$\mathbf{v}_i(t) = \frac{\mathbf{R}_i(t + \Delta t) - \mathbf{R}_i(t - \Delta t)}{2\Delta t}, \tag{3.11}$$

and this expression for the velocity is only accurate to order of Δt^2. The Verlet Leap-frog algorithm is used the velocities at half time step defined as

$$\mathbf{v}_i(t + \frac{\Delta t}{2}) = \frac{\mathbf{F}_i(t)}{M_i}\Delta t + \mathbf{v}_i(t - \frac{\Delta t}{2}), \tag{3.12}$$

to obtain more accurate velocities. Then, the velocities at time t can be also computed from

$$\mathbf{v}_i(t) = \frac{\mathbf{v}_i(t + \frac{\Delta t}{2}) + \mathbf{v}_i(t - \frac{\Delta t}{2})}{2}, \tag{3.13}$$

where the ionic positions are then obtained from

$$\mathbf{R}_i(t + \Delta t) = \mathbf{R}_i(t) + \mathbf{v}_i(t + \frac{\Delta t}{2})\Delta t \tag{3.14}$$

Schematically, the Verlet Leap-frog algorithm can be shown as:

(1). Given current position, $\mathbf{R}_i(t)$ and velocity at last half-step, $\mathbf{v}_i(t - \frac{\Delta t}{2})$.

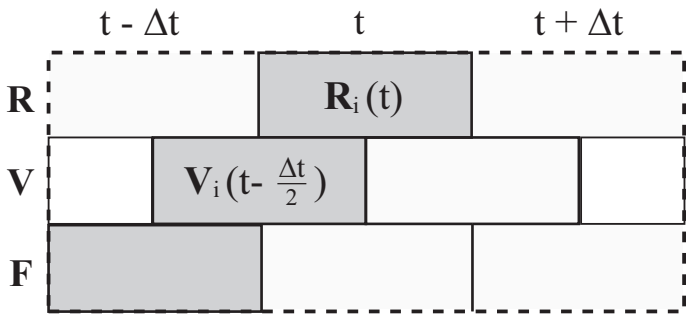

(2). Compute current force, $\mathbf{F}_i(t)$ via the Hellman-Feynman theorem $\mathbf{F}_i = -\nabla_{\mathbf{R}_i} E_g$.

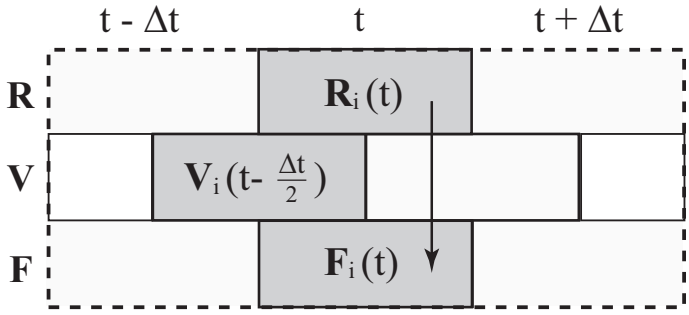

(3). Compute velocity at next half-step, $\mathbf{v}_i(t + \frac{\Delta t}{2})$ via Eqn. (3.12) using current force, $\mathbf{F}_i(t)$ and velocity at last half-step, $\mathbf{v}_i(t - \frac{\Delta t}{2})$.

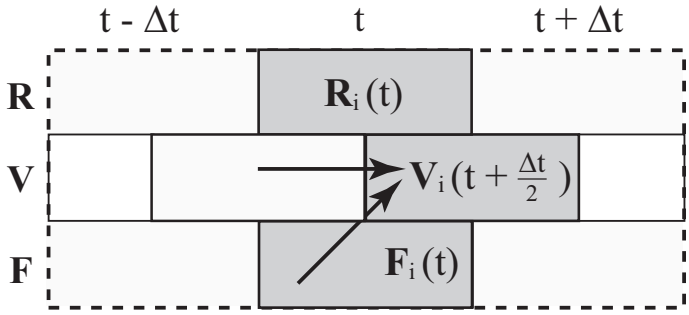

(4). Compute next position, $\mathbf{R}_i(t+\Delta t)$ via Eqn. (3.14) using current position, $\mathbf{R}_i(t)$ and velocity at next half-step, $\mathbf{v}_i(t+\frac{\Delta t}{2})$.

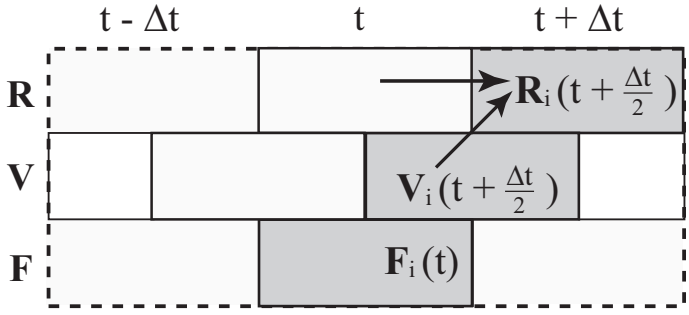

(5). Advance to next time step, repeat.

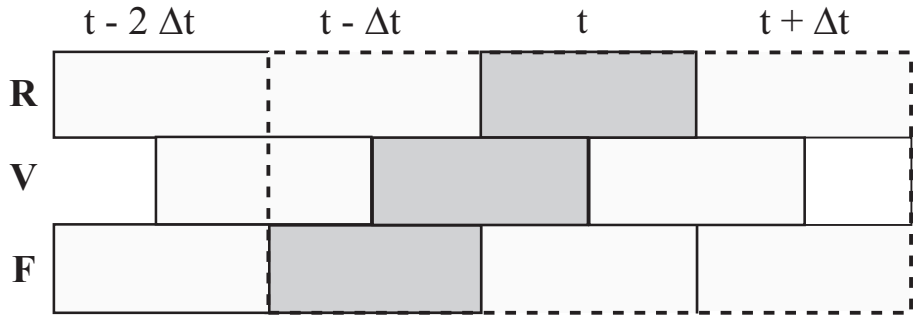

3.1.4 Periodic Boundary Conditions

Periodic boundary conditions (PBC) are a set of boundary conditions. The N particles (atoms, molecules or ions) may be confined by a cubical container, which prevents them from drifting apart. But these arrangements are not good for the simulation of bulk liquids, due to artificial surface effects. During such a simulation the large fraction of molecules lie on the surface of the cube containing these particles. Particles on the surface will have different behaviour from particles in the bulk. Periodic

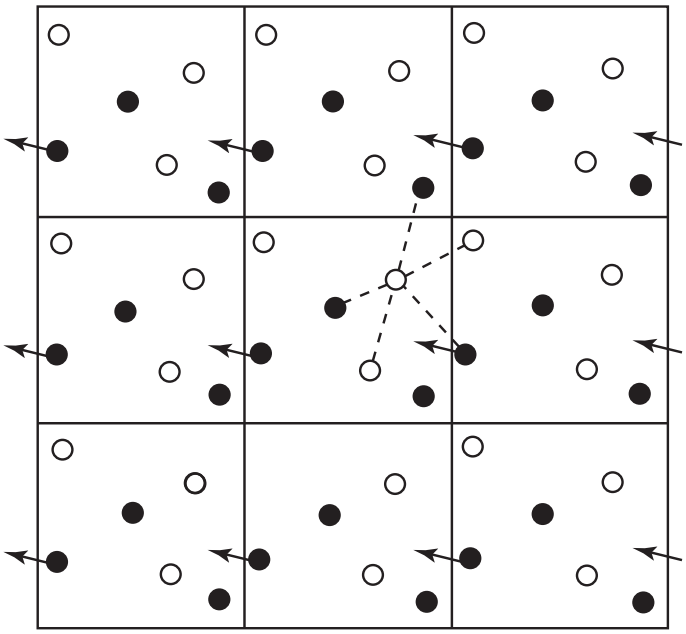

Figure 3.1: Schematic diagram of periodic boundary conditions used in computer experiments [125].

boundary conditions are commonly used in molecular dynamics simulations to ignor problems of such artificial surface effects from the computation for all system sizes. The original simulation cubic box, with the states of all the particles within it, is replicated throughout the whole of space. The simulation box and the replicated boxes together form an infinite lattice. The basic idea behind the PBC is that when a particle moves in the original box, its periodic images in the neighbouring boxes move in the same fashion. When a particle leaves the central box, one of its images will enter through the opposite face with exactly the same velocity, since there are no walls at the boundaries of the central box and no surface particles. For this reason, the number of particles in the central box (and hence in the entire system) is conserved. A two-dimensional version of such a periodic system is shown in Figure 3.1. For

normal liquids, the interaction potential is relatively short range in MD simulations. For example, such case the Lennard-Jones potential is often used in the case of CMD. This means that the only significant contributions to the force on any given particle come from particles in its immediate vicinity. Accordingly, MD simulations often use the "minimum image convention" with periodic boundary conditions. The minimum image convention states that each atom in the system interacts with the neraest atom or image in the periodic array. An alternative is to employ a cut-off radius, which is typically taken to be considerably smaller than $\frac{L}{2}$ (the maximum radius of a sphere that can be packed into the cubic box) where L stands for the side of the cube. For long range potentials, these methods are likely to introduce serious errors in the force calculation, and therefore in the resulting trajectories of the particles. Instead, one must include the force contributions from all particles in the main simulation box as well as from all the particles in every periodic replica (*i.e.*, from an infinite number of particles). In reality, this is very challenging task to handle it in computer simulation of particles; thus it is accomplished by the famous Ewald summation [126, 127].

Chapter 4

Theoretical Background

4.1 Electronic Structure Theory

Most physical and chemical properties of a material are determined by the electronic structure, especially the structure of the outermost shell. Therefore study of the electronic structure of materials is an important part of research in material science. The basic idea behind the electronic structure theory is that we fix the ions at specified locations and generally this is done within the context of the Born-Oppenheimer approximation. Then we deal with the Hamiltonian of electronic motions and find all the eigenfunctions of that Hamiltonian eventually we get the eigenvalues which are the energy of the corresponding eigenstates. As the electronic structure theory is very broad and versatile so in this Chapter we will focus only on the theory, methods and implementations of electronic structure theory related to us. Density functional theory (DFT) is often reconized as the cornerstone for studying electronic structure of many-body system. DFT provides us an approximate way to solve the

Schrödinger equation of many-body system. The present simulation is performed using the Hohenberg-Kohn (HK) version of density functional theory [3], using the local density approximation [13] to exchange correlation energy and, the external potential of a system created by ions is approximated by the local model pseudopotential [17]. The kinetic energy (KE) functional is the most important ingredient of HK version of DFT, and a reliable KE functional is used in the present work to approximate it [15].

4.1.1 Schrödinger's Equation

The Schrödinger equation (SE) is the primitive equation associated with quantum mechanics for describing the electronic structure of matter in condensed matter physics. It is also commonly known as the Schrödinger wave equation, and is a partial differential equation that describes how the wavefunction of a physical system evolves over time. Based on the de Broglie hypothesis, in 1926, Erwin Schrödinger constructed an equation for describing the so-called wave behavior of matter, for example, the electron. The equation was later named Schrödinger equation and the complete form of the famous equation is known to be the time-dependent Schrödinger equation [128]. It can be written for N particles as

$$i\hbar\frac{\partial}{\partial t}\Psi(\{\mathbf{r}_i\},t) = \hat{H}\Psi(\{\mathbf{r}_i\},t) \tag{4.1}$$

where $\mathbf{r}_i$ represents the position coordinate of i-th particle and $\hat{H}$ is the Hamiltonian defined as

$$\hat{H} = -\frac{\hbar^2}{2}\sum_{i=1}^{N}\frac{1}{m_i}\nabla_i^2 + V(\mathbf{r}_1,\mathbf{r}_2,\ldots,\mathbf{r}_N,t). \tag{4.2}$$

If the Hamiltonian itself has no time-dependency the SE becomes

$$\hat{H}\Psi(\mathbf{r}_1, \mathbf{r}_2, \ldots, \mathbf{r}_N) = E\Psi(\mathbf{r}_1, \mathbf{r}_2, \ldots, \mathbf{r}_N) \tag{4.3}$$

with the Hamiltonian $\hat{H}$ equal to

$$\hat{H} = -\frac{\hbar^2}{2}\sum_{i=1}^{N}\frac{\nabla_i{}^2}{m_i} + V(\mathbf{r}_1, \mathbf{r}_2, \ldots, \mathbf{r}_N) \tag{4.4}$$

and E is the total energy of the system.

4.1.2 The wave Function

The wave function is a mysterious function that lies at the heart of quantum mechanics. The wave function in quantum mechanics contains all information of a given system. The time-independent wave function is considered owing to simplicity. A question always arising with physical quantities is about its possible interpretations as well as observations. But the wave function itself has no physical interpretation. It is not a physically observable quantity; that is, the wavefunction is purely a mathematical fashion. The Born probability interpretation of the wave function provides a physical meaning of wave function. The square of the wave function multiplied by volume elements gives the probability [129, 130] as

$$P = \mid \Psi(\mathbf{r}_1, \mathbf{r}_2, \ldots, \mathbf{r}_N) \mid^2 d\mathbf{r}_1 d\mathbf{r}_2 \ldots d\mathbf{r}_N. \tag{4.5}$$

Eqn. (4.5) describes the probability that particles 1,2,...,N are located simultaneously in the corresponding volume element $d\mathbf{r}_1 d\mathbf{r}_2 \ldots d\mathbf{r}_N$ [131]. All particles must be found somewhere in space so it follows that

$$\int d\mathbf{r}_1 \int d\mathbf{r}_2 \ldots \int d\mathbf{r}_N \mid \Psi(\mathbf{r}_1, \mathbf{r}_2, \ldots, \mathbf{r}_N) \mid^2 = 1, \tag{4.6}$$

which is generally known as the normalization condition for the wave function. The Eqn. (4.6) also gives insight on the requirement that a wave function must fulfill in order to be physically acceptable. The wave function must be continuous over the full spatial range and square-integratable [132]. Another important property of the wave function is that, calculation of the expectation values of operators with a wave function provides the expectation value of the corresponding observable for that wave function [133]. For an observable $A(\mathbf{r}_1, \mathbf{r}_2, \ldots, \mathbf{r}_N)$, one can generally be written as

$$A = \left\langle \hat{A} \right\rangle = \int d\mathbf{r}_1 \int d\mathbf{r}_2 \ldots \int d\mathbf{r}_N \Psi^*(\mathbf{r}_1, \mathbf{r}_2, \ldots, \mathbf{r}_N) \hat{A} \Psi(\mathbf{r}_1, \mathbf{r}_2, \ldots, \mathbf{r}_N). \tag{4.7}$$

4.1.3 The Electron Density

In an electronic system, the number of elctrons per unit volume in a given state is the electron density for that state. If the spin coordinates are neglected, the electron density $\rho(\mathbf{r})$ can be expressed as measurable observable

$$\rho(\mathbf{r}) = N \int d\mathbf{r}_2 \ldots \int d\mathbf{r}_N \Psi^*(\mathbf{r}_1, \mathbf{r}_2, \ldots, \mathbf{r}_N) \Psi(\mathbf{r}_1, \mathbf{r}_2, \ldots, \mathbf{r}_N), \tag{4.8}$$

which only depends on spatial coordinates [3,134]. The density $\rho(\mathbf{r})$ can be measured by X-ray diffraction [135]. When quantum-mechanical effects are significant, the electron density $\rho(\mathbf{r})$ gives the probability of finding any electron within the volume element $d\mathbf{r}$ from the total N number of electrons. Some fundamental properties of the electron density are as follows:

(i.) $\rho(\mathbf{r}) \to 0$ as $\mathbf{r} \to \infty$.

(ii.) Integration of the density gives the total number of electrons, $\int \rho(\mathbf{r}) d\mathbf{r} = N$.

Note that the density $\rho(\mathbf{r})$ is a function and has only 3 degrees of freedom. Before presenting an approach using the electron density as variable, it has to be ensured that it truly contains all necessary informations about the system. That means it has to contain information about the total number of electrons, N as well as the external potential characterized by V_{ext} [135]. The total number of electrons can be obtained by integration of the electron density over the spatial coordinates [135]

$$N = \int \rho(\mathbf{r}) d\mathbf{r}. \tag{4.9}$$

The external potential is characterized uniquely by the ground state electron density. The term uniquely means up to an additive constant as proved by the first Hohenberg and Kohn (HK) theorem. This proof will be discussed in the forthcoming subsection 4.2.2.

4.1.4 The Hamiltonian of a Molecular System

The starting point of a quantum theory of materials is the Hamiltonian of the many body system. The complete Hamiltonian for a system composed of N electrons and M neclei in atomic units (*i.e.* m_e=$\hbar$=e=1) is given by

$$\begin{aligned} \hat{H}_{ne}(\mathbf{r},\mathbf{R}) &= \sum_{i=1}^{N} -\frac{1}{2}\nabla_i^2 - \sum_{I=1}^{M} \frac{1}{2M_I}\nabla_I^2 + \sum_{i=1}^{N}\sum_{I=1}^{M} \frac{-Z_I}{\mid \mathbf{r}_i - \mathbf{R}_I \mid} + \sum_{i=1}^{N}\sum_{i<j}^{N} \frac{1}{\mid \mathbf{r}_i - \mathbf{r}_j \mid} \\ &\quad + \sum_{I=1}^{M}\sum_{J>I}^{M} \frac{Z_I Z_J}{\mid \mathbf{R}_I - \mathbf{R}_J \mid} \\ &= \hat{T}_e + \hat{T}_n + \hat{V}_{ne} + \hat{V}_{ee} + \hat{V}_{nn}, \end{aligned} \tag{4.10}$$

where, the indices I, J run over the M nuclei, whereas i and j run over the N electrons, M_I and Z_I are the mass and charge of the I-th nucleus, respectively. In

the above equation $\mathbf{R_I}$ is the position of the I-th nucleus and $\mathbf{r_i}$ is the position of the i-th electron. In Eqn. (4.10), the first two terms describe the kinetic energy operators for the electrons and the nuclei, respectively. The latter three terms represent the electron-nucleus, electron-electron and nuclei-nuclei interaction potential operators, respectively.

4.1.5 The Born-Oppenheimer Approximation

The very complicated Schrödinger equation for a molecule is simplified with the help of the Born-Oppenheimer (BO) approximation. This approximation was proposed in 1927, in the early period of quantum mechanics, by Max Born and J. Robert Oppenheimer [136] and is still indispensable in quantum chemistry and molecular physics. In quantum chemistry and molecular physics, the BO approximation is the assumption that the motion of atomic nuclei and electrons in a system can be separated. The very essential ingredient of the BO appproximation comes from the fact that the mass of an atomic nucleus in a system is much larger than the mass of an electron. This means that there must be a large difference in speed between them. Therefore it is logical to assume that the nuclei are nearly fixed with respect to electron motion. Consequently, the nuclear kinetic energy is zero and their potential energy is merely a constant. This is called the BO approximation. Thus, the complete Hamiltonian $\hat{H}_{ne}$ is replaced by the so-called the electronic Hamiltonian

$$\begin{aligned} \hat{H}(\,\mathbf{r}\,;\mathbf{R}\,) &= \sum_{i=1}^{N} -\frac{1}{2}\nabla_i^2 + \sum_{i=1}^{N}\sum_{I=1}^{M} \frac{-Z_I}{\mid \mathbf{r}_i - \mathbf{R}_I \mid} + \sum_{i=1}^{N}\sum_{i<j}^{N} \frac{1}{\mid \mathbf{r}_i - \mathbf{r}_j \mid} \\ &= \hat{T}_e + \hat{V}_{ne} + \hat{V}_{ee}. \end{aligned} \tag{4.11}$$

Any problem in the electronic structure of matter is covered by Schrödinger's

equation including the time. In most cases, however, one is concerned with atoms and molecules without time-dependent interactions [137]. Hence, for now only the electronic time-independent Schrödinger equation is of our interest. The nuclear degrees of freedom (*e.g.*, the crystal lattice in a solid) appear only in the form of a potential $V(\mathbf{r})$ acting on the electrons, so that the wave function depends only on the electronic coordinates [133]. The solution of the Schrödinger equation

$$\hat{H}\Psi = E_e\Psi \tag{4.12}$$

with electronic Hamiltonian is the electronic wave function $\Psi = \Psi(\mathbf{r}_1, \mathbf{r}_2, \ldots, \mathbf{r}_N; \mathbf{R})$ and the electronic energy E_e, where $\mathbf{R}$ is the ionic coordinates. The total energy E for some fixed configurations of the nuclei is then the sum of E_e and the constant nuclear repulsion term

$$E_{II} = \sum_{I=1}^{M}\sum_{J>I}^{M} \frac{Z_I Z_J}{\mid \mathbf{R}_I - \mathbf{R}_J \mid}$$

leading to

$$E = E_e + E_{II}. \tag{4.13}$$

In general, under the Born-Oppenheimer approximation the electronic structure problem reduces difficulties to solving Eqn. (4.12) and the total energies are obtained by solving Eqn. (4.12) and Eqn. (4.13). However, one should keep in mind that the Born-Oppenheimer approximation is certainly not valid universally. It is established that the Born- Oppenheimer approximation will break down when there are multiple potential energy surfaces close to each other in energy or crossing each other [138]. The major difficulty in solving Eqn. (4.12) is the interaction between electrons, where all the many-body quantum effects are hidden. Many approximate methods have been

developed to solve Schrödinger or Schrödinger-like equations by mapping the N-electron Schrödinger equation into effective one-electron Schrödinger-like equations, which are easier to tackle computationally. In the present work, density functional theory (DFT) is used to approximate the ground state energy of Eqn. (4.12), where the electron density is the key quantity.

4.1.6 Hellmann-Feynman Theorem

The calculation of the forces acting on the ions are performed in the present work via the Hellman-Feynman theorem. The Hellmann-Feynman theorem is a powerful and popular method to efficiently calculate forces in a variety of dynamical processes. Let us consider a many-body system with electronic Hamiltonian $\hat{H}(\mathbf{r};\mathbf{R})$. The general form of the force on I-th atom, $\mathbf{F}_I$ is the negative gradient of the total electronic energy with respect to atomic position $\mathbf{R}_I$. Mathematically this can be written as

$$\mathbf{F}_I = -\frac{\partial E}{\partial \mathbf{R}_I}, \tag{4.14}$$

where, $E = \langle \Psi \mid \hat{H} \mid \Psi \rangle + E_{II}$. Then, the force can be written as

$$\mathbf{F}_I = -\frac{\partial E}{\partial \mathbf{R}_I} = -\big\langle \Psi \mid \frac{\partial \hat{H}}{\partial \mathbf{R}_I} \mid \Psi \big\rangle - \big\langle \frac{\partial \Psi}{\partial \mathbf{R}_I} \mid \hat{H} \mid \Psi \big\rangle - \big\langle \Psi \mid \hat{H} \mid \frac{\partial \Psi}{\partial \mathbf{R}_I} \big\rangle - \frac{\partial E_{II}}{\partial \mathbf{R}_I}. \tag{4.15}$$

The 2nd and 3rd terms of the above equation vanish due to the variational principle and then one finds

$$\mathbf{F}_I = -\big\langle \Psi \mid \frac{\partial \hat{H}}{\partial \mathbf{R}_I} \mid \Psi \big\rangle - \frac{\partial E_{II}}{\partial \mathbf{R}_I}. \tag{4.16}$$

This is often called the Hellmann-Feynman theorem or the force theorem [139, 140]. Further it is possible to show that $\mathbf{F}_I$ only depends on the electron density and the

positions of the nuclei

$$\mathbf{F}_I = -\int d\mathbf{r}\rho(\mathbf{r})\frac{\partial V_{ext}(\mathbf{r})}{\partial \mathbf{R}_I} - \frac{\partial E_{II}}{\partial \mathbf{R}_I}. \tag{4.17}$$

4.1.7 Bloch's Theorem

The most common example of Bloch's theorem is describing electrons in a crystal. The ions in a perfect crystal are arranged in a regular periodic way (at $0K$). The requirement needed for the use of Bloch's theorem is that, the external potential felt by the electrons will also be periodic; the period being the same as the length of the cell, **L**. Plane wave basis sets have become the natural choice for the treatment of periodic systems, like solids, because of Bloch's theorem. Bloch's theorem states that the wave function of an electron within a perfectly periodic potential can be written in the following form

$$\psi_{n,\mathbf{k}}(\mathbf{r}) = e^{i\mathbf{k}.\mathbf{r}}u_{n,\mathbf{k}}(\mathbf{r}), \tag{4.18}$$

where, $u_{n,\mathbf{k}}(\mathbf{r})$ is a function that possesses the periodicity as the potential of the one-electron Hamiltonian, *i.e.* $u_{n,\mathbf{k}}(\mathbf{r}+\mathbf{R}) = u_{n,\mathbf{k}}(\mathbf{r})$, where **R** is Bravais lattice vector. For a cell in computer simulation $\mathbf{R} = \mathbf{L}$, where **L** is the size of cell. In Eqn. (4.18), n is the band index and **k** is a wavevector confined in the first Brillouin Zone. Since $u_{n,\mathbf{k}}(\mathbf{r})$ is a periodic function, we may expand it with plane waves in terms of a Fourier series

$$u_{n,\mathbf{k}}(\mathbf{r}) = \sum_{\mathbf{G}} C_{n,\mathbf{G}}\, e^{i\mathbf{G}.\mathbf{r}}, \tag{4.19}$$

where, the **G** are reciprocal lattice vectors defined through $\mathbf{G}.\mathbf{R} = 2\pi m$, where m is an integer and the $C_{n,\mathbf{G}}$ are plane wave expansion coefficients. The electron wave-

functions may therefore be written as

$$\psi_{n,\mathbf{k}}(\mathbf{r}) = \sum_{\mathbf{G}} C_{n,\mathbf{k}+\mathbf{G}}\, e^{i(\mathbf{k}+\mathbf{G}).\mathbf{r}}, \tag{4.20}$$

which is a linear combination of plane waves.

4.2 Density Functional Theory

Density functional theory (DFT) is a theory of electronic structure and the name DFT arises due to the use of functionals (*i.e.* function of another function) of the electron density. The DFT scheme is based on functionals of the electron density (for N electrons) defined as Eqn. (4.8) instead of the many-body wave function $\Psi(\{\mathbf{r}\})$. For this reason, the electron density is the basic variable in DFT to describe the quantum many electrons system. DFT is an alternative way to solve the Schrödinger equation of a many-electron system to calculate the ground state electronic density and energy. For this reason, DFT is known as the ground-state theory and it is also called "a first principles theory". The DFT is a variational method which is at present the most promising and successful approach to compute the electronic structure of matter. Its applicability ranges from atoms, molecules and solids to nuclei and quantum and classical fluids. DFT is also popular due to its balance between accuracy and computational cost. As the density is a function of $\mathbb{R}^3$, the DFT is computationally very simple and readily be applied to much larger systems, containing hundreds or even thosands of atoms. For these reasons DFT has become one of the most powerful tools in first-principles calculations aimed at describing or even predicting properties of molecular and condensed matter systems [137]. The

most two popular versions of the density functional theories are Kohn and Sham (KS) DFT and Hohenberg and Kohn (HK)DFT, which is also known as the orbital free (OF) DFT. DFT expresses the ground state energy for any system as a functional of its electron desity $\rho(\mathbf{r})$ as $E_g = E[\rho(\mathbf{r})]$. The density functional theory by Hohenberg and Kohn (HK) [3] has brought about a satisfactory progress in material science from a theoretical point of view. They have proved that the total energy of a system can be expressed in terms of a functional of the electron charge density. Starting from the HK theory, Kohn and Sham [4] (KS) have derived an expression for the total energy of a system, which is known as KS-DFT. In the KS-DFT, the kinetic energy of the electrons is calculated by solving one-particle like Schrödinger equations which are called KS equation. By incorporating the many particle interaction terms into the exchange correlation energy, E_{xc} they have represented the kinetic energy as that of non-interacting particles. The E_{xc} is defined as the difference between the exact expectation value of the kinetic energy and electron-electron interaction and the expectation value of the kinetic energy T_s and Hartree energy E_H of the auxiliary system (KS model). They also used the local density approximation for E_{xc}, which is based on the homogeneous electron gas. In KS theory, the exchange correlation potential energy is locally approximated by that of homogeneous electron gas, and they are expressed only in the functional of electron charge density. In KS-DFT, the KE term can be approximated in terms of electron density instead of KS orbitals which is the so-called OF-DFT method. The OF-DFT method is the main focus of the present work. The details of the KS-DFT and OF-DFT methods will be dicussed in the section 4.5.

4.2.1 Thomas-Fermi Model

For the first time the Thomas-Fermi (TF) model gives an explicit expression for energy functional and developed independently by Thomas [14] and Fermi [141]. In TF model, the kinetic energy of the electrons is derived from the quantum statistical theory based on the uniform free electron gas, but the electron-nucleus and electron-electron interactions are treated classically. In TF model, the kinetic energy functional has the form

$$T_{TF}[\rho(\mathbf{r})] = \frac{3}{10}\big(3\pi^2\big)^{\frac{2}{3}} \int \rho^{\frac{5}{3}}(\mathbf{r}) d\mathbf{r}. \tag{4.21}$$

The energy formula for an atom is finally obtained using the classical expression for the electron-nucleus potential and the electron-electron potential in terms of electron density alone

$$E_{TF}[\rho] = \frac{3}{10}\big(3\pi^2\big)^{\frac{2}{3}} \int \rho^{\frac{5}{3}}(\mathbf{r}) d\mathbf{r} - Z \int \frac{\rho(\mathbf{r})}{\mathbf{r}} d\mathbf{r} + \frac{1}{2} \int\int \frac{\rho(\mathbf{r}_1)\rho(\mathbf{r}_2)}{\mid \mathbf{r}_1 - \mathbf{r}_2 \mid} d\mathbf{r}_1 d\mathbf{r}_2. \tag{4.22}$$

This is the energy functional of the Thomas-Fermi theory of atoms. In order to determine the correct density to be included in the above equation, they employed a variational principle. They assumed that the ground state of the system is connected to $\rho(\mathbf{r})$ for which the energy E_{TF} is minimized under the constraint

$$\int \rho(\mathbf{r}) d\mathbf{r} = N, \tag{4.23}$$

where, N is the total number of electrons in the atom. Then the ground state electron density must satisfy the variational principle

$$\delta\big\{E_{TF}[\rho] - \mu_{TF}\big(\int \rho(\mathbf{r}) d\mathbf{r} - N\big)\big\} = 0, \tag{4.24}$$

which yields the chemical potential

$$\mu_{TF} = \frac{\delta E_{TF}[\rho]}{\delta \rho(\mathbf{r})} = \frac{1}{2}\big(3\pi^2\big)^{\frac{2}{3}}\rho^{\frac{2}{3}}(\mathbf{r}) - \phi(\mathbf{r}), \tag{4.25}$$

where $\phi(\mathbf{r})$ is the electrostatic potential at point $\mathbf{r}$ due to the nucleus and the entire electron distribution

$$\phi(\mathbf{r}) = \frac{Z}{\mathbf{r}} - \int d\mathbf{r}_2 \frac{\rho(\mathbf{r}_2)}{\mid \mathbf{r} - \mathbf{r}_2 \mid}. \tag{4.26}$$

Eqn. (4.25) can be solved in conjunction with the constraint (4.23), and the resulting electron density then inserted in Eqn. (4.22) to yield the total energy. This is the Thomas-Fermi theory of the atom, an exquisitely simple model [137]. We note that the TF model leads no atomic binding to form molecules or solids.

4.2.2 Hohenberg and Kohn Theorems

The starting point of any discussion of DFT is the Hohenberg-Kohn (HK) theorems. For this reason, the foundation of the density functional theory is the HK theorems. P. Hohenberg and W. Kohn [3] formulated and proved two well known theorems based on the Thomas-Fermi model, which are usually known as the first HK theorem and the second HK theorem. Let us consider the following discussions before starting these theorems.

Let $\hat{H}$ be an electronic Hamiltonian for a system of N electrons. When a system is in the state Ψ, which may or may not satisfy $\hat{H}\Psi = E\Psi$. The average of many measurements of the energy is given by

$$E[\Psi] = \frac{\big\langle \Psi \mid \hat{H} \mid \Psi \big\rangle}{\big\langle \Psi \mid \Psi \big\rangle}, \tag{4.27}$$

where

$$\left\langle \Psi \mid \hat{H} \mid \Psi \right\rangle = \int \Psi^* \hat{H} \Psi d\mathbf{r} \tag{4.28}$$

and

$$E[\Psi] \geq E_g. \tag{4.29}$$

The variational principle states that the energy computed from a guessed Ψ is an upper bound to the true ground state energy E_g. Full minimization of the functional $E[\Psi]$ with respect to all allowed N-electrons wave functions will give the true ground state Ψ_g and energy $E[\Psi_g]$=E_g; that is,

$$E_g = \min_{\Psi} E[\Psi] = \left\langle \Psi_{min} \mid \hat{T} + \hat{V}_{ne} + \hat{V}_{ee} \mid \Psi_{min} \right\rangle. \tag{4.30}$$

Thus, a system of N electrons and given nuclear potential V_{ext}, the variational principle defines a procedure to determine the ground state wave function Ψ_g and hence the ground state energy and other properties of interest. In other words, the ground state energy is a functional of the number of electrons N and the nuclear potential V_{ext}

$$E_g = E_g[N, V_{ext}]. \tag{4.31}$$

It is well established that the external potential in principle determines all the properties of the system [137]. The first Hohenberg-Kohn theorem demonstrates that the ground state density $\rho(r)$ uniquely determines the external potential, up to an arbitrary constant. The energy of the system can be denoted as

$$\begin{aligned} E &= \left\langle \Psi \mid \hat{H} \mid \Psi \right\rangle \\ &= \left\langle \Psi \mid \hat{T} + \hat{V}_{ne} + \hat{V}_{ee} \mid \Psi \right\rangle \\ &= \int V_{ext}(\mathbf{r}) \rho(\mathbf{r}) d\mathbf{r} + \left\langle \Psi \mid \hat{T} + \hat{V}_{ee} \mid \Psi \right\rangle, \end{aligned} \tag{4.32}$$

which is used for the proof of Hohenberg and Kohn first theorem. The proof is done in a simple and extremely elegant manner using the principle of *reductio-ad-absurdum* and this is derived for a non-degenerate system [142].

Suppose there exists two potentials $V_{ext}(\mathbf{r})$ and $V'_{ext}(\mathbf{r})$ differing by more than a constant, yielding the same charge density, $\rho(r)$. The associated Hamiltonians, $\hat{H}_1$ and $\hat{H}'_2$, will therefore have different ground wavefunctions, Ψ_1 and Ψ'_2, that each yield the same charge density, $\rho(r)$. Let us consider E_g and E'_g are the two ground state energies for $\hat{H}_1$ and $\hat{H}'_2$ respectively. Taking Ψ'_2 as a trial function for $\hat{H}_1$ then the Rayleigh-Ritz minimal principle states that

$$\begin{aligned} E_g < \left\langle \Psi'_2 \mid \hat{H}_1 \mid \Psi'_2 \right\rangle &= \left\langle \Psi'_2 \mid \hat{H}'_2 \mid \Psi'_2 \right\rangle + \left\langle \Psi'_2 \mid \hat{H}_1 - \hat{H}'_2 \mid \Psi'_2 \right\rangle \\ &= E'_g + \int [V_{ext}(\mathbf{r}) - V'_{ext}(\mathbf{r})]\rho(\mathbf{r})d\mathbf{r}. \end{aligned} \tag{4.33}$$

Similarly, we have

$$\begin{aligned} E'_g < \left\langle \Psi_1 \mid \hat{H}'_2 \mid \Psi_1 \right\rangle &= \left\langle \Psi_1 \mid \hat{H}_1 \mid \Psi_1 \right\rangle + \left\langle \Psi_1 \mid \hat{H}'_2 - \hat{H}_1 \mid \Psi_1 \right\rangle \\ &= E_g - \int [V_{ext}(\mathbf{r}) - V'_{ext}(\mathbf{r})]\rho(\mathbf{r})d\mathbf{r}. \end{aligned} \tag{4.34}$$

By summing up of Eqn. (4.33) and Eqn. (4.34) the inequality

$$E_g + E'_g < E_g + E'_g \tag{4.35}$$

is obtained, which represents an obvious contradiction, and so there can not be two different $V_{ext}(\mathbf{r})$ that give the same $\rho(\mathbf{r})$ for their ground states. Thus, $\rho(\mathbf{r})$ determines the total number of electrons N in the atom and the external potential $V_{ext}(\mathbf{r})$ and hence all properties related to the ground state. Therefore, the total energy can be

written as a functional of the electron density

$$\begin{aligned} E[\rho] &= T[\rho] + E_{ne}[\rho] + E_{ee}[\rho] \\ &= \int V_{ext}(\mathbf{r})\rho(\mathbf{r})d\mathbf{r} + F_{HK}[\rho], \end{aligned} \tag{4.36}$$

where

$$F_{HK}[\rho] = T[\rho] + E_{ee}[\rho]. \tag{4.37}$$

This functional $F_{HK}[\rho]$ does not depend upon the potential V_{ext} and is the holy grail of density functional theory and contains the functional for the kinetic energy, $T[\rho]$ and that for the electron-electron interaction, $E_{ee}[\rho]$. To obtain the explicit form of the functional F_{HK} is the major challange in DFT.

The second HK theorem introduces that the energy functional is variational. It states that for a trial density $\tilde{\rho}(\mathbf{r})$ that satisfies the conditions, $\tilde{\rho}(\mathbf{r}) \geq 0$ and $\int \tilde{\rho}(\mathbf{r})d\mathbf{r} = N$ for all $\mathbf{r}$, the inequality $E_g \leq E[\tilde{\rho}]$ holds, where $E[\tilde{\rho}] = T[\tilde{\rho}] + E_{ne}[\tilde{\rho}] + E_{ee}[\tilde{\rho}]$.

Following the first Hohenberg-Kohn theorem, suppose that the ground state wave function is Ψ_g and it is related to electron density $\rho(\mathbf{r})$. Thus the ground state density $\rho(\mathbf{r})$ uniquely determines the external potential $V_{ext}(\mathbf{r})$. Let us consider the trial density $\tilde{\rho}$ that determines its own wave function $\tilde{\Psi}$ with a arbitrary variation from Ψ_g, then we can obtain,

$$\begin{aligned} \left\langle \tilde{\Psi} \mid \hat{H} \mid \tilde{\Psi} \right\rangle &= \int \tilde{\rho} V_{ext} d\mathbf{r} + T[\tilde{\rho}] + E_{ee}[\tilde{\rho}] \\ &= E[\tilde{\rho}] \geq E_g[\rho]. \end{aligned} \tag{4.38}$$

So the energy will reach the minimum only when the electron density is equal to the ground state electron density. The above two theorems lead to the fundamental

statement of density functional theory

$$\delta\big\{E[\rho] - \mu\big(\int \rho(\mathbf{r})d\mathbf{r} - N\big)\big\} = 0. \tag{4.39}$$

The ground state energy and density correspond to the minimum of some functional $E[\rho]$ subject to the constraint $\int \rho(\mathbf{r})d\mathbf{r} = N$, provide the correct number of electrons. The Lagrange multiplier of this constraint is the electronic chemical potential μ. Let $\mu(\mathbf{r})=\frac{\delta E[\rho]}{\delta\rho(\mathbf{r})} = V_{ext}(\mathbf{r}) + \frac{\delta F_{HK}[\rho]}{\delta\rho(\mathbf{r})}$. Then Eqn. (4.39) gives the Euler-Lagrange equation

$$\mu(\mathbf{r}) - \mu = 0. \tag{4.40}$$

Due to the HK theorems, the ground state properties can be evaluated using only the density as the variational variable and a universal functional $F_{HK}[\rho]$. The functional $F_{HK}[\rho]$ exists, but its explicit form completely remain in the dark. However, some approximations to $F_{HK}[\rho]$ are known to us and can be used in equation:

$$E_g[N, V_{ext}] = \min_{\rho,\, \rho\to N} E[\rho, V_{ext}] = E_g[\rho, V_{ext}], \tag{4.41}$$

for approximate solution, where $\rho \to N$ means $\int \rho d\mathbf{r} = N$. The functional $E[\rho, V_{ext}]$ contains the classical Coulomb interaction due to the electron density, which can be separated out as

$$E[\rho, V_{ext}] = \int V_{ext}(\mathbf{r})\rho(\mathbf{r})d\mathbf{r} + \frac{1}{2}\int\int \frac{\rho(\mathbf{r}_1)\rho(\mathbf{r}_2)}{\mid \mathbf{r}_1 - \mathbf{r}_2 \mid} d\mathbf{r}_1 d\mathbf{r}_2 + G[\rho]. \tag{4.42}$$

Here $G[\rho]$ includes the kinetic energy and difference between the exact electron-electron energy E_{ee} and the electrostatic interaction energy due to the electron density $\rho(\mathbf{r})$. Hence $G[\rho]$ contains the electron correlations and this effects arising from the exchange term.

4.2.3 The Kohn-Sham Equations

The Kohn-Sham (KS) equations map the relationship between the ground state density of a system and its ground state wave function. The famous Kohn-Sham equations are at the heart of modern density functional theory. The kinetic energy functional of the Thomas-Fermi model that leads to a good description of molecular systems is far from reality. To overcome this problem, Kohn and Sham [4] introduced a fictitious system of non-interacting electrons (referred to as the KS system) in 1965, which generates the same density as the given system of interacting electrons. For this system the kinetic energy is calculated exactly and the total energy functional of the system can be written in the following decomposed form:

$$E[\rho] = T_s[\rho] + E_{ext}[\rho] + E_H[\rho] + E_{xc}[\rho], \tag{4.43}$$

with the external potential energy term $E_{ext}[\rho] = \int V_{ext}(\mathbf{r})\rho(\mathbf{r})d\mathbf{r}$ and the Hartree term $E_H = \frac{1}{2}\int\int \frac{\rho(\mathbf{r}_1)\rho(\mathbf{r}_2)}{|\mathbf{r}_1-\mathbf{r}_2|}d\mathbf{r}_1 d\mathbf{r}_2$. While the first term, $T_s[\rho(\mathbf{r})]$ of Eqn. (4.43) is the kinetic energy functional of a system of non-interacting electrons with density $\rho(\mathbf{r})$ and the last term represents the exchange correlation energy functional defined as the remainder:

$$E_{xc}[\rho] = (T[\rho] - T_s[\rho]) + (E_{ee}[\rho] - E_H[\rho]). \tag{4.44}$$

The Hartree term E_H describes the electrostatic energy of the electronic system within the mean-field appproximation and it is the classical electrostatic energy of a charge density $\rho(\mathbf{r})$. The exchange correlation energy is mainly the difference between the true electrostatic energy E_{ee} and the mean field term E_H but also contains a contribution from the kinetic energy, $T[\rho] - T_s[\rho]$.

The Kohn-Sham equations can represent all of the above terms exactly in terms of the electronic density, except for the exchange correlation energy. Kohn and Sham proposed that the electronic density can be expressed as

$$\rho(\mathbf{r}) = \sum_{i}^{N} \mid \psi_i \mid^2, \tag{4.45}$$

which is the sum of the density of a set of N non-interacting single-particle wave functions (orbitals), ψ_i.

The kinetic energy functional in Kohn-Sham theory is

$$T_s[\rho] = \sum_{i}^{N} -\frac{1}{2} \int \psi_i^*(\mathbf{r}) \nabla^2 \psi_i(\mathbf{r}) d\mathbf{r}, \tag{4.46}$$

which depends explicitly on the orbitals. All remaining terms, including the exchange correlation term $E_{xc}[\rho]$, depend only implicitly on the orbitals, because the density is calculated from the single particle wave functions. The minimization of $E[\rho(\mathbf{r})]$ with respect to $\rho(\mathbf{r})$ subject to the constraint that the number of electrons must be constant, which yields N Hartree-type one-electron equations

$$\big[-\frac{1}{2}\nabla^2 + V_{KS}(\mathbf{r}) \big] \psi_i = \varepsilon_i \psi_i, \tag{4.47}$$

where ψ_i are Kohn-Sham orbitals, ε_i are Kohn-Sham orbital energies and V_{KS} is the one-body effective fictitious external potential, and is defined as

$$V_{KS}(\mathbf{r}) = V_{ext}(\mathbf{r}) + \int \frac{\rho(\mathbf{r_1})}{\mid \mathbf{r} - \mathbf{r}_1 \mid} d\mathbf{r_1} + V_{xc}[\rho(\mathbf{r})], \tag{4.48}$$

which depends on $\rho(\mathbf{r})$. In Eqn. (4.48) $V_{xc} = \frac{\delta E_{xc}}{\delta \rho}$ is the exchange correlation potential.

Eqns. (4.45), (4.47) and (4.48) are known as the famous Kohn-Sham equations where only unknown term is E_{xc}. It is widely known that the KS equation gives the

exact total energy of a system. The KS Eqn. (4.47) requires to be solved iteratively until the self-consistent orbitals are determined due to the density dependence on the one-electron KS effective potential, $V_{KS}(\mathbf{r})$. Finally, the total energy can be determined from the Kohn-Sham eigenenergies and the ground state density $\rho(\mathbf{r})$ as

$$E = \sum_{i=1}^{N} \varepsilon_i - \int d^3r \big[\frac{1}{2} V_H(\mathbf{r}) + V_{xc}(\mathbf{r})\big]\rho(\mathbf{r}) + E_{xc}[\rho(\mathbf{r})].$$

If each term in the KS energy functional was known, we would be able to obtain the exact ground state density and total energy. Unfortunately, we do not know the exact form of the exchange correlation energy functional, E_{xc} and even it is impossible to find an exact expression for E_{xc} except for a free electron gas. This term includes the non-classical aspects (electron exchange and electron correlation) of the electron-electron interaction, along with the component of the kinetic energy of the real system different from the non-interacting electrons system. At this point, finding the approximate form for the exchange correlation energy functional with a sufficient accuracy is the biggest challange of the modern DFT. Kohn and Sham [4,137] proposed a form for the exchange correlation (XC) energy functional which was exact for the uniform electron gas (UEG) system, known as the local density approximation (LDA). In the next section we will focus on various approximations for XC functionals.

4.3 Exchange Correlation Energy Functionals

The ground state energy contribution that needs practical approximations within KS-DFT approach is the exchange correlation functional. The exchange correlation functional is also used in the OF-DFT method similar to that of the KS-DFT

method. The success of a DFT calculation scheme critically depends on the quality of the exchange correlation. The exchange arises from antisymmetry due to the Pauli exclusion principle. On the other hand the correlation accounts for the remaining complicated many-body effects that need many determinants to be fully described. The problem of finding exact form of E_{xc} is the greatest challange in the DFT because E_{xc} is not known that we have already mentioned before. It will be very difficult to express E_{xc} in a closed mathematical form. Finding of such mathematical form would be considered as a great success in the density functional theory. Since the form of exchange correlation energy in terms of the density is, in general, unknown and therefore it is necessary to use an approximation for E_{xc}. There are two most common approximations for E_{xc} widely used by the scientists. These are namely local density approximation (LDA) and generalized gradient appproximation (GGA).

4.3.1 Local Density Approximation

The Local density approximation (LDA) is the first approximation for the exchange correlation (XC) functional $E_{xc}[\rho]$. LDA states that the density can be treated locally as an uniform electron gas and the exchange and correlation energy at each point in the system is the same as that of an uniform electron gas (UEG) of the same density. This approximation was originally introduced by Kohn and Sham [4] and strictly, the LDA is valid only if the density $\rho(\mathbf{r})$ varies extremely slow with $\mathbf{r}$. In local density approximation (LDA) to the DFT one assumes that $E_{xc}[\rho]$ is given by

$$E_{xc}^{LDA}[\rho(\mathbf{r})] = \int \rho(\mathbf{r})\varepsilon_{xc}^{LDA}[\rho(\mathbf{r})]d\mathbf{r}, \tag{4.49}$$

where, ε_{xc}^{LDA} is the exchange correlation energy per particle in an uniform electron gas, which is a function of the density $\rho(\mathbf{r})$ only. The $\varepsilon_{xc}^{LDA}(\rho)$ can be decomposed into an exchange part and a correlation part, such as $\varepsilon_{xc}^{LDA}[\rho] = \varepsilon_{x}^{LDA}[\rho] + \varepsilon_{c}^{LDA}[\rho]$.

The exchange part is simple and given by the Dirac energy functional [10]

$$\varepsilon_{x}^{LDA}[\rho(\mathbf{r})] = -\frac{3}{4}\left(\frac{3}{\pi}\right)^{\frac{1}{3}} \rho(\mathbf{r})^{\frac{1}{3}}, \tag{4.50}$$

while the correlation energy $\varepsilon_c(\rho)$ is more complicated. The accurate values for $\varepsilon_c(\rho)$ have been determined by the Quantum Monte Carlo (QMC) calculations of Ceperley and Alder [11]. The common LDA functionals for $\varepsilon_{c}^{LDA}[\rho(\mathbf{r})]$ are the Perdew-Zunger (PZ) [13], Perdew-Wang (PW) [143] and Vosko-Wilk-Nusair (VWN) [12] functionals. Mostly used approximation for the correlation is the Perdew-Zunger approximation [13]. It has the form

$$\varepsilon_{c}^{LDA}[\rho] = \begin{cases} 0.0311\,\mathrm{l}nr_s - 0.0480 + 0.0020\,r_s\,\mathrm{l}nr_s - 0.0116r_s & \text{for } r_s < 1 \\ -\frac{0.1423}{1+1.0529\sqrt{r_s}+0.3334r_s} & \text{for } r_s \geq 1. \end{cases} \tag{4.51}$$

This is used in the present simulation. The functional derivative of $E_{xc}^{LDA}[\rho]$ gives the exchange correlation potential within LDA,

$$V_{xc}^{LDA} = \frac{\delta E_{xc}^{LDA}[\rho]}{\delta\rho(\mathbf{r})} = \varepsilon_{xc}[\rho(\mathbf{r})] + \rho(\mathbf{r})\frac{\partial\varepsilon_{xc}[\rho]}{\partial\rho}.$$

4.3.2 Generalized Gradient Appproximation

The exchange correlation energy not only depends on the local density but also on the gradient of the density, allowing to take into account the variations of the electron density in very inhomogeneous systems. The LDA is appropriate for smooth $\rho(\mathbf{r})$,

i.e. for solids close to the homogeneous electron gas. But LDA is not accurate for inhomogeneous systems such as molecules, clusters or layers. An improvement to this approximation can be achieved by considering the gradient of the electron density, which is known to be the so-called generalized gradient approximation (GGA).

The generic formulation of the GGA approximation to $E_{xc}[\rho]$ is

$$E_{xc}^{GGA}[\rho] = \int \rho(\mathbf{r})\varepsilon_{xc}^{GGA}\big[\rho(\mathbf{r}), \mid \nabla\rho(\mathbf{r}) \mid \big]d\mathbf{r} \tag{4.52}$$

and the general procedure for constructing GGA functional is to express the correlation energy as

$$E_{xc}^{GGA}[\rho(\mathbf{r})] = \int \rho\, \varepsilon_{xc}^{LDA}[\rho(\mathbf{r})]d\mathbf{r} + \int F_{xc}[\rho(\mathbf{r}), \mid \nabla\rho(\mathbf{r}) \mid]d\mathbf{r}, \tag{4.53}$$

where, $F_{xc}[\rho(\mathbf{r}), \mid \nabla\rho(\mathbf{r}) \mid]$ is known to be the exchange correlation enhancement factor. Unlike the LDA, there is no unique form for the GGA, and indeed many suitable variations are possible [8, 9, 144, 145], each corresponding to a different enhancement factor. The GGA succeeds in reducing the effects of LDA overbinding [146], and is significantly more successful when applied to molecules. The Perdew-Burke-Ernzerhof (PBE) functional [8] is the most popular GGA.

4.4 Pseudopotentials

In this section we will introduce the concept of pseudopotentials. It is well established that the most interesting physical properties of solids are largely determined by the valence electrons rather than the tightly bound core electrons. This is the reason why the pseudopotential approximation come into play in the theory. This approximation

uses the fact to remove the core electrons including the nucleus and replace them with a weaker pseudopotential which acts on a set of pseudo wavefunctions rather than the true valence wavefunctions. In fact, the pseudopotential can be optimised so that, in practice, it is even weaker than the frozen core potential [147].

The core electrons and the nuclei are treated as unit which interacts with the valence electrons through the external potential V_{ext}, which usually is the pseudopotential. The solid is made up of lighter electrons and heavier nuclei. In many problems of molecular and atomic physics, the electrons of the system can be divided into the category of valence electrons and core electrons per atom. The core electrons are tightly bound near the nuclei which known as core region. The fundamental concept involved in a pseudopotential calculation is that the ion core can be neglected. The use of pseudopotentials rely on the fact that the core electrons are tightly bound to their host nuclei while only the valence electrons are involved in the chemical bonding. In the pseudopotential approximation, the core electrons density is assumed to be of the same form as for isolated atoms. Core electrons screen the nuclear potentials seen by the valence electrons. At the same time, core electrons are much lower in energy than valence electrons. Thus due to the requirement of orthogonal wave functions, valence electrons wave functions have a strong oscillatory part in the internal regions. This requires many more basis functions to accurately describe the valence electrons wave functions. Pseudopotentials are fictitious potentials that act in the internal regions of the atom, reproducing the screening effect of the core electrons within core region which is determined by cutoff radius. Both the potentials and wave functions outside of the core region are fitted to reproduce the real ones. The

quality of a pseudopotential is measured by its transferability, *i.e.*, the capacity of reproducing accurate results for all-electron calculations. A pseudopotential is not unique, therefore several popular models are also exist in the literature.

These pseudopotentials should have the following four fundamental properties [148]:

(i). Real and pseudo valence eigenvalues agree for a chosen prototype atomic configureation.

(ii). Real and pseudo atomic wave functions agree beyond a chosen core radius R_c.

(iii). The integrals from 0 to r of the real and pseudo charge densities agree for $r \geq R_c$ for each valence state (norm conservation).

(iv). The logarithmic derivatives of the real and pseudo wave function and their first energy derivatives agree for $r \geq R_c$.

The pseudopotential potential may be either local or non-local. Both the non-local and local form of pseudopotential give accurate prediction for the properties of materials [149]. Particularly, the non-local pseudopotentials are energy eigenvalue dependent. So the exact form of pseudopotential is quite complicated and its formulation is therefore often difficult. The two most popular non-local pseudopotential are norm conserving pseudopotentials and ultrasoft pseudopotential. Norm-conserving pseudopotentials require that the all-electron and pseudo wave function agree beyond a chosen radius R_c. Also the integrated density inside R_c for the all-electron wave function and pseudo wave function are the same ("norm conservation"). There are many types of norm-conserving pseudopotentials from different authors such as

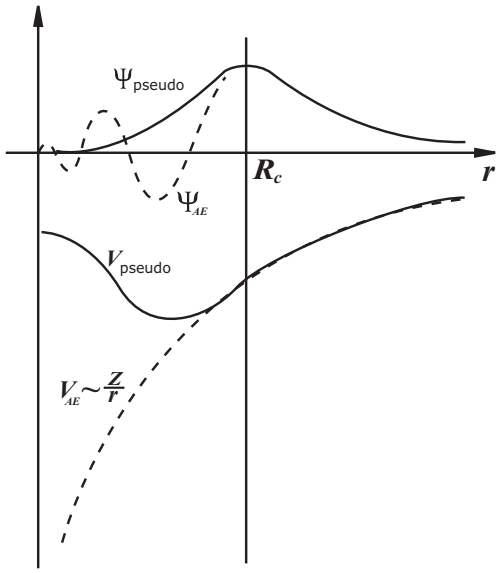

Figure 4.1: Schematic diagram of pseudopotential method [155], V_{AE}, Ψ_{AE} are the all electron potential and wave function, respectively.

Troullier and Martins [150], Kerker [151], Hamann, Schlüter and Chiang [152], Vanderbilt [153], Goedecker-Teter-Hutter [154]. The local model pseudopotential depends on the ion positions only. Hence they are generally used to investigate the properties of the matter for the simplicity in the computations. Up till present we have observed that for the construction of the local potential one must consider:

(i). The bare-ion local potential by which the electrons interacts with the ions.

(ii). Hartree screening to take account of Coulomb interactions with the other conduction electrons.

(iii). Effect of exchange and correlation.

The KS-AIMD method usually employs non-local pseudopotentials obtained by fitting to some properties of the free atom [150, 156–158]. However, in the OF-AIMD

method the valence electron density is the basic variable. The lack of orbitals requires that the pseudopotential must be independent of angular momentum, but a function of radius only. Most modern pseudopotentials such as norm-conserving or ultra-soft pseudopotential contain several angular momentum contributions. They are described nonlocally and can not be used in the OF method. Hence, local pseudopotentials (LPS) are needed for the OF-AIMD simulation method. Therefore, we have here used a local ionic pseudopotential proposed by Bhuiyan *et al.* [17]. The concept of pseudopotential is shown schematically in Figure 4.1 [155]. It is clear from the Figure 4.1 that the pseudopotential is much weaker than the all-electron potential and the pseudo wave function has no radial node inside the core region. We also see that outside the core region, the pseudopotential and wave function becomes the same with the corresponding all-electron ones.

The present local ionic pseudopotential in combination with the OF-AIMD method has provided a good description of several static and dynamic properties of liquid Sn, Cu, Ag, Au, Cd, Hg and Zn at thermodynamic states near their respective melting points [5, 17, 18] and above. The pseudopotential used in our purpose has the form

$$v_{ps}(r) = \begin{cases} A + B\,\exp(-r/a) & \text{for } r < R_c \\ -\frac{Z}{r} & \text{for } r > R_c, \end{cases} \tag{4.54}$$

where, A and B are constants, R_c is the core radius and a is the softness parameter. Moreover, the parameter B has been fixed by the condition that the logarithmic derivative of the potential inside and outside the core exactly matches at the core radius. The other parameters R_c, A and a have been fixed by imposing that the OF-

AIMD simulation reproduces the experimental static structure factor. The values of the parameters R_c, A and a used in our calculations are listed in the Table 6.1. The form factor of $v_{ps}(r)$ in reciprocal space is

$$\begin{aligned} v_{ps}(q) &= \frac{1}{V}\big[\cos qR_c\big\{-\frac{4\pi AR_c}{q^2}-\frac{4\pi}{q^2}-\frac{4\pi Ba^2R_ce^{-\frac{R_c}{a}}}{(1+a^2q^2)}-\frac{8\pi Ba^3R_ce^{-\frac{R_c}{a}}}{(1+a^2q^2)^2}\big\}+ \\ &\quad \sin qR_c\big\{\frac{4\pi A}{q^3}-\frac{4\pi BaR_ce^{-\frac{R_c}{a}}}{q(1+a^2q^2)}+\frac{4\pi Ba^4qe^{-\frac{R_c}{a}}}{(1+a^2q^2)^2}-\frac{4\pi Ba^2e^{-\frac{R_c}{a}}}{q(1+a^2q^2)^2}\big\}+ \\ &\quad \frac{4\pi}{q^2}+\frac{8\pi Ba^3}{(1+a^2q^2)^2}\big] \end{aligned}$$

where, the constant B is given by $B=\frac{Aae^{\frac{R_c}{a}}}{R_c-a}$ and V is the volume of a system.

4.5 Orbital Free Density Functional Theory (OF-DFT)

The total energy function of OF-DFT is construct by taking approximations in the KE functional and the external potential energy functional of KS-DFT. Therefore, the main difference between KS-DFT and OF-DFT is the kinetic energy (KE) and external potential energy functional appproximations. In KS-DFT theory, the KE depends on the KS fictitious orbitals for noninteracting system while the external potential energy is described by the nonlocal pseudopotentials. On the other hand the KE in OF-DFT depends on the electron density and external potential energy is described by the local pseudopotentials.

In KS-DFT, the numerical value of $T_s[\rho]$ could be determined exactly although it is not directly from the density itself. It is done by introducing a set of N one electron wave functions (KS orbitals) to solve the N coupled KS equations that describe the fictitious noninteracting system. By using these results along with the relatively

simple appproximations for the small contribution term E_{xc}, the resulting KS-DFT has proven successful in many applicaions. Multiple approximations to the exchange correlation term exist [12, 13, 143] which provide acceptable accuracy in simulation to study specific properties for specific class of materials. Different approximations are used in different applications. In KS-DFT, it is necessary to compute at least as many orbitals as there are electrons (or pairs thereof). Futher, the KS equation must be solved iteratively because of V_{KS} depends on ρ. The solution involves large basis set expansions of the orbitals. The use of the KS orbitals usually generates a relatively expensive $O(N^3)$ scaling of computational cost with the number of electrons. This cubic scaling is the bottleneck for the application of DFT for very large systems. Despite of all limiations we need for a routine *ab initio* calculation on large systems. The basic algorithm of KS-DFT to find the ground state energy and the density of a system of N electron moving in a specific external potential $V_{ext}(\mathbf{r})$ is then as follows:

(i). Guess an initial density, $\rho(\mathbf{r})$.

(ii). Computation of the potential using

$$V_{KS}(\mathbf{r}) = V_{ext}(\mathbf{r}) + \int \frac{\rho(\mathbf{r_1})}{\mid \mathbf{r} - \mathbf{r}_1 \mid} d\mathbf{r_1} + V_{xc}[\rho(\mathbf{r})].$$

(iii). Find the N lowest-energy solutions of Schrödinger equations

$$\big[-\frac{1}{2}\nabla^2 + V_{KS}(\mathbf{r})\big]\psi_i = \varepsilon_i \psi_i.$$

(iv). Construct a new density from the wave functions for all occupied states,

$$\rho(\mathbf{r}) = \sum_{i}^{N} \mid \psi_i \mid^2.$$

(v). If the density does not converge, go to step (ii).

(vi). Compute the ground state energy from

$$E = \sum_{i=1}^{N} \varepsilon_i - \int d^3r \big[\frac{1}{2} V_H(\mathbf{r}) + V_{xc}(\mathbf{r})\big] \rho(\mathbf{r}) + E_{xc}[\rho(\mathbf{r})].$$

The bottleneck of KS-DFT could be removed if there were a proper treatment of the KE using the electron density only. The spirit of the DFT by Hohenberg and Kohn is to express the ground state energy in terms of the charge density without using wave functions, such DFT is called orbital free DFT. The scaling of OF-DFT is linear. This spirit comes from an earlier density functional theory proposed by Thomas [14] and Fermi (TF) [141], which expresses an exact energy for the system of

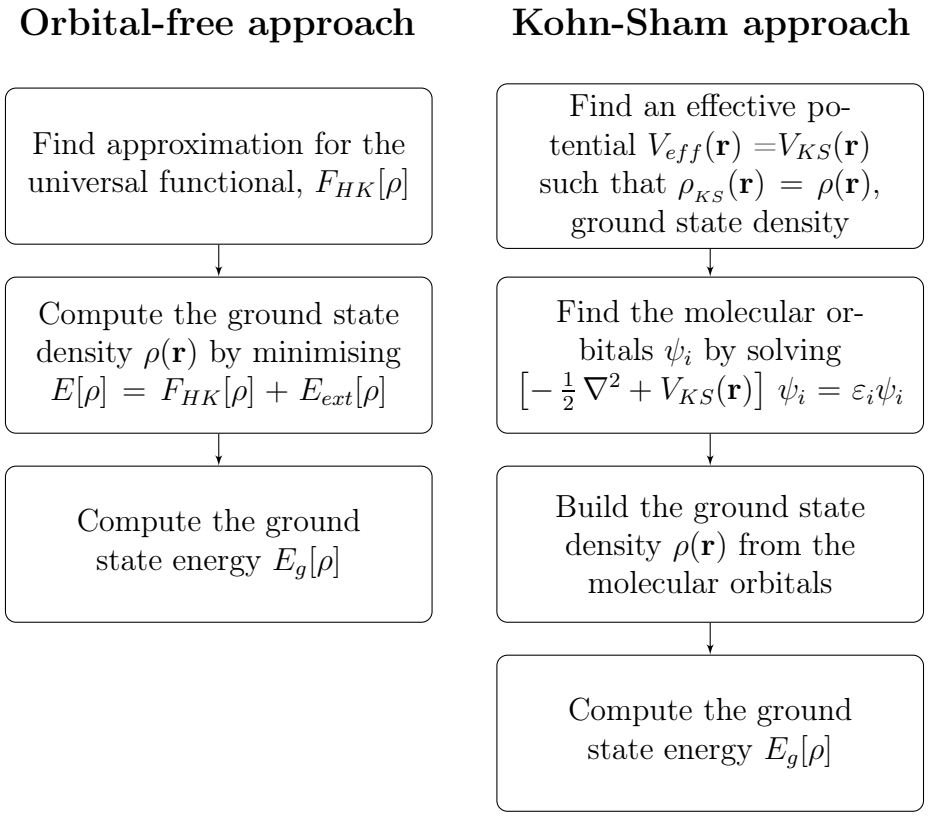

Figure 4.2: Orbital-free approache *vs.* Kohn-Sham DFT approache.

the non-interacting homogeneous electron gas. This functional is called TF energy functional. In the KS theory, a long computational time is required depending on the number of orbitals. However, if we can evaluate the kinetic energy without solving the KS equations, we can obtain the total energy in a short computational time. Among all the first-principles methods calculation based on DFT [3, 4], the linear scaling OF-DFT is the most capable scheme for handling large systems ($>$ 1000 particles) within reasonable computational times [159–168]. Unlike traditional orbital-based first-principles techniques, such as Hartree-Fock [169–171] and KS-DFT [4] , the OF-DFT method avoids solving self-consistently for one-electron orbitals and instead only utilizes the electron density, a function of three coordinates, as its main variational parameter [172]. Consequently, the costs associated with manipulating orbitals (*e.g.*, orthonormalization) are completely eliminated. For periodic systems, the advantage of using OF-DFT is even more remarkable, since no k-point sampling is necessary, leading to many orders of magnitude savings for metallic systems, in particular [159].

Although the earliest OF-DFT, namely, the TF model [14, 141] appeared much earlier before as widely used today KS-DFT and OF-DFT have not become the mainstream quantum mechanics method for practical applications. The major obstacle of applying OF-DFT lies in the lack of transferability of kinetic energy density functionals (KEDF). If this stumbling block could be removed, one could fully exploit the power of the original Hohenberg-Kohn theorems [3]. There are several KEDF approximations exist in literature [14, 141, 173–176]. The TF kinetic energy functional $T_{TF}[\rho(\mathbf{r})] = \frac{3}{10}\left(3\pi^2\right)^{\frac{2}{3}} \int \rho^{\frac{5}{3}}(\mathbf{r}) d\mathbf{r}$ is valid for slowly varying densities but not sufficient for application in rapidly varying densities. So, von Weizsäcker [173] proposed

a correction term for the TF energy functional which is $T_W[\rho(\mathbf{r})] = \frac{1}{8}\int \frac{|\nabla\rho(\mathbf{r})|^2}{\rho(\mathbf{r})}d\mathbf{r}$. It is called von Weizsäcker kinetic energy functional and it is exact for one-electron and two-electron singlet states [173]. A linear combination of these two simplest approximations, TF and von Weizsäcker KE functionals, is called Thomas-Fermi-von Weizsäcker KE functional. It has seen to appear in many OF-DFT applications [177]. Jones and Young [178, 179] have shown that the TF energy functional gives a correct second-order kinetic energy for the slowly varying density limit and the von Weizsäcker energy functional gives the correct one for the rapidly varying density limit. The OF-DFT and KS-DFT calculation steps are shown in Figure 4.2.

4.5.1 Kinetic Energy Functional Approximmation

The kinetic energy functional $T_s[\rho]$ is a critical ingredient of the total energy functional of a system. It is generally considered that the von Weizsäcker term $T_W[\rho(\mathbf{r})]$ is essential for a good description of the kinetic energy [173]. It applies in the case of rapidly varying densities, and it is exact for one, or two-electron systems. Further terms are usually added to the functional in order to reproduce some exactly known limits correctly [15]. In the uniform density limit, the exact kinetic energy is given by the Thomas-Fermi functional

$$T_{TF}[\rho] = \frac{3}{10}\int \rho(\mathbf{r})k_F(\mathbf{r})^2 d\mathbf{r}, \tag{4.55}$$

where $k_F(\mathbf{r}) = \left(3\pi^2\rho\right)^{\frac{1}{3}}$ is the local Fermi wave vector. In the limit of almost uniform density, the linear response theory (LRT) is correct, with a response function corresponding to a noninteracting uniform electron gas, which is given by the Lindhard function $\chi_L(q, \rho_0)$ [104, 180].

There has been an increasing interest in the development of accurate kinetic energy functional due to the tremendous advantages of the OF-AIMD simulation. Depending on Perrot's [176] work as the basis, Madden and co-workers [181, 182] improved functionals which recovers the Thomas-Fermi and linear-response limits correctly, and it is also comprised the quadratic response. Later, Wang *et al.* [183, 184] examined these functionals and suggested a linear combination of them as a satisfactory form for T_s. They also derived another expression which includes density-dependent kernels. Unfortunately, an undesirable feature of these functionals is that they are not positive definite, so that a minimization of the energy functional can lead to an unphysical negative kinetic energy. Chacón *et al.* [185] developed a different type of kinetic energy functional, which employs an "averaged density" which recovers LRT and the uniform density limits. Their functional was investigated and generalized by García-González *et al.* [186–188]. These functionals have the merit of being positive definite, but they are somewhat complicated to apply and require N order more fast Fourier transforms (FFT) than simpler functionals. This diminishes the advantage of the orbital free approach over the full Kohn-Sham method [15].

4.5.2 Simplified Average Density Form for $T_s[\rho]$

The KE functional is the key portion for OF-DFT approach. So a reliable density functional for the kinetic energy (KE) is needed for a successful OF-DFT calculation. For $T_s[\rho]$, we have used an explicit, albeit approximate functional of the valence electron density. Several expressions were proposed for $T_s[\rho]$ and in the vicinity of the present work we have used an averaged density model [15, 19, 186–188] which has

the following form

$$T_s[\rho] = T_W[\rho] + T_\beta[\rho], \text{ with} \tag{4.56}$$

$$T_W[\rho(\mathbf{r})] = \frac{1}{8}\int \frac{\mid \nabla\rho(\mathbf{r}) \mid^2}{\rho(\mathbf{r})} d\mathbf{r} \tag{4.57}$$

$$T_\beta[\rho] = \frac{3}{10}\int d\mathbf{r}\rho(\mathbf{r})^{\frac{5}{3}-2\beta}\tilde{k}(\mathbf{r})^2, \text{where} \tag{4.58}$$

$$\tilde{k}(\mathbf{r}) = (2k_F^0)^3 \int d\mathbf{s}k(\mathbf{s})w_\beta(2k_F^0 \mid \mathbf{r}-\mathbf{s} \mid), \tag{4.59}$$

$$k(\mathbf{r}) = (3\pi^2)^{\frac{1}{3}}\rho(\mathbf{r})^\beta. \tag{4.60}$$

Here k_F^0 being the Fermi wave vector corresponding to a mean electron density $\rho_0 = \frac{N_e}{V}$. In Eqn. (4.59), the weight function, $w_\beta(x)$, is chosen so that both the linear response theory and Thomas-Fermi limits are correctly recovered. It is worth noticed that $\tilde{k}(\mathbf{r})$ appears as a convolution which can be performed rapidly by the usual FFT techniques. This functional is one of the generalization with $\beta = \frac{1}{3}$, used by Gómez *et al.* [189] earlier to study the expanded liquid Cs. Further details are appeared in reference [15].

The main characteristics of the KE functional are as follows:

(i). β is a real positive number whose maximum value is ≈ 0.6 which leads to a mathematically well behaved weight function.

(ii). The functional is positive definite and recovers LRT and the uniform density limits.

(iii). When $k_F^0 \to 0$, the mean electron density vanishes (*e.g.*, for a finite system), the von Weizsäcker term is recovered if $\beta = 4/9$, whereas for other values of β, the limit is $T_W + C^2 T_{TF}$.

(iv). For values of $\beta > 0.5$, it is expected that the driving force for the dynamic minimization of the energy, $\mu(\mathbf{r})\psi(\mathbf{r})$ [see Eqn. (4.73)], remains finite even for very small electronic densities $\rho(\mathbf{r})$.

The last two properties mentioned above are important for the case of expanded liquid metals because of the appearance of large inhomogeneities in the atomic distribution, and therefore in the electron density, with regions where it becomes very small. Indeed, this situation has already been observed in the *ab initio* simulations of expanded liquid Na [190]. In systems for which the appearance of isolated atoms or clusters is likely, the von Weizsäcker term would be appropriate, and a functional with a value of β as close as possible to 4/9 would be recommended. For the present simulations we have used $\beta = 0.51$ which gives $C = 0.046$ [15] in the limit $\rho_0 \to 0$ and guarantees at least for the preferred thermodynamic states, $\mu(\mathbf{r})\psi(\mathbf{r})$ remains finite and not too large everywhere so that the energy minimization can be achieved.

4.5.3 Energy Minimization Technique in OF-DFT

In this section we have described the main features of the energy functional and its calculational scheme. Liquid metals which can be dropped in the group of simple liquids are generally modelled as disordered systems in the long range but ordered in short range. Let us consider that N ions each of valence Z are kept in a volume V, and interacting with $N_e = NZ$ valence electrons through a potential $v(r)$. The total potential energy of the system can be written, within the Born-Oppenheimer approximation, as the sum of the direct ion-ion coulombic interaction energy plus the ground state energy of the electronic system under the external potential created by

the ions, $V_{\rm ext}(\mathbf{r},\{\mathbf{R}_l\}) = \sum_{i=1}^{N} v(|\mathbf{r}-\mathbf{R}_i|)$,

$$E[\rho,\{\mathbf{R}_l\}] = \sum_{i<j} \frac{Z^2}{|\mathbf{R}_i-\mathbf{R}_j|} + E_g[\rho(\mathbf{r}), V_{\rm ext}(\mathbf{r},\{\mathbf{R}_l\})]\,, \tag{4.61}$$

where $\rho(\mathbf{r})$ is the ground state valence electronic density and $\mathbf{R}_l$ $(l = 1, 2, \ldots N)$ are the ionic positions. Now according to the DFT, the ground state valence electronic density, $\rho(\mathbf{r})$, minimizes the energy functional $E[\rho]$ as defined in Eqn. (4.43).

For a given set of ionic positions $\{\mathbf{R}_l\}$, that is, for a given external potential $V_{\rm ext}$, the ground state is obtained from the variational principle,

$$\frac{\delta\mathcal{F}}{\delta\rho(\mathbf{r})} \equiv \frac{\delta}{\delta\rho(\mathbf{r})}(E[\rho,\{\mathbf{R}_l\}] - \mu\int\rho(\mathbf{r})d\mathbf{r}) = 0, \tag{4.62}$$

where, μ is the chemical potential of electrons chosen in such a way that it gives the desired number of electrons $N_{\rm e}$. If we define the position dependent chemical potential, $\mu(\mathbf{r})$, by

$$\begin{aligned}\mu(\mathbf{r}) &= \frac{\delta E}{\delta\rho(\mathbf{r})} \\ &= \frac{\delta T_s}{\delta\rho(\mathbf{r})} + \frac{1}{2}\int\int\frac{\rho(\mathbf{r}_2)}{|\,\mathbf{r}-\mathbf{r}_2\,|}d\mathbf{r}_2 + V_{\rm ext}(\mathbf{r}) + V_{xc}(\mathbf{r}),\end{aligned} \tag{4.63}$$

with $V_{xc} = \frac{\delta E_{xc}}{\delta\rho(\mathbf{r})}$, the ground state density and energy are found self-consistently by solving the equation

$$\frac{\delta\mathcal{F}}{\delta\rho(\mathbf{r})} \equiv \mu(\mathbf{r}) - \mu = 0 \tag{4.64}$$

together with the normalization constraint

$$\mathcal{G}[\rho(\mathbf{r})] = \int_v \rho(\mathbf{r})d\mathbf{r} = N_e. \tag{4.65}$$

We have found it is convenient to work in terms of a single effective orbital $\psi(\mathbf{r})$ instead of $\rho(\mathbf{r})$, such that

$$\rho(\mathbf{r}) = |\,\psi(\mathbf{r})\,|^2, \tag{4.66}$$

and to vary $\psi(\mathbf{r})$ rather than $\rho(\mathbf{r})$ [181, 182, 191–197]. This has the advantage of maintaining $\rho(\mathbf{r}) \geq 0$ if ψ is real. The effective orbital, $\psi(\mathbf{r})$ can be expanded into Fourier series in plane waves compatible with the simple cubic periodic boundary conditions of the simulation as

$$\psi(\mathbf{r}) = \sum_{\mathbf{G}} c_{\mathbf{G}} e^{-i\mathbf{G}.\mathbf{r}} \tag{4.67}$$

$$c_{\mathbf{G}} = \frac{1}{V} \int_{\mathrm{v}} d\mathbf{r} \psi(\mathbf{r}) e^{i\mathbf{G}.\mathbf{r}} \tag{4.68}$$

$$\mathbf{G} = \frac{2\pi}{L}(n_1, n_2, n_3), \tag{4.69}$$

where L stands for the side of the cube, V is the volume of the cell and $\mathbf{G}$ is a reciprocal lattice vector of the superlattice. This expansion is truncated at wave vectors corresponding to a given cutoff energy, E_{cut}. A real $\psi(\mathbf{r})$ implies that $c_{-\mathbf{G}} = c^*_{\mathbf{G}}$, with a real c_0. As a result only the half-set $\{c_{-\mathbf{G}}\}$'s need be treated as variables. Now the energy minimization with respect to $\{c_{-\mathbf{G}}\}$'s instead of the electron density, leading to the following equations

$$\frac{\partial \mathcal{F}}{\partial c_0} = 2 \int_{\mathrm{v}} d\mathbf{r} \mu(\mathbf{r}) \psi(\mathbf{r}) - 2\mu V c_0 = 0, \tag{4.70}$$

$$\frac{\partial \mathcal{F}}{\partial c_{\mathbf{G}}} = 4 \int_{\mathrm{v}} d\mathbf{r} \mu(\mathbf{r}) \psi(\mathbf{r}) e^{i\mathbf{G}.\mathbf{r}} - 4\mu V c_{\mathbf{G}} = 0, \tag{4.71}$$

for the ground state density. A simple quenching method is employed to perform the minimization of the energy functional at each time step of the simulation. A fictitious kinetic energy for electrons

$$T_e = \frac{1}{2} M_e \sum_{\mathbf{G}} | \dot{c}_{\mathbf{G}} |^2 \tag{4.72}$$

is introduced following Car and Parrinello [119], where M_e is the fictitious mass of electrons and the dot denotes the derivative with respect to the fictitious time t_e. This

kinetic energy, rewritten in terms of the set $c_{\mathbf{G}}$, together with the "potential energy" $\mathcal{F}$, leads to the following equation of motion for the electron density ($\forall\ c_{\mathbf{G}} \in \{c_{\mathbf{G}}\}$) as [15]

$$M_e \ddot{c}_{\mathbf{G}} = -2 \int_{\mathrm{v}} d\mathbf{r} \mu(\mathbf{r}) \psi(\mathbf{r}) e^{-i\mathbf{G}.\mathbf{r}} + 2\mu V c_{\mathbf{G}}. \tag{4.73}$$

These equations are solved numerically by using the Verlet Leap-frog algorithm [124] with an electronic time step, Δt_e. The velocities are quenched at every time step until the minimum is reached within preset tolerances on T_e and the gradient of the potential energy, $\mathcal{F}$. The chemical potential μ is not known in advance of the minimization, but replacing μ in Eqn. (4.73) by its stationary value

$$\frac{\int d\mathbf{r} \mu(\mathbf{r}) n(\mathbf{r})}{\int d\mathbf{r} n(\mathbf{r})}, \tag{4.74}$$

at each time step, gives a good convergence to the ground state with the "displaced" density $n(\mathbf{r}) = \rho(\mathbf{r}) - \rho_0$ [15].

The interatomic forces are obtained from the electronic ground state via the Hellman-Feynman theorem

$$\mathbf{F}_i = -\nabla_{\mathbf{R}_i} E_g[\rho(\mathbf{r}), \{\mathbf{R}_l\}],\ (i = 1, \ldots, N), \tag{4.75}$$

and the Newton's equations of motion for the ions

$$\frac{d^2 \mathbf{R}_i}{dt^2} = \frac{\mathbf{F}_i}{M_i} \tag{4.76}$$

are solved numerically by using the Verlet Leap-frog algorithm [124] with an appropriate time step, Δt.

Chapter 5

Liquid State Theories

This chapter deals with the static and dynamic properties related theories of the liquid systems. We have also discussed the technique how these properties are being calculated. Within the scope of the present work the description of the following topics namely, the pair distribution function, static structure factor, self-intermediate scattering function, intermediate scattering function, self-diffusion coefficient, dynamic structure factor and shear viscosity are given. The transport coefficient such as the sound velocity is calculated from the slope of the dispersion curve which is obtained from the position of the side peaks of the dynamic structure factor.

5.1 Static Properties

Theories for the static properties such as the static structure factor, isothermal compressibility, pair distribution function and coordination number are briefly described in this section. Static properties depend only on a single time point. The static

structure factor of matter can be directly measured by X-ray or neutron diffraction experiment and it is related to the pair distribution function (PDF). The PDF is a very important ingredient in the theory of liquids and is used to identify the lattice structure of the crystalline solids. Different static distribution functions are often used to have the detailed information regarding the structure of atomic systems. Among them the PDF is the most important one and this can not be measured directly from the experiment. Therefore, we may calculate PDF either from the molecular dynamics (MD) simulation or from the numerical Fourier transformation (FT) of the static structure factor. The PDF obtained from the MD simulation is more reliable than that obtained from the numerical Fourier transformation due to the mathematical complexity of FT. In the present work, the static structure factor and pair distribution function are calculated directly from the phase-space trajectory generated in MD simulation. We may also calculate the isothermal compressibility and coordination number from the static structure factor and pair distribution function, respectively.

5.1.1 Pair Distribution Function

In simulation we may compute the PDF, $g(r)$, in two different ways, firstly it can be calculated directly from the trajectory in MD simulation and secondly $g(r)$ can be obtained from the Fourier transformation of the static structure factor, $S(q)$. This $S(q)$ is directly found from the MD trajectory. The complete description of the structure of a liquid usually refers to particle densities and therefore the closely related, equilibrium particle distribution function. [125]. The physical meaning of $g(r)$ is the probability of finding a particle at the same instant at a distance r from

a reference particle sitting at the origin. The PDF is a dimensionless quantity. A typical form of the the PDF, $g(r)$, is shown in Figure 5.1. This figure shows that the

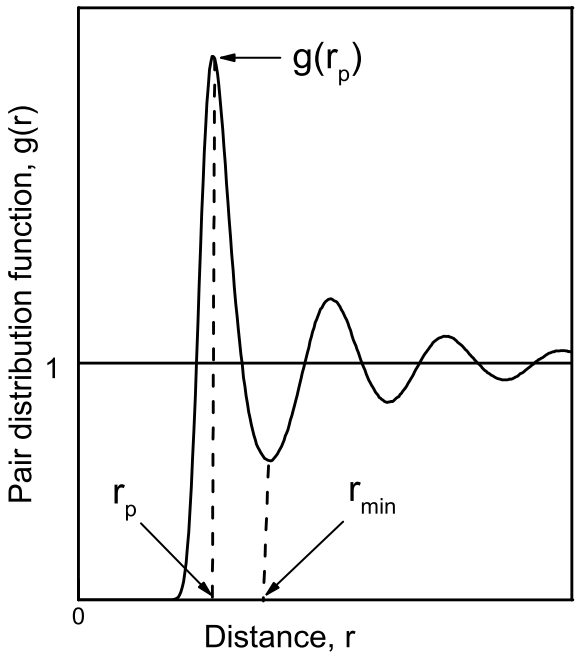

Figure 5.1: Schematic diagram of pair distribution function, $g(r)$ in liquid state.

first peak of $g(r)$ occurs at r_p having a value of $g(r_p)$. This means that the probability of finding two particles at the separation $r \approx r_p$ is likely to be $g(r_p)$ times. The PDF then falls for $r > r_p$ and passes through a minimum point at around $r \approx r_{min}$. This means that the probability of finding two particles at this separation is less.

Consider a liquid system of N particles enclosed in volume V at temperature T. Let ρ be the average number density defined as $\rho = \frac{N}{V}$ and where the particle coordinates are $\mathbf{r}_i$ having $i = 1, 2, \ldots, N$. Now we may define the particle density of

a system microscopically as [125]

$$\rho(\mathbf{r}) = \sum_{i=1}^{N} \delta(\mathbf{r} - \mathbf{r}_i). \tag{5.1}$$

Then, the average density at point $\mathbf{r}$ (single particle density) is given by the ensemble average

$$\begin{aligned} \rho^{(1)}(\mathbf{r}) = \langle \rho(\mathbf{r}) \rangle &= \Big\langle \sum_{i=1}^{N} \delta(\mathbf{r} - \mathbf{r}_i) \Big\rangle \\ &= \frac{\int \ldots \int d\mathbf{r}_1 d\mathbf{r}_2 \ldots d\mathbf{r}_N \sum_{i=1}^{N} \delta(\mathbf{r} - \mathbf{r}_i) e^{-\beta U_N}}{Z_N}, \end{aligned} \tag{5.2}$$

where, $\beta = \frac{1}{k_B T}$ and $U_N(\mathbf{r}_1, \mathbf{r}_2, \ldots, \mathbf{r}_N)$ is the potential energy due to the interaction between particles and

$$Z_N = \int \ldots \int e^{-\beta U_N} d\mathbf{r}_1 d\mathbf{r}_2 \ldots d\mathbf{r}_N, \tag{5.3}$$

is the configureational partition function. The mean number density comes from the average over all space: $\frac{1}{V} \int \rho^{(1)}(\mathbf{r}) d\mathbf{r} = \rho$. In the same way we can define the pair density function as

$$\rho^{(2)}(\mathbf{r}_1, \mathbf{r}_2) = \Big\langle \sum_{i=1}^{N} \sum_{j \neq i}^{N} \delta(\mathbf{r}_1 - \mathbf{r}_i) \delta(\mathbf{r}_2 - \mathbf{r}_j) \Big\rangle. \tag{5.4}$$

If we define $\mathbf{r} = \mathbf{r}_1 - \mathbf{r}_2$ and we assume that $\rho^{(2)}$ depends on only $\mathbf{r}$, then

$$\rho^{(2)}(\mathbf{r}) = \Big\langle \sum_{i=1}^{N} \sum_{j \neq i}^{N} \delta(\mathbf{r} + \mathbf{r}_2 - \mathbf{r}_i) \delta(\mathbf{r}_2 - \mathbf{r}_j) \Big\rangle.$$

Two body distribution function must be a function of $\mathbf{r}_i - \mathbf{r}_j$. It should not depend on $\mathbf{r}_2$, separately. Thus

$$\begin{aligned} \rho^{(2)}(\mathbf{r}) &= \frac{1}{V} \Big\langle \int d\mathbf{r}_2 \sum_{i=1}^{N} \sum_{j \neq i}^{N} \delta(\mathbf{r} + \mathbf{r}_2 - \mathbf{r}_i) \delta(\mathbf{r}_2 - \mathbf{r}_j) \Big\rangle \\ &= \frac{1}{V} \Big\langle \sum_{i=1}^{N} \sum_{j \neq i}^{N} \delta(\mathbf{r} + \mathbf{r}_j - \mathbf{r}_i) \Big\rangle. \end{aligned} \tag{5.5}$$

Since the pair distribution function $g(r)$ gives a probability of finding a pair of atoms at distance r apart, relative to the probability expected for a completely random distribution at the same density we may define as

$$\begin{aligned} g(r) &= \frac{\rho^{(2)}(\mathbf{r})}{\rho^2} \\ &= \frac{V}{N^2}\Big\langle \sum_{i=1}^{N}\sum_{j\neq i}^{N} \delta(\mathbf{r}-\mathbf{r}_{ij})\Big\rangle. \end{aligned} \tag{5.6}$$

Using MD simulation, $g(r)$ can not be measured at a point r. It can be evaluated taking average value over a shell of width Δr. Then, Eqn. (5.6) can be written as

$$g(r) = \frac{1}{V(r,\Delta r)\rho N}\langle \sum_{i} n_i(r,\Delta r)\rangle, \tag{5.7}$$

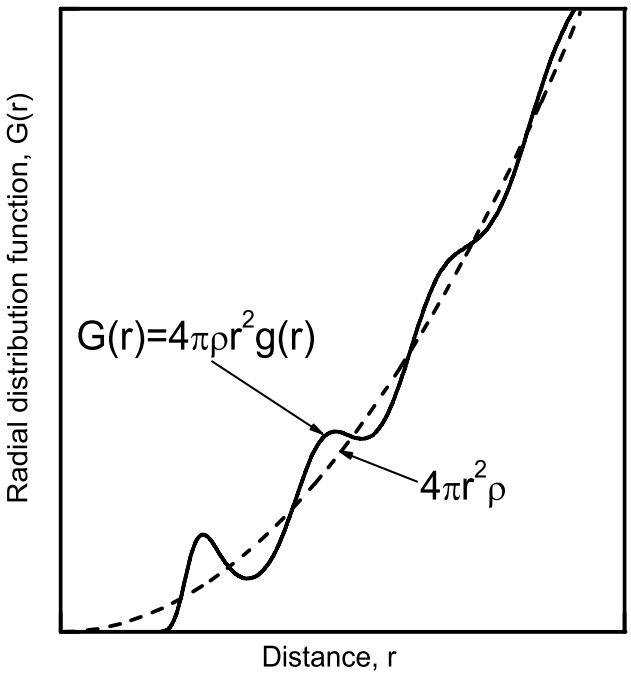

Figure 5.2: Typical curve of the radial distribution function (RDF) and parabolic function ($4\pi r^2\rho$). These are shown in arbitrary unit.

where, $n_i(r, \Delta r)$ is the number of particles in the spherical shell between r and $r + \Delta r$ of volume $V(r, \Delta r) = \frac{4}{3}\pi[(r + \Delta r)^3 - r^3]$. The PDF plays a key role to understand the underlying physics of liquids. The radial distribution function (RDF) $G(r) = 4\pi r^2 \rho g(r)$ [27] is another form of distribution function that is related to $g(r)$. The quantity $4\pi r^2 \rho g(r)\Delta r$ gives the average number of particles in the spherical shell of thickness Δr. Therefore, the RDF is also an important distribution function to study the liquid systems because, thermodynamic properties can be studied from the radial distribution function [125]. A typical form of the RDF is shown in Figure 5.2.

The peaks of the PDF indicate the structural features of liquid systems. The fact that $g(r) = 0$ for $r \to 0$ indicates the probability of finding another atom at this separation is negligible due to the strong repulsive force. Whereas the presence of several oscillations after this region implies that the molecules are preferentially located in particular regions that correspond to the various 'coordination' shells in the liquid [198]. The magnitude of the peaks decays exponentially with distance as $g(r)$ approaches 1. This departure of $g(r)$ from unity shows the existence of short-range order around the reference atom. It is being also noticed in Figure 5.1 and Figure 5.2 that when $r \to \infty$, then $g(r) \to 1$ and the RDF approaches to the parabolic function, $4\pi r^2 \rho$, where ρ is the number density.

5.1.2 Static Structure Factor

Static structure factor can also be calculated using two different ways as we have mentioned it for $g(r)$ in previous section. First of all, we may calculate static structure factor $S(q)$ directly from the trajectory generated in MD simulation in momentum

space. Alternatively, we may get $S(q)$ from the Fourier transformation of $g(r)$ generated from MD simulation. The static structure factor (SSF) describes how a material scatters incident radiation. The structure factor is particularly a very useful tool for interpreting the interference patterns obtained from X-ray diffraction or neutron diffraction experiments.

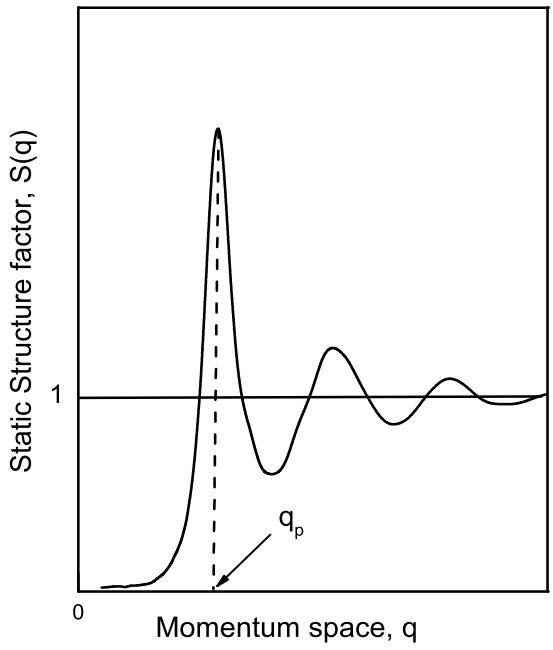

Figure 5.3: Schematic diagram of static structure factor, $S(q)$ in the liquid range.

The autocorrelation function of the Fourier components of the particle density is called the static structure factor [125]. Mathematically, this autocorrelation function is defined as

$$S(\mathbf{q}) = \frac{1}{N}\langle \rho_{\mathbf{q}} \rho_{-\mathbf{q}} \rangle, \tag{5.8}$$

where, $\rho_{\mathbf{q}}$ is a Fourier component of the particle density defined as

$$\rho_{\mathbf{q}} = \sum_{i=1}^{N} e^{-i\mathbf{q}.\mathbf{r}_i}, \tag{5.9}$$

and this quantity can be obtained easily and quickly from a given configureation. The atomic form factor Eqn. (5.9) is the building block of the construction of the static structure factor. The structure factor contains all the information regarding the position of the particles. It can be also expressed in terms of $g(r)$ as

$$\begin{aligned} S(\mathbf{q}) &= \frac{1}{N}\sum_{i=1}^{N}\sum_{j=1}^{N}\left\langle e^{-i\mathbf{q}.\mathbf{r}_i}e^{i\mathbf{q}.\mathbf{r}_j}\right\rangle \\ &= 1+\frac{1}{N}\sum_{i=1}^{N}\sum_{j\neq i}^{N}\Big\langle \int\int e^{-i\mathbf{q}.(\mathbf{r}_1-\mathbf{r}_2)}\delta(\mathbf{r}_1-\mathbf{r}_i)\delta(\mathbf{r}_2-\mathbf{r}_j)d\mathbf{r}_1 d\mathbf{r}_2\Big\rangle \\ &= 1+\frac{1}{N}\frac{N(N-1)}{V^2}\int\int e^{-i\mathbf{q}.(\mathbf{r}_1-\mathbf{r}_2)}g(\mathbf{r}_1-\mathbf{r}_2)d\mathbf{r}_1 d\mathbf{r}_2 \\ &= 1+\rho\int e^{-i\mathbf{q}.\mathbf{r}}g(\mathbf{r})d\mathbf{r}. \end{aligned} \tag{5.10}$$

Due to the asymptotic behavior of $g(\mathbf{r})$, one finds that

$$S(\mathbf{q}) = 1+\rho\int e^{-i\mathbf{q}.\mathbf{r}}[g(\mathbf{r})-1]d\mathbf{r}. \tag{5.11}$$

For isotropic systems, $g(\mathbf{r}) \equiv g(r)$, and $S(\mathbf{q}) \equiv S(q)$. Thus one obtains

$$S(q) = 1+\rho\int e^{-i\mathbf{q}.\mathbf{r}}[g(r)-1]d\mathbf{r}. \tag{5.12}$$

The schematic diagram of the $S(q)$ is given in Figure 5.3.

The quantity $S(q)$ is callled the static structure factor because it describes the average distribution of molecular separations in the fluid. It is the quantity of central interest in the equilibrium theory of fluids. Broadly speaking, the behavior of $S(q)$ generally resembles that of $g(r)$, although of course the physical meaning to be

attributed to the various features is completely different in the wave vector domain. Thus, the first peak of $S(q)$ reflects the existence of a dominant nearly regular arrangement of the particles in real space. The asymptotic value of $S(q)$ at large q is also unity and indicates the vanishing of pair correlations at short wavelengths. Eventually, at large wave vectors, $S(q)$ probes the 'hard core' region where $g(r)$ is vanishingly small. In the opposite extreme, $S(q \to 0)$ reflects in an average sense the features of $g(r)$, including its asymptotic approach to unity at very large separations. As a consequence, $S(0)$ can be expected to be associated with some macroscopic property of the system [123]. The main peak of $S(q)$ is called the first diffraction maximum. Since $S(q)$ is a measure of the spatial correlation effects in the liquid, the position of the first maximum in liquid q_p, gives the distance $\frac{2\pi}{q_p}$ over which the correlation effects are strongest. There is no obvious direct connection between r_p and $\frac{2\pi}{q_p}$, where r_p is the position where $g(r)$ has its first maximum. We therefore expect $\frac{2\pi}{q_p}$ to be somewhat less than d (hard sphere diameter), while r_p should be somewhat greater than d [199].

In the present OF-AIMD simulation, the static static structure factor is calculated directly from MD trajectory via

$$S(\mathbf{q}) = \frac{1}{N}\Big\langle \sum_{i,j} e^{-i\mathbf{q}.(\mathbf{r}_i - \mathbf{r}_j)} \Big\rangle, \tag{5.13}$$

where, N is the total number of atoms in the spherical cell while $\mathbf{r}_i$ and $\mathbf{r}_j$ are the coordinates of particles of index i and j respectively. The q vectors should be included that are related to the reciprocal lattice vectors of the simulation for simple cubic cell, *i.e.* $q = \frac{2\pi}{L}(n_1, n_2, n_3)$, where L is the size of the simulation cell. This means we will obtain a histogram representation of $S(q)$ which has better resolution as q become

larger. The minimum q accessible in a simulation is $q_{min} = \frac{2\pi}{L}$.

The another important thermodynamic quantity is the isothermal compressibility which is the measure of the relative change in volume of a system as the pressure changes while the temperature remains constant. The isothermal compressibility is related to the static structure factor. In the limit $q \to 0$, the structure factor yields the important compressibility equation [199]

$$\begin{aligned} \lim_{q\to 0} S(q) &= 1 + \rho \int [g(r) - 1] d^3r \\ &= \frac{\left\langle N^2 \right\rangle - \left\langle N \right\rangle^2}{\left\langle N \right\rangle} = \rho k_B T \kappa_T, \end{aligned} \tag{5.14}$$

where, $\left\langle N^2 \right\rangle - \left\langle N \right\rangle^2$ is the mean square fluctuation in particle number and κ_T is the isothermal compressibility. Thus, it is noticed from Eqn. (5.14), the $q \to 0$ limit of $S(q)$ is sensitive to temperature and density. In the present work, the isothermal compressibility is calculated from the relation

$$\kappa_T = \frac{S(0)}{\rho k_B T}. \tag{5.15}$$

Here ρ, k_B, and T denote average ionic number density, Boltzmann's constant and temperature, respectively. The value of $S(0)$ is calculated by fitting the simulated q at lower q values with

$$S(q) = a_0 + a_2 q^2, \tag{5.16}$$

where a_0 and a_2 are fitting constant. In the same way the isothermal compressibility could also be found from the experimental $S(q)$. From the inverse Fourier transformation of the static structure, $S(q)$ after subtracting the "self-correlation" [125] we may get PDF as follows

$$\rho[g(\mathbf{r}) - 1] = \frac{1}{(2\pi)^3} \int d\mathbf{q}\, e^{i\mathbf{q}.\mathbf{r}} [S(\mathbf{q}) - 1]. \tag{5.17}$$

Simple liquids are isotropic by nature. Thus, one finds

$$\rho[g(r) - 1] = \frac{1}{(2\pi)^3} \int d\mathbf{q}\, e^{i\mathbf{q}.\mathbf{r}}[S(q) - 1]. \tag{5.18}$$

5.1.3 Coordination Number

The coordination number, N_c is an important quantity in liquid systems which gives a convenient picture of total number of nearest-neighbor atoms in the liquid structure. The strong spatial correlations exist in the liquid state is clearly indicated by the sharp structure in $g(r)$, where the first peak is representing the coordination shell of the nearest neighbors, the second peak is representing the next nearest neighbors, and so on [199]. The properties of a liquid essentially depend on the first coordination number. It is frequently used as a parameter in the structural study of non-crystalline materials. Therefore, the concept of the coordination number, particularly refers to the first coordination number. Due to the inherent atomic vibration, this concept is somewhat ambiguous in liquids as it is compared with the crystals. The quantity $\rho g(r)$ gives the average density of particles at a distance, r, while the reference particle is sitting at the origin. There are few popular schemes [27] to estimate the first coordination number. Among them a common method is the integration of the RDF, $G(r)$ from $r = r_0$ to the first minimum of $g(r)$ or the first minimum of $G(r)$, with the two choices yielding slightly different N_c values. In the present work, the coordination number is calculated according to the formula [27, 200, 201]

$$N_c = \int_{r_0}^{r_{min}} 4\pi r^2 \rho g(r) dr, \tag{5.19}$$

where, r_0 is the left-hand edge of the first peak of $G(r)$ starting from $r_0 = 0$ and r_{min} is equal to the first minimum of the RDF. Similarly, one can also get the experimental

coordination number from the RDF, $G(r)$ corresponding to the experimental $g(r)$.

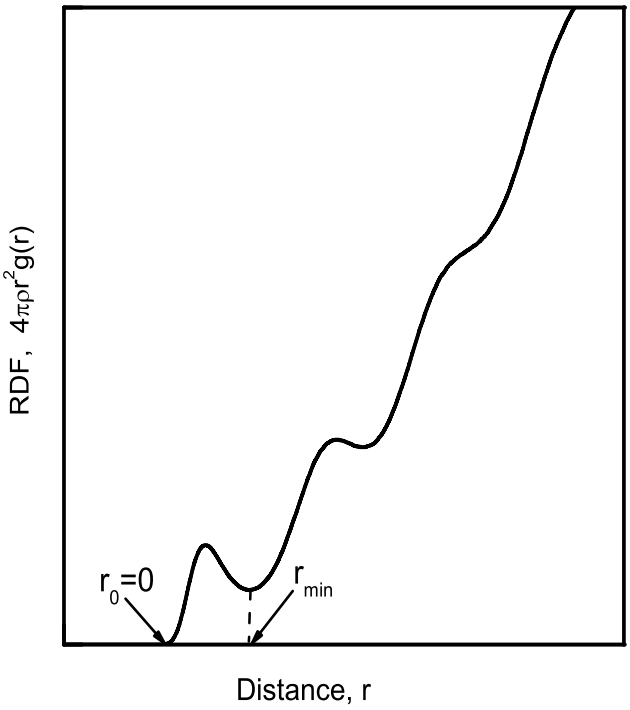

Figure 5.4: Schematic diagram of RDF for calculating the first coordination number in the liquid range.

5.2 Dynamic Properties

Dynamic properties depend on correlation between two different time points of particles. Dynamic properties can be classified into two different categories namely, single particle and collective dynamics. In the present work, the self-diffusion coefficient and self-intermediate scattering function are studied as single particle dynamics. On the other hand, the intermediate scattering function, dynamic structure factor and

shear viscosity falls into the category of the collective dynamics.

5.2.1 Self-diffusion Coefficient

Diffusion is the process of atomic mass transport which mostly occurs due to the existence of concentration gradient in the system. In such process the kinetic energy is acquired from the interactions with the neighboring atoms. A concentration gradient exists until the diffused substance is evenly distributed. While the self-diffusion coefficent describes the motion of molecules in same material in the absence of any gradient that could cause mass transfer in the system [202]. Estimation and prediction of diffusivities of substances is of great importance in industrial processes. It finds its application in rating of existing units, designing and developing new units and equipments and also in research [203]. There are two common methods to calculate the self-diffusion coefficient. The first one is from the positions of particles and the second one is from velocities of particles. Theoretically, both methods yield the same result. Obtaining the self-diffusivity from the velocities of particles involves the integration of the velocity autocorrelation function, which is known to be Green-Kubo relation [1]. On the other hand, calculation of self-diffusion coefficient from the Einstein relation [1] uses the positions of particles. The velocity autocorrelation function (VACF) is one of the prime example of a time dependent correlation function. It is important to study the underlying nature of the dynamical process operating in the molecular system. The VACF is the measurement how quickly a grain velocity becomes decorrelated with its initial velocity. The normalized VACF is defined as

$$Z(t) = \frac{\langle \mathbf{v}\,(0).\mathbf{v}\,(t)\rangle}{\langle v^2\rangle}, \tag{5.20}$$

where, $\langle .....\rangle$ stands for the ensemble average and $Z(t)$ gives the projection of the particle velocity at time t with the velocity along its initial direction. The schematic diagram of the normalized VACF is shown in Figure 5.5.

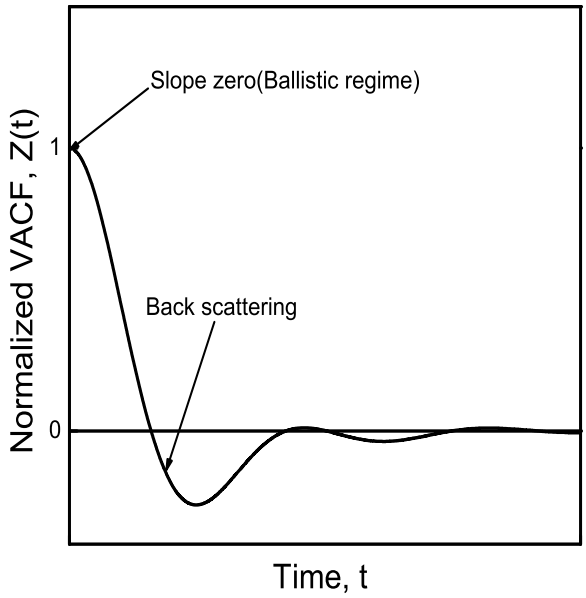

Figure 5.5: Schematic diagram of the normalized velocity autocorrelation function of liquid metal near the melting point.

The VACF is a very slowly decaying function which is not a simple exponential. The negative value of $Z(t)$ indicates a high probability of large angle deflections (near 180 °) in particle collisions, which occurs due to cage effects. The cage effect describes how the properties of molecules are affected by the surrounding. In the first region, which occurs ($t \to 0$), the VACF shows slow decay as particles move in free flight. This means the particle velocity remains essentially the same as its initial value. The region $t \to 0$ is called ballistic regime. In the second region, which occurs at short to moderate time, the VACF decays rapidly due to the onset of collisions with surrounding particles. The third region, represents for time $t \to \infty$, the VACF decays

to zero, indicating the absence of any residual correlation. The plot of VACF in this region is almost horizontal, implies very weak forces are acting in the liquid system.

5.2.2 Einstein Relation of Self-diffusion

The self-diffusion coefficient of liquid systems can be calculated by using time-dependent correlation functions known as the Einstein relation (ER) [123]. This relation is related to the mean square displacement (MSD). MSD is a measure of the average distance travels by a particle defined as

$$\langle \delta R^2(t) \rangle = \langle \mid \mathbf{R}_i(t + t_0) - \mathbf{R}_i(t_0) \mid^2 \rangle. \tag{5.21}$$

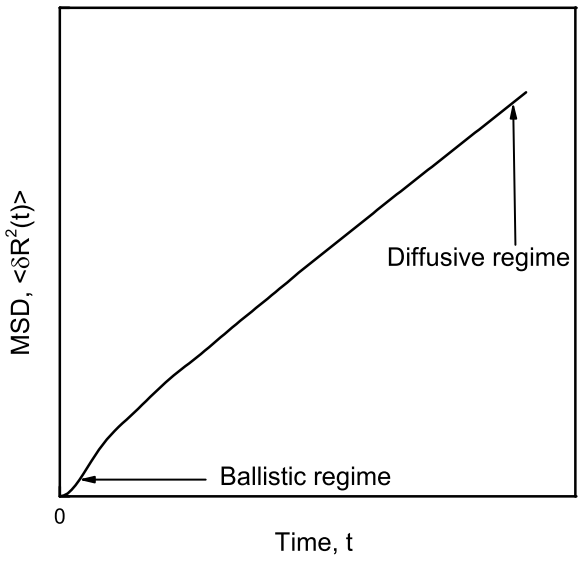

Figure 5.6: Schematic diagram of the MSD function of liquid metals near its melting point.

The MSD also contains information on the diffusion of particles. MSD may be inde-

pendent on the t_0 in the thermal equilibrium condition. A typical form of the MSD function is illustrated in Figure 5.6. In liquid system, quadratic behavior holds only for a very short time interval ($t \to 0$), which is of the order of the mean collision time. Beyond this time scale the motion of the particle is described as a random walk for which the MSD only increases linearly with time.

Consider a set of N particles with time dependent position coordinates $\mathbf{R}_i(t)$, where $i = 1, 2, \ldots, N$ and t is the time. The van Hove distribution function $G(\mathbf{R}, t)$ [204], comes after the name of van Hove characterises the dynamical structure measured in inelastic neutron scattering experiments. $G(\mathbf{R}, t)$ is the real-space dynamical correlation function for characterising the spatial and temporal disributions of particle pairs in a fluid. Time correlation functions can be generalized into correlation functions in space and time. Let us consider the microscopic number density

$$\rho(\mathbf{R}, t) = \sum_{i=1}^{N} \delta(\mathbf{R} - \mathbf{R}_i(t)) \tag{5.22}$$

with the average defined as

$$\langle \rho(\mathbf{R}, t) \rangle = \lim_{T \to \infty} \frac{1}{T} \int_0^T dt \; \frac{1}{V} \int_v d\mathbf{r} \, \rho(\mathbf{R}, t),$$

which gives

$$\langle \rho(\mathbf{R}, t) \rangle = \frac{N}{V} = \rho$$

Let us construct the density-density correlation

$$G(\mathbf{R}'', \mathbf{R}'; t'', t_0) = \frac{1}{\rho} \langle \rho(\mathbf{R}'', t'') \rho(\mathbf{R}', t_0) \rangle, \tag{5.23}$$

which is a generalisation of the equilibrium density-density correlation function define as [125]

$$H(\mathbf{R}, \mathbf{R}') = \frac{1}{N} \big\langle \big[\rho(\mathbf{R}') - \langle \rho(\mathbf{R}') \rangle \big] \big[\rho(\mathbf{R}' + \mathbf{R}) - \langle \rho(\mathbf{R}' + \mathbf{R}) \rangle \big] \big\rangle. \tag{5.24}$$

For homogenous system at equilibrium Eqn. (5.23) only depends on the space and time differences, $\mathbf{R} \equiv \mathbf{R}'' - \mathbf{R}'$ and $t \equiv t'' - t_0$. Then

$$G(\mathbf{R}, t) = \frac{1}{N} \Big\langle \sum_{i=1}^{N} \sum_{j=1}^{N} \delta\big(\mathbf{R} + \mathbf{R}_j(t_0) - \mathbf{R}_i(t + t_0)\big) \Big\rangle, \tag{5.25}$$

where, $\delta(\ldots)$ is the three-dimensional Dirac delta function. Eqn. (5.25) is known as the van Hove correlation function (vHCF). We can physically interpret the van Hove function as the proportional to the probability to find a particle i at the position $\mathbf{R}''$ at time t'', while the reference particle j was located at the position $\mathbf{R}'$ at time t_0.

The vHCF, $G(\mathbf{R}, t)$ can be naturally separated into two terms. Conventionally which is referred as "self" and "distinct" part, by discriminating between the cases $i = j$ and $i \neq j$, respectively. Thus one finds

$$\begin{aligned} G(\mathbf{R}, t) &= \frac{1}{N} \langle \sum_{i=1}^{N} \delta(\mathbf{R} + \mathbf{R}_i(t_0) - \mathbf{R}_i(t + t_0) \rangle + \frac{1}{N} \langle \sum_{i \neq j}^{N} \delta(\mathbf{R} + \mathbf{R}_j(t_0) - \mathbf{R}_i(t + t_0)) \rangle \\ &= G_s(\mathbf{R}, t) + G_d(\mathbf{R}, t). \end{aligned} \tag{5.26}$$

The self part, $G_s(\mathbf{R}, t)$, describes the average motion of the particle that was initially at the origin and the distinct part, $G_d(\mathbf{R}, t)$, describes the behavior of the remaining N-1 particles. Furthermore, liquids are isotropic by nature and hence $G(\mathbf{R}, t)$ will only depend on the scalar quantity $\mid \mathbf{R} \mid = R$. In the hydrodynamic limit of long distances and times, the self part of the distribution function $G_s(R, t)$ obeys the equation [205]

$$\frac{\partial G_s(R, t)}{\partial t} = D \nabla^2 G_s(R, t), \tag{5.27}$$

where, D is the self-diffusion coefficient. The solution of Eqn. (5.27) with the Dirac delta initial condition $G_s(R, t_0) = \delta(\mathbf{R})$ is of the Gaussian form [205]

$$G_s(R, t) = (4\pi D t)^{-\frac{3}{2}} e^{-\frac{R^2}{4Dt}}. \tag{5.28}$$

Therefore, the mean square displacement of a tagged particle over time t is given by

$$\begin{aligned}\langle \delta R^2(t) \rangle &= \langle \mid \mathbf{R}(t+t_0) - \mathbf{R}(t_0) \mid^2 \\ &= \int R^2 G_s(R,t) d\mathbf{R} \\ &= 6Dt. \end{aligned} \tag{5.29}$$

Taking the limit of $t \to \infty$ such that the ratio $\frac{\langle \delta R^2(t) \rangle}{t}$ becomes constant, then the self-diffusion coefficient becomes

$$D = \lim_{t \to \infty} \frac{\langle \delta R^2(t) \rangle}{6t}, \tag{5.30}$$

which is the famous Einstein relation for self-diffusion.

5.2.3 Green-Kubo Relation of Self-diffusion

The Green-Kubo (G-K) relation is the another technique to calculate the self-diffusion coefficient from the time-dependent correlation functions [125]. If $\mathbf{v}(t)$ is the velocity of the particle at any arbitary time t, then one gets

$$\delta \mathbf{R}\,(t) = \int_0^t \mathbf{v}\,(t') dt' \tag{5.31}$$

By squaring and averaging Eqn. (5.31) over time origins gives

$$\begin{aligned}\langle \delta R^2 \rangle &= \int_0^t dt'' \int_0^t dt' \langle \mathbf{v}\,(t').\mathbf{v}\,(t'') \rangle \\ &= 2 \int_0^t dt'' \int_0^{t''} dt' \langle \mathbf{v}\,(t').\mathbf{v}\,(t'') \rangle. \end{aligned} \tag{5.32}$$

The factor 2 in Eqn. (5.32) appears due to the symmetric property of the integrand in time t' and t''. The velocity autocorrelation function $\langle \mathbf{v}\,(t').\mathbf{v}\,(t'') \rangle$ depends on the

time difference. By introducing $\tau = t'' - t'$ one can write Eqn. (5.32) as [1]

$$\begin{aligned}
\langle \delta R^2 \rangle &= 2\int_0^t dt'' \int_0^{t''} d\tau \big\langle \mathbf{v}(\tau).\mathbf{v}(0) \big\rangle \\
&= 2\int_0^t d\tau \langle \mathbf{v}(\tau).\mathbf{v}(0) \rangle \int_\tau^t dt'' \\
&= 2\int_0^t d\tau \langle \mathbf{v}(\tau).\mathbf{v}(0) \rangle (t-\tau) \\
\text{or, } \frac{\langle \delta R^2 \rangle}{2t} &= \int_0^t d\tau \langle \mathbf{v}(0).\mathbf{v}(\tau) \rangle (1 - \frac{\tau}{t})
\end{aligned} \tag{5.33}$$

Taking the long-time limit, we find

$$\lim_{t\to\infty} \frac{\langle \delta R^2 \rangle}{2t} = \int_0^\infty d\tau \langle \mathbf{v}(0).\mathbf{v}(\tau) \rangle \tag{5.34}$$

Using Eqn. (5.30) we may arrive at

$$D = \frac{1}{3}\int_0^\infty dt \langle \mathbf{v}(0).\mathbf{v}(t) \rangle \tag{5.35}$$

Using Eqn. (5.20) one finds

$$D = \frac{k_B T}{m}\int_0^\infty Z(t)dt. \tag{5.36}$$

In Eqn. (5.36), the factor $\frac{k_B T}{m}$ comes from the average kinetic energy of the particle [205] as follows

$$\frac{1}{2}m\langle \mid v \mid^2 \rangle = \frac{3}{2}k_B T. \tag{5.37}$$

The Einstein relation and the Green-Kubo formula are equivalent theory. They are very important theories for liquid state. The Einstein relation and Green-Kubo formula are often known as MSD and VACF methods, respectively. A number of theories have been proposed to describe the transport phenomena namely the mass, momentum or energy transfer in simple dense fluids. None of these theories are capable to

predict exact result. Alongside with the theoretical values of self-diffusion coefficients we have a little experimental data available in the litterature at different thermodynamic states. Therfore, MD simulation has become an useful method for studying self-diffusion coefficients of real fluids composed of relatively simple molecules [203]. In the present case we have calculated self-diffusion coefficients of liquid systems from $Z(t)$ and $\langle \delta R^2(t) \rangle$ through the Green-Kubo and Einstein relations, respectively. It is worth noticing that $Z(t)$ and $\langle \delta R^2(t) \rangle$ are obtained from OF-AIMD simulation method in the present work.

5.2.4 Self-intermediate Scattering Function

The self-intermediate scattering function (SISF), $F_s(\mathbf{q}, t)$ is one of the simplest time-dependent quantity. The $F_s(\mathbf{q}, t)$ gives the probability that a tagged particle at time t has moved a specified distance from its initial position. Thus, the SISF provides the most complete information about the single particle motion. This corresponds the single particle dynamics are not same length scales, ranging from the hydrodynamic limit to the free particle limit. Area under $F_s(\mathbf{q}, t)$ can be used to define a relaxation time τ. The dynamical variable for i-th particle reads as

$$\rho_{s,i}(\mathbf{R}, t) = \delta(\mathbf{R} - \mathbf{R}_i(t)), \tag{5.38}$$

which is usually referred to as the i-th single-particle (or self-) density at the point $\mathbf{R}$ and time t. The interpretation of $\rho_{s,i}(\mathbf{R}, t)$ as a 'density' comes from the integration of Eqn. (5.38) over the full range of $\mathbf{R}$. We write the normalization condition as

$$\int \rho_{s,i}(\mathbf{R}, t)\, d\mathbf{R} = 1, \tag{5.39}$$

which simply means that the tagged particle certainly be counted somewhere in the volume V at any time [123]. As is clear from its definition, $\rho_{s,i}(\mathbf{R},t)$ is expected to change very rapidly as a function of $\mathbf{R}$ and t. The gross measure of this variable is provided by its statistical average yields [123]

$$\langle \rho_{s,i}(\mathbf{R},t)\rangle = \langle \rho_{s,i}(\mathbf{R},t_0)\rangle = \frac{1}{V}, \tag{5.40}$$

which is consistent with the previous interpretation of $\rho_{s,i}(\mathbf{R},t)$ as a number density. The space Fourier transformation of the i-th self-density is

$$\rho_{s,i}(\mathbf{q},t) = \int d\mathbf{R} e^{-i\mathbf{q}.\mathbf{R}} \rho_{s,i}(\mathbf{R},t) = e^{-i\mathbf{q}.\mathbf{R}_i(t)}. \tag{5.41}$$

We have computed $F_s(q,t)$ from the positions of the particles. The time correlation associated with $\rho_{s,i}(\mathbf{R},t)$ is usually referred to as the self-intermediate scattering function and is defined as [15, 123, 125]

$$\begin{aligned} F_s(\mathbf{q},t) &= \langle \rho_{s,i}(\mathbf{q},t+t_0)\rho^*_{s,i}(\mathbf{q},t_0) \\ &= \frac{1}{N}\Big\langle \sum_{i=1}^{N} e^{-i\mathbf{q}.\mathbf{R}_i(t+t_0)} e^{i\mathbf{q}.\mathbf{R}_i(t_0)} \Big\rangle, \end{aligned} \tag{5.42}$$

where, $\langle ... \rangle$ is the average over time origins and wavevectors with the same modulus, N is the total number of particles and $\mathbf{R}_i(t)$ is the position of the i-th particle at time t. Eqn. (5.42) has been used in OF-AIMD simulation for calculating self-intermediate scattering functions. The present work is concerned with isotropic systems only, for which the self-intermediate scattering function depends on the magnitude q of $\mathbf{q}$. Alternatively, $F_s(q,t)$ can be calculated by taking the Fourier transformation of the self part of vHCF, $G_s(R,t)$ defined as

$$F_s(q,t) = \int d\mathbf{R} \, \exp\left[-i\mathbf{q}.\mathbf{R}\right] G_s(\mathbf{R},t). \tag{5.43}$$

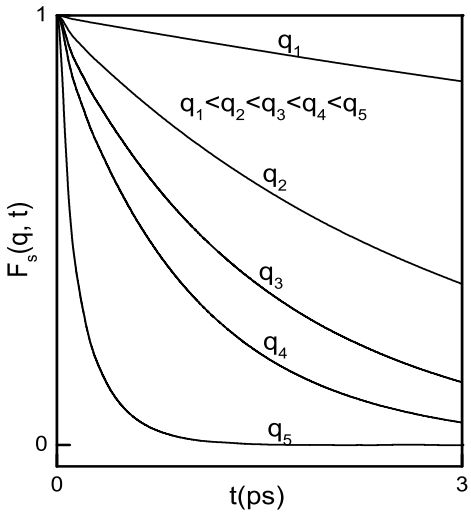

Figure 5.7: Schematic diagram of the self-intermediate scattering in the liquid range.

This method, however, has the disadvantage to involve Fourier transformation artefacts due to the finite size of our simulation box. The general behavior of $F_s(q,t)$ is shown schematically in Figure 5.7.

$F_s(q,0) = 1$ due to the facts that the tagged molecule is localized to the origin at time t=0. As time evolves and the molecule begins to move away from its initial position, $F_s(q,t)$ decreases in a smooth manner. The decay rate seems to be increased with q, indicating that the short-wavelength fluctuations die out much more rapidly [199]. There is an interesting relation between the self-intermediate function and the self-diffusion coefficient which is known as the Gaussian approximation for self-intermediate scattering function. The self part of the van Hove function $G_s(\mathbf{R},t)$ can be written as a Gaussian function of R in the form [125, 206]

$$\begin{aligned} G_s(\mathbf{R},t) &= \frac{1}{\sqrt{4\pi D\, t}} \exp\left[-\frac{R^2}{4Dt}\right] \\ &= \frac{1}{(2\pi)^3} \int d\mathbf{q} e^{-Dq^2 t} e^{i\mathbf{q}.\mathbf{R}}, \end{aligned} \tag{5.44}$$

where, D is the self-diffusion coefficient. By using Eqn. (5.44), one can read from Eqn. (5.43)

$$\begin{aligned} F_s(q,t) &= \exp\big[-Dq^2t\big] \\ &= \exp\big[\frac{-q^2\langle\delta R^2(t)\rangle}{6}\big], \end{aligned} \tag{5.45}$$

which is a well-known Gaussian approximation for $F_s(q,t)$. The $F_s(q,t)$ obtained from the Gaussian approximation agrees well with that directly calculated from the molecular dynamics simulations for both small and large wavevectors. This approximation agrees quite well with simulated $F_s(q,t)$ for $q \to 0$. This means that the self-intermediate scattering function is controlled by the self-diffusion coefficient. In the liquid range, the discrepancies between them are found to be rather small, and mainly occur in the intermediate range of wave vectors and times, as expected [123]. Even, on the basis of these direct comparisons the overall results predicted by the Gaussian ansatz are quite acceptable. As expected, the main shortcomings are found to occur at the intermediate wavevectors, where the deviations may even rises up to about 20% [123].

5.2.5 Intermediate Scattering Function and Dynamic Structure Factor

The density of particles at a point $\mathbf{R}$ at time t is defined as Eqn. (5.22) and in the collective case with Fourier components defined as

$$\rho_{\mathbf{q}}(t) = \sum_{i=1}^{N} e^{-i\mathbf{q}.\mathbf{R}_i(t)}. \tag{5.46}$$

The intermediate scattering function (ISF), $F(\mathbf{q},t)$, is a density autocorrelation function. This provides the information about the collective dynamics of density fluctuations over both the length and time scales. As the system under consideration is isotropic, $F(\mathbf{q},t)$ depends only on the magnitude of $\mathbf{q}$ and not on its direction. Thus, $F(\mathbf{q},t)$ is a function only of the wavenumber $q =\mid \mathbf{q} \mid$ and t.

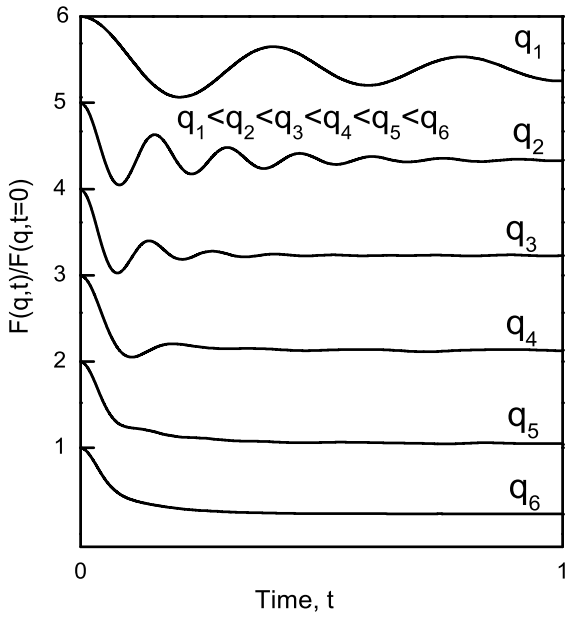

Figure 5.8: Schematic diagram of the intermediate scattering function of liquid metal near the melting point.

In the present OF-AIMD simulation, we have directly computed the ISF, $F(q,t)$, from the atomic trajectories. It is defined as [15, 123, 125]

$$\begin{aligned} F(q,t) &= \frac{1}{N}\langle \rho_{\mathbf{q}}(t+t_0)\rho_{-\mathbf{q}}(t_0)\rangle \\ &= \frac{1}{N}\Big\langle \Big(\sum_{i=1}^{N} e^{-i\mathbf{q}.\mathbf{R}_i(t+t_0)}\Big)\Big(\sum_{j=1}^{N} e^{i\mathbf{q}.\mathbf{R}_j(t_0)}\Big)\Big\rangle, \end{aligned} \tag{5.47}$$

where, N is the total number of particles and $\mathbf{R}_j(t)$ is the position of the j-th particle at time t. Instead of direct computation, $F(q,t)$ can be calculated by taking the Fourier transformation (FT) of the vHCF generated in MD simulation, *i.e.*

$$F(q,t) = \int d\mathbf{R}\, \exp[-i\mathbf{q}.\mathbf{R}]\, G(\mathbf{R},t). \tag{5.48}$$

Accuracy of $F(q,t)$ obtained from FT is less than that obtained from direct calculation of $F(q,t)$. This is because of the mathematical complexity of FT. The quantity $F(q,t)$ is directly accessible in light and neutron scattering experiments [125]. A typical behavior of $F(q,t)$ for liquid metal is shown in Figure 5.8.

Fluctuations of $F(q,t)$ implies dynamical heterogeneities. $F(q,t)$ exhibits an oscillatory behavior and the amplitude of the oscillations being stronger for the smaller q values for liquid metals near melting [123]. As q increases and the length scale $\frac{2\pi}{q}$ becomes more and more microscopic, the liquid is not able to support any collective excitation, and $F(q,t)$ should decay monotonically [123]. The slow decay of $F(q,t)$ at $q \approx q_p$ known as "de Gennes narrowing", which is induced by the strong spatial correlations appearing at those q values around q_p [123]. In the limit $q \to 0$, $F(q,t)$ decays more slowly than the self-intermediate scattering function, $F_s(q,t)$. For large q, the intermediate scattering function, $F(q,t) \to F_s(q,t)$ [199].

The dynamic structure factor (DSF) is a mathematical function that contains information about inter-particle correlations and their time evolution. The DSF is related to the intermediate scattering function $F(q,t)$. It is defined by the Fourier transform of the $F(q,t)$ into the frequency domain with an appropriate window to

smooth out truncation effects as

$$S(q,\omega) = \frac{1}{2\pi}\int_{-\infty}^{\infty} F(q,t)\exp[-i\omega t]dt. \tag{5.49}$$

This technique has been used to evaluate the dynamic structure factor in the present OF-AIMD simulation. The DSF describes thermal fluctuations in a material which has experimental relevance because it is directly related to the scattered intensity in the inelastic neutron scattering (INS) or the inelastic X-ray scattering (IXS). Notice that, since $F(q,t)$ is a real function which is even in t, the dynamic structure factor will be even in ω. The DSF exhibits well defined side peaks for lower values of q and exist up to $q \approx q_p$, where q_p is the main peak position of $S(q)$. The well defined side

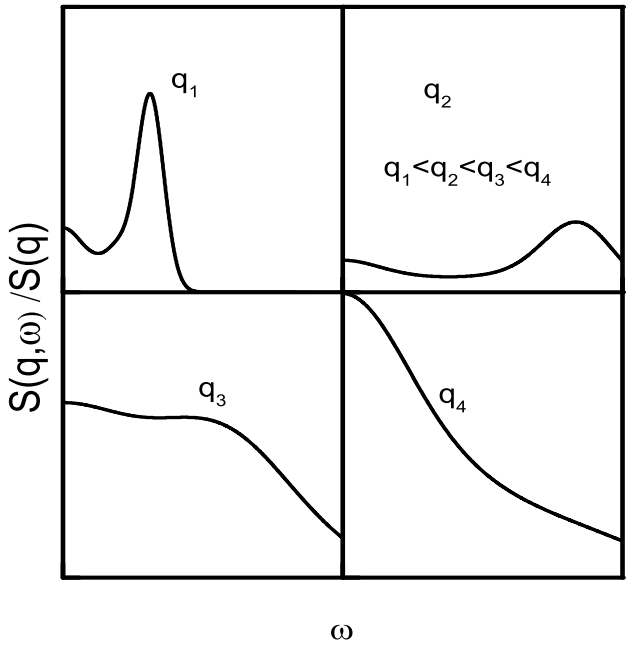

Figure 5.9: Schematic diagram of the normalized DSF of liquid metal near the melting point.

peaks indicating the existence of collective density excitation and after almost $q > q_p$, the side peak of $S(q, \omega)$ appears to be a shoulder instead of peak and then decreases monotonically for large q values. Eventually, at the largest value of q where $S(q) \approx 1$, $S(q, \omega)$ approaches the 'self' spectrum $S_s(q, \omega)$ [123]. From the position of the side peaks of $S(q, \omega)$, a dispersion relation can be obtained and the slope of the dispersion curve at $q \to 0$ yields the adiabatic sound velocity. The ISF and therefore the DSF, is more challenging to compute than ststic properties like $g(r)$ and $S(q)$. Because the static properties are defined as an ensemble average of a dynamical variable at certain time, whereas the ISF involves the ensemble average at two different times. The general behavior of the normalized DSF is illustrated in Figure 5.9.

5.2.6 Viscosity

Viscosity gives the measurement of resistance to flow [207]. Two adjacent layers slip past each other, each exerts a frictional resistive force on the other, and this internal friction gives rise to viscosity. Besides nonequilibrium molecular dynamics, in which the shear viscosity, η, is determined from the response of the system to a shearing force. Whereas the equilibrium methods are appealing in the context of AIMD since they have crucial advantage of keeping the possibility to calculate all the other physical properties in the same simulation. A usual way of extracting η in the framework of equilibrium simulations is from the Green-Kubo formalism, i.e., the time integration of the stress autocorrelation function obtained from the off-diagonal component of the stress tensor [66]. An alternative method based on the transverse time correlation function $J_t(q, t)$ is incorporated in the present work. It has the advantage of yielding

a generalized q-dependent viscosity from which the hydrodynamic regime can be detected and finite size effect can be evaluated [66]. The general behavior of $J_t(q,t)$ is shown schematically in Figure 5.10.

The vectorial variable

$$\mathbf{j}(q,t) = \sum_{j=1}^{N} \mathbf{v}_j(t) e^{i\mathbf{q}.\mathbf{R}_j(t)} \tag{5.50}$$

is known as the current density associated with the overall motion of the particles. The current density may be split as

$$\mathbf{j}(q,t) = \mathbf{j}_l(q,t) + \mathbf{j}_t(q,t), \tag{5.51}$$

where, $\mathbf{j}_l(q,t)$ and $\mathbf{j}_t(q,t)$ are the longitudinal component parallel to $\mathbf{q}$ and transverse component perpendicular to $\mathbf{q}$, respectively.

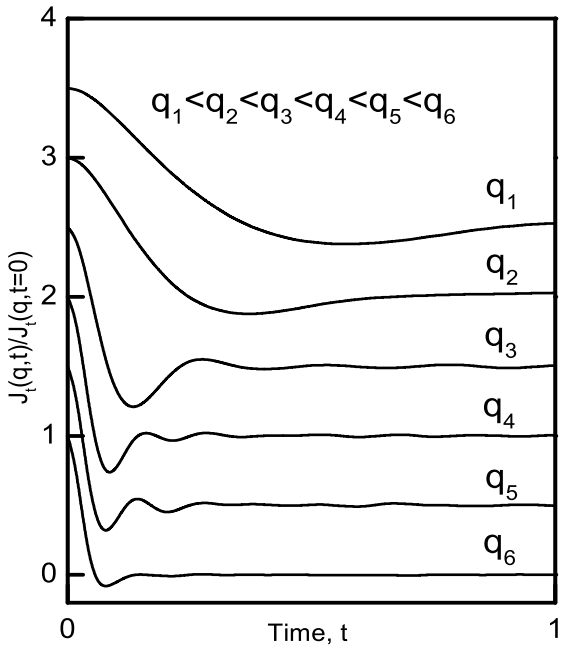

Figure 5.10: Schematic diagram of the transverse time correlation function, $J_t(q,t)$ near melting point.

Let us assume that waves propagating in the z-direction. Longitudinal current exists when the direction of motion of the particles (the velocity) is parallel with the direction of propagation of the waves. On the other hand, transverse current exists when the direction of motion of the particles is perpendicular to the direction of propagation of the waves [123]. The longitudinal, $J_l(q,t)$, and transverse, $J_t(q,t)$, current correlation functions are defined as

$$J_t(q,t) = \frac{1}{2N}\langle \mathbf{j}_t{}^*(q,0).\mathbf{j}_t(q,t)\rangle \tag{5.52}$$

and

$$J_l(q,t) = \frac{1}{N}\langle \mathbf{j}_l{}^*(q,0).\mathbf{j}_l(q,t)\rangle. \tag{5.53}$$

The transverse current time correlation function, $J_t(q,t)$ is an interesting dynamical magnitude. It is not associated with any measurable quantity and can only be determined by means of computer simulations. It gives information about the shear modes.

The shear viscosity coefficent, η, can be expressed in tetms of a simple Green-Kubo integral

$$\begin{aligned} \eta &= \frac{1}{k_B TV}\int_0^\infty dt\,\langle \sigma^{zx}(0)\sigma^{zx}(t)\rangle \\ &= \int_0^\infty dt\,\eta(t). \end{aligned} \tag{5.54}$$

The quantity $\eta(t) = \eta(q \to 0, t) = \frac{1}{k_B TV}\langle \sigma^{zx}(0)\sigma^{zx}(t)\rangle$, often referred to as the transverse (or shear) stress autocorrelation function [123] with

$$\sigma^{zx} = \sum_{i=1}^{N}\big[mv_{i,z}v_{i,x} - \frac{1}{2}\sum_{i,j\neq i}^{N}\big(\frac{z_{ij}x_{ij}}{r_{ij}}\big)\phi'(r_{ij})\big], \tag{5.55}$$

where, the notation $v_{i,z}$ means the z component of velocity of particle i at time t, and $x_{ij} =\mid x_i - x_j \mid$. The hydrodynamic method for computing the shear viscosity is based on the transverse part of the linearised Naviér-Stokes equation. This equation can be written as [199]

$$\frac{\partial}{\partial t} J_t(q,t) = -\frac{q^2 \eta}{\rho m} J_t(q,t), \tag{5.56}$$

with the time dependent transverse current correlation function defined as

$$J_t(q,t) = \frac{1}{N} \langle \mathbf{j}_x{}^*(q,0).\mathbf{j}_x(q,t) \rangle \tag{5.57}$$

and wave number q. The short-time features of the transverse current correlation function $J_t(q,t)$ is given by [123]

$$J_t(q,0) = \frac{k_B T}{m} = \frac{1}{\beta m} \tag{5.58}$$

From Eqn. (5.56), one obtains an exponential decay for the transverse current correlation function

$$\begin{aligned} J_t(q,t) &= J_t(q,0) \exp\big[-\frac{\eta}{m\rho} q^2 \mid t \mid \big] \\ &= \frac{1}{\beta m} \exp\big[-\frac{\eta}{m\rho} q^2 \mid t \mid \big]. \end{aligned} \tag{5.59}$$

The solution of

$$\frac{\partial}{\partial t} J_t(q \to 0, t) = -\frac{\eta q^2}{\rho m} J_t(q \to 0, t), \tag{5.60}$$

which arises when the transverse current correlation function reach a Markovian situation [123] with the hydrodynamic result defined as Eqn. (5.59), gives the ordinary shear viscosity η. Thus we get

$$J_t(q \to 0, t) = \frac{1}{\beta m} \exp\big(-q^2 \frac{\eta \mid t \mid}{\rho m} \big) \tag{5.61}$$

where, η is the shear viscosity coefficient defined as Eqn. (5.54). Therefore, the shape of $J_t(q,t)$ evolves from a Gaussian, in both q and t, for the free-particle $q \to \infty$ limit towards a Gaussian in q and exponential in t for the hydrodynamic limit ($q \to 0$). For the intermediate values of q, $J_t(q,t)$ exhibits complicated behavior, because it may oscillate signaling the propagation of shear waves. From the results for $J_t(q,t)$ we can readily obtain the shear viscosity coefficent, η [123]. However, the memory function representation of $J_t(q,t)$ is

$$\tilde{J}_t(q,z) = \frac{1}{\beta m}\big[z + \frac{q^2}{\rho m}\tilde{\eta}(q,z)\big]^{-1}, \tag{5.62}$$

where, the tilde denotes the Laplace transform, introduces a generalized shear viscosity coefficent $\tilde{\eta}(q,z)$. The area under the normalized $J_t(q,t)$, gives $\beta m\tilde{J}_t(q,z=0)$, from which values for

$$\tilde{\eta}(q,z=0) = \frac{\rho m}{q^2\beta m\tilde{J}_t(q,z=0)} \tag{5.63}$$

can be obtained, and then the shear viscosity coefficent η is derived from the limit $q \to 0$. This is performed by extrapolating the property that the inversion is the symmetry in the system which allows to approximate [208]

$$\tilde{\eta}(q) = \eta(1 - \alpha q^2). \tag{5.64}$$

The transverse current spectrum, $J_t(q,\omega)$ is the time Fourier transform of $J_t(q,t)$ and is defined as

$$J_t(q,\omega) = \frac{1}{2\pi}\int_{-\infty}^{\infty} J_t(q,t)\exp[-i\omega t]. \tag{5.65}$$

The $J_t(q,\omega)$ show peaks within some q-range, which are connected with propagating shear waves.

5.2.7 Stokes-Einstein Relation

The self-diffusion constants, D, the shear viscosity, η, and the effective diameter of the particle, d, *i.e.* the position of the first peak of the PDF are related through the Stokes-Einstein relation (SE) [123, 125, 199]

$$d = \frac{k_B T}{C\pi\eta D}, \tag{5.66}$$

where, k_B is the Boltzmann constant and C is a constant depending on the boundary condition of the flow. This relation was originally introduced to describe the diffusive motion of a large brownian particle in a continuous fluid with shear viscosity, η. Due to the stick boundary condition, the fluid velocity at the surface matches with that of the particle velocity and $C = 3$ in this case. On the other hand, the normal component of the fluid velocity is set equal to the normal component of the particle velocity with non tangential force acting on the sphere owing to the slip boundary condition. In this case one finds $C = 2$. The SE relation was purely derived from macroscopic considerations. It is surprisingly found to work well in simple liquids on the atomic scale. The more reasonable values of the effective diameter d can be found if the slip boundary condition is imposed.

Chapter 6

Results and Discussion

The OF-AIMD simulations have been performed for liquid Cr (l-Cr), l-Mn, l-Fe, l-Co, l-Ni, l-Pd, l-Pt, l-Zn, l-Cd and l-Hg at thermodynamic states near their respective triple points; more specific information is given in Table 6.1. We have performed simulation at two thermodynamic states for the systems Fe, Co, Zn, Hg and at one thermodynamic state for Cr, Mn, Ni, Pd, Pt and Cd depending on the availability of the experimental structure. In the simulations, we have considered 500 particles inside a periodic cubical cell with a size determined by the corresponding ionic number density of the systems at a given thermodynamic state. For given ionic positions at time t, the electronic energy functional is minimized with respect to $\rho(\mathbf{r})$, represented by a single effective orbital, $\psi(\mathbf{r})$ defined as $\rho(\mathbf{r}) = |\psi(\mathbf{r})|^2$. The orbital is expanded by plane wave basis set which is finally truncated at the cutoff energy. These cutoff energies E_{cut} for the systems under study are given in Table 6.2. Figures 6.1-6.3 show the non-Coulombic electron-ion interaction in q space for liquid (Cr, Mn, Fe, Co), (Ni, Pd, Pt) and (Zn, Cd and Hg), respectively. These figures show that in the long

Table 6.1: Input parameters used in the present calculations: temperature T, ionic number density ρ, amplitude in the core A, softness parameter a, core radius R_c and ionic valence Z.

Systems	T(K)	ρ(Å^{-3})	R_c(a.u.)	A(a.u.)	a(a.u.)	Z
Cr	2173	0.0726	1.37	0.050	0.65	1.50
Mn	1533	0.0655	1.40	0.005	0.75	1.50
Fe	1833	0.0756	1.25	0.005	0.85	1.69
	1923	0.0742	„	„	„	1.69
Co	1823	0.0786	1.39	0.005	0.85	1.50
	1923	0.0774	„	„	„	1.50
Ni	1773	0.0792	1.20	0.005	0.65	1.50
Pd	1853	0.0594	1.45	0.005	0.30	1.60
Pt	2053	0.0577	1.45	0.050	0.70	1.60
Zn	0723	0.0636	1.05	0.004	0.85	2.00
	0833	0.0620	„	„	„	2.00
Cd	0623	0.0428	1.26	0.005	0.85	2.00
Hg	0293	0.0407	1.26	-0.06	0.90	2.00
	0353	0.0402	„	„	„	2.00

wavelength limit ($q \to 0$), the value of $v_{ps}(q)$ is the largest for l-Pt, the smallest for l-Zn and all others lie in between. The values of the parameters R_c (core radius), A (amplitude in the core) and a (softness parameter) that are used to calculate the non-Coulombic electron-ion interaction are given in the Table 6.1. The depths of the $v_{ps}(q)$ are shown in Figure 6.4. The Figure 6.5 shows that the similarity of the phase of the oscillations allows us to group the elements as (Cr, Mn and Co), (Pd and Pt) and (Fe, Cd and Hg). Whereas l-Zn and l-Ni oscillate completely in different phase. The oscillatory behavior occurs at $q > 3.5\,(a.u^{-1})$.

The electronic energy minimization with respect to the Fourier coefficents of ex-

pansion is performed every ionic time step using quenching method which gives the ground state electron density and ground state energy. The ionic forces are essential ingredients to perform the molecular dynamics simulations. These forces are dreived from the ground state electronic energy by using the Hellman-Feynman theorem. The

Table 6.2: Cutoff energy of the systems under study at their respective melting points.

Systems	T(K)	E_{cut}(Ryd.)	Systems	T(K)	E_{cut}(Ryd.)
Cr	2173	14	Pd	1853	11
Mn	1533	11	Pt	2053	20
Fe	1833	20	Zn	0723	22
	1923	20		0833	22
Co	1823	14	Cd	0623	22
	1923	14	Hg	0293	22
Ni	1773	14		0353	22

ionic motion characterized by the position and velocity are updated at each time step by solving the Newton's equations of motion. To solve the Newton's equations of motion numerically we have used the Verlet Leap-frog algorithm with a finite time step. Finite time step for systems l-Cr, l-Mn, l-Co , l-Ni, l-Pd, l-Pt, l-Zn, l-Cd, l-Hg is taken 7.6×10^{-3} ps and for the system l-Fe is taken 5×10^{-3} ps. In the case of l-Fe we have chosen time step 5×10^{-3} ps rather than 7.6×10^{-3} ps to have a better description for liquid structure. After equilibration, the calculation of properties was performed by averaging over 10000 configurations for systems (Cr, Mn, Co, Fe, Zn, Cd, Hg) and 5000 configurations for systems (Ni, Pd, Pt). This leads to a simulation

time of 76 ps for l-Cr, l-Mn, l-Co, l-Zn, l-Hg, l-Cd, 50 ps for l-Fe and 38 ps for l-Ni, l-Pd, l-Pt.

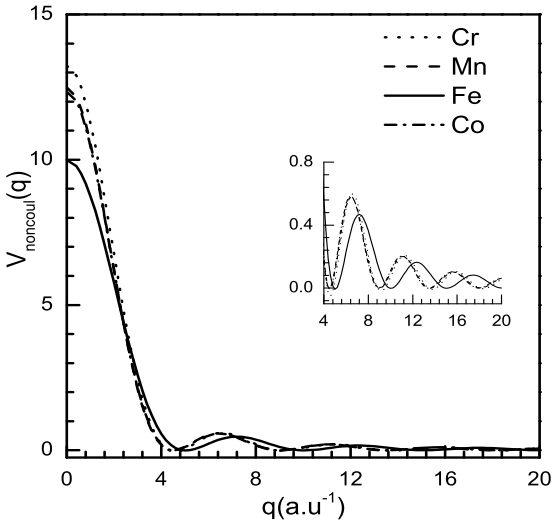

Figure 6.1: Non-Coulombic part of the ionic pseudopotentials used for liquid Cr, Mn, Fe, and Co. The inset shows a magnified display of the oscillations.

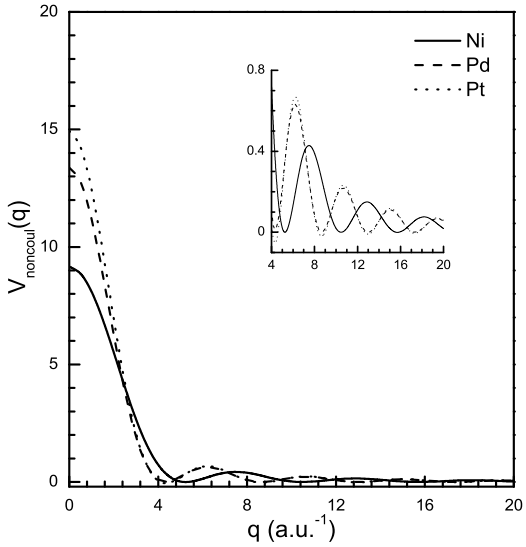

Figure 6.2: Non-Coulombic part of the ionic pseudopotentials used for liquid Ni, Pd and Pt. The inset shows a magnified display of the oscillations.

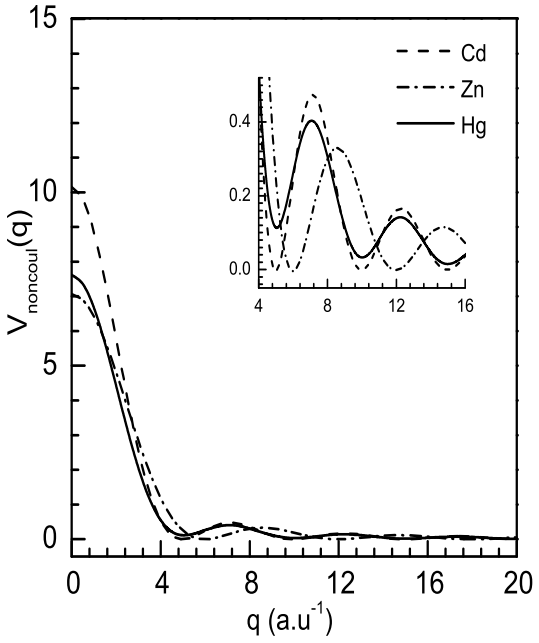

Figure 6.3: Non-Coulombic part of the ionic pseudopotentials used for liquid Zn, Cd and Hg. The inset shows a magnified display of the oscillations.

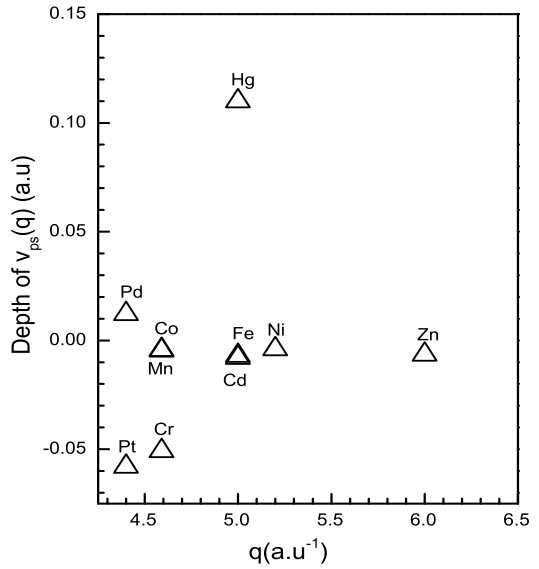

Figure 6.4: Depth of the non-Coulombic part of the ionic pseudopotentials for the systems under study.

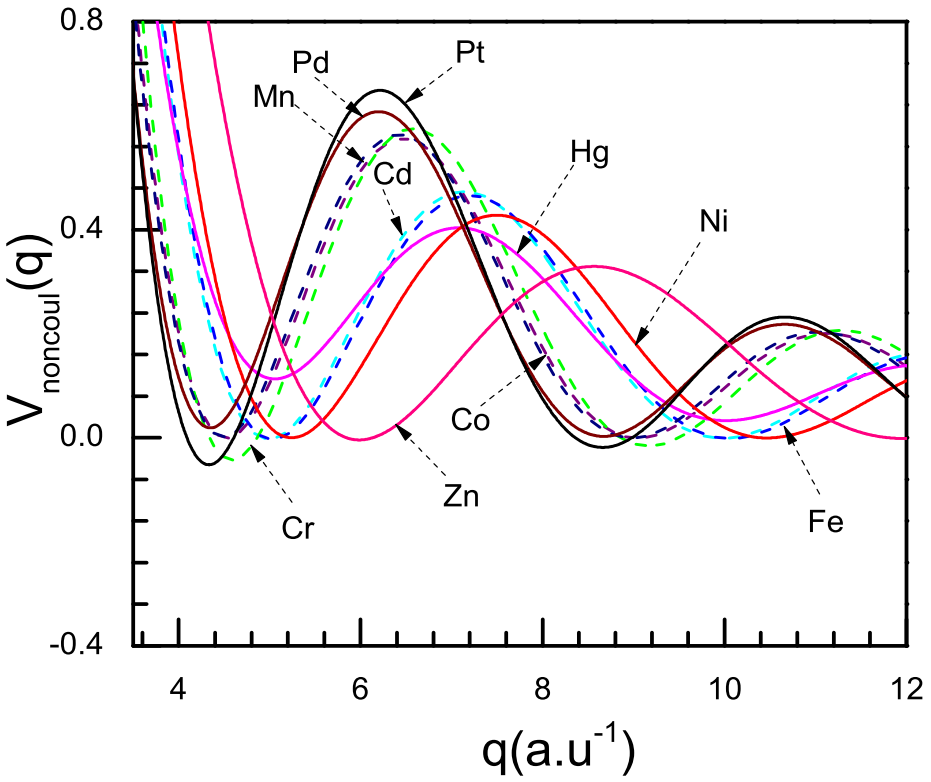

Figure 6.5: Phase of the oscillations for the non-Coulombic part of the ionic pseudopotentials of the systems under study.

6.1 Static Properties

6.1.1 Liquid Cr

The static structure factor $S(q)$ and it's real space counterpart the pair distribution function $g(r)$ are related through the Fourier transformation (FT) within the theory of statistical mechanics. But the OF-AIMD simulation allows us a direct computation of both $S(q)$ and $g(r)$ (without using any FT). This feature thus deserves in their

own right of presentation for both $S(q)$ and $g(r)$ with equal importance. Figure 6.6 shows $S(q)$ along with the XRD data [27] for l-Cr at $T = 2173$ K. The principal peak is somewhat overestimated but the position of the main peak ($q_p \approx 2.90\,\text{Å}^{-1}$) agrees well with experimental peak position ($q_p \approx 3.0\,\text{Å}^{-1}$) [27]. Beyond the principal peak, other peak values, position of the peaks and phase of oscillations also agree well within the uncertanity of the experimental data. This is worth noting that, the neutron diffraction data sometimes yields larger peak of $S(q)$ than that of the XR diffraction ones [18]; moreover, the principal peak values are found to vary among different set of XRD data (see Figure 6.10 for l-Fe). Unfortunately, neutron diffraction data or other set of XRD data are not available for l-Cr. In the long wavelength limit of the static structure factor, $S(q \to 0)$, is connected to the thermodynamics via the Eqn. (5.15). As the size of the simulation box determines the lowest value of $q = \frac{2\pi}{L}$, we do not have S(q) at $q \to 0$ from simulation. We have, therefore, fitted the OF-AIMD low q ($q < 0.7\,\text{Å}^{-1}$) values of $S(q)$ by the Eqn. (5.16) to have $S(0)$ and from the value of $S(0)$ we have estimated κ_T using the Eqn. (5.15). From this calculation we have obtained $\kappa_T = 0.79 \pm 0.01$ (in 10^{-12}cm^2 dyne^{-1} units) for l-Cr. To the best of our knowledge, no experimental data for κ_T is available for l-Cr. Here we note that, a value derived from the experimental $S(q)$ at $q \to 0$ is found to be 0.82 ± 0.10 (in 10^{-12} cm^2 dyne^{-1} units) which is slightly overestimated in magnitude from our estimated result. On the other hand, κ_T of solid Cr at room temperature is 0.60 (in 10^{-12}cm^2 dyne^{-1} units). The isothermal compressibility in the liquid state is 32% larger than that of its solid phase, which qualifies that we are on the right track.

The pair distribution function, $g(r)$, provides information about the short range

order in the liquid state. Figure 6.7 shows $g(r)$ for l-Cr at $T = 2173$ K, where the X-ray (XR) diffraction data of Waseda [27] are also dipicted for comparison. In this

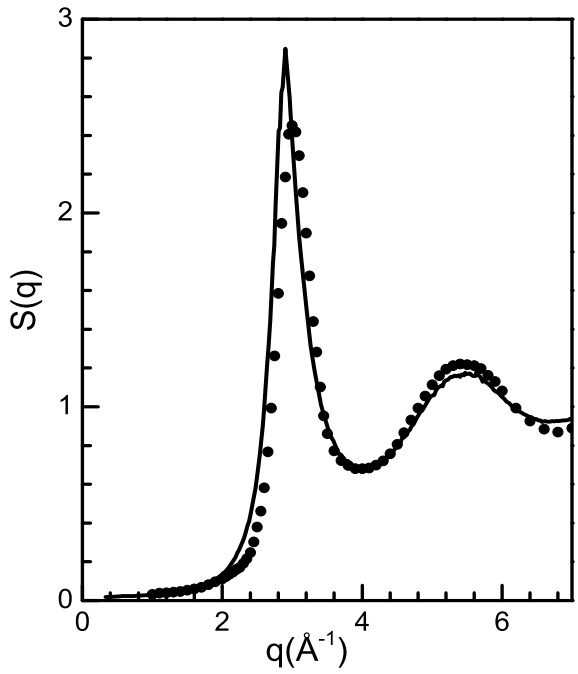

Figure 6.6: Static structure factor, $S(q)$ for l-Cr at $T = 2173$ K. The solid line stands for OF-AIMD results, the closed circles for XR diffraction data [27].

case the amplitude of the principal peak occurs at $r_p = 2.53\,\text{Å}$ of the simulated $g(r)$ is somewhat underestimated than that of experimental $g(r)$, occuring at $r_p = 2.50\,\text{Å}$. But the overall agreement with the position of subsequent peaks and phase of oscillations lies within the few percent of the experimental data as we have seen in the case of $S(q)$. The coordination number is obtained from Eqn. (5.19), where the upper limit of integration is the first minimum ($r_{\min} = 3.45\,\text{Å}$) of RDF, $G(r)$, is found to be $N_c = 12.08$. The coordination number calculated from the experimental pair distribution function was found to be $N_c = 11.68$. In this case the agreement is found

to be fairly good.

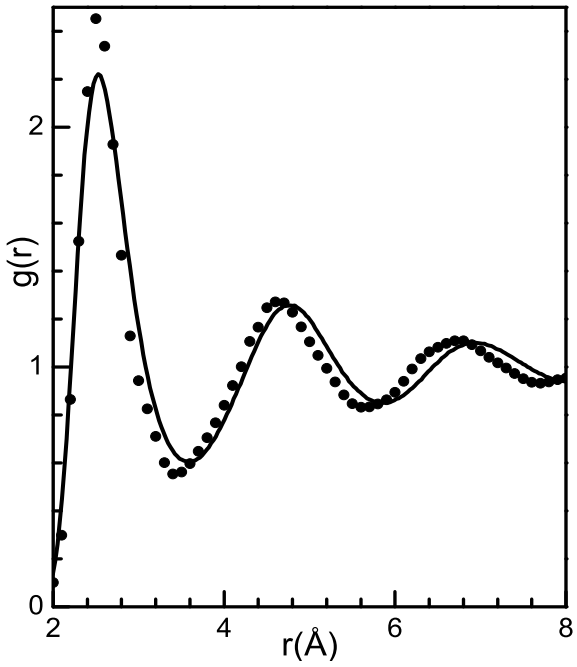

Figure 6.7: Pair distribution function, $g(r)$ for l-Cr at $T = 2173$ K. The solid line stands for OF-AIMD results and the closed circles represent XR diffraction data [27].

6.1.2 Liquid Mn

Figure 6.8 shows the static structure factor, $S(q)$, for l-Mn at $T = 1533$ K, where the principal peak is located at $q_p \approx 2.76\,\text{Å}^{-1}$. But the principal peak position of XRD data [27] is at $q_p \approx 2.85\,\text{Å}^{-1}$, which is slightly greater than the calculation. It is seen that the principal peak is somewhat overestimated, but the overall agreement with the corresponding XR diffraction data [27] is good. In this case the quality of the agreement is better than that of l-Cr. The isothermal compressiblity is calculated in the same manner as it is done for l-Cr. The computed value for κ_T is found to be 1.27$\pm$ 0.03 (in 10^{-12}cm^2 dyne^{-1} units) which is somewhat smaller than the experimental one

$\kappa_T = 1.73$ (in 10^{-12}cm^2 dyne^{-1} units) [27]. The isothermal compressiblity of Mn in the solid phase is 0.83 (in 10^{-12}cm^2 dyne^{-1} units).

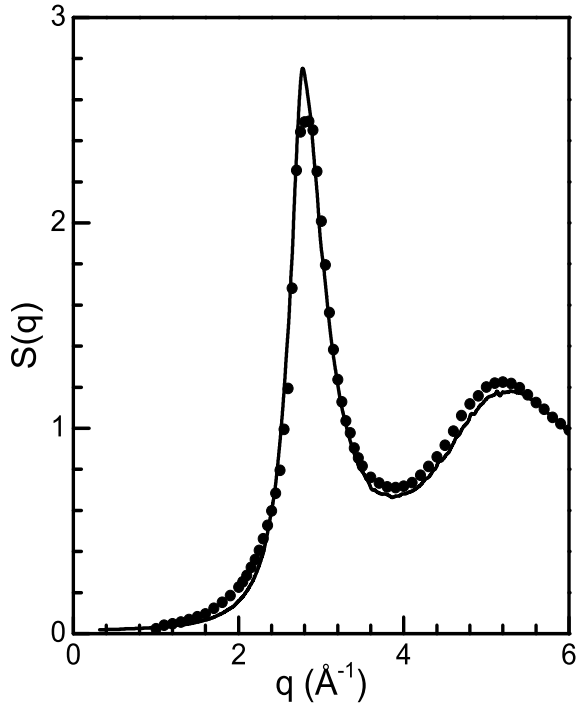

Figure 6.8: Static structure factor, $S(q)$ for l-Mn at $T = 1533$ K. The solid line stands for OF-AIMD results, the closed circles are the XRD data [27].

Figure 6.9 displays pair correlation function, $g(r)$ for l-Mn at $T = 1533$ K along with the corresponding XR diffraction data [27]. In this case the agreement with the experimental data is excellent. Here it is to be noted that the peak position of $g(r)$ occurs at $r_p = 2.61$ Å and coincided with XRD data [27]. The coordination number $N_c = 12$ is calculated via Eqn. (5.19), where the upper limit of the integration is taken from the first minimum, $r_{min} = 3.57$ Å of $G(r)$ as before. The experimental $g(r)$ [27] provides $N_c = 11.69$. The OF-AIMD value of N_c agrees within 2.6% of the experimental one.

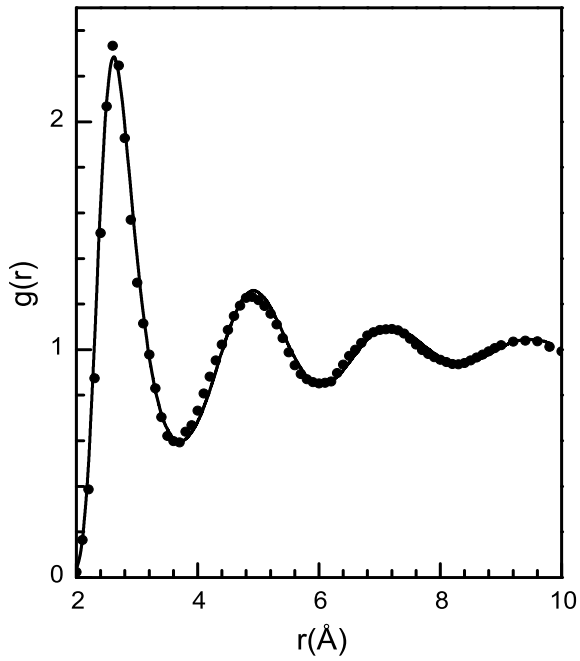

Figure 6.9: Pair distribution function, $g(r)$ for l-Mn at $T = 1533$ K. The solid line stands for OF-AIMD results and the closed circles stand for XRD data [27].

6.1.3 Liquid Fe

For liquid Fe, we have performed simulation at two different temperatures because of the availability of experimental XR diffraction data. Note that we have kept parameters unchanged of the pseudopotential for both thermodynamic states. This gave us a chance to examine the temperature dependence for which parameters remain effective in describing structure of l-Fe. Figure 6.10 shows the OF-AIMD structure factor, $S(q)$, for l-Fe at temperatures $T = 1833$ and 1923 K. To compare our results we have presented the XRD data obtained from two different sources. One performed by Inui *et al.* [209] and other one by Waseda [27]. We also presented the neutron diffraction data of Schenk *et al.* [210]. It is seen that the positions of the principal

and other peaks, height of the peaks and the phase of oscillations are in excellent agreement with those of Inui *et al.* [209]. Very recently, Marques *et al.* [52] performed AIMD simulation study for l-Fe at $T = 1873$ K, which is shown in Figure 6.11 and we have compared this result with the present OF-AIMD calculation. Qualitatively

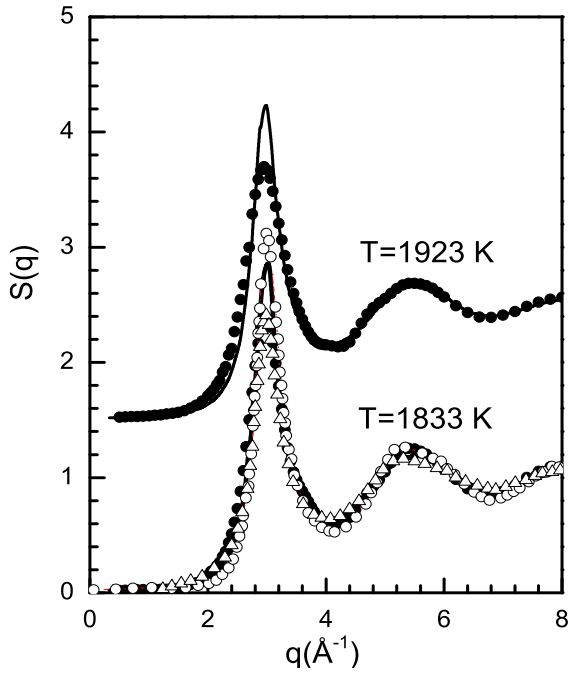

Figure 6.10: Static structure factor, $S(q)$ for liquid Fe at $T = 1833$ and 1923 K. The solid lines stand for OF-AIMD results, the closed circles are the XRD data [27] and open circles are the XRD data of M. Inui *et al.* [209] at $T = 1843$ K and open triangles are the neutron diffraction data from Schenk *et al.* [210] at $T = 1873$ K.

our OF-AIMD structure agrees well with those of AIMD [52]. The principal peak of $S(q)$ calculated by Marques *et al.* occurs at $q_p \approx 2.99\,\text{Å}^{-1}$ and its height is $S(q_p) \approx 2.8$. The principal peak position of OF-AIMD $S(q)$ is found at $q_p \approx 3.00\,\text{Å}^{-1}$ having $S(q_p) \approx 2.85$. On the other hand, the experimental peak position occurs at $q_p \approx 2.97\,\text{Å}^{-1}$ [27]. The isothermal compressiblity calculated from the long wavelength

limit of $S(q)$ yields a value $\kappa_T = 0.91 \pm 0.03$ and 0.94 ± 0.02 (in 10^{-12}cm^2 dyne^{-1} units) at $T = 1833$ and 1923 K temperatures, respectively. But the values derived from the experimental $S(q)$ are found to be 0.92 and 1.15 (in 10^{-12}cm^2 dyne^{-1} units), respectively. The compressibility of Fe in solid phase at room temperature is 0.59 (in 10^{-12}cm^2 dyne^{-1} units).

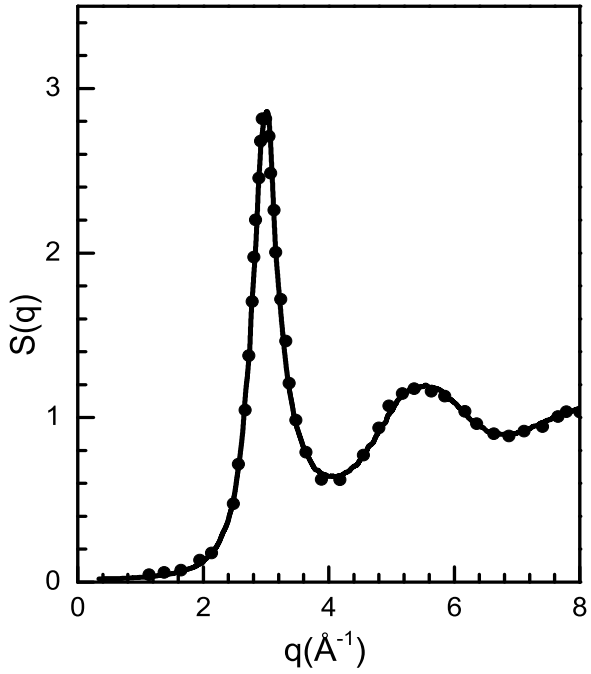

Figure 6.11: Static structure factor, $S(q)$ for l-Fe at $T = 1833$ K. The solid line stands for OF-AIMD results, the closed circles for AIMD results of Marques *et al.* [52].

Figure 6.12 shows the OF-AIMD $g(r)$ for l-Fe at $T = 1833$ and 1923 K along with the XR diffraction data [27]. It is seen from the figure that the principal peak of $g(r)$ is slightly underestimated for $T = 1833$ K and produced exactly as XRD data [27] for $T = 1923$ K. The peak positions of OF-AIMD $g(r)$ for both temperatures occur at $r_p = 2.50\,\text{Å}$ whereas the experimental peak positions are seen to be occured at

$r_p = 2.60\,\text{Å}$. Figure shows a fairly good agreement for both positions and phase of oscillations when compared with XRD data [27]. The coordination numbers calculated at $T = 1833$ and 1923 K (from Eqn. (5.19)) by integrating up to the first minimum $r_{min} = 3.38\,\text{Å}$ of $G(r)$, the values are found to be $N_c = 11.91$ and 11.84, respectively. Values obtained from the experimental $g(r)$ are $N_c = 11.41$ and 11.28 at $T = 1833$ and 1923 K, respectively. An *ab-initio* MD study by Marques *et al.* [52] yields $N_c = 12.5$ at $T = 1873$ K.

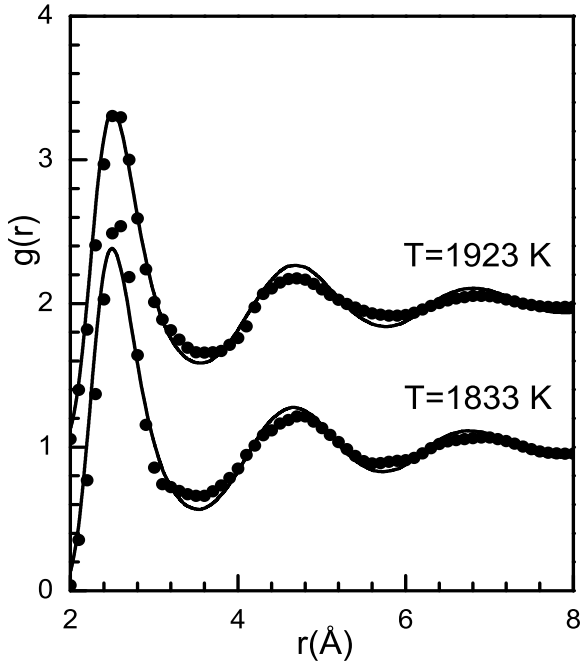

Figure 6.12: Pair distribution function, $g(r)$ for l-Fe at $T = 1833$ and 1923 K. The solid lines stand for OF-AIMD results and the closed circles stand for XRD data [27].

6.1.4 Liquid Co

The OF-AIMD static structure factors, $S(q)$, for l-Co are plotted in Figure 6.13. We have also plotted the corresponding XRD data of Waseda [27] in the same figure.

Figure shows that both the peak positions and corresponding oscillations are in good agreement with XRD data of Waseda [27], although the height of the main peak is somewhat overestimated. This overestimation at the level of the principal peak is also noticed in other systems as discussed before. The position of the principal peak is at $q_p \approx 2.97\,\text{Å}^{-1}$, which is very close to experimental value $q_p \approx 2.97\,\text{Å}^{-1}$ [27]. The isothermal compressibility, κ_T derived from the long wavelength limit of $S(q)$ is found to be 0.69 ± 0.01 and 0.71 ± 0.01 (in 10^{-12}cm^2 dyne^{-1} units) at $T = 1823$ and 1923 K, respectively. These results are comparable with $\kappa_T = 0.89$ and 1.05 (in 10^{-12}cm^2 dyne^{-1} units), which are obtained from experimental $S(q)$. The compressibility of solid Co at room temperature is 0.55 (in 10^{-12}cm^2 dyne^{-1} units).

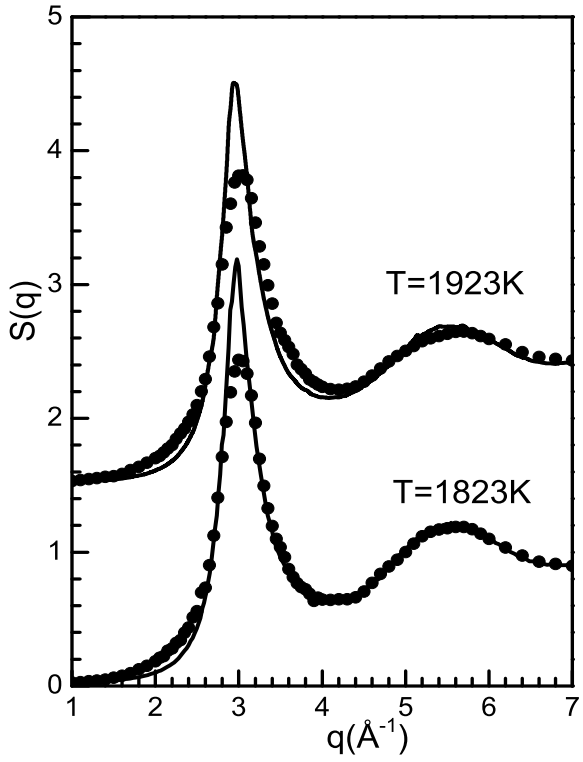

Figure 6.13: Static structure factor, $S(q)$ for l-Co at $T = 1823$ and 1923 K. The solid lines stand for OF-AIMD results, the closed circles are the XRD data [27].

The pair correlation function, $g(r)$ for l-Co are shown in Figure 6.14. It is seen that agreement at the level of main peak is very good for both temperatures. We have found the main peak positions at $r_p \approx 2.46\,\text{Å}$ for both temperatures, here the experimental peak positions [27] agree in excellent way. The second peak amplitudes are also in good agreement with experiment but in the case of peak position the agreement is just fair. The coordination numbers calculated from the OF-AIMD $g(r)$, according to the Eqn. (5.19), having the integration upper limit up to $r_{min} = 3.35\,\text{Å}$ of $G(r)$ are found to be $N_c = 12.43$ and 12.23 at $T = 1823$ and 1923 K, respectively. The corresponding coordination numbers estimated from the eperimental $g(r)$ are 11.75 and 11.27, respectively.

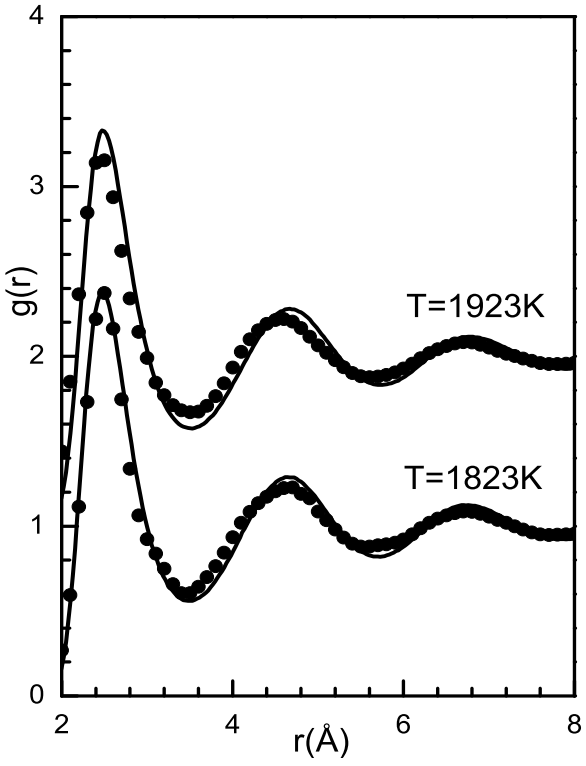

Figure 6.14: Pair distribution function, $g(r)$ for l-Co at $T = 1823$ and 1923 K. The solid lines stand for OF-AIMD results and the closed circles stand for XRD data [27].

6.1.5 Liquid Ni

The computed $S(q)$ for l-Ni at $T = 1773$ K is illustrated in Figure 6.15 along with the XRD data of Waseda [27]. Although the height of the principal peak is slightly overestimated and the amplitude of the second peak is slightly underestimated, the overall agreement is good. The position for the main peak, q_p, is slightly smaller than experiment, that is $q_p \approx 3.03\,\text{Å}^{-1}$ whereas the XRD data gives $q_p \approx 3.10\,\text{Å}^{-1}$ [27]. We observed from the Figure 6.15, the height of the main peak is somewhat over estimated in AIMD calculation done by González *et al.* [211] than that of experiment

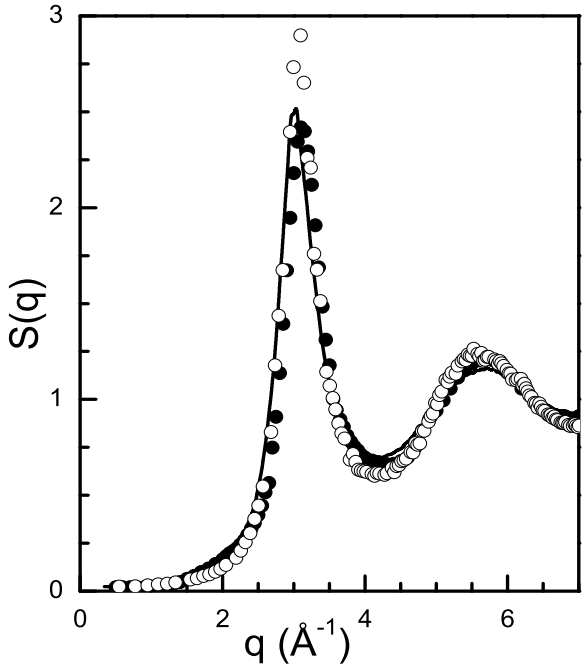

Figure 6.15: Static structure factor, $S(q)$ for l-Ni at $T = 1773$ K. The solid line stands for OF-AIMD results, the full circles are the XR diffraction data [27], while the open circle represents the AIMD results obtained by González *et al.* [211].

and OF-AIMD calculations. We also observed that the AIMD main peak appears at the location $q_p \approx 3.09\,\text{Å}^{-1}$. The long wavelength limit of the $S(q)$ is linked to

the thermodynamics through the isothermal compressibility κ_T, and the relation is defined by Eqn. (5.15). Therefore, we have fitted the obtained OF-AIMD $S(q)$ for small q values by the expression Eqn. (5.16) for the estimation of κ_T which gives a value 0.81 ± 0.02 (in 10^{-12} cm^2 dyne^{-1} units). To best of our knowledge, there is no available experimental data for κ_T at this tmperature. But an estimation obtained from experimental $S(q)$ [27] is 1.02 ± 0.03 (in 10^{-12} cm^2 dyne^{-1} units), which is somewhat greater than the OF-AIMD value.

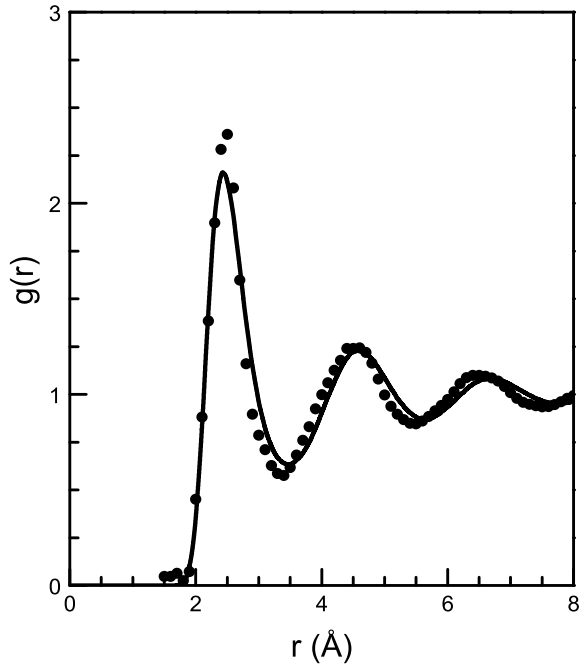

Figure 6.16: Pair distribution function, $g(r)$ for l-Ni at $T = 1773$ K. The solid line stands for OF-AIMD results and the full circles stand for XR diffraction data [27].

The pair distribution function, $g(r)$ provides information about the short range order in the liquid and Figure 6.16 shows the calculated $g(r)$ for l-Ni at $T = 1773$ K along with the XR diffraction data of Waseda [27]. For comparison, we obtain a good

agreement with the experiment for positions and phase of oscillations of the main and subsequent peaks although the height of the main peak is somewhat underestimated. The position of the principal peak for the system l-Ni is found to be at $r_p \approx 2.43\,\text{Å}$ while the experimental $g(r)$ yields $r_p \approx 2.43\,\text{Å}$. We note here that an AIMD simulation gives $r_p \approx 2.44\,\text{Å}$ [211]. This result is very close to our OF-AIMD calculation. The average number of nearest neighbors, also known as the coordination number N_c, has been obtained from the Eqn. (5.19) by integrating up to the first minimum position r_{min} of $G(r)$. Our calculated $g(r)$ yields $r_{min} = 3.35\,\text{Å}$ at $T = 1773$ K and the calculated coordination number is $N_c = 11.85$. For comparison, we note that the XRD-based $g(r)$ data yields $r_{min} = 3.35\,\text{Å}$ and $N_c = 11.70$. So, the OF-AIMD coordination number agrees within 1.3% of the experimental value.

6.1.6 Liquid Pd

The simulated $S(q)$ for l-Pd at $T = 1853$ K is illustrated in Figure 6.17 together with the XR diffraction data [27]. Figure shows a reasonably good agreement with experiment, although the height of the main peak of our simulated $S(q)$ is somewhat overestimated while the amplitude of the second peak is slightly underestimated. The main peak is located at $q_p \approx 2.77\,\text{Å}^{-1}$ whereas from the XRD data [27] it is observed at $q_p \approx 2.76\,\text{Å}^{-1}$. Interestingly, our OF-AIMD results are better in agreement with experiment than that of AIMD peak position ($q_p = 2.79\,\text{Å}^{-1}$) and height simulated by González *et al.* [212]. From the long wavelength limit of simulated $S(q)$ we have computed the isothermal compressiblity $\kappa_T = 1.23 \pm 0.03$ (in units of 10^{-12} cm^2 dyne^{-1}) for l-Pd at $T = 1853$ K. This is little bit larger than the experimental

1.02 ± 0.07 (in 10^{-12} cm^2 dyne^{-1} units) value [27]. González *et al.* have reported, $\kappa_T = 4.70 \pm 0.20$ (in 10^{-12} cm^2 dyne^{-1} units) from their KS-AIMD study [212].

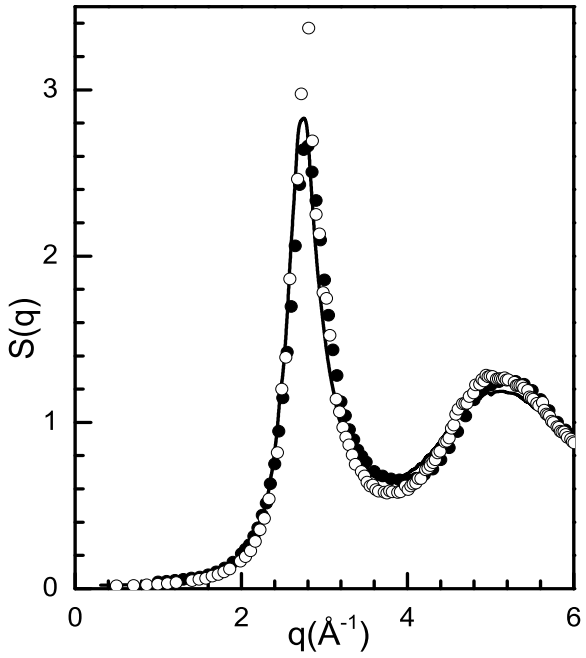

Figure 6.17: Static structure factor, $S(q)$ for liquid Pd at $T = 1853$ K. The solid lines stand for OF-AIMD results, the full circles are the XR diffraction data [27], while the open circles represent the AIMD results obtained by González *et al.* [212].

The pair distribution function, $g(r)$ for l-Pd at $T = 1853$ K is plotted in Figure 6.18 along with the XR diffraction data [27]. Figure shows a good agreement with experiment, although the height of the main peak seems to be underestimated. We note here that the main peak of $g(r)$ occurs at $r_p \approx 2.70$ Å and $r_p \approx 2.60$ Å for simulated and experimental $g(r)$ [27], respectively. While González *et al.* have reported from their KS-AIMD study [212] that the main peak of $g(r)$ occurs at $r_p \approx 2.69$ Å. By integrating the RDF, $G(r)$ from 0 to $r_{min} = 3.69$ Å we have obtained the total number of nearest neighbors, $N_c \approx 11.65$, which is closer to the experimental value,

$N_c \approx 10.90$ calculated from the experimental $g(r)$ data of Waseda [27]. An AIMD simulation study gives $N_c \approx 12.8$ [212] having $r_{min} = 3.77\,\text{Å}$ of $g(r)$.

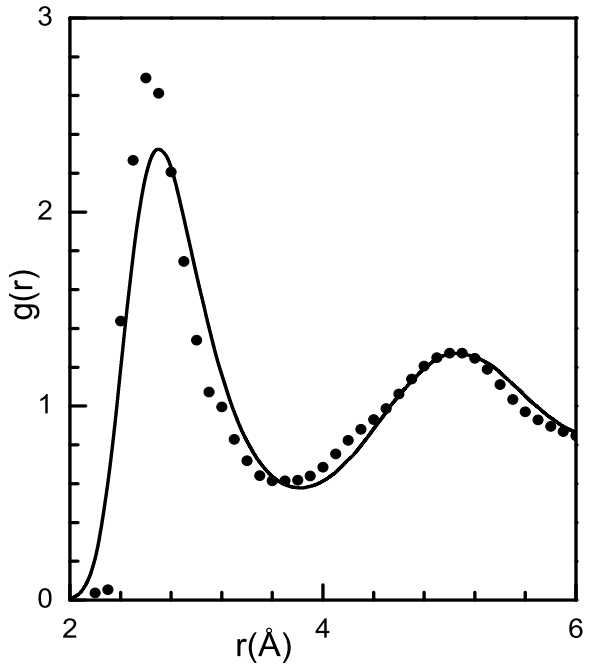

Figure 6.18: Pair distribution function, $g(r)$ for liquid Pd at $T = 1853$ K. The solid line stands for OF-AIMD results and the full circles stand for XR diffraction data [27].

6.1.7 Liquid Pt

The OF-AIMD static structure factor, $S(q)$ of l-Pt at $T = 2053$ K together with the XRD data of Waseda [27] is shown in Figure 6.19. A fair agreement is found for both the positions and phase of the oscillations although a small deviation in height of the main peak is observed, which is approximately 4.5% higher than that of the height of experimental main peak [27]. Figure 6.19 reveals that l-Pt has symmetric main peak located at $q_p \approx 2.73\,\text{Å}^{-1}$ whereas the XRD main peak position of $S(q)$ is located at $q_p \approx 2.76\,\text{Å}^{-1}$ [27]. If we compare the present OF-AIMD results with

the AIMD calculations performed by González *et al.* [212], clearly it appears that the height and position of the main peak and subsequent oscillations in the case of OF-AIMD results are slightly fitted better with the experiment. Here AIMD main peak is found at $q_p \approx 2.72\,\text{Å}^{-1}$ [212]. We have estimated the isothermal compressiblity $\kappa_T = 1.25 \pm 0.05$ (in units of 10^{-12} cm^2 dyne^{-1}) via Eqn. (5.15) for l-Pt at $T = 2053$ K, which is reasonably closer to the experimental value $\kappa_T = 1.44 \pm 0.32$ (in 10^{-12} cm^2 dyne^{-1} units) [27]. On the other hand, an AIMD calculation done by González *et al.* yield a value $\kappa_T = 1.80 \pm 0.15$ (in the same units) [212].

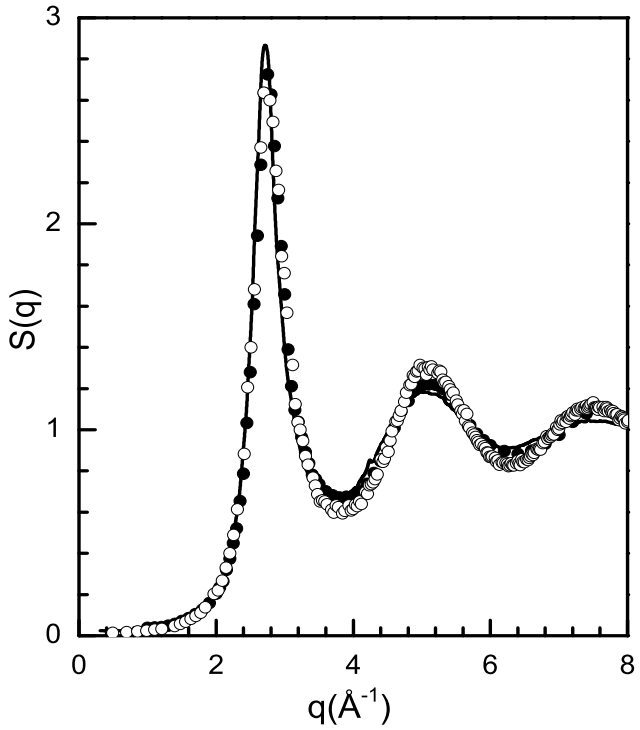

Figure 6.19: Static structure factor, $S(q)$ for liquid Pt at $T = 2053$ K . The solid line stands for OF-AIMD results, the full circles are the XR diffraction data [27], the open circles are the AIMD results performed by González *et al.* [212].

The associated $g(r)$ is plotted in Figure 6.20 along with the XR diffraction data

taken from Waseda [27]. It is worth noting that the main peak positions of $g(r)$ for OF-AIMD and experiment [27] are found at $r_p \approx 2.72$ Å and $r_p \approx 2.70$ Å respectively. The main peak position of $g(r)$ for l-Pt is found at $r_p \approx 2.69$ Å from the KS-AIMD simulations [212]. Here we have found a fair agreement with experiment although the height of the main peak is somewhat underestimated. Our calculated coordination number is $N_c \approx 12.34$ while the first minima located at $r_{min} = 3.74$ Å of $G(r)$, which is close to the experimental coordination number 11.75 computed from the $g(r)$ data of Waseda [27]. González *et al.* have calculated $N_c \approx 12.80$ [212](which is very close to our calculation) from an AIMD calculation while they found the first minimum of $g(r)$ at $r_{min} = 3.77$ Å.

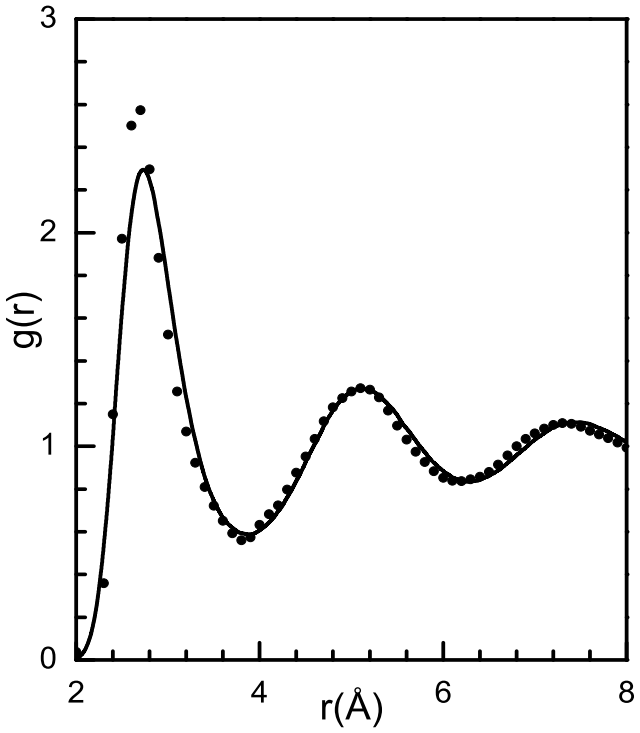

Figure 6.20: Pair distribution function, $g(r)$ for liquid Pt at $T = 2053$ K. The solid line stands for OF-AIMD results and the full circles stand for XR diffraction data [27].

6.1.8 Liquid Zn

The calculated $S(q)$ for l-Zn at $T = 723$ and 833 K are depicted in Figure 6.21 along with the XRD data of Waseda [27] and the NS data of North *et al.* [95]. A peculiar feature of the experimental $S(q)$ of l-Zn (and l-Cd) is the asymmetric shape of the main peak, with the low angle side being less steep than the high angle side whereas the subsequent oscillations show a symmetric shape. Although our results for $S(q)$ show an overall good agreement for the positions and amplitudes of the oscillations. However some differences are visible in the region of the main peak of $S(q)$, namely, the asymmetric shape of the experimental $S(q)$. The calculated main peak's position, q_p, is slightly smaller than experiment as the calculations give $q_p \approx 2.83\,\text{Å}^{-1}$ for both temperatures whereas the XRD data [27] give $q_p \approx 2.92\,\text{Å}^{-1}$ and the NS data [95] at $T = 723$ K is $q_p \approx 2.87\,\text{Å}^{-1}$. So, the OF-AIMD value is closer to that of neutron scattering data. For comparison, we note that the calculations of Lai *et al.* [86] were able to reproduce some asymmetric of the main peak although there was some underestimation of its height; moreover, it was suggested that this asymmetry was related to the medium and long range attractive parts of the interatomic pair potentials. The long wavelength limit of the $S(q)$ is linked to the thermodynamics through the isothermal compressibility κ_T, namely by the Eqn. (5.15). Therefore, we have fitted the obtained OF-AIMD $S(q)$ for small q values to an expression Eqn. (5.16) and we have estimated $\kappa_T = 2.2 \pm 0.1$ and 2.4 ± 0.1 (in 10^{-12} cm^2 dyne^{-1} units) for $T = 723$ and 833 K, respectively. To our knowledge, there are no experimental data found available for κ_T at those temperatures, but an estimate derived from experimental values of other thermodynamic magnitudes, suggests [213] $\kappa_T \approx 2.42$

and 2.60 (in 10^{-12} cm^2 dyne^{-1}) respectively.

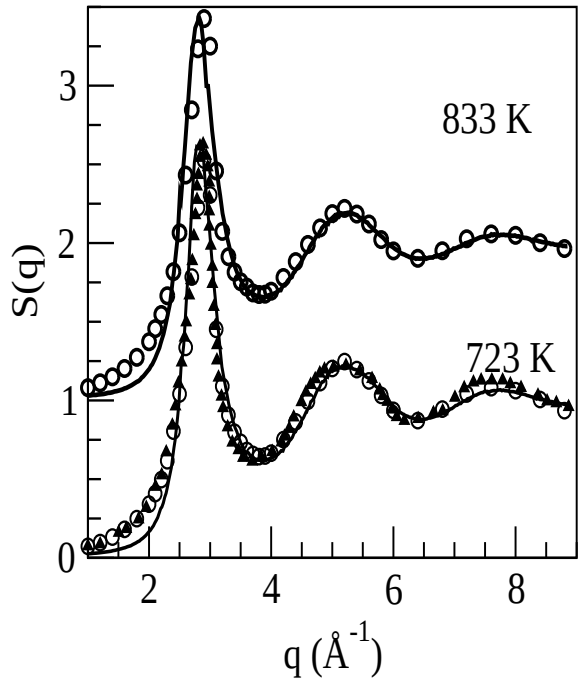

Figure 6.21: Static structure factor, $S(q)$ for l-Zn at $T = 723$ K and 833 K. The solid lines stand for OF-AIMD results, the open circles are the XR diffraction data [27] and the full triangles are the NS data at $T = 723$ K [95].

The pair distribution function, $g(r)$ provides information about the short range order in the liquid and Figure 6.22 shows the calculated $g(r)$ for l-Zn at T=723 and 833 K along with those derived from the XR diffraction data of Waseda [27]. The principal peak positions of theoretical and experimental [27] $g(r)$ are found at $r_p \approx 2.61$ Å and $r_p \approx 2.70$ Å, respectively. For comparison, we note that the EAM model of Belashchenko [87] for l-Zn produced a similar $g(r)$ for T=723 K but for higher temperatures it is underestimated the height of the main peak as well as the amplitude of the subsequent oscillations. The coordination number, N_c has been

obtained by the Eqn. (5.19) usig the radial distribution function (RDF), $4\pi r^2 \rho g(r)$, up to the position of its first minimum, r_{min}. Our calculated $g(r)$ gave $r_{min} = 3.55\,\text{Å}$ for T=723 and 833 K and the associated coordination numbers are $N_c = 12.1$ and 11.8 respectively. For comparison, we mention that the XRD-based $g(r)$ [27] gave $r_{min} = 3.50\,\text{Å}$ with associated $N_c = 11.3$ and 11.1 respectively.

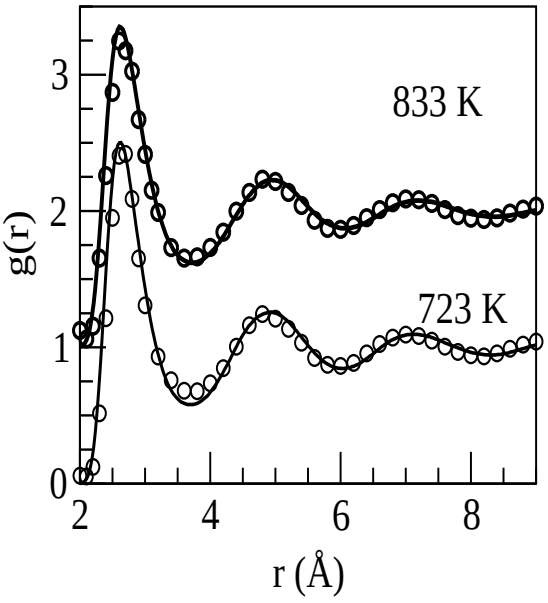

Figure 6.22: Pair distribution function, $g(r)$ for l-Zn at $T = 723$ K and 833 K. The solid lines stand for OF-AIMD results and the open circles stand for XR diffraction data [27].

6.1.9 Liquid Cd

The calculated $S(q)$ for l-Cd at $T = 623$ K is depicted in Figure 6.23 along with the XR diffraction data [27]. The calculated main peak position is at $q_p \approx 2.52\,\text{Å}^{-1}$, which

agrees reasonably well with the experimental main peak position $q_p \approx 2.60\,\text{Å}^{-1}$ [27]. We observed an overall qualitative good agreement with experiment, although our calculated $S(q)$ does not account for the slightly asymmetric shape of the experimental main peak. Nevertheless, the position and height of the subsequent oscillations are

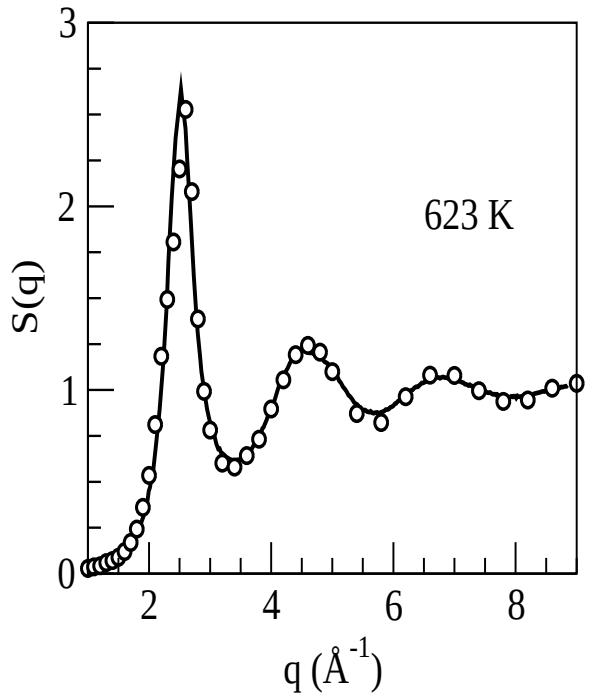

Figure 6.23: Static structure factor, $S(q)$ for liquid Cd at $T = 623$ K. The solid lines stand for OF-AIMD results, the open circles are the XR diffraction data [27].

well reproduced. Again, we note that the calculations of Lai *et al.* [86] as well as those of Calderin *et al.* [90] did reproduce the asymmetric shape of the main peak. However, the KS-AIMD approach of Calderin *et al.* does not resort to an interatomic pair potential picture of the interactions in the liquid which precludes a check on the suggestion about the role played by the medium and long range attractive parts

of the interatomic pair potential. By following the procedure outlined above, we have estimated the isothermal compressiblity for l-Cd at $T = 623$ K, and we have obtained $\kappa_T = 4.50 \pm 0.4$ (in units of 10^{-12} cm^2 dyne^{-1}); this is somewhat greater than the experimental [205] data of 3.20 (in the same units). Again, we note that the KS-AIMD calculations of Calderin *et al.* [90] gave a more accurate estimate, namely, $\kappa_T = 3.30 \pm 0.4$.

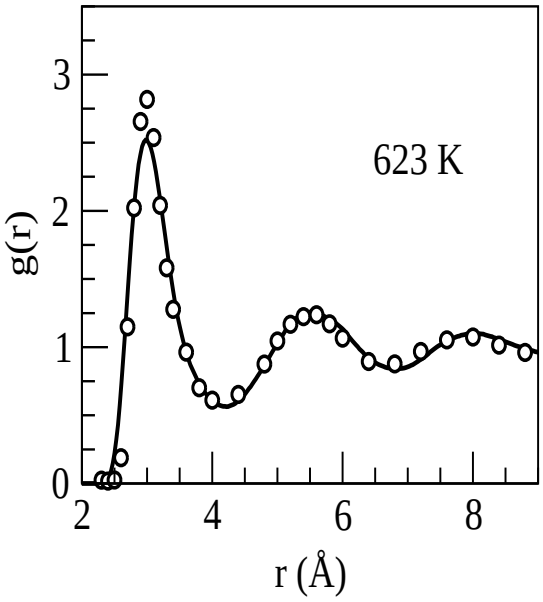

Figure 6.24: Pair distribution function, $g(r)$ for liquid Cd at $T = 623$ K. The solid line stands for OF-AIMD results and the open circles stand for XR diffraction data [27].

The pair distribution function $g(r)$ for l-Cd at $T = 623$ K is depicted in Figure 6.24 along with the XR diffraction data [27]. There is a qualitative good agreement with experiment, although the height of the main peak which is somewhat underestimated.

While the main peak positions of $g(r)$ both for OF-AIMD and experiment [27] are located at $r_p \approx 2.97\,\text{Å}$ and $r_p \approx 3.0\,\text{Å}$, respectively. As for the coordination number, we have obtained a value $N_c = 12.0$ which is somewhat greater than the value $N_c = 11.0$ derived from the experimental $g(r)$ [27].

6.1.10 Liquid Hg

Figure 6.25 shows the OF-AIMD results for the $S(q)$ of l-Hg at $T = 293$ and 353 K along with the XR diffraction data of Waseda [27] and Tamura *et al.* [214].

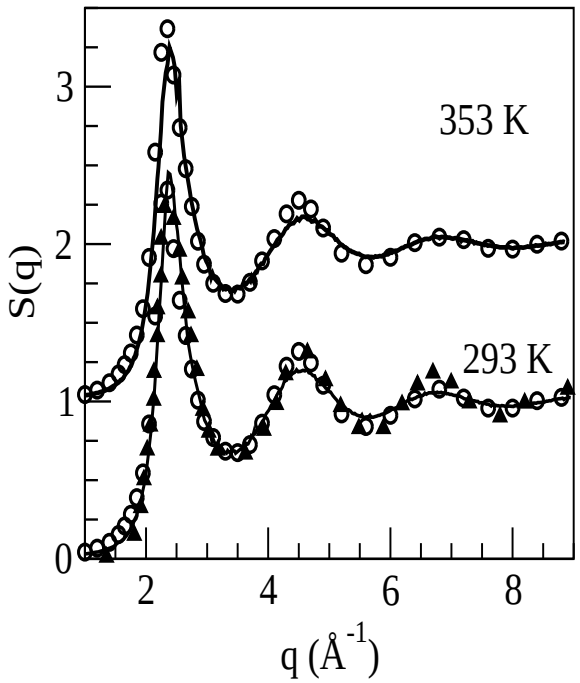

Figure 6.25: Static structure factor, $S(q)$ for liquid Hg at $T = 293$ K and 353 K. The solid lines stand for OF-AIMD results, the open circles are the XR diffraction data [27] and the full triangles are the XRD data of Tamura *et al.* [214].

The calculated main peak position is located at $q_p \approx 2.38\,\text{Å}^{-1}$ for $T = 293$K and 353K

which closely agrees with the corresponding experimental data $q_p \approx 2.30\,\text{Å}^{-1}$ [27]. There is an overall good agreement with experiment for both the positions and phase of the oscillations although the amplitudes are somewhat underestimated.

The associated $g(r)$ are plotted in Figure 6.26 along with those derived from the XR diffraction data of Waseda [27]. We obtain a fair agreement with experiment, although the height of the main peak occured at $r_p \approx 3.03\,\text{Å}$ is slightly underestimated. For both states, the experimental main peak position is located at $r_p \approx 3.10\,\text{Å}$ [27]. At room temperature, our calculated coordination number is $N_c \approx 12.0$ which is close to the number 11.6 derived from the experimental $g(r)$ [27].

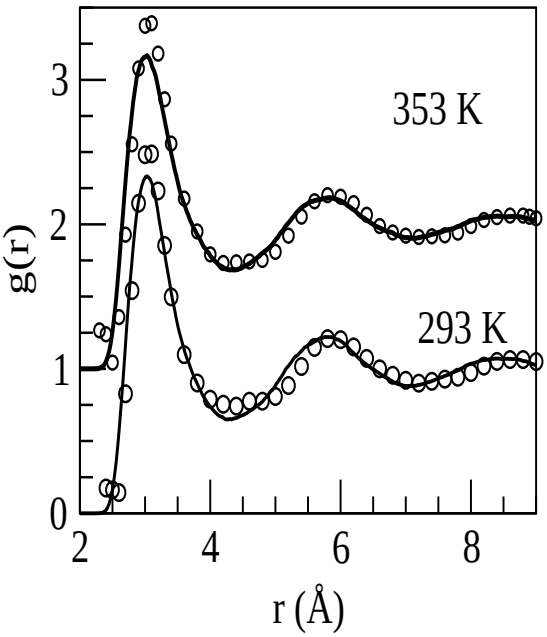

Figure 6.26: Pair distribution function, $g(r)$ for liquid Hg at $T = 293$ K and 353 K. The solid lines stand for OF-AIMD results and the open circles stand for XR diffraction data [27].

6.2 Dynamic Properties: Single Particle Dynamics

In this section we will focus to analyze some magnitudes related to the single particle dynamics obtained from the OF-AIMD simulation. First of all, we have presented the results for the velocity autocorrelation function (VACF), $Z(t)$, of a tagged ion in the fluid, which is defined in Eqn. (5.20). To study the atomic transport properties of liquid system, the self-diffusion coefficient, D is an interesting magnitude, which can be obtained from either the time integral of $Z(t)$ as appear in Eqn. (5.36) or the slope of the mean square displacement as described by the Eqn. (5.30). We have used both of these routes to evaluate, D which practically leads to the same value.

Another important magnitude is the self-intermediate scattering function, $F_s(q,t)$ which is defined in Eqn. (5.42). The time Fourier transform (FT) of $F_s(q,t)$ is the self-dynamic structure factor, $S_s(q,\omega)$ which has experimental relevance due to its connection with the incoherent part of INS cross-section. It is interesting to note that, $F_s(q,t)$ may be expressed within the Gaussian approximation by the Eqn. (5.45). Now, this is of interest to compare the nature of the results of Eqn. (5.42) and Eqn. (5.45).

6.2.1 Liquid Cr

The velocity autocorrelation function, $Z(t)$, is depicted in Figure 6.27 for l-Cr. The function $Z(t)$ shows an oscillatory behavior with time t. The negative values of $Z(t)$ indicate backscattering of ions due to cage effects produced by surrounding neighbours [123]. The self-diffusion coefficient has been calculated from both $Z(t)$ and $\langle \delta R^2(t) \rangle$. Both routes provide the same result D$= 0.71 \pm 0.01$ Å^2 ps^{-1}. To the

best of our knowledge, no experimental data for D is available for l-Cr. Therefore a comparison with other theoretical results may worthful. A theoretical calculation [68] employing the scaling law defined by Dzugutov [69] yields a value of D=0.712 $\text{Å}^2\,\text{ps}^{-1}$ for l-Cr, which is very close to our result. This agreement gives at least a feeling that our simulated value is reliable.

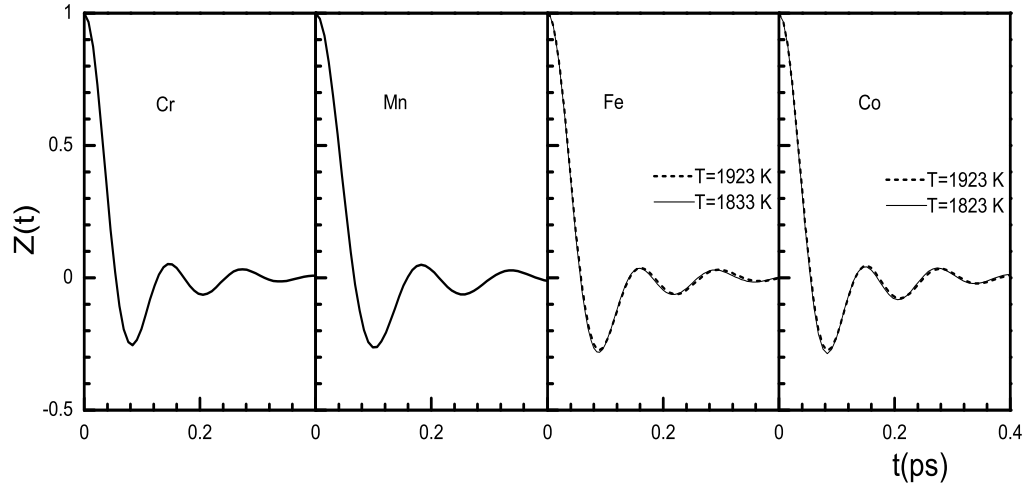

Figure 6.27: Normalized velocity autocorrelation functions for l-Cr at T = 2173 K, l-Mn at T = 1533 K, l-Fe at T = 1833 and 1923 K and l-Co at T = 1823 K and T = 1923 K.

Figure 6.28 shows the self-intermediate scattering function, $F_s(q,t)$ at several q values for l-Cr. Here the solid line represents the OF-AIMD $F_s(q,t)$ as defined in Eqn. (5.42) and, the filled circles represent the Gaussian approximation of $F_s(q,t)$ as given by Eqn. (5.45). It displays the typical monotonic non-linear decrease with time which becomes faster with increasing q/q_p values. In fact, this trend is similar to that of the simple liquid metals near their respective triple points [15,19,123,215]. On the other hand, it is also noticed from the same figure that, Eqn. (5.42) and Eqn. (5.45)

completely merge with each other for low q values but deviates somewhat at small t for large q. This clearly reveals the shortcomings of the Gaussian approximation.

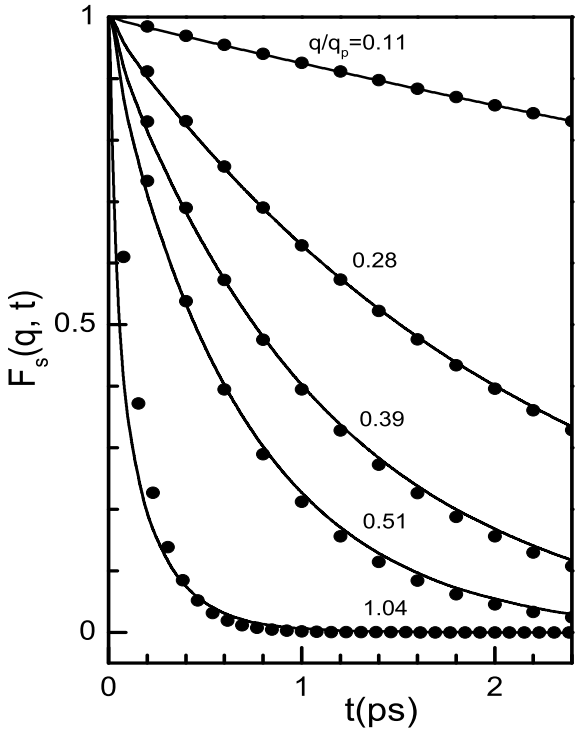

Figure 6.28: Self-intermediate scattering function, $F_s(q,t)$ for l-Cr at $T = 2173$ K for several q/q_p values along with the Gaussian approximation for $F_s(q,t)$. Full lines: present OF-AIMD results. Filled circles: Gaussian approximation.

6.2.2 Liquid Mn

Figure 6.27 shows $Z(t)$ for l-Mn at $T = 1533$ K. It is seen that the cage effect causes the $Z(t)$ to be negative, reflecting the backscattering of ions as mentioned before. The first minimum appears at t $\approx$ 0.10 ps and the subsequent oscillations are very weak as in the case of l-Cr. The self-diffusion coefficients are calculated using the two routes as mentioned before, and obtained the same result. The OF-AIMD value of

D is found to be 0.53 ± 0.01 Å^2 ps^{-1} for l-Mn at $T = 1533$ K. We are not aware of any experimental data for l-Mn to compare with our results. But results from other calculations give values $D = 0.52$ Å^2 ps^{-1} [68] and $D = 0.42$ Å^2 ps^{-1} [77]. Our result is almost same to that of Thakor *et al.* [68] and pretty close to Gosh *et al.* [77].

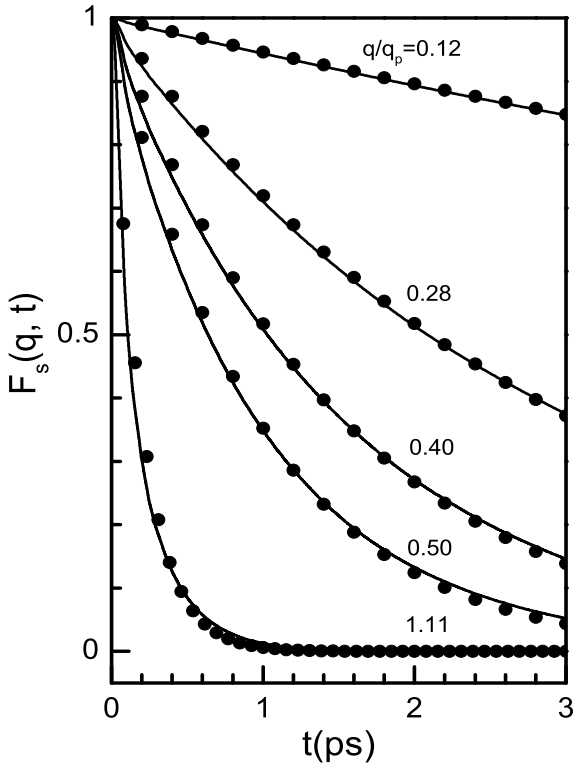

Figure 6.29: Self-intermediate scattering functions, $F_s(q,t)$ at several q/q_p values for l-Mn at $T = 1533$ K along with the Gaussian approximation for $F_s(q,t)$. Full lines: present OF-AIMD results. Full circles: Gaussian approximation.

The OF-AIMD self-intermediate scattering function, $F_s(q,t)$ for l-Mn for different q values at $T = 1533$ K are displayed in Figure 6.29. The observed monotonic behaviour of $F_s(q,t)$ as a function of t is similar to that of l-Cr. But in this case the matching between the Gaussian approximation and our calculation is much better

even for high q values at small t.

6.2.3 Liquid Fe

Figure 6.27 shows the velocity autocorrelation function, $Z(t)$ for l-Fe at $T = 1833$ and 1923 K. It is noticed that, the typical cage effect is also present there as in the case of l-Cr and l-Mn. It is also noticed that the value of the first minimum of $Z(t)$ is affected by the temperature, that is, the depth becomes shallower as temperature increases. Physically, it means that the backscattering effect becomes less significant with increasing temperature due to the decrease of ionic number density. In the case of l-Fe, the first minimum of the $Z(t)$ occurs at time t $\approx$ 0.08 ps. However, the self-diffusion coefficients calculated from Eqn. (5.30) and Eqn. (5.36) are almost same. The magnitude of D is found to be $0.49 \pm 0.02\,\text{Å}^2\,\text{ps}^{-1}$ and $0.54 \pm 0.01\,\text{Å}^2\,\text{ps}^{-1}$ at $T =$ 1833 and 1923 K, respectively. These results show the temperature dependent trends correctly, that is, when temperature increases the density decreases and consequently diffusivity increases. Yet we are not aware of any experimental data of D for l-Fe, so it would be of worth to compare the OF-AIMD value with other calculated results. Protopapas *et al.* [61] calculated the self-diffusion coefficient by extending the Enskog theory [76] within the assumption that the self-diffusion coefficient of a dense metallic fluid is the same as that of an appropriate hard sphere fluid. Thus, they found $D = 0.416\,\text{Å}^2\,\text{ps}^{-1}$ and $0.585\,\text{Å}^2\,\text{ps}^{-1}$ at $T = 1808$ and 1973 K, respectively. Yokoyama *et al.* [71] calculated D_{HS} for l-Fe by using the scaling law along with an excess entropy obtained for the hardsphere liquid. The values obtained by them were $D_{\text{HS}} = 0.42\,\text{Å}^2\,\text{ps}^{-1}$ and $0.73\,\text{Å}^2\,\text{ps}^{-1}$ at $T = 1833$ and 1923 K, respectively.

Another study by Korkmaz *et al.* [72] using the same procedure but taking the values of excess entropy calculated from the integral equation theory yields $D = 0.45\,\text{Å}^2\,\text{ps}^{-1}$ and $D = 0.55\,\text{Å}^2\,\text{ps}^{-1}$ at $T = 1833$ and 1923 K, respectively. Very recently, Marques *et al.* [52] found a value $D = 0.37 \pm 0.02\,\text{Å}^2\,\text{ps}^{-1}$ at $T = 1873$ K for l-Fe.

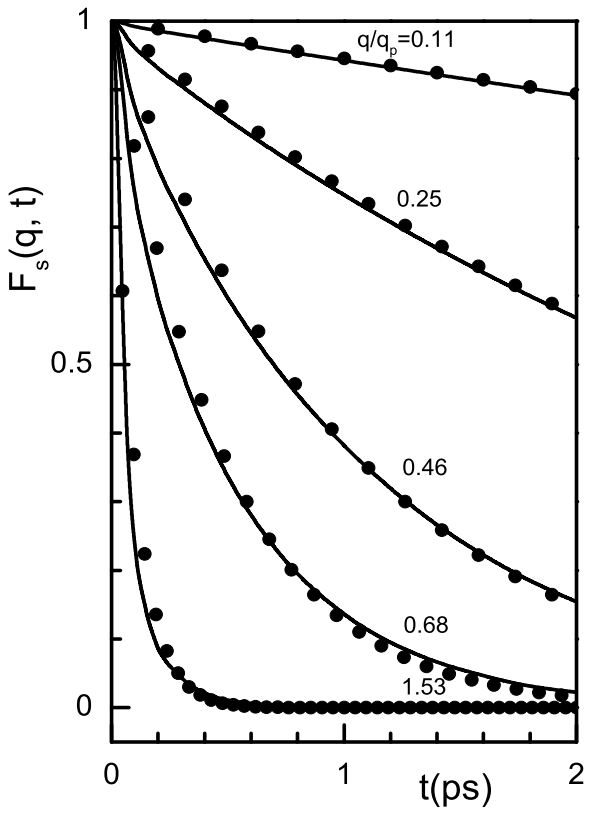

Figure 6.30: Self-intermediate scattering functions, $F_s(q,t)$, at several q/q_p values of l-Fe for T= 1833 K along with the Gaussian approximation for $F_s(q,t)$. Full lines: present OF-AIMD results. Full circles: Gaussian approximation.

The self-intermediate scattering function, $F_s(q,t)$ for l-Fe is shown in Figure 6.30 for several values of q. Monotonic decrease for low q values and rapid decrement for large q values in a way similar to Cr and Mn is also noticed for l-Fe. The OF-AIMD result and the Gaussian approximation match well for both small and large q values.

But for some intermediate values (viz. q/q_p=0.46 and 0.68) agreement at small t is somewhat deviated than the case of l-Cr and l-Mn.

6.2.4 Liquid Co

The velocity autocorrelation function $Z(t)$ for l-Co at $T = 1823$ and 1923 K are shown in Figure 6.27. Figure shows a typical backscattering effect and oscillations in a way similar to those liquid systems discussed earlier. Here the first minimum of $Z(t)$ is located at $t \approx 0.085$ ps. The temperature effect on $Z(t)$ causes the reduction in the depth of the principal minimum. This is because, the density decreases with increase of temperature and as a result the cage effect becomes less relevant. The self-diffusion coefficients calculated from the OF-AIMD configurations are found to be D=0.41 $\pm$ 0.02 $\text{Å}^2\,\text{p}s^{-1}$ and 0.48$\pm$0.02 $\text{Å}^2\,\text{p}s^{-1}$ at $T = 1823$ and 1923 K, respectively. To the best of our knowledge, no experimental data of D is available for l-Co. It is therefore worth to compare with other theoretical results. For example, the value of D calculated by Yokoyama [70] is 0.41 $\text{Å}^2\,\text{p}s^{-1}$ at $T = 1823$ K and Yokoyama *et al.* [71] computed values, D=0.35 $\text{Å}^2\,\text{p}s^{-1}$ and 0.46 $\text{Å}^2\,\text{p}s^{-1}$ at $T = 1823$ and 1923 K, respectively. An AIMD study [216] gives values of $D = 0.37\,\text{Å}^2\,\text{p}s^{-1}$ and 0.44 $\text{Å}^2\,\text{p}s^{-1}$ for $T = 1823$ and 1923 K, respectively. Our values agree very well with these calculated results and the agreement is within 10% of the value calculated from AIMD [216].

The self-intermediate scattering function, $F_s(q,t)$, for l-Co is plotted for several values of q in Figure 6.31 for $T = 1823$ K. Figure shows the typical monotonic decay as the function of t. This feature is similar to that of the systems discussed previously. That is, the rate of decay is high for large value of q. On the other hand, the agreement

with the Gaussian approximation is just fair in this case for q/q_p values higher than 0.11 of l-Co.

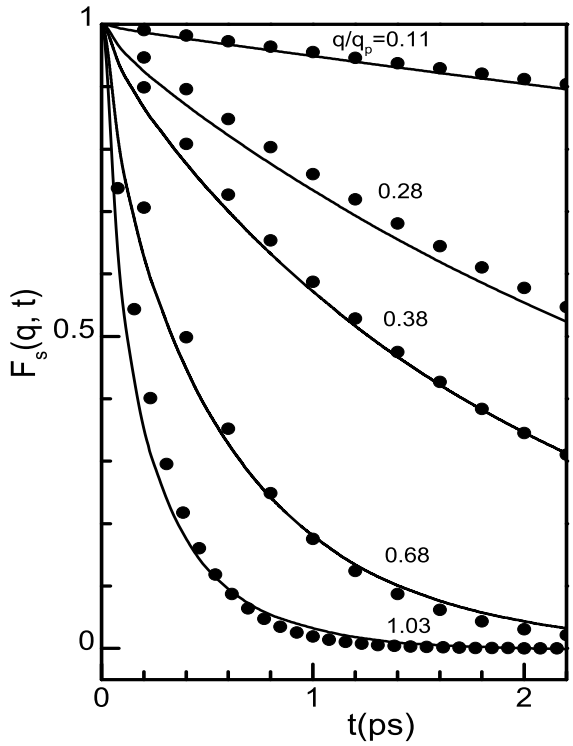

Figure 6.31: Self-intermediate scattering functions, $F_s(q,t)$, at several q/q_p values of l-Co for $T = 1823$ K along with the Gaussian approximation for $F_s(q,t)$. Full lines: present OF-AIMD results. Full circles: Gaussian approximation.

6.2.5 Liquid Ni

The calculated $Z(t)$ for l-Ni is shown in Figure 6.32. It shows the typical backscattering behavior with a first minimum at t $\approx$ 0.10 ps and the amplitude of subsequent oscillations are weak. We recall here that the negative values of $Z(t)$ represent a backscattering effect induced by the cage effect. The self-diffusion coefficient has been calculated by the time integral of $Z(t)$ and also from the slope of the mean

square displacement. Interestingly, both routes lead to similar results. Thus, we have

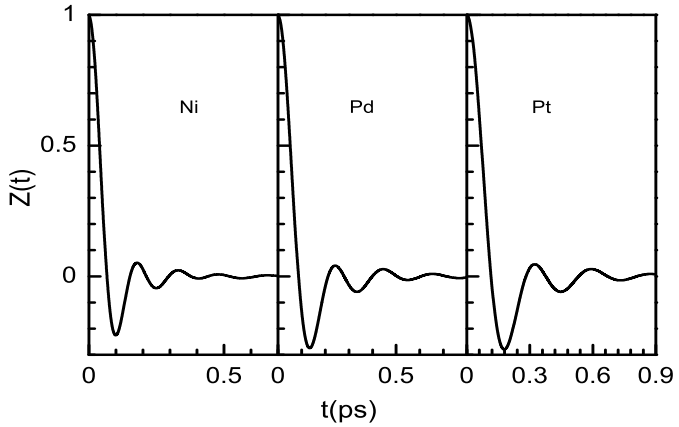

Figure 6.32: Normalized velocity autocorrelation functions of liquid Ni at T = 1773 K, Pd at T = 1853 K and Pt at T = 2053 K.

obtained the same D=0.68 ± 0.01 Å^2 ps^{-1} from either case. The CMD study of Kart *et al.* [59] gave D_{cal} = 0.548 Å^2 ps^{-1} and D_{cal} = 0.545 Å^2 ps^{-1} from $Z(t)$ and the slope of the mean square displacement for l-Ni at T = 1773 K, respectively. To best of our knowledge, no experimental data exist for comparison of this system. The value of D_{pre} predicted by Protopapas *et al.* is 0.461 Å^2 ps^{-1} [61]. Some authors [59] refered this predicted value as experimental one. This value of D_{pre} is almost 32% less than that of our calculated result. The CMD study of Alemany *et al.* [54] reported a result of D=0.252 ± 0.004 Å^2 ps^{-1} at T = 1775 K. A recent AIMD study by Jakse *et al.* [66] reports a value D=0.44 ± 0.03 Å^2 ps^{-1} at T = 1850 K. Our result seems to be qualitatively agrees with this result.

Figure 6.33 shows the OF-AIMD results of $F_s(q,t)$ for l-Ni for several q/q_p values at T = 1773 K. It displays the behavior of typical monotonic, non-linear decrease with time which becomes faster with increasing values q/q_p. In fact this trend is similar

to that of the liquid metals near their respective triple points [15, 16, 19–21, 123, 215, 217, 218]. By using Eqn. (5.45), we have verified that the Gaussian approximation provides a good description of OF-AIMD $F_s(q,t)$. This is shown in Figure 6.33 where we have plotted the OF-AIMD $F_s(q,t)$ for several q/q_p values as well as the results predicted by the Gaussian approximation.

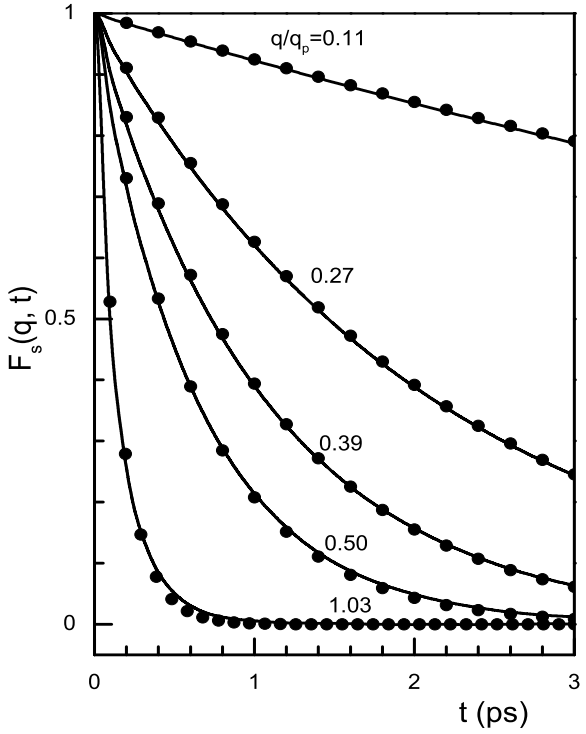

Figure 6.33: Self-intermediate scattering function, $F_s(q,t)$ of liquid Ni at $T = 1773$ K for several q/q_p values along wth the Gaussian approximation for $F_s(q,t)$. Full lines: present OF-AIMD results. Full circles: Gaussian approximation.

6.2.6 Liquid Pd

The calculated $Z(t)$ for l-Pd at $T = 1853$ K is plotted in Figure 6.32, where we have observed the typical cage effect with a first minimum at t $\approx$ 0.13 ps and the

subsequent oscillations seem to be very weak. According to the technique mentioned

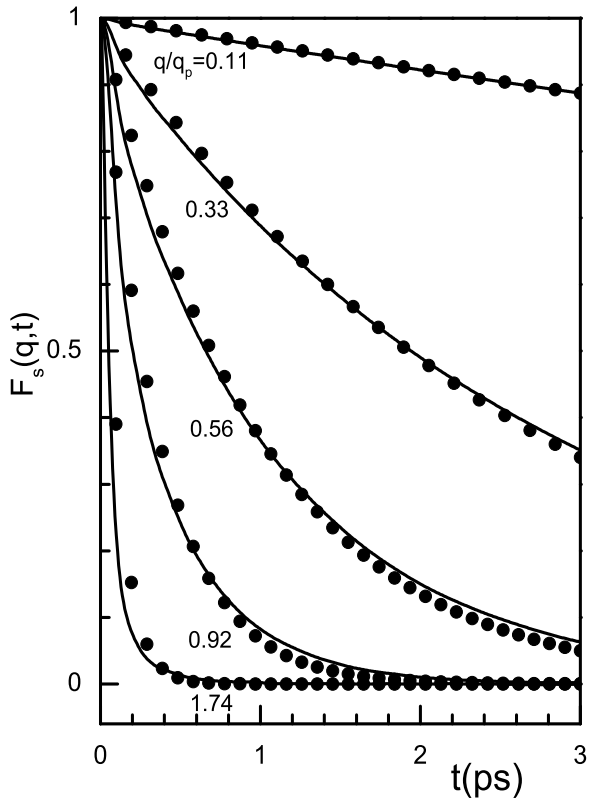

Figure 6.34: Self-intermediate scattering functions, $F_s(q,t)$, at several q/q_p values, for l-Pd at $T = 1853$ K along wth the Gaussian approximation for $F_s(q,t)$. Full lines: present OF-AIMD results. Full circles: Gaussian approximation.

earlier, the self-diffusion coefficient has been evaluated and we obtained D=0.40 $\pm$ 0.01 Å^2 ps^{-1} for l-Pd at $T = 1853$ K. The CMD study by Kart *et al.* [59] yield values for self-diffusion coefficient from $Z(t)$ and the slope of the mean square dispacement are $D_{cal} = 0.498\pm0.005$ Å^2 ps^{-1} and , $D_{cal} = 0.494\pm0.007$ Å^2 ps^{-1} for l-Pd at $T = 1853$ K, respectively. For comparison, we note here that the CMD study of Alemany *et al.* [54] using the TB-SMA method computed D=0.403 $\pm$ 0.003 Å^2 ps^{-1}. In another CMD study using embedded atom model, Alemany *et al.* [57] have also calculated

$D = 0.38 \pm 0.004\,\text{Å}^2\,\text{ps}^{-1}$. To the best of our knowledge, no experimental data is found in scientific literature for l-Pd at $T = 1853$ K. Our result is very close to the values found by Alemany *et al.* [54, 57]. The KS-AIMD calculation done by González *et al.* yielded $D_{KS-AIMD} = 0.27 \pm 0.02\,\text{Å}^2\,\text{ps}^{-1}$ [212].

Figure 6.34 shows OF-AIMD $F_s(q,t)$ at several q/q_p values for l-Pd at $T = 1853$ K. We notice that the features are very similar to those liquid systems already explained before. By using Eqn. (5.45), we have verified that the Gaussian approximation also provides a good description of OF-AIMD $F_s(q,t)$. This is shown in Figure 6.34 where we have plotted the OF-AIMD $F_s(q,t)$ for several q/q_p values as well as the results predicted by the Gaussian approximation.

6.2.7 Liquid Pt

The calculated $Z(t)$ of l-Pt at $T = 2053$ K is presented in Figure 6.32. The $Z(t)$ shows the typical back scattering behaviour with a first minimum located at t ≈ 0.18 ps, which is greater than that for Ni and Pd. This is because, the atomic mass of Pt is larger than that for Ni and Pd, therefore the longer times are necessary to reverse the initial particle's velocity and thus, the minimum's position moves towards longer times. The calculation of the self-diffusion coefficient gives D=$0.33 \pm 0.01\,\text{Å}^2\,\text{ps}^{-1}$ for l-Pt at $T = 2053$ K. While the CMD study of Alemany *et al.* computed values D=0.281 ± 0.003 [57] and $0.284 \pm 0.003\,\text{Å}^2\,\text{ps}^{-1}$ [54]. Therefore, it seems that our OF-AIMD result agrees well with the results obtained by Alemany *et al.* [54, 57]. We do not find any experimental data in the available literature to compare our result for l-Pt at $T = 2053$ K. Due to the lack of experimental data, we have compared

our result wtih the KS-AIMD study performed by González *et al.* where they have reported a value D=$0.27 \pm 0.02\,\text{Å}^2\,\text{ps}^{-1}$ [212].

Figure 6.35 shows the OF-AIMD $F_s(q,t)$ for several q/q_p values of l-Pt at $T = 2053$ K. The typical monotonic decay also present in this case. From the figure we may conclude that the small deviation of Gaussian approximation for $F_s(q,t)$ from the OF-AIMD $F_s(q,t)$ increases with increasing value of q/q_p at smaller value of t for l-Pt. Even though we may say that the Gaussian approximation provides a good description of OF-AIMD $F_s(q,t)$, which is plotted in Figure 6.35 for several q/q_p values.

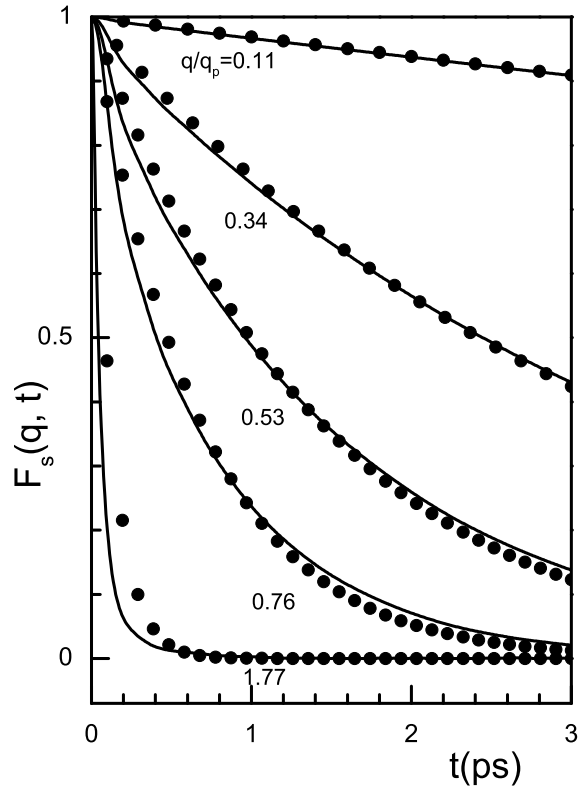

Figure 6.35: Self-intermediate scattering functions, $F_s(q,t)$, at several q/q_p values, for l-Pt at $T = 2053$ K along wth the Gaussian approximation for $F_s(q,t)$. Full lines: present OF-AIMD results. Full circles: Gaussian approximation.

6.2.8 Liquid Zn

The calculated $Z(t)$ of l-Zn are depicted in Figure 6.36. They show the typical backscattering behaviour with a first minimum at t $\approx$ 0.15 ps and the subsequent oscillations have a weak amplitude. We recall that the negative values of $Z(t)$ represent a backscattering effect induced by the cage effect; moreover, with increasing temperature (and decreasing density) it becomes less relevant *i.e.* the first minimum in $Z(t)$ is shallower and the subsequent oscillations are rather weak. The self-diffusion

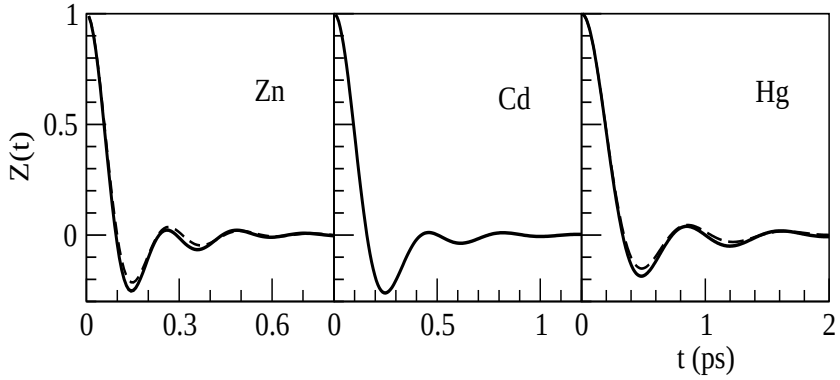

Figure 6.36: Normalized velocity autocorrelation functions of liquid Zn at $T = 723$ K (full line) and $T = 833$ K (dashed line), Cd at $T = 623$ K and Hg at $T = 293$K (full line) and $T = 353$ K (dashed line).

coefficient has been calculated by both the time integral of $Z(t)$ and from the slope of the mean square displacement, with both routes leading to similar results. From these two methods we have obtained $D = 0.26 \pm 0.03$ and $0.37 \pm 0.04\,\text{Å}^2\,\text{ps}^{-1}$ at $T = 723$ and 833 K, respectively. For comparison, we note that when the experimental value [219] for l-Zn at melting ($T = 693$ K), $D_{exp} = 0.203\,\text{Å}^2\,\text{ps}^{-1}$, is extrapolated to $T = 723$ and 833 K we obtain $D = 0.24 \pm 0.03$ and $0.40 \pm 0.02\,\text{Å}^2\,\text{ps}^{-1}$.

We have also calculated the $F_s(q,t)$ of l-Zn for several q values at $T = 723$ K. It

displays the typical monotonic, non-linear decrease with time which becomes faster with increasing q values; in fact this trend is similar to that of the simple liquid metals near their respective triple points [15, 16, 19–21, 123, 215, 217, 218].

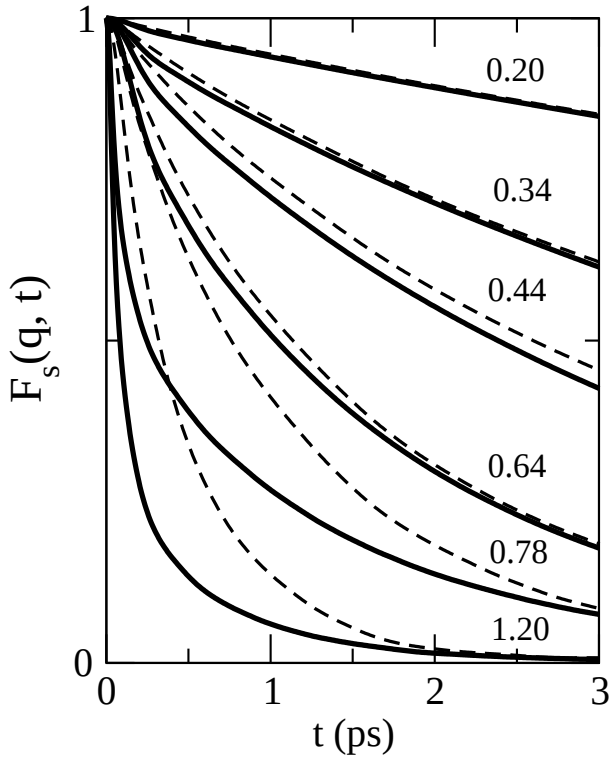

Figure 6.37: Self-intermediate scattering functions, $F_s(q,t)$, at several q/q_p values, for l-Cd at $T = 623$ K. Full lines: present OF-AIMD results. Dotted lines: KS-AIMD results of Calderin *et al.* [90].

6.2.9 Liquid Cd

The calculated $Z(t)$ for l-Cd at $T = 623$ K is plotted in Figure 6.36 where we observe the typical cage effect with a first minimum at t $\approx$ 0.25 ps and the subsequent oscillations are very weak. As previously mentioned, the self-diffusion coefficient has been evaluated and we have obtained a value $D = 0.21 \pm 0.02$ Å^2 ps^{-1} for l-Cd at $T =$

623 K. To compare with experiment, we have extrapolated the two available data for l-Cd near melting ($T = 594$ K), namely $D_{exp} = 0.178\,\text{Å}^2\,\text{ps}^{-1}$ and $0.220\,\text{Å}^2\,\text{ps}^{-1}$ [220–222]; its extrapolation to the higher temperature $T = 623$ K leads to the estimates $D = 0.215\,\text{Å}^2\,\text{ps}^{-1}$ and $0.252\,\text{Å}^2\,\text{ps}^{-1}$, which are close to our result. For comparison, we note that the KS-AIMD study of Calderin *et al.* [90] produced a result $D = 0.22 \pm 0.02\,\text{Å}^2\,\text{ps}^{-1}$ for l-Cd at $T = 625$ K.

Figure 6.37 shows $F_s(q,t)$, for several q/q_p values of l-Cd at $T = 623$ K. It shows the typical monotonic decay but in order to check its accuracy we have also plotted KS-AIMD results of Calderin *et al.* [90]. It is observed that both methods give similar $F_s(q,t)$ for q/q_p smaller than ≈ 0.65; indeed there is a practical coincidence for q/q_p smaller than ≈ 0.20. This is understandable because in the hydrodynamic limit ($q \to 0$), the shape of the $F_s(q,t)$ is practically controlled by the value of the self-diffusion coefficient and, as shown previously, both the OF-AIMD and KS-AIMD give very similar results for D. However, with increasing q/q_p values, clear discrepancies are visible.

6.2.10 Liquid Hg

The calculated $Z(t)$ of l-Hg at $T = 293$ and 353 K are depicted in Figure 6.36. The $Z(t)$ shows the typical back scattering behaviour with a first minimum which is located at t $\approx$ 0.5 ps, which is greater than that for Zn and Cd. This is so, because with increasing atomic mass, longer times are necessary to reverse the initial particle's velocity and therefore, the minimum's position moves towards longer times. The calculation of the self-diffusion coefficient gave $D = 0.165 \pm 0.010$ and $0.230 \pm$

$0.010\,\text{Å}^2\,\text{ps}^{-1}$ for l-Hg at T= 293 and 353 K respectively. These results compare well with the available experimental data, namely $D_{exp} = 0.144$ and $0.159\,\text{Å}^2\,\text{ps}^{-1}$ for l-Hg at T= 283 and 298 K respectively [223, 224]. More recently, the room temperature INS measurements by Bove *et al.* [98, 99] have yielded a value $D_{exp} = 0.157\,\text{Å}^2\,\text{ps}^{-1}$. For comparison, we note that the KS-AIMD study of Calderin *et al.* [91–93] produced a result of $D = 0.13 \pm 0.01\,\text{Å}^2\,\text{ps}^{-1}$ for l-Hg at $T = 298$ K.

6.3 Dynamic Properties: Collective Dynamics

The intermediate scattering function, $F(q,t)$, provides information about the collective dynamics of density fluctuations. $F(q,t)$ is defined in Eqn. (5.47). The time FT of $F(q,t)$ gives the dynamic structure factor $S(q,\omega)$, which has a direct relation with the scattered intensity in INS or IXS experiments. Another important dynamic magnitude is the microscopic current density, $\mathbf{j}(q,t)$ due to the overall motion of particles, defined in Eqn. (5.50). This is usually split into a longitudinal component $\mathbf{j}_l(q,t)$ parallel to $\mathbf{q}$ and a transverse component $\mathbf{j}_t(q,t)$ perpendicular to $\mathbf{q}$. The transverse and longitudinal current correlation functions are defined in Eqns. (5.52) and (5.53), respectively. The transverse current correlation function $J_t(q,t)$ gives information about shear modes and in the hydrodynamic limit ($q \to 0$), can be approximatted by Eqn. (5.61), where, η is the shear viscosity. For intermediate q values, $J_t(q,t)$ shows a complicated behaviour, because it may oscillate signaling the propagation of shear waves. It is possible to derive the shear viscosity coefficient, η from the calculated, $J_t(q,t)$ [123, 208, 225]. The memory function representation of $J_t(q,t)$ is defined in Eqn. (5.62), where the tilde denotes the Laplace transformation and $\tilde{\eta}(q,z)$ is the

generalized shear viscosity coefficient. The area under the normalized $J_t(q,t)$ gives $\beta m\tilde{J}_t(q,z=0)$, from which $\tilde{\eta}(q,z=0) \equiv \tilde{\eta}(q)$ can be obtained from Eqn. (5.63) and when extrapolated to $q \to 0$ produces a usual shear viscosity coefficient, η. This is performed by extrapolating the property that inversion is a symmetry in the system and, therefore, $\tilde{\eta}(q)$ should be an even function of q which allows to approximate Eqn. (5.64)(when $q \to 0$) [208].

6.3.1 Liquid Cr

Figure 6.38 shows the normalized intermediate scattering function, $F(q,t)$ for several values of q scaled by q_p of $S(q)$. Figure shows oscillatory behaviour upto $q/q_p \approx 0.73$.

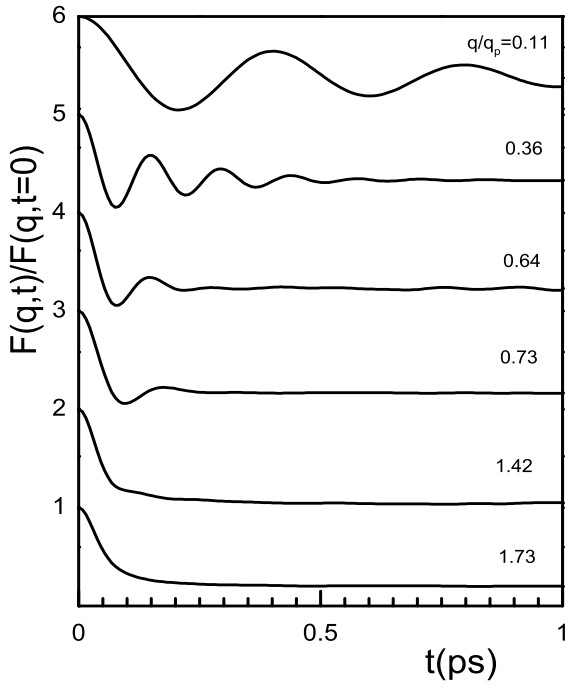

Figure 6.38: Normalized intermediate scattering functions, $F(q,t)$ at several q/q_p values, for l-Cr at $T = 2173$ K.

It is clear that the amplitude of oscillations diminishing for increasing q values. We stress that this behaviour is very similar to that one found for the simple and noble liquid metals [15, 18, 19, 123, 215]. We have performed the time Fourier transform of $F(q,t)$ with an appropriate window to smooth out the truncation effect to obtain associated dynamic structure factor, $S(q,\omega)$ which is dipicted in Figure 6.39 for several q values.

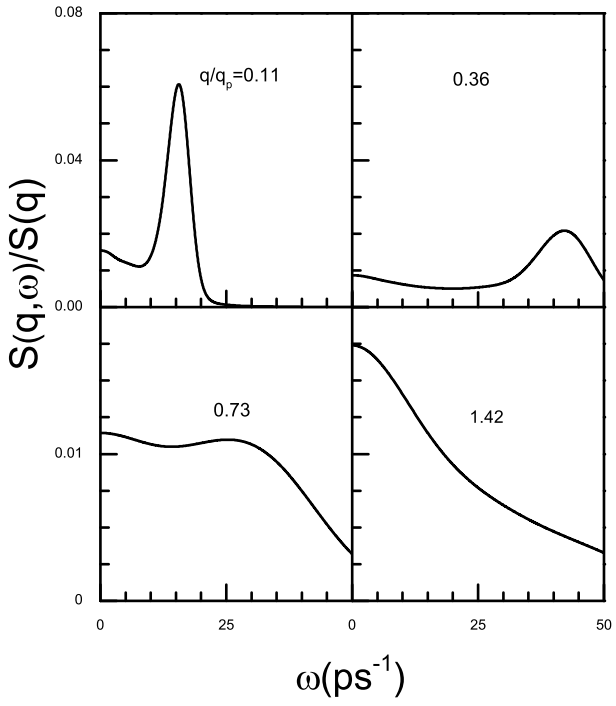

Figure 6.39: Dynamic structure factors $S(q,\omega)$ of l-Cr at $T = 2173$ K for several q/q_p values.

It is noticed that upto $q/q_p \approx 0.73$, the calculated $S(q,\omega)$ exhibit the well defined side peaks indicating the existence of collective density excitation. For $q > 0.73q_p$, a shoulder is observed instead of peak and after then it decreases monotonically with

increasing q. From Figure 6.39 it is also seen that the sharpness of peak decreases with increasing q, becomes blunt at a stage and finally disappears. This is because, at small q, wavelength is large relative to interatomic distance, consequently collective excitation occurs. At large q, wavelength becomes small, so collective excitation can not occur. From the positions of the side peaks, $\omega_m(q)$ for different q one can evaluate a dispersion relation. This dispersion curve is shown in Figure 6.40.

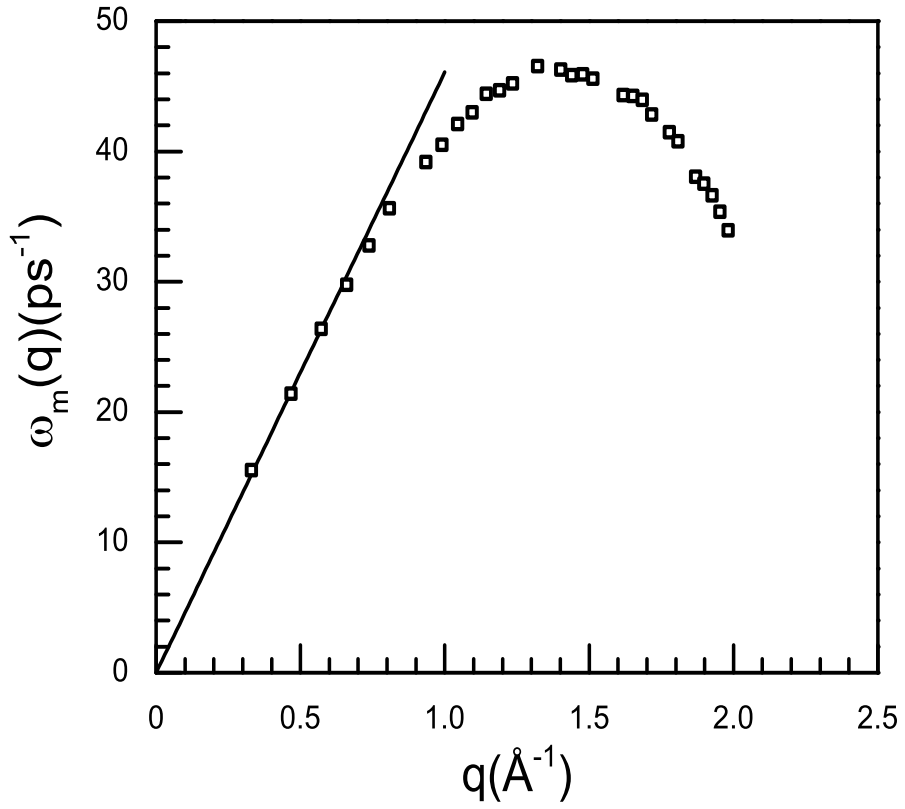

Figure 6.40: Dispersion relation for l-Cr at $T = 2173$ K. Open squares: peak positions $\omega_m(q)$ from the OF-AIMD $S(q,\omega)$. Full line: linear dispersion with the adiabatic sound velocity $c_s = 4586$ ms^{-1}.

The slope of the dispersion curve evaluated at $q \to 0$ provides an estimation of

adiabatic sound velocity c_s. The value of c_s for l-Cr is found to be $c_s \approx 4586 \pm 25$ ms^{-1}, which is in good agreement with experimental value 4520 ms^{-1} [63] at $T = 2173$ K. A hard sphere model studied by Yokoyama [65] gives a value $c_s = 4313$ ms^{-1} at $T = 2173$ K.

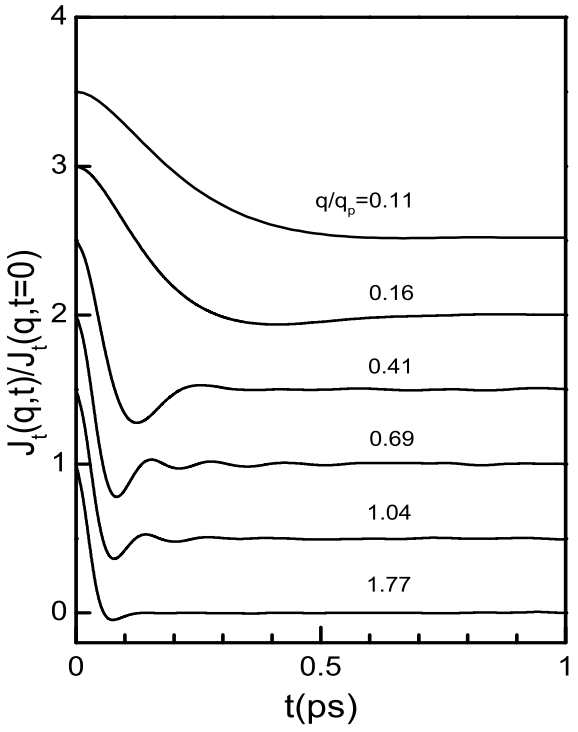

Figure 6.41: Transverse current correlation function, $J_t(q,t)$ for liquid Cr at $T = 2173$ K for several q/q_p values.

Figure 6.41 shows the normalized transverse current correlation functions $J_t(q,t)$ for several values of q for l-Cr at $T = 2173$ K. It is noticed that $J_t(q,t)$ decreases slowly for small values of q and this decrement becomes faster with increasing q. We therefrom obtained the shear viscosity $\eta = 2.96 \pm 0.16$ GPa ps, which agrees well with the value of 2.96 GPa ps obtained by Thakor *et al.* [68] following the prescription

of scaling law proposed by Dzugutov [69]. Another theoretical study by Khaleque *et al.* [226] yield a value of 2.11 GPa ps. To the best of our knowledge, there is no experimental result for shear viscosity of l-Cr. Figure 6.42 illustrates the time Fourier

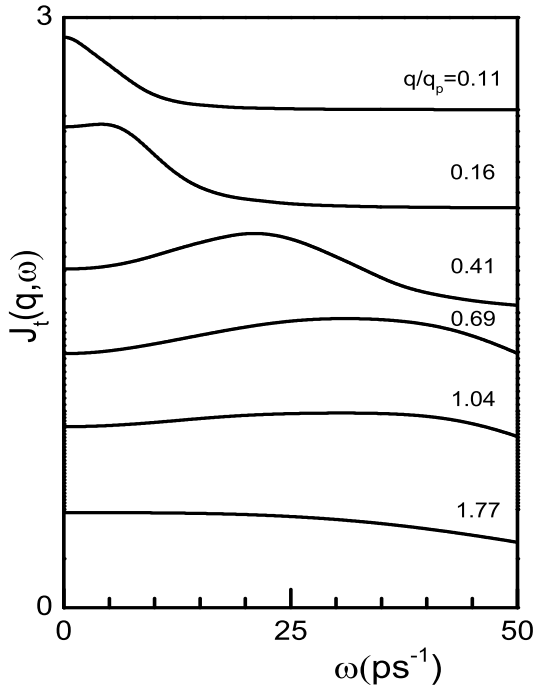

Figure 6.42: Transverse current correlation function spectra, $J_t(q,\omega)$ for liquid Cr at $T = 2173$ K at several q/q_p values.

transform, $J_t(q,\omega)$, of the transverse current correlation function. It is seen that no clear side peak exists for the smallest q value allowed by the size of the simulation box. For some intermediate q-range, we see an inelastic peak at non-zero frequency of $J_t(q,\omega)$ spectrum, representing the propagation of shear wave. This peak seems to be appeared from $q \approx 0.16q_p$ and persists up to $q \approx q_p$. The associated peak frequency increases with q, takes a maximum value at around $q \approx q_p$, after that it decreases

with increasing q.

6.3.2 Liquid Mn

The OF-AIMD results for the intermediate scattering function $F(q,t)$, for l-Mn at $T = 1533$ K are plotted in Figure 6.43 for several values of q. The salient features are

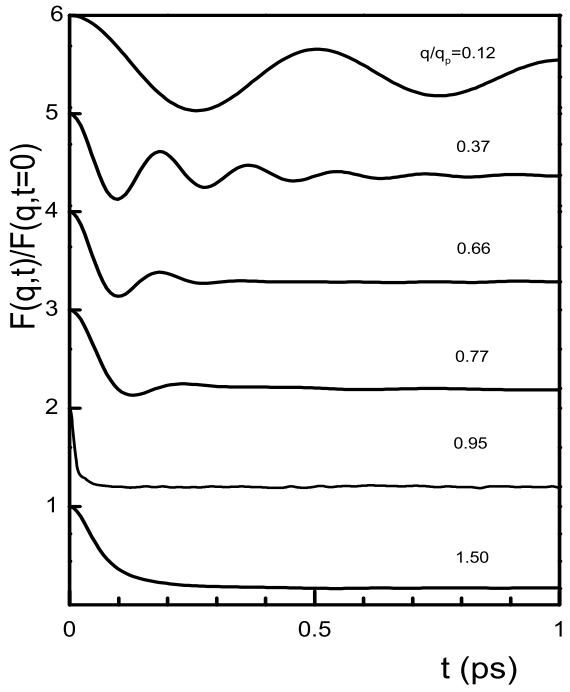

Figure 6.43: Normalized intermediate scattering functions, $F(q,t)$ at several q/q_p values, for l-Mn at $T = 1533$ K.

similar to those found for l-Cr with an oscillatory behaviour ended at $q/q_p \approx 0.77$. The corresponding dynamic structure factors, $S(q,\omega)$, are plotted in Figure 6.44. Side peaks are seen for a range of small q values, but the sharpness of the peak decreases with increasing q values as in the case of l-Cr. From the positions of the side peaks,

$\omega_m(q)$ we have plotted the dispersion relation $\omega_m(q)$ *vs.* q in Figure 6.45 for l-Mn.

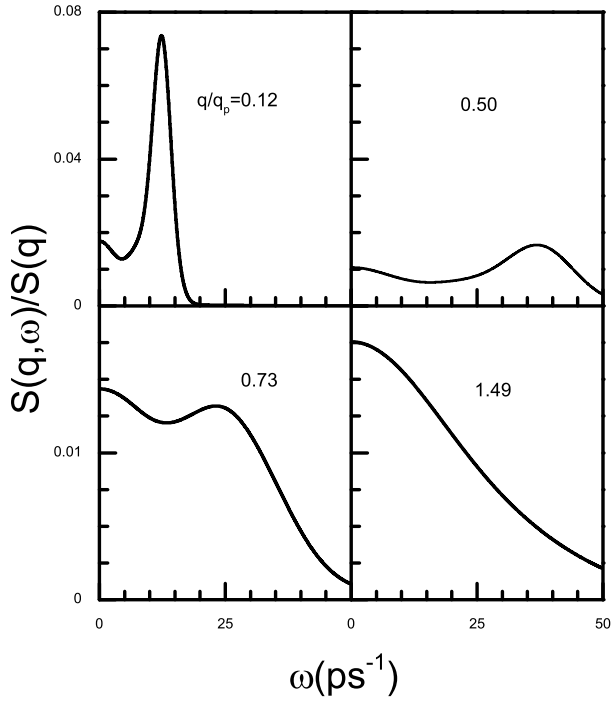

Figure 6.44: Dynamic structure factors $S(q,\omega)$ for l-Mn at $T = 1533$ K for several q/q_p values.

The slope of the dispersion curve in the hydrodynamic limit (q$\rightarrow$ 0) yields the adiabatic sound velocity c_s. The estimated value of c_s for l-Mn is found to be $c_s \approx 3790 \pm 90$ ms^{-1}, which agrees within 2% of the experimental result 3710 ms^{-1} [63] at $T = 1533$ K. A calculation using the hardsphere theory of liquid yields a value of 3524 ms^{-1} [65].

Figure 6.46 shows the OF-AIMD transverse current correlation functions, $J_t(q,t)$ for l-Mn at $T = 1533$ K, for several values of q. The behaviour of $J_t(q,t)$ for different q is similar to that of l-Cr. The shear viscosity evaluated from this profile is found to

be $\eta = 2.74 \pm 0.20\,\mathrm{GPa\,ps}$. We are not aware of any experimental data for η of l-Mn.

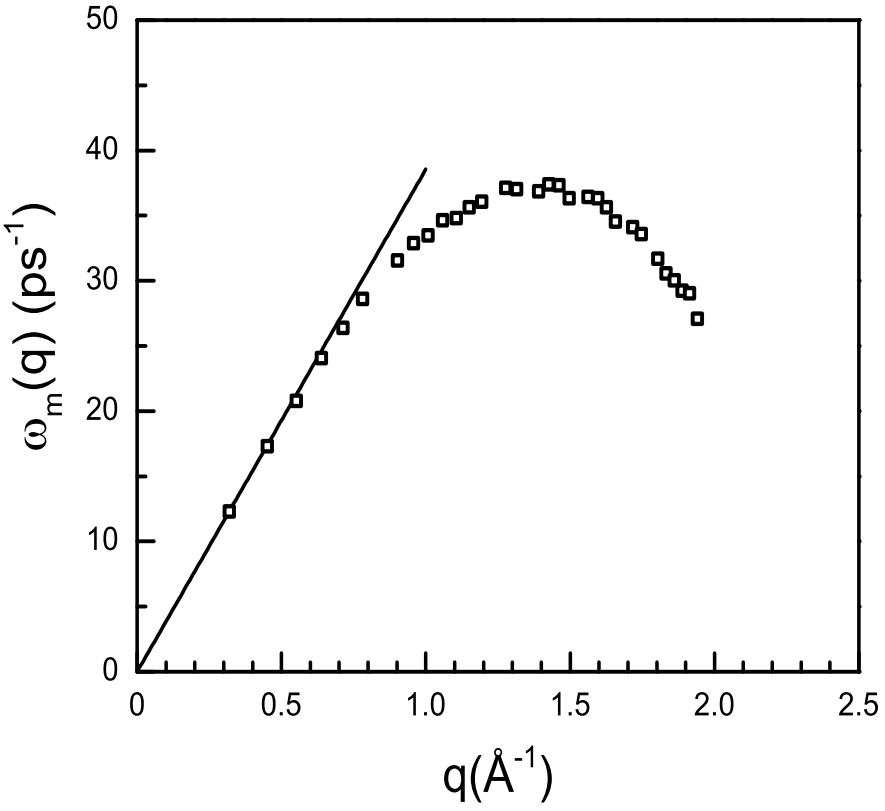

Figure 6.45: Dispersion relation for l-Mn at $T = 1533$ K. Open squares: peak positions $\omega_m(q)$ from the OF-AIMD $S(q,\omega)$. Full line: linear dispersion with the adiabatic sound velocity $c_s = 3790$ ms^{-1}.

So, it is worth to compare with other theoretical values. A study [68] using the scaling law of Dzugutov [69] along with the excess entropy calculated from hardsphere pair correlation function gives $\eta = 2.73\,\mathrm{GPa\,ps}$ at $T = 1533$ K, which is pretty close to our result. Another computed value for η is $1.63\,\mathrm{GPa\,ps}$ [226]. The time Fourier transform of $J_t(q,t)$ is shown in Figure 6.47 for several q values. Here, the salient features are similar to that of l-Cr.

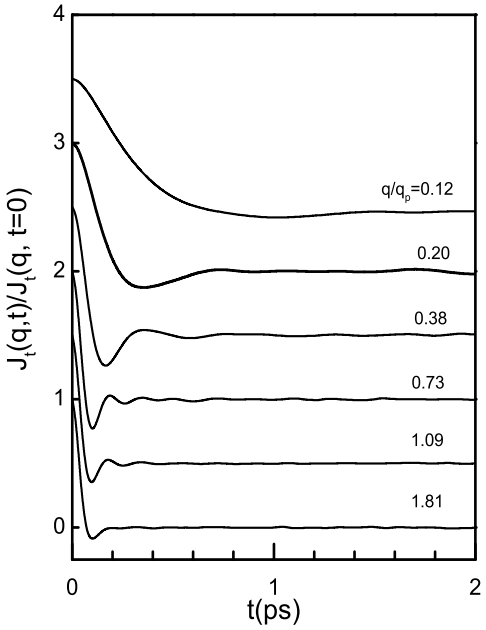

Figure 6.46: Transverse current correlation function, $J_t(q,t)$, for l-Mn at $T = 1533$ K for several q/q_p values.

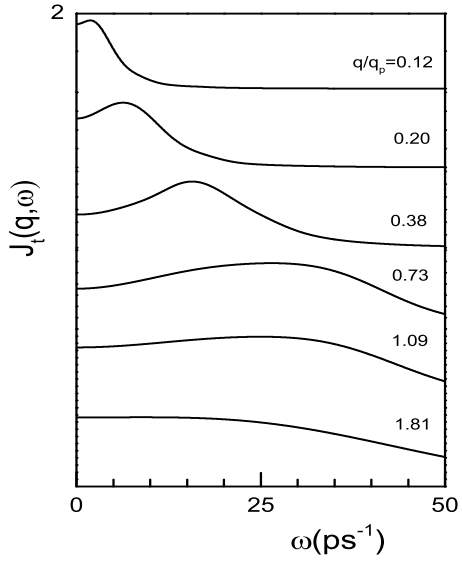

Figure 6.47: Transverse current correlation function spectra, $J_t(q,\omega)$ for l-Mn at $T = 1533$ K for several q/q_p values.

6.3.3 Liquid Fe

Figure 6.48 shows the OF-AIMD results for the intermediate scattering function, $F(q,t)$, of l-Fe for several values of q at $T = 1833$ K. The main characteristic features are similar to those of l-Cr and l-Mn with an oscillatory nature upto $q \approx 0.73q_p$. The dynamic structure factor $S(q,\omega)$ corresponding to $F(q,t)$ is plotted in Figure. 6.49. Similar to l-Cr and l-Mn, side peaks are noticed for an approximate range of small q values starting from $0.11q_p$ to $0.73q_p$. From the positions of the side peaks, $\omega_m(q)$, a dispersion curve is plotted in Figure 6.50 for the density fluctuations at $T = 1833$ K.

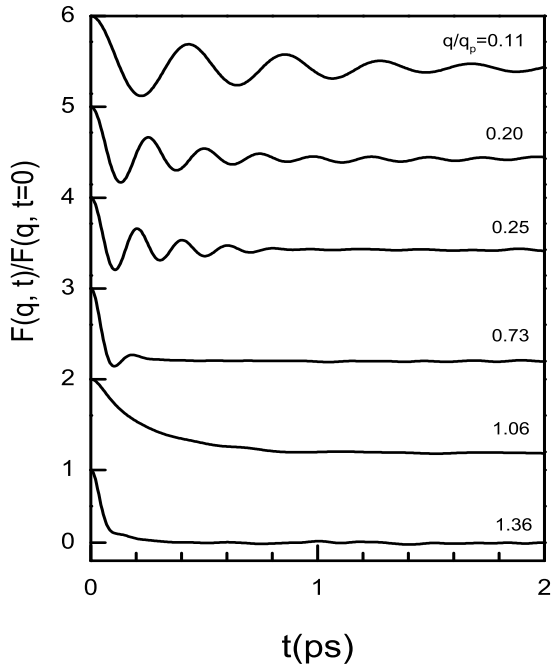

Figure 6.48: Normalized intermediate scattering functions, $F(q,t)$ for l-Fe at $T = 1833$ K for several q/q_p values.

The slope of the dispersion curve at $q \to 0$ provides an estimate of the adiabatic

sound velocity, c_s. For the present case of l-Fe, the value of c_s is approximately 4223±26 ms^{-1} at $T = 1833$ K. Similarly, we have obtained c_s at $T = 1923$ K, this value is 4162±12 ms^{-1}. Whereas the experimental value of c_s at $T = 1833$ K is 4370 ms^{-1} [62]. So, the agreement of the OF-AIMD result is within the 3.4% of the experimental one. A recent AIMD simulation study reports a value $c_s = 3950 \pm 150$ ms^{-1} [52] at $T = 1873$ K.

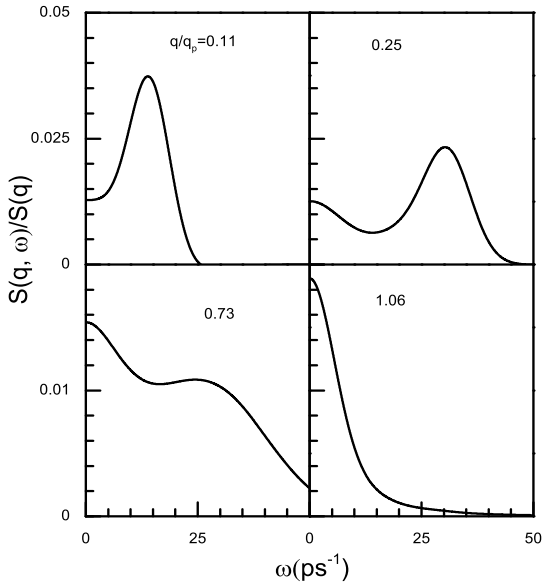

Figure 6.49: Dynamic structure factors $S(q, \omega)$ of l-Fe at $T = 1833$ K for several q/q_p values.

The normalized $J_t(q, t)$ for l-Fe at $T = 1833$ K is plotted in Figure 6.51 for some values of q. The shear viscosity calculated from the OF-AIMD $J_t(q, t)$ is found to be $\eta = 5.50 \pm 0.18\,\text{GPa ps}$ and $3.78 \pm 0.42\,\text{GPa ps}$ for temperatures $T = 1833$ and 1923 K, respectively. The corresponding experimental values measured by Egry [227]

are $\eta = 4.9\,\mathrm{GPa\,ps}$ and $4.3\,\mathrm{GPa\,ps}$, respectively. The experimental values reported by Sato *et al.* [228] are $\eta = 5.65\,\mathrm{GPa\,ps}$ and $4.88\,\mathrm{GPa\,ps}$, respectively. Morita and Iida [229] reported shear viscosities for l-Fe as 6.64 and 5.76 GPa ps at $T = 1833$ and 1923 K, respectively. The hardsphere model caculation by Yokoyama [70] gives a value $\eta = 4.11\mathrm{GPa\,ps}$ at $T = 1833$ K. Values calculated [72] from the scaling law and

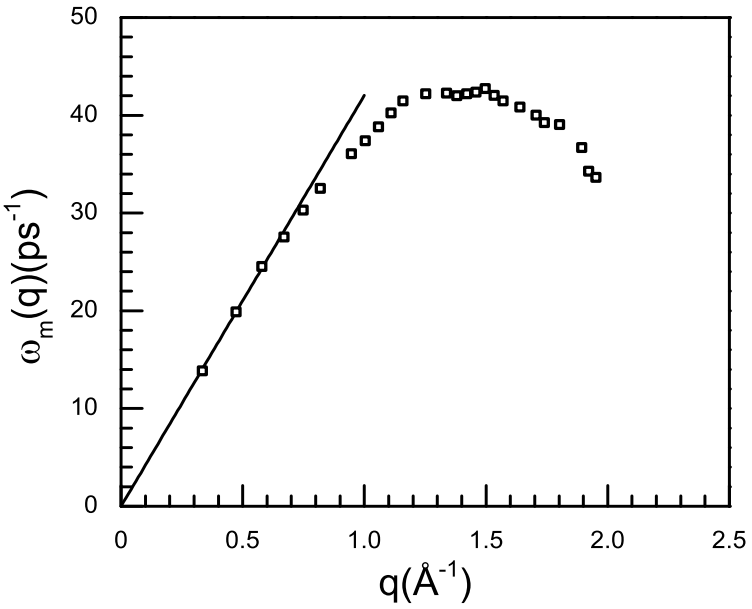

Figure 6.50: Dispersion relation for l-Fe at $T = 1833$ K. Open squares: peak positions $\omega_m(q)$ from the OF-AIMD $S(q,\omega)$. Full line: linear dispersion with the adiabatic sound velocity $c_s = 4223$ ms^{-1}.

defined by Li *et al.* [73,74] are 3.95 GPa ps and 3.37 GPa ps at $T = 1833$ and 1923 K, respectively. Marques *et al.* [52] in their AIMD study found a value $\eta = 5.0 \pm 0.3\,\mathrm{GPa\,ps}$ at $T = 1873$ K. The time Fourier transform of transverse current correlation function $J_t(q,\omega)$ is plotted in Figure 6.52. It is noticed that the main features of $J_t(q,t)$ and $J_t(q,\omega)$ for l-Fe are similar to those of l-Cr and l-Mn.

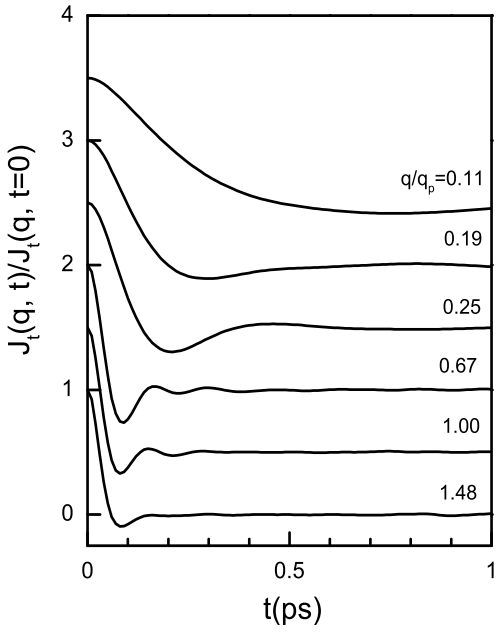

Figure 6.51: Transverse current correlation function, $J_t(q,t)$, for l-Fe at $T = 1833$ K for several q/q_p values.

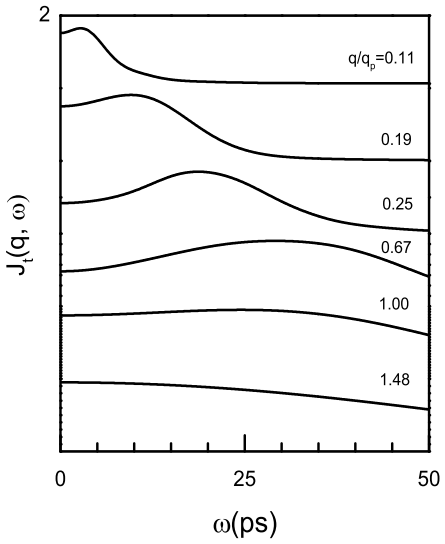

Figure 6.52: Transverse current correlation function spectra, $J_t(q,\omega)$, for l-Fe at $T = 1833$ K for several q/q_p values.

6.3.4 Liquid Co

Figure 6.53 shows the OF-AIMD $F(q,t)$ for l-Co for several q values at temperature

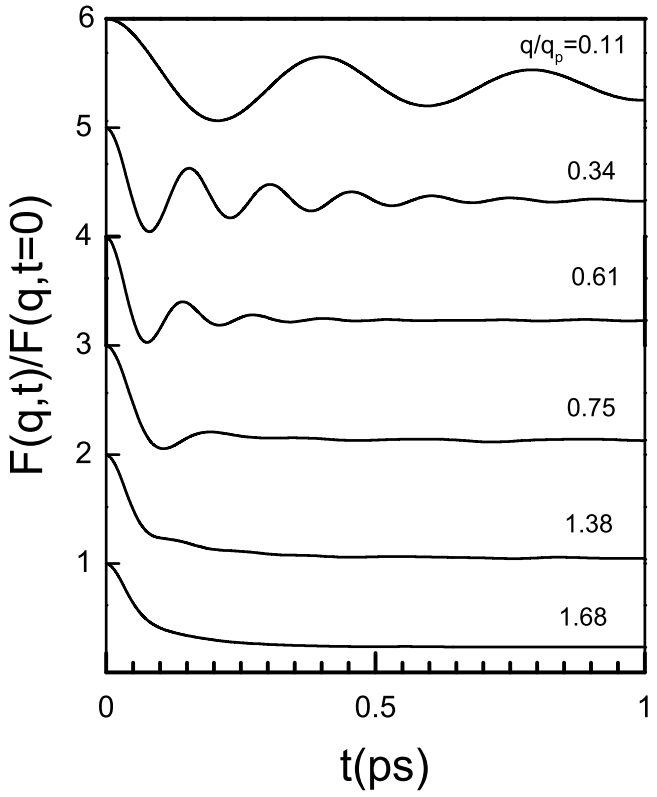

Figure 6.53: Normalized intermediate scattering functions, $F(q,t)$, for l-Co for several q/q_p values at $T = 1823$ K.

$T = 1823$ K. It is seen that the salient feature of the curves are similar as those of previous systems (l-Cr, l-Mn, l-Fe) with an oscillation up to $q \approx 0.75q_p$. The corresponding dynamic structure factors, $S(q,\omega)$ are presented in Figure 6.54. It is clear from the figure that the side peaks are seen for $q \leq 0.75q_p$. The higher q value corresponds to smaller length scale in real space, which can not produce the

collective excitation of density as discussed before. A plot of the positions of the side peaks, $\omega_m(q)$ for different q values gives the dispersion curve. This dispersion curve is presented in Figure 6.55.

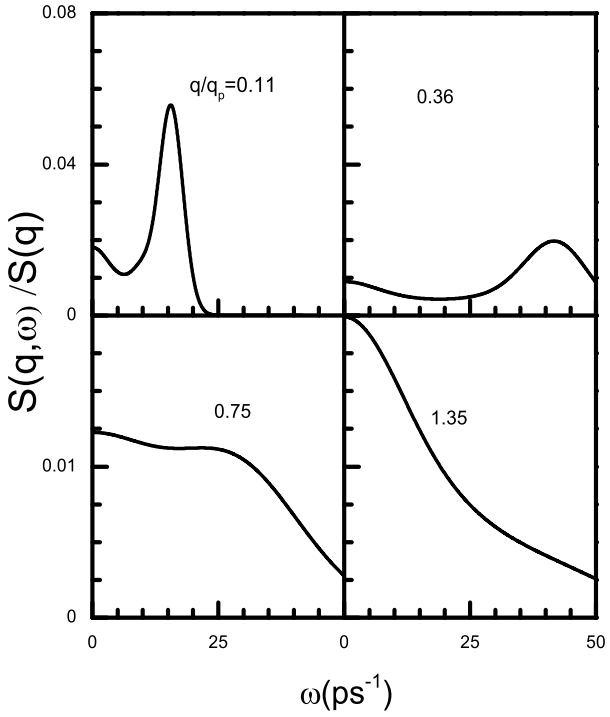

Figure 6.54: Dynamic structure factors $S(q,\omega)$ of l-Co at $T = 1823$ K for several q/q_p values.

The slope of the dispersion curve at $q \to 0$ gives the adiabatic sound velocity $c_s = 4547 \pm 14$ ms^{-1} and 4500 ± 17 ms^{-1} at temperatures $T = 1823$ and 1923 K, respectively. The corresponding experimental value is 4090 ms^{-1} [62] at $T = 1765$ K. S. Blairs's acumulated experimental data shows a value of 4031 ms^{-1} [67] at melting temperature $T = 1765$ K. The agreement of our calculation is within 13% of this experimental value [67] approving our result is fairly good.

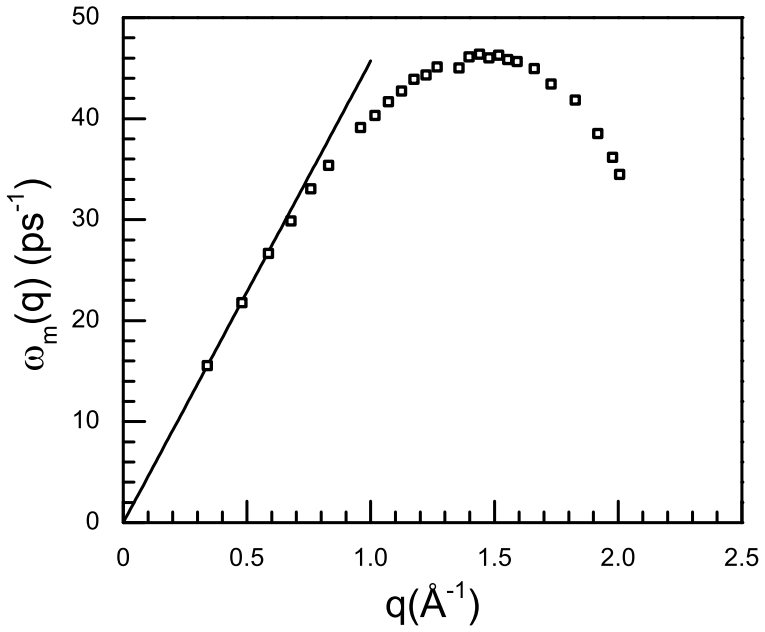

Figure 6.55: Dispersion relation for l-Co at $T = 1823$ K. Open squares: peak positions $\omega_m(q)$ from the OF-AIMD $S(q, \omega)$. Full line: linear dispersion with the adiabatic sound velocity $c_s = 4547$ ms^{-1}.

The normalized transverse current correlation functions, $J_t(q, t)$ for l-Co at $T = 1823$ K are shown in Figure 6.56, for some values of q. The nature of the $J_t(q, t)$ curves are similar to those of other systems under study. Figure shows a monotonic decrease of $J_t(q, t)$ at low q values and oscillating nature for relatively large q values. However, the shear viscosity calculated from the OF-AIMD $J_t(q, t)$ for l-Co are found to be $\eta = 4.15 \pm 0.26$ GPa ps and 3.91 ± 0.11 GPa ps for $T = 1823$ and 1923 K, respectively. The corresponding experimental values measured by Egry [227] are 3.9 GPa ps and 3.4 GPa ps at temperature $T = 1823$ and 1923 K, respectively. Kaptay reported in ref. [230] that the experimental value of viscosity for l-Co lies in the range of $4.1 - 5.3$ GPa ps at melting ($T = 1765$ K) which encompasses our result. The corresponding

spectrum of $J_t(q,\omega)$ is shown in Figure 6.57.

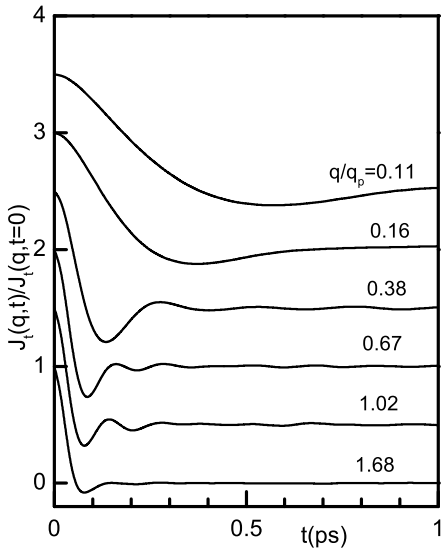

Figure 6.56: Transverse current correlation function, $J_t(q,t)$, for liquid Co at $T = 1823$ K for several q/q_p values.

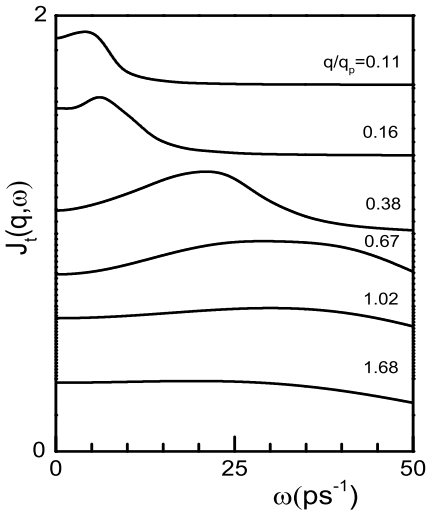

Figure 6.57: Transverse current correlation function spectra, $J_t(q,\omega)$, for liquid Co at $T = 1823$ K for several q/q_p values.

6.3.5 Liquid Ni

The calculated $F(q,t)/F(q,t=0)$ for l-Ni at $T = 1773$ K is illustrated in Figure 6.58 at several q/q_p values. The $F(q,t)$ shows an oscillatory behaviour for low q/q_p values

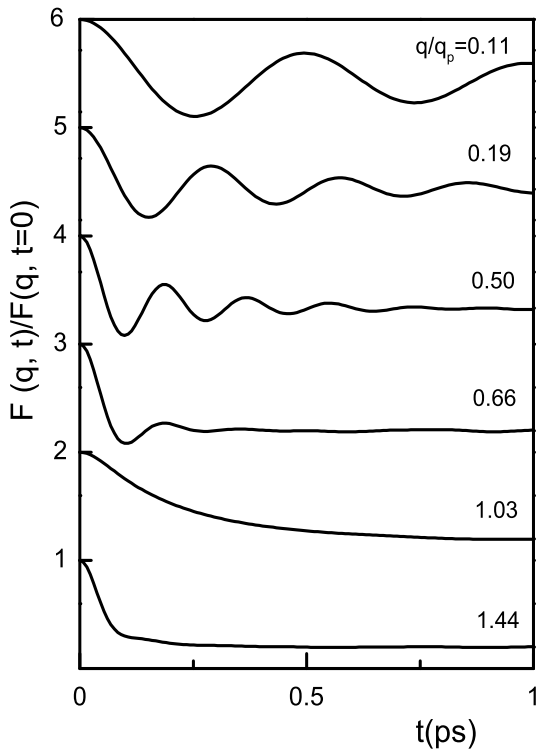

Figure 6.58: Normalized intermediate scattering functions, $F(q,t)$, at several q/q_p values, for l-Ni at $T = 1773$ K.

which is gradually decreased with increasing q/q_p values until it is disappeared for $q/q_p > 0.66$. We stress that this trend is similar to those have already been observed in other liquid metals near melting, by either computer simulation [15,16,19–21,231,232] or theoretical models [123]. The associated $S(q,\omega)$ has been computed by direct numerical time FT with an appropriate window to smooth out the truncation effect.

The obtained $S(q,\omega)$ are demonstrated in Figure 6.59. We obtain clear side peaks, which point to the existence of collective density excitations, up to $q/q_p \approx 0.66$; after that the side peaks become shoulders and for $q/q_p \geq 0.66$, $S(q,\omega)$ shows a monotonic decreasing behaviour. From the positions of the side peaks, $\omega_m(q)$, a dispersion curve for the density fluctuations can be obtained. This curve is shown in Figure 6.60.

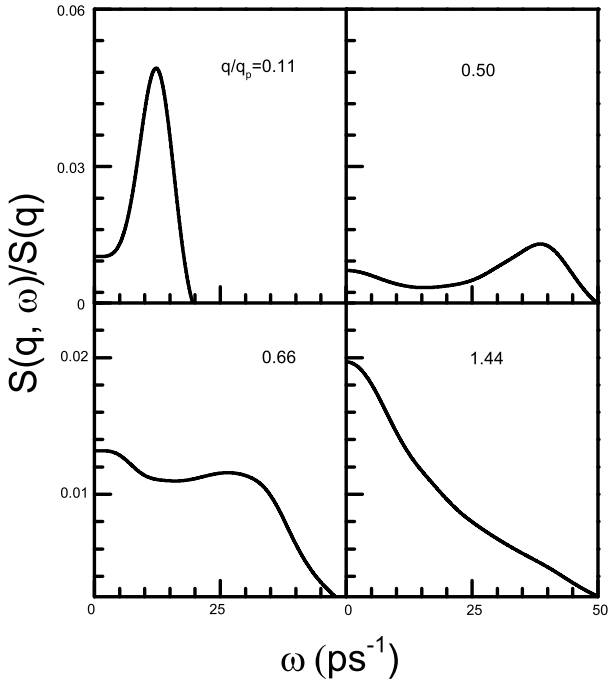

Figure 6.59: Dynamic structure factors $S(q,\omega)$ of l-Ni at $T = 1773$ K for several q/q_p values.

The slope of this dispersion curve at $q \to 0$ provides an estimate of the adiabatic sound velocity, c_s. Thus, we have obtained $c_s \approx 3649 \pm 10$ ms^{-1}, other authors calculated a value of 4122 ms^{-1} [65]. We also note that the INS study of Bermejo *et al.* [64] measured a value of $c_s = 4280$ ms^{-1} at $T = 1763$ K and the experimental

value is 4045 ms^{-1} [62] at melting. An *ab initio* simulation study using Vienna *ab initio* simulation package (VASP) by Jakse *et al.* [66] report a value c_s =4350 ms^{-1} at temperature $T = 1850$ K. So our result for l-Ni agrees within 10% of the experimental data [62].

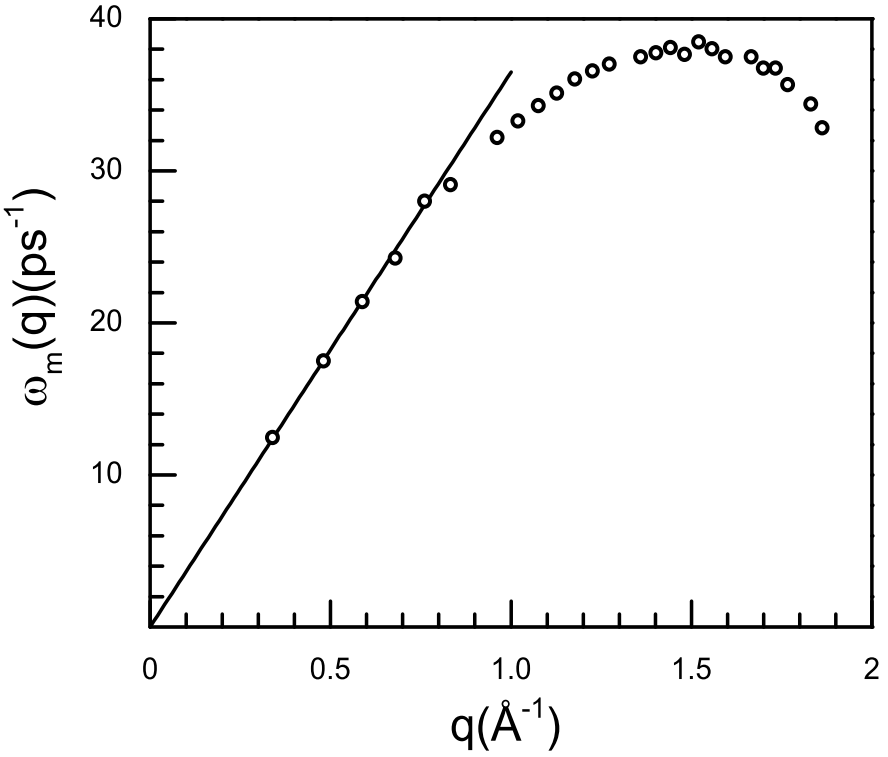

Figure 6.60: Dispersion curve for l-Ni for $T = 1773$ K. Open circles: peak positions $\omega_m(q)$ from the OF-AIMD $S(q, \omega)$. Full line: linear dispersion with the adiabatic sound velocity $c_s = 3649$ ms^{-1}.

We have calculated the normalized transverse current correlation function $J_t(q, t)$ for l-Ni presented in Figure 6.61 and therefrom we have evaluated the shear viscosity for l-Ni at $T = 1773$ K. We have obtained, $\eta = 2.64 \pm 0.28$ GPa ps, which is clearly

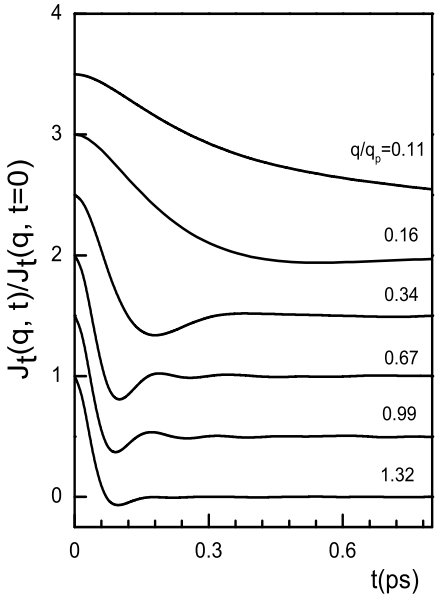

Figure 6.61: Transverse current correlation function, $J_t(q,t)$, for liquid Ni at $T = 1773$ K for several q/q_p values.

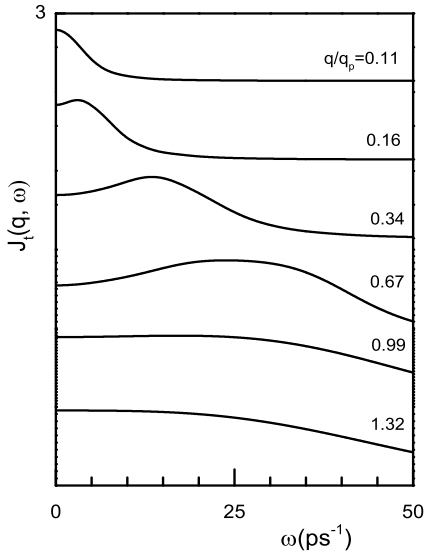

Figure 6.62: Transverse current correlation function spectra, $J_t(q,\omega)$, for liquid Ni at $T = 1773$ K at several q/q_p values.

smaller than experimental value of 4.8 GPa ps [227] at $T = 1773$ K. The agreement with experiment is within a factor of 2. But our obtained value is very close to the calculated value $\eta = 2.50$ GPa ps at $T = 1773$ K of Kart *et al.* [59]. Also Alemany *et al.* [54] reported a result of η=5.76 ± 0.80GPa ps at $T = 1775$ K. An *ab initio* study by Jakse *et al.* [66] reports a value $\eta = 3.9 \pm 0.20$GPa ps. It is noticed that for small q's, the corresponding $J_t(q,t)$ decreases slowly with time for small t but it becomes faster with increasing q values. The corresponding spectrum of $J_t(q,\omega)$ is shown in Figure 6.62 and no clear side peak for the smallest q value reached by the simulation. The peak frequency increases with q, takes a maximum value at $q \approx q_p$, and then decreases with increasing q as $J_t(q,\omega)$ evolves towards a Gaussian shape.

6.3.6 Liquid Pd

Figure 6.63 shows the result of OF-AIMD $F(q,t)/F(q,t=0)$ for some q/q_p values of l-Pd at $T = 1853$ K. The main characteristics features are similar to those found for previously described systems. In the case of l-Pd, the oscillatory behavior lasting up to $q \approx 0.73q_p$. The corresponding $S(q,\omega)$ are plotted in the Figure 6.64, where we observe clear side-peaks for a small range of q/q_p values. Particularly, it is seen up to $q \approx 0.73q_p$ in the present case. From the positions of the side peaks, $\omega_m(q)$, we have obtained a dispersion curve for the density fluctuations which is given in Figure 6.65.

The slope of this dispersion curve in the limit $q \to 0$ yields an estimate of the adiabatic sound velocity, c_s. From our calculation, we have obtained $c_s \approx 2906 \pm 25\,\mathrm{ms}^{-1}$. Whereas a calculation by Blairs [67] gives value $2657\,\mathrm{ms}^{-1}$ at melting. No experimental data for l-Pd is found in available literature. The AIMD study of

González *et al.* [212] have reported a value $c_s = 3450 \pm 150$ ms^{-1} which is almost 15% larger than that of our OF-AIMD result.

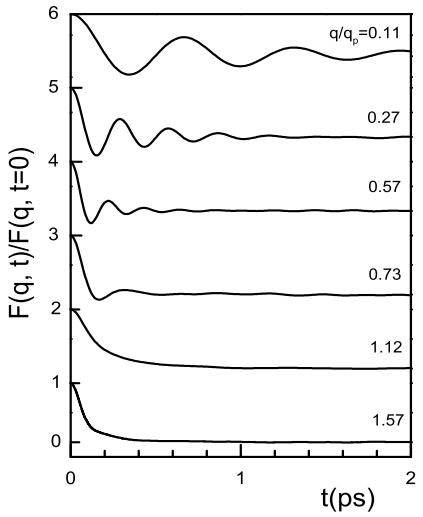

Figure 6.63: Normalized intermediate scattering functions, $F(q,t)$, at several q/q_p values, for l-Pd at $T = 1853$ K.

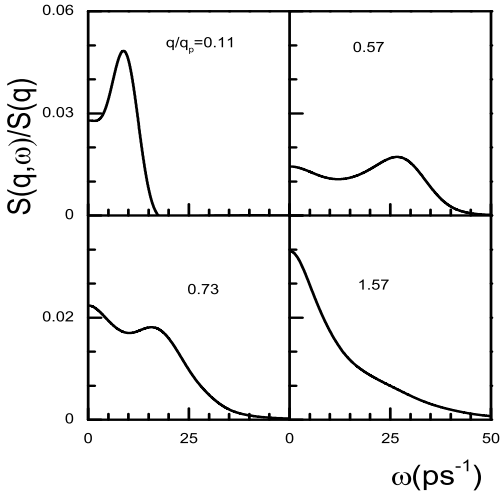

Figure 6.64: Dynamic structure factors $S(q,\omega)$ of l-Pd at $T = 1853$ K for several q/q_p values.

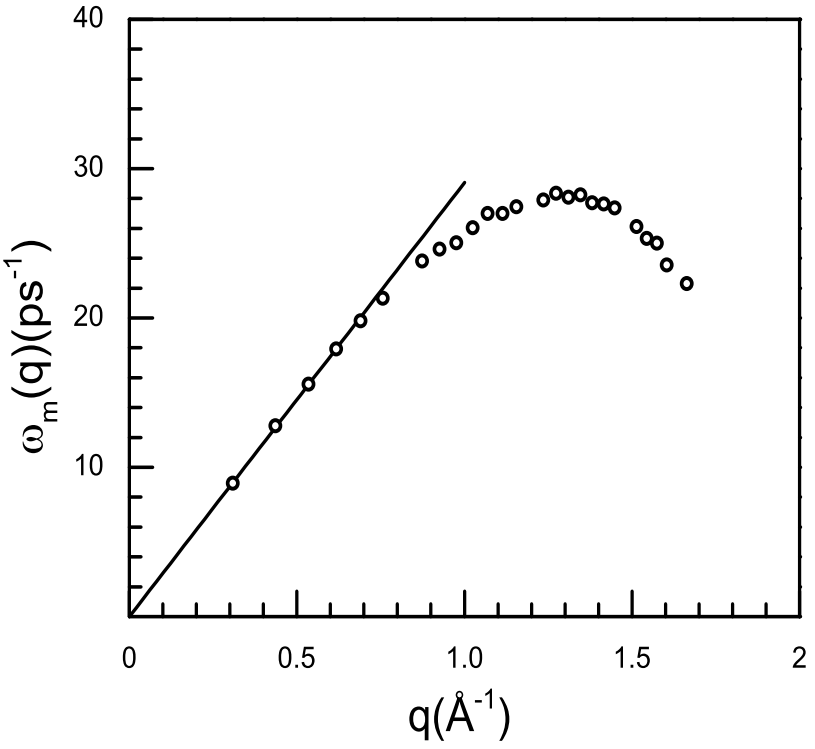

Figure 6.65: Dispersion curve for l-Pd at $T = 1853$ K. Open circles: peak positions $\omega_m(q)$ from the OF-AIMD $S(q,\omega)$. Full line: linear dispersion with the adiabatic sound velocity, $c_s = 2906$ ms^{-1}.

The calculated normalized transverse current correlation functions, $J_t(q,t)$ of l-Pd at $T = 1853$ K are illustrated in Figure 6.66 for several q/q_p values and therefrom we have calculated the shear viscosity for l-Pd at $T = 1853$ K. Our OF-AIMD calculation yields $\eta = 4.07 \pm 0.50$ GPa ps, which is very close to the CMD simulated value of 4.01 ± 0.48 GPa ps by Alemany *et al.* [57] at $T = 1853$ K. The other computed values using the TBM-SMA and classical molecular dynamics simulation methods are 3.68 ± 0.48 GPa ps [54] and 2.91 ± 0.86 GPa ps [59], respectively. These values are relatively smaller than that of our OF-AIMD result. The experimental value for

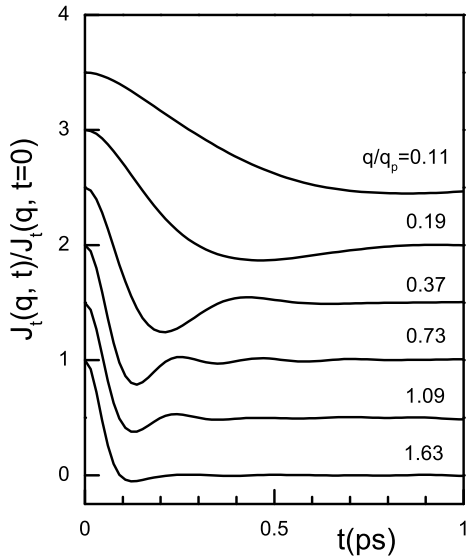

Figure 6.66: Transverse current correlation function, $J_t(q,t)$, for liquid Pd at $T = 1853$ K at several q/q_p values.

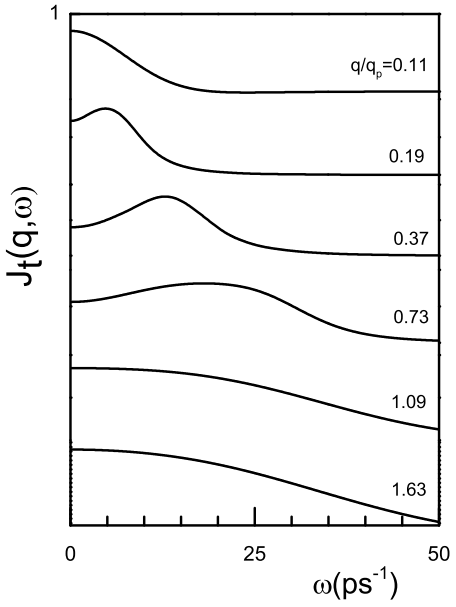

Figure 6.67: Transverse current correlation function spectra, $J_t(q,\omega)$, for liquid Pd at $T = 1853$ K for several q/q_p values.

l-Pd is $\eta_{exp} = 4.22 \pm 0.15$ GPa ps [233], which is very close to our OF-AIMD result. Our OF-AIMD result also agrees well with the KS-AIMD result, $\eta_{KS-AIMD} = 4.57 \pm 0.15$ GPa ps [212]. The corresponding spectrum of $J_t(q, \omega)$ are shown in Figure 6.67. We note that the main features for $J_t(q, t)$ and $J_t(q, \omega)$ are similar to all those systems studied previously.

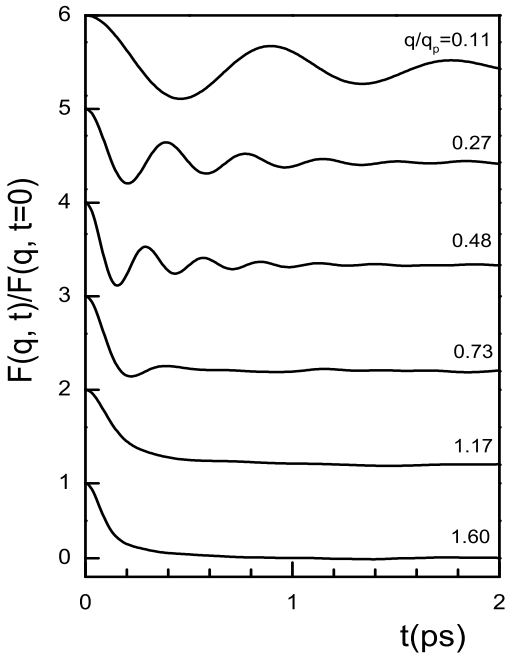

Figure 6.68: Normalized intermediate scattering functions, $F(q, t)$, at several q/q_p values, for l-Pt at $T = 2053$ K.

6.3.7 Liquid Pt

The calculated $F(q, t)/F(q, t = 0)$ are depicted in Figure 6.68 for l-Pt at $T = 2053$ K. The expected behaviour of $F(q, t)/F(q, t = 0)$ for different q values are seen as we have observed for other systems of our concern studied previously. The oscillations

are showing up to $q \approx 0.73q_p$. The corresponding dynamic structure factors are demonstrated in Figure 6.69. From this figure it is observed that the calculated OF-AIMD $S(q,\omega)$ show clear side peaks up to $q \approx 0.73q_p$. One can obtain the dispersion

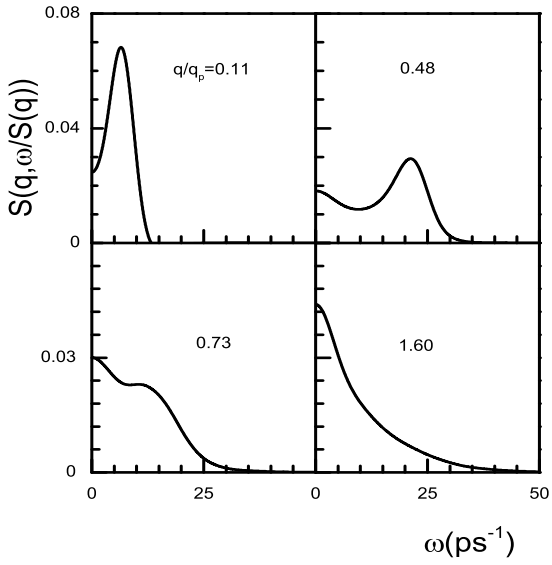

Figure 6.69: Dynamic structure factors $S(q,\omega)$ of l-Pt at $T = 2053$ K for several q/q_p values.

curve from the positions of the side peaks of $S(q,\omega)$. The dispersion curve is shown in Figure 6.70.

The slope of the dispersion curve at $q \to 0$ limit, gives the adiabatic sound velocity $c_s = 2184 \pm 24$ ms^{-1} for l-Pt at $T = 2053$ K, whereas the experimental adiabatic sound velocity is $c_s = 3053$ ms^{-1} [234] at the melting temperature. We may note here that the KS-AIMD study produces higher value for the velocity of sound, $c_s = 3000 \pm 150$ ms^{-1} [212] for l-Pt as compared to our result. On the other hand the Gitis-Mikhailov model and modified Einstein-Lindemann model give $c_s = 2193$ ms^{-1} and $c_s = 2713$

ms^{-1} [234], respectively, at the melting point.

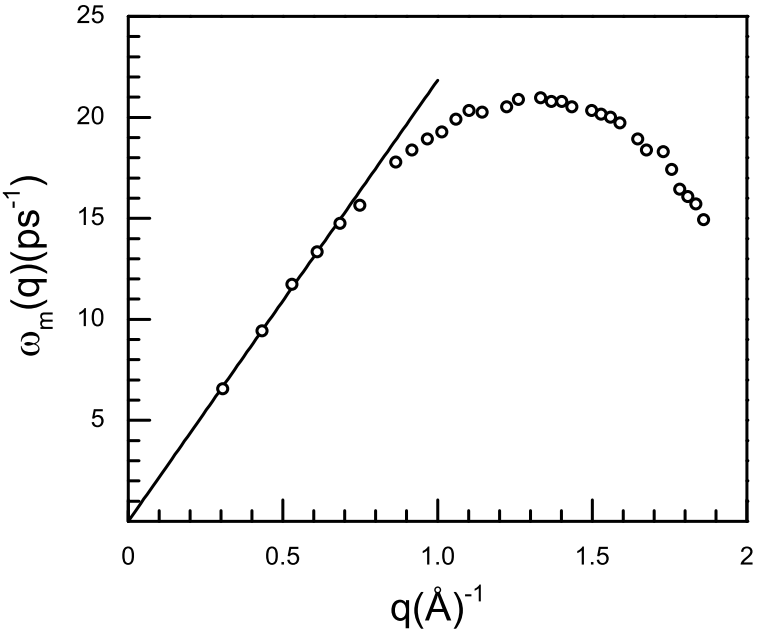

Figure 6.70: Dispersion curve for l-Pt at $T = 2053$ K. Open circles: peak positions $\omega_m(q)$ from the OF-AIMD $S(q, \omega)$. Full line: linear dispersion with the adiabatic sound velocity $c_s = 2184$ ms^{-1}.

The normalized transverse current correlation function $J_t(q, t)$ for l-Pt at $T = 2053$ K is illustrated in Figure 6.71 for several q/q_p values. The calculation of the shear viscosity for l-Pt at $T = 2053$ K yields $\eta = 4.6 \pm 0.49$ GPa ps, whereas the calculations of the EAM and TBM-SMA methods gave $\eta = 5.92 \pm 0.48$ GPa ps [57] and $\eta = 6.09 \pm 0.96$ GPa ps [54], respectively. For l-Pt, the experimental values are $\eta_{exp} = 4.82$ and 6.74 GPa ps [233]. The first one is very close to our calculated value but the latter is more closer to the results obtained from CMD simulation [54]. On the other hand, the KS-AIMD study of González *et al.* gave $\eta_{KS-AIMD} = 4.90 \pm 0.25$ GPa ps [212],

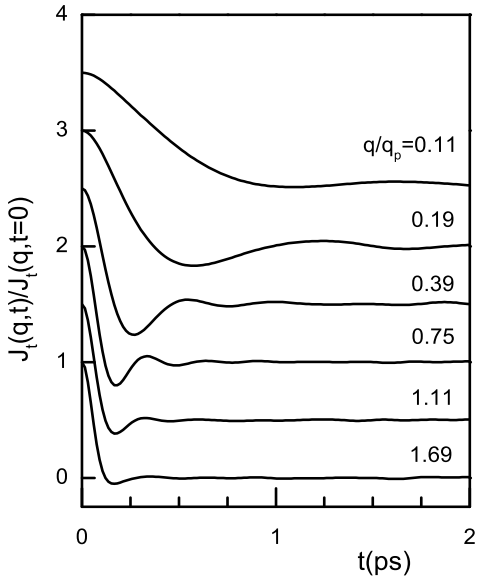

Figure 6.71: Transverse current correlation function, $J_t(q,t)$, for liquid Pt at $T = 2053$ K for several q/q_p values.

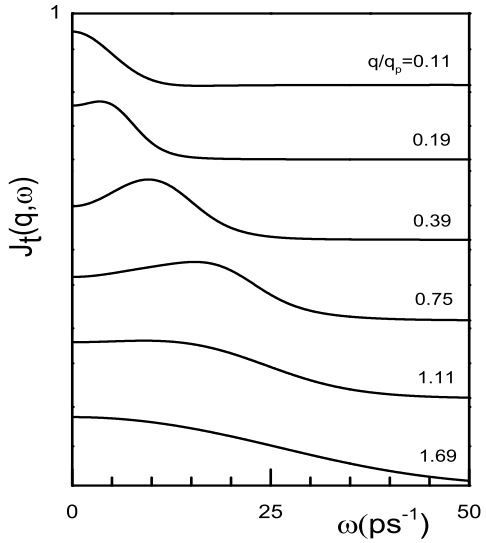

Figure 6.72: Transverse current correlation function spectra, $J_t(q,\omega)$, for liquid Pt at $T = 2053$ K at several q/q_p values.

which is again close to our calculated OF-AIMD result. The corresponding spectrums of $J_t(q,\omega)$ are plotted in Figure 6.72.

6.3.8 Liquid Zn

The calculated $F(q,t)$ for l-Zn at $T = 723$ K is depicted in Figure 6.73 for several

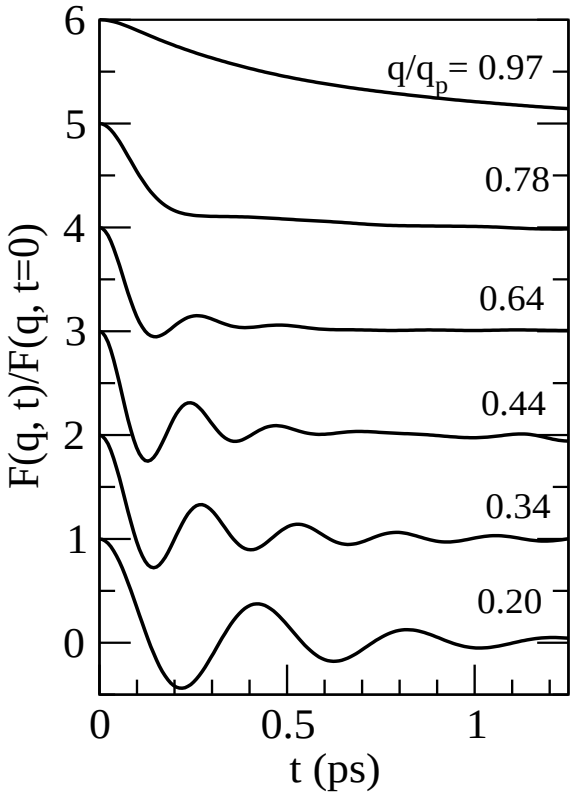

Figure 6.73: Normalized intermediate scattering functions, $F(q,t)$, at several q/q_p values, for l-Zn at $T = 723$ K. Full lines: present OF-AIMD results.

q/q_p values. The $F(q,t)$ shows an oscillatory behaviour up to $q/q_p \approx 0.70$, with the amplitude of the oscillations fading away with increasing q/q_p values. We stress that this trend is similar to what has already been observed in other liquid metals near melting, by either computer simulation [15, 16, 19–21, 231, 232] or theoretical

models [123]. The associated $S(q,\omega)$ has been computed by direct numerical time FT (with an appropriate window to smooth out the truncation effect) and some results are depicted in Figure 6.74. We obtain clear side peaks, which point to the existence of collective density excitations, up to $q/q_p \approx 0.6$; then the side peaks become shoulders and for $q/q_p \geq 0.6$ the $S(q,\omega)$ shows a monotonic decreasing behaviour. From the positions of the side peaks, $\omega_m(q)$, a dispersion relation for the density fluctuations can be obtained and its slope at $q \to 0$ provides an estimate of the adiabatic sound velocity, c_s. Thus, we have estimated $c_s \approx 2740 \pm 100$ ms^{-1} which agrees within 4% of the experimental value of 2850 ms^{-1} [62,67] for l-Zn at melting. A similar calculation for the state at $T = 833$ K gave an estimate $c_s \approx 2650 \pm 100$ ms^{-1} whereas its experimental value is ≈ 2800 ms^{-1} [62,67].

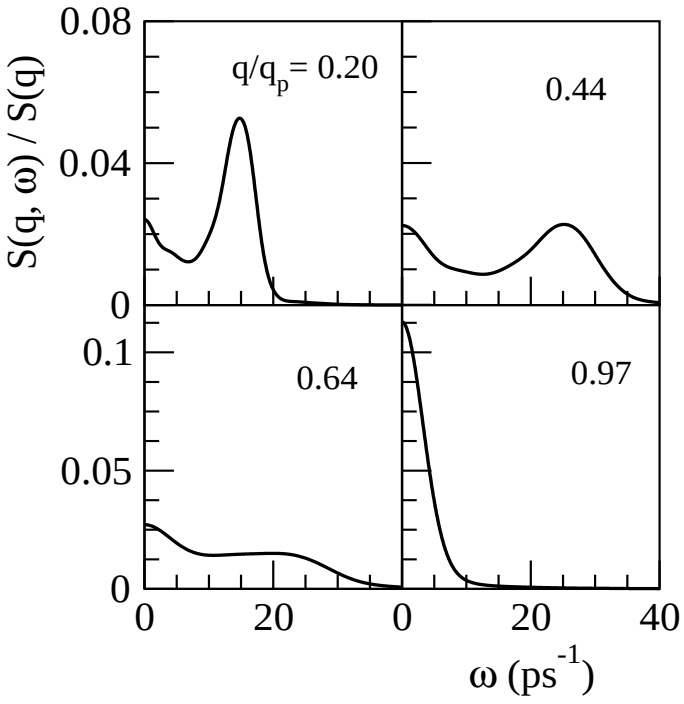

Figure 6.74: Dynamic structure factors $S(q,\omega)$ of l-Zn at $T = 723$ K for several q-values. Full lines: present OF-AIMD results.

We have calculated the normalized transverse current correlation function $J_t(q,t)$ for l-Zn at $T = 723$ K and 833 K, and therefrom we have evaluated the shear viscosity for l-Zn at $T = 723$ K and 833 K; we have obtained $\eta = 2.10 \pm 0.20$ and 1.49 ± 0.20 GPa ps, which are clearly smaller than the respective extrapolated experimental values of $\approx 3.50 \pm 0.10$, and $\approx 2.70 \pm 0.10$ GPa ps [220–222].

6.3.9 Liquid Cd

Figure 6.75 shows, for some q/q_p values, the present OF-AIMD results for the $F(q,t)$ of l-Cd at $T = 623$ K. The main characteristics are similar to those found for liquid systems (Cr, Mn, Co, Fe, Ni, Pd, Pt, Zn) with an oscillatory behaviour lasting up to $q/q_p \approx 0.70$. For comparison, we have also plotted the corresponding KS-AIMD results, $F_{KS-AIMD}(q,t)$, obtained by Calderin *et al.* [90], and several important differences are noticeable: (i) the oscillations of the $F_{KS-AIMD}(q,t)$ have a shorter period and smaller amplitude, (ii) the oscillatory behavior of the $F_{KS-AIMD}(q,t)$ is less marked and for $q/q_p \geq 0.5$, the oscillations have practically disappeared, (iii) the $F_{KS-AIMD}(q,t)$ shows a weak diffusive behaviour which is not delivered by the present calculations, (iv) for $q/q_p \geq 1$, the calculated $F(q,t)$ practically coincide with the corresponding $F_{KS-AIMD}(q,t)$. These differences are also reflected in the corresponding dynamic structure factors, $S(q,\omega)$ which are depicted, for some q/q_p values, in Figure 6.76. Our calculated $S(q,\omega)$ show clear side peaks up to $q/q_p \approx 0.6$ and similar features are also observed in the corresponding $S_{KS-AIMD}(q,\omega)$ although their side peaks disappear at smaller q/q_p values. More interestingly, for any q/q_p value the positions of the side peaks in our calculated $S(q,\omega)$ are always located at smaller

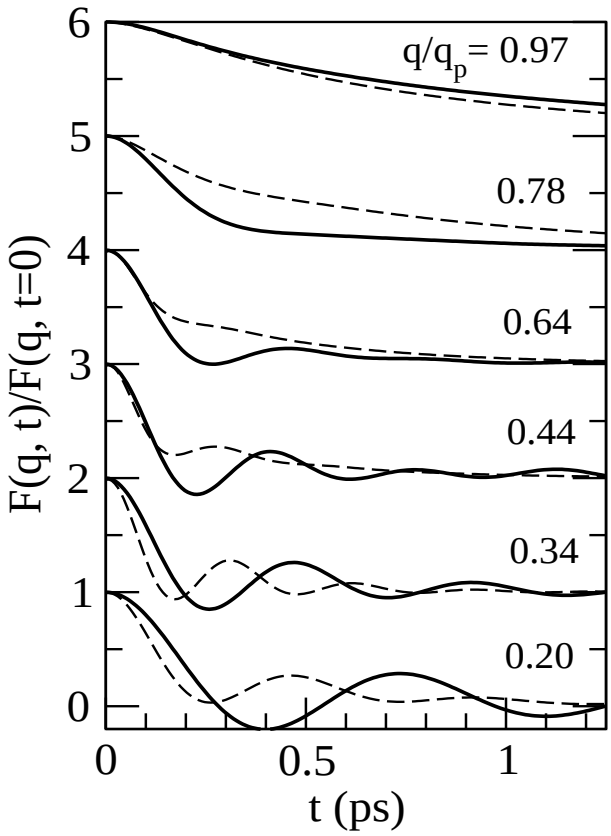

Figure 6.75: Normalized intermediate scattering functions, $F(q,t)$, at several q/q_p values, for l-Cd at $T = 623$ K. Full lines: present OF-AIMD results. Dotted lines: KS-AIMD results of Calderin *et al.* [90].

ω values. Again, from the positions of the side peaks we have calculated the dispersion relation of the density fluctuations and, in the $q \to 0$ limit, we have obtained a value $c_s = 1950 \pm 100$ ms^{-1} for the adiabatic sound velocity of l-Cd at $T = 623$ K. For comparison, we note that the corresponding experimental value for l-Cd at melting is $c_s = 2256$ ms^{-1} [62, 67] and that the KS-AIMD calculation [90] gave a value $c_s = 2350 \pm 150$ ms^{-1} which is much closer to experiment. This result, which is related to the positions of the side peaks in the corresponding $S(q,\omega)$, suggests that $S_{KS-AIMD}(q,\omega)$ are more reliable than those obtained by the present OF-AIMD

method for l-Cd. Furthermore, given that the $S(q,\omega)$ are derived from the corresponding $F(q,t)$, a similar assertion can be made concerning the $F_{KS-AIMD}(q,t)$.

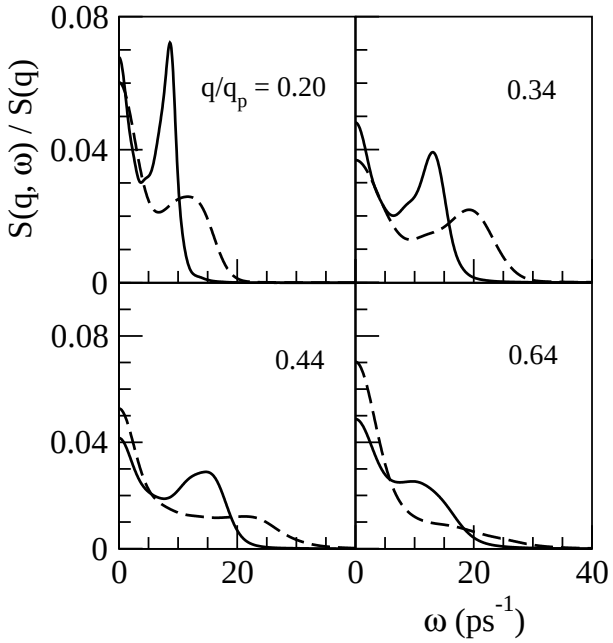

Figure 6.76: Dynamic structure factors $S(q,\omega)$ of l-Cd at $T = 623$ K for several q/q_p values. Full lines: present OF-AIMD results. Dotted lines: KS-AIMD results of Calderin *et al.* [90].

The calculated normalized transverse current correlation functions, $J_t(q,t)$, for l-Cd at $T = 623$ K are depicted in Figure 6.77 for several q/q_p values and we have also included the corresponding KS-AIMD results of Calderin *et al.* [90]. Notice that our calculated $J_t(q,t)$ shows a slower decay and its oscillations have a greater amplitude and longer period than those of the KS-AIMD calculations. The associated spectrum, $J_t(q,\omega)$, is also plotted in Figure 6.77 where we observe, for some q/q_p range, the appearance of an inelastic peak. This peak, which is related to the existence of shear waves in the liquid, appears for $q/q_p \approx 0.1$ and lasts up to $q/q_p \approx 1.5$. The frequency of

the peak, $\omega_t(q)$, increases with q, has a maximum at around $q/q_p \approx 0.8$ and therefrom it decreases with increasing q/q_p values. Comparison with the KS-AIMD results of Calderin *et al.* [90] reveals that the corresponding $\omega_t(q)$ has an analogous shape, with a maximum located at similar q/q_p value. The shear viscosity has been evaluated and we have obtained a value $\eta = 2.00 \pm 0.20$ GPa ps for l-Cd at $T = 623$ K, whereas the corresponding experimental data [220–222] is 2.50 ± 0.05 GPa ps. Again, we notice that the KS-AIMD calculation [90] gave a more accurate result, *i.e.* $\eta_{\mathrm{KS-AIMD}}$=2.30 $\pm$ 0.15 GPa ps.

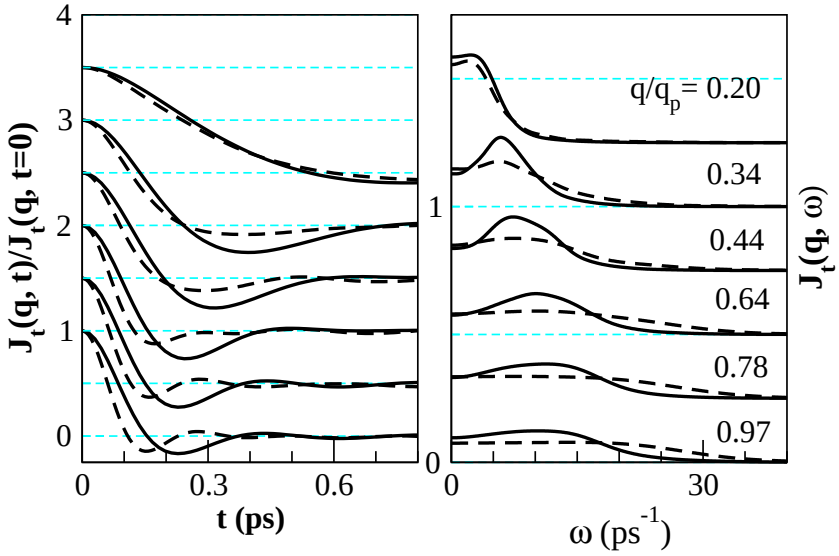

Figure 6.77: Transverse current correlation function, $J_t(q,t)$, and its spectra, $J_t(q,\omega)$, for liquid Cd at $T = 623$ K and $q/q_p = 0.20$, 0.34, 0.44, 0.64, 0.78 and 0.97. Full curves: Present calculations. Dashed curves: KS-AIMD results of Calderin *et al.* [90].

6.3.10 Liquid Hg

The calculated $F(q,t)$ are depicted in Figure 6.78 for l-Hg at $T = 293$ K. Its behavior is very similar to what has been obtained for other liquid systems (Cr, Mn, Co, Fe,

Ni, Pd, Pt, Zn, Cd), with the oscillations showing up to $q/q_p \approx 0.70$. Figure 6.78 also provides a comparison with the KS-AIMD results of Calderin *et al.* [91–93]. It is observed that the main differences with the present OF-AIMD results are basically

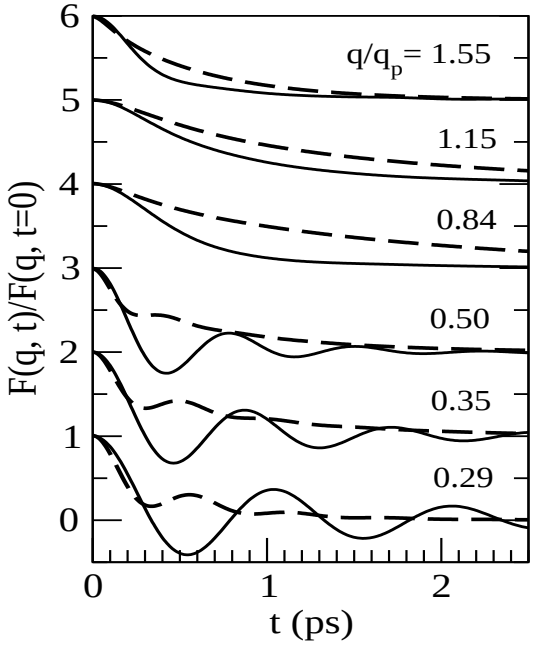

Figure 6.78: Normalized intermediate scattering functions, $F(q,t)$, at several q/q_p values, for l-Hg at $T = 293$ K. Full lines: present OF-AIMD results. Dotted lines: KS-AIMD results of Calderin *et al.* [91–93].

the same as those we have already mentioned for l-Cd. These differences are also transferred to the corresponding dynamic structure factors which are depicted in Figure 6.79 where it is observed that the OF-AIMD calculated $S(q,\omega)$ shows clear side peaks up to $q/q_p \approx 0.6$. Comparison with the corresponding $S_{KS-AIMD}(q,\omega)$ shows similar qualitative features although their side peaks are always located at smaller ω values and they disappear at smaller q/q_p values. From the positions of the side peaks and by taking the $q \to 0$ limit, we have obtained a value $c_s = 950 \pm 100$ ms^{-1}

for the adiabatic sound velocity of l-Hg at $T = 293$ K. For comparison, we note that the corresponding experimental value for l-Hg at melting is $c_s = 1455$ ms^{-1} [62, 67] and the KS-AIMD calculation [91–93] gave a value $c_s = 1550 \pm 150$ ms^{-1}.

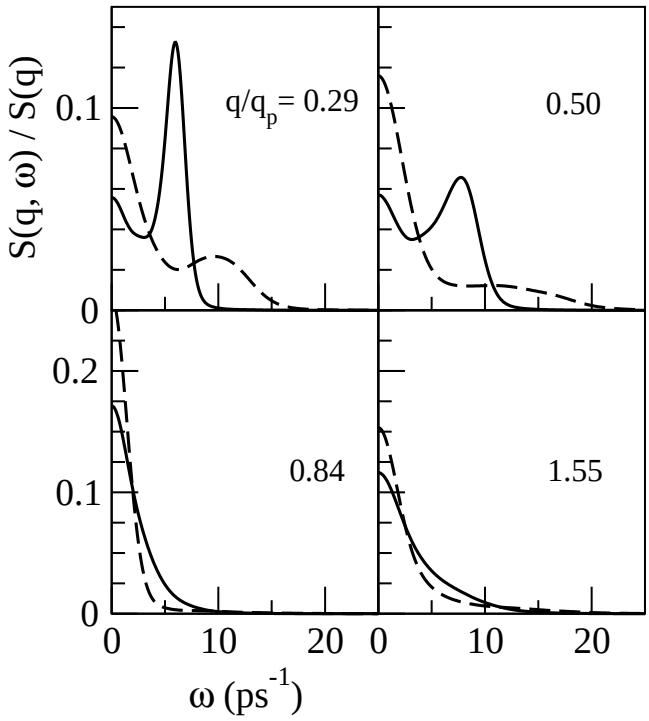

Figure 6.79: Dynamic structure factors $S(q, \omega)$ of l-Hg at $T = 293$ K for several q/q_p values. Full lines: present OF-AIMD results. Dotted lines: AIMD results of Calderin *et al.* [91–93].

The normalized transverse current correlation function $J_t(q, t)$ for l-Hg at $T = 293$ K is depicted in Figure 6.80 for several q/q_p values and we have also plotted the KS-AIMD results of Calderin *et al.* [91–93]. Comparison reveals similar features as those already encountered for l-Cd. The calculation of the shear viscosity for l-Hg at $T = 293$ K gave $\eta = 1.20 \pm 0.15$ GPa ps. On the other hand, extrapolation to $T = 298$ K of the experimental value for l-Hg at melting [220–222] gives $\eta \approx 1.53$ GPa ps which

is greater than our estimate. Again, we notice that the AIMD calculation [91–93] gave a result closer to experiment, *i.e.* $\eta_{\mathrm{KS-AIMD}} = 1.40 \pm 0.15$ GPa ps.

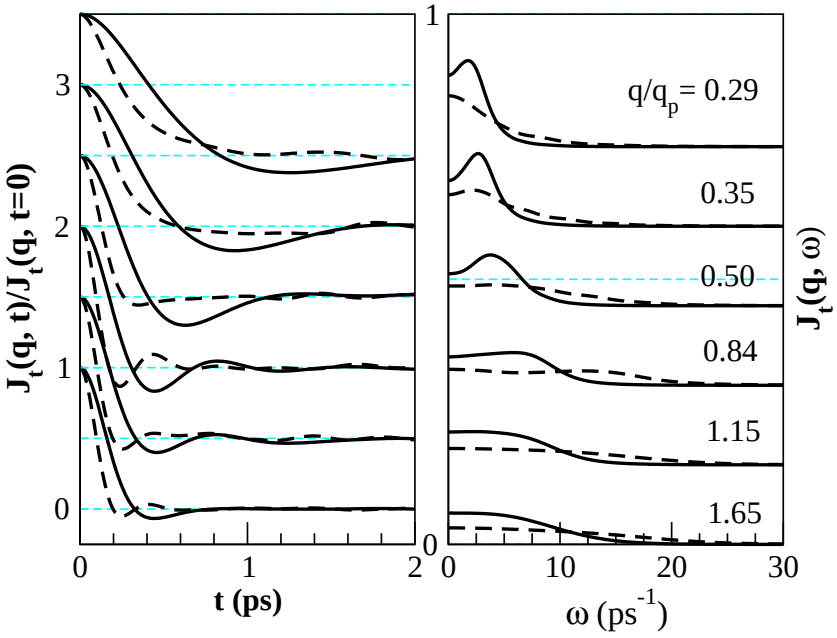

Figure 6.80: Transverse current correlation function, $J_t(q,t)$, and its spectra, $J_t(q,\omega)$, for liquid Hg at $T = 293$ K and $q/q_p = 0.29$, 0.35, 0.50, 0.84, 1.15 and 1.65. Full curves: OF-AIMD calculations. Dashed curves: AIMD results of Calderin *et al.* [91–93].

6.3.11 Comparative Analysis and Findings

The theory of brownian motion provides an exact relation between the diffusion coefficient, D, of a brownian particle of diameter, d, and the shear viscosity, η, of the surrounding liquid, namely

$$\eta D = k_B T/(2\pi d). \tag{6.1}$$

This is the so-called Stokes-Einstein (SE) relation, which despite being approximate at the microscopic level, has often been applied successfully to analyze the diffusion of atoms/ions in liquids. If d is identified with the main peak position of the $g(r)$, then

predictions of η using measured values of D lead usually to a reasonable agreement with experiment (to within 40% for a wide range of liquid metals). Indeed, simulation studies on the hard-sphere liquid [235] demonstrate that the accuracy of the SE relation remains very good even at high pressure. Using our calculated results for η, D and d, we have proceeded to analyze the accuracy of the SE relation by evaluating both left and right sides of the SE relation of the form mentioned above. The results are shown in Table 6.3. It is noticed that the OF-AIMD method gives estimation that follow rather well for both sides of the SE relation. The difference between both members of the Eqn. (6.1) is less than 10% for l-Co, l-Pt, l-Cd, l-Hg and 12% for l-Cr, l-Mn, l-Ni and l-Zn. However for l-Fe and l-Pd the difference is 50% and 23%, respectively. We have also included a similar comparison by using the experimental data for η, D and d where we have obtained for l-Cd and l-Hg , the difference is less

Table 6.3: Check on the validity of the Stokes-Einstein relation. The values are given in units of 10^{-12}N.

Systems	T(K)	OF-AIMD		Experiment	
		ηD	$\frac{k_B T}{2\pi d}$	ηD	$\frac{k_B T}{2\pi d}$
Cr	2173	21.02	18.86	....	19.09
Mn	1533	14.52	12.90	....	12.95
Fe	1833	26.95	16.10	20.38	15.48
Co	1823	17.02	16.28	....	16.01
Ni	1773	17.95	16.03	22.95	15.58
Pd	1853	19.20	15.19	.....	15.65
Pt	2053	15.18	16.58	.....	16.70
Zn	0723	06.10	05.50	08.40	06.00
Cd	0623	04.30	04.60	05.40	04.60
Hg	0293	02.00	02.10	02.50	02.10

than 20%, however for l-Fe, l-Ni and l-Zn it becomes within ≈ 27%, 38% and 33%, respectively. For the liquid systems Cr, Mn, Co, Pd and Pt, no experimental data for D and η are available in the literature. From Table 6.3 it is noticed that the OF-AIMD part of $\frac{k_BT}{2\pi d}$ agrees well with the experimental part of $\frac{k_BT}{2\pi d}$ for all systems under study. Which clearly indicates that the OF-AIMD main peak positions of $g(r)$ for all systems under study are almost same to that of the experimental main peak positios of $g(r)$ [27] for the corresponding systems.

The dynamical heterogeneity is related to the break down of the Stokes-Einstein's relation as described for supercooled liquid [236, 237]. One of the indicators of this

Table 6.4: Comparision of Stokes-Einstein relation for different values of C.

Systems	T (K)	OF-AIMD	$\eta = \frac{k_BT}{C\pi Dd}$ (GPa ps)		OF-AIMD
		D($Å^2\,ps^{-1}$)	C=2	C=3	η (GPa ps)
Cr	2173	0.71	2.64	1.77	2.96
Mn	1533	0.53	2.43	1.62	2.74
Fe	1833	0.49	3.28	2.19	5.50
	1923	0.54	3.12	2.09	3.78
Co	1823	0.41	3.96	2.65	4.15
	1923	0.48	3.57	2.38	3.91
Ni	1773	0.68	2.36	1.57	2.64
Pd	1853	0.40	3.76	2.51	4.07
Pt	2053	0.33	5.02	3.35	4.60
Zn	0723	0.26	2.34	1.56	2.10
	0833	0.37	1.89	1.26	1.49
Cd	0623	0.21	2.19	1.46	2.00
Hg	0293	0.165	1.28	0.85	1.20

feature is non-exponential decay of the correlation function, $g(r)$. From our results for $g(r)$, it apparently seems that the decay of the correlation function is not exactly exponential. So, a deviation from the Stokes-Einstein relation ($\eta = \frac{k_B T}{C \pi D d}$) might be observed, where C is a constant depending on the boundary condition of the flow. But it requires further investigation in detail. It is, however, interesting and simple to investigate from the point of Stoke-Einstein theory, which of the boundary condition from the choice of slip or stick is appropriate for our liquid systems. Table 6.4 illustrates values of shear viscosities with $C = 2$ and 3, and $d = r_p$ (r_p is the position

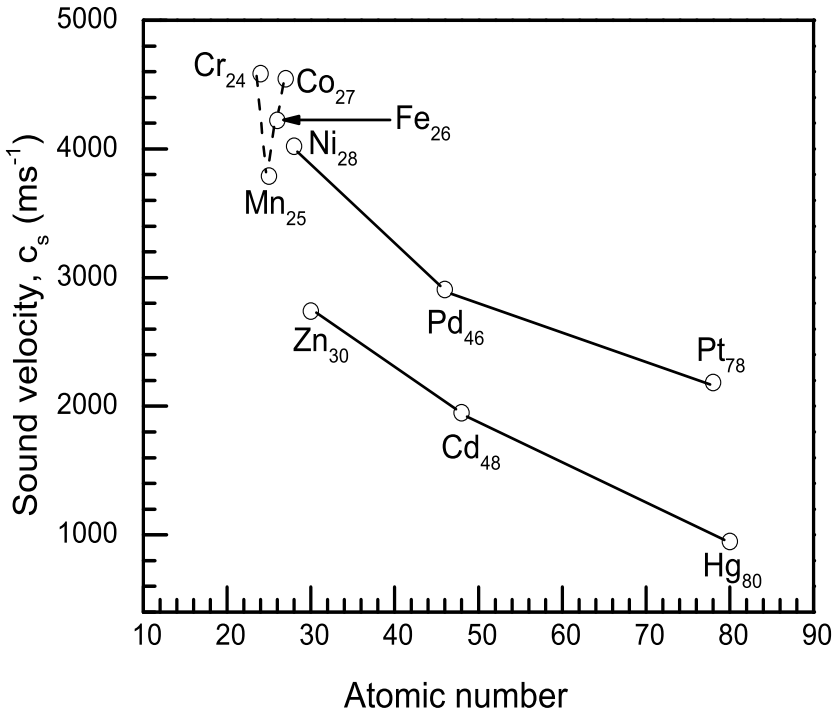

Figure 6.81: Calculated sound velocity, c_s *vs.* atomic number. The suffix in the symbol of element represents the atomic number for the corresponding element.

of the main peak of $g(r)$). Please note here that $C = 2$ and 3 correspond to the slip and stick boundary conditions [238], respectively. We note that some authors [236, 237] used $C = 4$ and 6 for slip and stick conditions, respectively for supercooled liquids. Our OF-AIMD results suggest that the slip boundary condition within the purview of Stoke-Einstein theory is more appropriate for l-Cr, l-Mn, l-Fe, l-Co, l-Ni, l-Pd, l-Pt, l-Zn, l-Cd and l-Hg systems. This also implies that the molecules of the liquid systems understudy are having the Brownian motion of different kind than those of supercooled liquid or glass. The shear viscosity is often determined empirically from the self-diffusion coefficient, D, using the Stokes-Einstein relation ($\eta = \frac{k_B T}{2\pi D\, d}$). The values of $\eta = \frac{k_B T}{2\pi D\, d}$ are presented in the Table 6.4 that obtained using the main peak positions, $r_p = d$ of simulated $g(r)$ and the OF-AIMD self-diffusion coefficients, D. These empirical values are reasonably good in agreement with the OF-AIMD results, η.

The Figure 6.81 represents the sound velocity versus atomic number for the liquid metals studied in the present work. From the above figure 6.81 we see that, for the liquid systems Zn, Cd and Hg of the group IIB elements in the periodic table, the sound velocity increases with decreasing atomic number. The similar behaviour is also observed for the liquid systems Ni, Pd and Pt in the right-most column of the group VIIIA elements of the periodic table. The sound velocity of the liquid systems Cr, Mn, Fe and Co show a rough parabolic variation.

Chapter 7

Conclusions

The static and dynamic properties of liquid Cr, Mn, Fe, Co, Ni, Pd, Pt, Zn, Cd and Hg are studied in this dissertation from the OF-AIMD simulation method at temperatures near their respective melting points and also at elevated temperature in few cases. Here the exchange correlation effect is described by the local density approximation and the external potential is described by a local model pseudopotential. The simulation results are reliable as long as the approximations involved in the calculations are valid. The static structure for all systems under study agrees within few percent of the experimental data. A closer look at the figures for static structure factors, $S(q)$, reveals that the values of the principal peak of $S(q)$ are somewhat overestimated when compared with the XRD data of Waseda [27] for the systems Cr, Mn, Fe and Co. But when OF-AIMD $S(q)$ for l-Fe is compared with XRD data of Inui *et al.* [209] an excellent agreement for the value of principal peak is found. From this point of view one can make a conjecture that the observed larger main peak values for l-Cr, l-Mn and l-Co would also lie within experimental uncertainty of different

measurements (if performed). From an exact quantitative comparison with experiment [27] we observed in the case of l-Ni, l-Pd, l-Pt and l-Cd, the heights of the main peak of $S(q)$ obtained from the OF-AIMD results are overestimated by a negligibly small amount. On the other hand the height of the principal peak of $S(q)$ for l-Zn at both temperatures are reproduced almost completely as the experiment [27]. But the height of the main peak of $S(q)$ for l-Hg is the same as the experiment at T=293 K, while the height of the main peak at higher temperature, T=353 K, differs only by a few percent of the experiment [27]. However, we also acknowledge that the OF-AIMD method can not account for some other finer details such as the low-q shape of the $S(q)$ in l-Zn and the asymmetric shape of the main peak in the $S(q)$ for l-Zn and l-Cd. It is interesting to note that $S(q)$ at low q (*i.e.* in the long wavelength limit) is related to the thermodynamics. In the present OF-AIMD study we found a good reproduction of $S(q)$ at low q. This claim is justified by the comparison of isothermal compressibility derived from OF-AIMD and that obtained from experiment [27]. On the other hand, the main peak positions and heights of $g(r)$ for all systems under study agree fairly well with the experiment [27] and the observed deviation for few systems lie within a very few percent. This is even justified by the comparison between the coordination numbers derived from OF-AIMD and the XRD data for $g(r)$. The dynamical heterogeneity is related to the break down of the Stokes-Einstein's relation as described for supercooled liquid [236, 237]. One of the indicators of this feature is non-exponential decay of the correlation function, $g(r)$. From our results for $g(r)$, apparently it seems that the decay of the correlation function is not exactly exponential. So, a deviation from the Stokes-Einstein relation ($\eta = \frac{k_B T}{C \pi D\, d}$) might be

observed. But it requires further investigation in detail. It is, however, interesting and simple to investigate, from the point of view of Stokes-Einstein theory which boundary condition, slip or stick, is appropriate for our liquid systems. This feature will be discussed later in this chapter.

As for the single particle dynamical properties, we begin with the velocity auto-correlation function, $Z(t)$, which exhibits the backscattering effect for a small time. The self-diffusion coefficients evaluated from the $Z(t)$ and $\langle \delta R^2(t) \rangle$ are almost same for all systems. The agreement of the calculated results lie within a very few percent of the available experimental data except for l-Ni. For the case of l-Ni, we notice a deviation about 32% of our result from the predicted value of Protopapas *et al.* [61] whereas the calculation of other authors show a variation 16% [59] and 84% [54] from the same predicted value. But a recent AIMD calculation by Jakse *et al.* [66] have been able to reproduced self-diffusion coefficient, D, within 4% of predicted value [61] for l-Ni. The systems for which experimental data are not available we have compared our results with other available theoretical values, and we have found that our results are in good agreement with those values. The self-intermediate scattering function, $F_s(q,t)$, obtained from the OF-AIMD and that of from the Gaussian approximation produce almost same results for all systems investigated here, such as liquid Cr, Mn, Fe, Co, Ni, Pd and Pt. Moreover, comparison with the more accurate KS-AIMD $F_s(q,t)$ results for l-Cd [90], show that the OF-AIMD results have a faster time decay. We note here that the structural relaxation time τ may be obtained from the relation $F_s(q,\tau) = \frac{1}{e}$, for any wave vector $\mathbf{q}$. This knowledge of τ is sometimes useful to investigate the degree of break down of the Stokes-Einstein relation for liquid

systems, because $F_s(q,t)$ is controlled by the self-diffusion coefficients.

The obtained intermediate scattering functions, $F(q,t)$, show for small q, the typical oscillatory behavior for all studied systems which becomes less marked with increasing q-values. However, closer comparison with the KS-AIMD results of Calderin for both l-Cd and l-Hg [90–93] shows that the oscillatory behavior of the calculated $F(q,t)$ by OF-AIMD has overestimated amplitudes (and periods). Moreover, the oscillations last for longer times. These limitations are also reflected in the OF-AIMD calculated dynamic structure factors, $S(q,\omega)$, which display side-peaks located at smaller frequencies than their KS-AIMD counterparts. A similar comparison has also been reported for the transverse current correlation functions. Results due to collective dynamics such as dynamic structure factor, $S(q,\omega)$, adiabatic sound velocity, shear viscosity exhibit the correct physical trends and agree well with available experimental data. For example, the position of side peak of $S(q,\omega)$ for different q values provide a dispersion relation; the slope of this curve at $q \to 0$ yields the adiabatic sound velocity. The agreement for sound velocity is found to be good for all systems except for l-Hg, for which it is just fair. We also noticed a deviation in magnitude of sound velocity for l-Pt. The shear viscosity, η, calculted from the OF-AIMD agree reasonably well with available experimental data as well as with some model calculated values. But for the case of l-Ni, the OF-AIMD viscosity is about 55% of experimental magnitude. Table 6.4 illustrates values of shear viscosities with $C = 2$ and 3, and $d = r_p$ (r_p is the position of the main peak of $g(r)$), where $C = 2$ and 3 correspond to the slip and stick boundary conditions [238], respectively. We note that some authors [236, 237] used $C = 4$, 6 for slip and stick conditions for

supercooled liquids. Our OF-AIMD results suggest that the slip boundary condition within the purview of Stokes-Einstein theory is more appropriate for all systems under study. This also implies that the molecules of the liquid systems understudy have different kind of Brownian motion than those of supercooled liquid or glass. Finally, we note that no consideration of spin polarization as mentioned in reference [52] yields physical properties that are largely deviated from the experimental data, but in the OF-AIMD simulation method study we have found results close to the experimental values.

Finally, although the OF-AIMD method can provide a reasonable qualitative description for a range of static and dynamic magnitudes as well as some transport coefficients in l-Cr, l-Mn, l-Fe, l-Co, l-Ni, l-Pd, l-Pt, l-Zn, l-Cd and l-Hg, the comparison with the more accurate KS-AIMD results allows to pinpoint those features which must be improved. The different decay rates and the oscillating periods of the OF-AIMD correlation functions reflect the difference between the OF and the KS forces. Therefore we suggest that some improvement could be obtained if the pseudopotentials were fixed by requiring, within the restricted possibilities of the method, a better reproduction of the KS forces instead of the static structure. We have already started exploring this approach in simpler metals and results look quite promising. In particular for several liquid alkaline earth metals we have been successful in decreasing the overall discrepancy between the OF and KS forces by one half by just modifying an initial pseudopotential in two regions of q space, namely near $q = 0$ and around $q = 2k_F^0$. It is still necessary to check if such simple modifications are enough for more complicated systems such as those studied here and the method looks promising. The

other obvious point that could in principle be improved is the description of the non-interacting electronic kinetic energy, ideally included additionally that coming from the *d*-electrons. This is however much more challenging task to perform theoretically, and we do not expect improvements in this aspect in the short term.

Liquid transition metals have got a tremendous interest in metallurgy and industry due to their interesting properties and versatile applications. So there is a huge scope of research in unvisited area of the field. We therefore have the opportunity to keep continue our research to study the surface properties of the elemental systems for which the calculation of the bulk properties have already been done. We are also interested in the bulk and surface properties of liquid transition metals binary alloys. The transition elements form many useful alloys with one another easily, because the atomic sizes of transition metals are very similar to each other and this attributes to their nature of alloy formation. As the atomic sizes are very similar, one metal can replace the other metal from its lattice site and form a solid solution. This solid solution is known as alloy. The transition metals also form alloys with other metallic elements. Properties of those alloys are also very interesting for research.

One may not be able to study the electronic transport properties from the OF-AIMD method. So the electronic structure has not been studied here for any of the system under study. It is, therefore, obvious that one needs to go for AIMD calculation to study electronic transport properties.

Bibliography

[1] J. M. Haile. *Molecular Dynamics Simulation.* John Wiley and Sons, New York, 1992.

[2] S. W. Peterson. *Acta Crystallographica*, **10**:70, 1957.

[3] P. Hohenberg, and W. Kohn. *Phys. Rev.*, **136**:864, 1964.

[4] W. Kohn, and L. J. Sham. *Phys. Rev. A*, **140**:1133, 1965.

[5] M. R. Molla, A. Z. Z. Ahmed, H. Sarker, G. M. Bhuiyan, M. R. Amin, L. E. González, and D. J. González. *J. Non-Crys. Solids*, **406**:45, 2014.

[6] A. D. Becke. *Phys. Rev. A*, **38**:3098, 1988.

[7] C. T. Lee, W. T. Yang, and R. G. Parr. *Phys. Rev. B*, **37**:785, 1988.

[8] J. P. Perdew, K. Burke, and M. Ernzerhof. *Phys. Rev. Lett.*, **77**:3865, 1996.

[9] J. P. Perdew, K. Burke, and M. Ernzerhof. *Phys. Rev. Lett. E*, **78**:1396, 1997.

[10] P. A. M. Dirac. *Proc. Cambridge Phil. Soc.*, **26**:376, 1930.

[11] D. M. Ceperley, and B.J. Alder. *Phys. Rev. Lett.*, **45**:566, 1980.

[12] S. J. Vosko, L. Wilk, and M. Nusair. *Can. J. Phys.*, **58**:1200, 1980.

[13] J. P. Perdew, and A. Zunger. *Phys. Rev. B*, **23**:5048, 1981.

[14] L. H. Thomas. *Proc. Cambridge Phil. Soc.*, **23**:542, 1927.

[15] D. J. González, L. E. González, and J. M. López, M. J. Stott. *Phys. Rev. B*, **65**:184201, 2002.

[16] L. E. González, D. J. González, and J. M. López. *J. Phys. Condens Matter*, **13**:7801, 2001.

[17] M. Bhuiyan, L. E. González, and D. J. González. *Euro. Phys. J. Web of Conference*, **15**:01011, 2011.

[18] G. Bhuiyan, L. E. González, and D. J. González. *Condens. Matt. Phys.*, **15(3)**:33604, 1, 2012.

[19] D. J. González, L. E. González, J. M. Lopez, and M. J. Stott. *J. Chem. Phys.*, **115**:2373, 2001.

[20] A. Delisle, D. J. González, and M. J. Stott. *Phys. Rev. B*, **73**:064202, 2006.

[21] L. E. González, and D. J. González. *Phys. Rev. E*, **77**:064202, 2008.

[22] J. Blanco, D. J. González, L. E. González, J. M. López, and M. J. Stott. *Phys. Rev. E*, **67**:041024, 2003.

[23] D. J. González, L. E. González, J. M. López, and M. J. Stott. *Phys. Rev. E*, **69**:031205, 2004.

[24] D. J. González, L. E. González, and M. J. Stott. *Phys. Rev. Lett.*, **92**:085501, 2004.

[25] D. J. González, L. E. González, and M. J. Stott. *Phys. Rev. Lett.*, **94**:077801, 2005.

[26] D. J. González, L. E. González, and M. J. Stott. *Phys. Rev. B*, **74**: 014207, 2006.

[27] Y. Waseda. *The Structure of Non-Crystaline Materials.* McGraw-Hill Inc., USA, 1980.

[28] Y. Waseda, and K. Suzuki. *Phys. Stat. Sol. B*, **39**:669, 1970.

[29] F. Aryasetiawan, M. Silbert, and M. J. Stott. *J. Phys. F: Metal Phys.*, **16**:1419, 1986.

[30] Ch. Hausleitner, G. Kahl, and J. Hafner. *J. Phys. Condens Matter*, **3**:1589, 1991.

[31] J. M. Wills, and W. A. Harrison. *Phys. Rev. B*, **28**:4363, 1983.

[32] G. M. Bhuiyan, M. Silbert, and M. J. Stott. *Phys. Rev. B*, **1**:96, 2005.

[33] S. M. Foiles. *Phys. Rev. B*, **32**:3409, 1985.

[34] G. M. Bhuiyan, J. L. Bretonnet, and M. Silbert. *J. Non-Crys. Solids*, **145**:156, 1993.

[35] L. Do Phuong, A. Pasturel, and D. Nguyen Manh. *J. Phys. Condens Matter*, **5**:1901, 1993.

[36] J. L. Bretonnet, and M. Silbert. *Phys. Chem. Liq.*, **24**:169, 1992.

[37] G. M. Bhuiyan, J. L. Bretonnet, and M. Silbert. *J. Phys. Condens Matter*, **4**:7651, 1992.

[38] M. A. Khaleque, G. M. Bhuiyan, S. Sharmin, R. I. M. A. Rashid, and S. M. Mujibur Rahman. *J. Phys. Condens Matter*, **26**:319, 2002.

[39] M. M. Faruk, G. M. Bhuiyan, A. Biswas, and Md. Sazzad Hossain. *J. Chem. Phys.*, **140**:134505, 2014.

[40] S. Chanda, A. Z. Ziauddin Ahmed, G. M. Bhuiyan, and M. Sahhjahan. *Physica B*, **403**:1695, 2008.

[41] G. M. Bhuiyan, M. A. Khaleque, R. I. M. A. Rashid, and S. M. Mujibur Rahman. *Phys. Chem. Liq.*, **35**:153, 1997.

[42] G. M. Bhuiyan, A. Rahman, M. A. Khaleque, R. I. M. A. Rashid, and S. M. Mujibur Rahman. *Phys. Chem. Liq.*, **38**:1, 2000.

[43] C. Fiolhais, J. P. Perdew, S. Q. Armster, J. M. Maclearn, and M. Brajczewska. *Phys. Rev. B*, **51**:14001, 1995.

[44] J. M. Holender. *Phys. Rev. B*, **41**:8054, 1990.

[45] L. Vočadlo, G. A. de Wijs, G. Kresse, M. Gillan, and G. D. Price. *Faraday Discuss*, **106**:205, 1997.

[46] G. Kresse, and J. Hafner. *Phys. Rev. B*, **48**:13115, 1993.

[47] A. Pasqnarello, K. Laasonen, R. Car, C. Lee, and D. Vanderbilt. *Phys. Rev. Lett.*, **69**:1982, 1992.

[48] P. Ganesh, and M. Widom. *Phys. Rev. B*, **74**:234205, 2006.

[49] H. Z. Fang, X. Hui, G. L. Chen, and Z. K. Liu. **372**:5831, 2008.

[50] A. Pasturel, E. S. Tasci, M. H. F. Sluiter, and N. Jakse. *Phys. Rev. B*, **81**:140202, 2010.

[51] Yu. Mitrohkin. *Comp. Mat. Science*, **36**:189, 2006.

[52] M. Marques, L. E. González, and D. J. González. *Phys. Rev. B*, **92**:134203, 2015.

[53] P. Ganesh, and M. Widom. *Phys. Rev. B*, **77**:014205, 2008.

[54] M. M. G. Alemany, O. Diéguez, C. Rey, and L. J. Gallego. *Phys. Rev. B*, **60**:9208, 1999.

[55] D. Tománek, A. A. Aligia and C. A. Balseiro. *Phys. Rev. B*, **32**:5051, 1985.

[56] F. Cleri and V. Rosato. *Phys. Rev. B*, **48**:22, 1993.

[57] M. M. G. Alemany, C. Rey, and L. J. Gallego. *J. Chem. Phys.*, **109**:5175, 1998.

[58] A. F. Voter and S. P. Chen. *Characterization of Defects in Materials.* edited by R. W. Siegel, J. R. Weertman and R. Sinclair, MRS Symposia Proceedings Vol. 82 (Materials Research Society), Pittsburgh, 1987.

[59] S. Ö. Kart, M. Tomak, M. Uludoğan, and T. Çağin. *J. Non-Crys. Solids*, **337**:101, 2004.

[60] T. Çağin, Y. Qi, H. Li, Y. Kimura, H. Ikeda, W. L. Johnson, W. A. Goddard III. *MRS Symposium Series*, **554**:43, 1999.

[61] P. Protopapas, H. C. Andersen, and N. A. D. Parlee. *J. Chem. Phys.*, **59**:15, 1973.

[62] T. Iida, and R. I. L. Guthrie. *The Physical Properties of Liquid Metals.* Clarendon Press, Oxford, 1993.

[63] T. Iida, and R. I. L. Guthrie. *Mater. Sci. Eng. A*, **178**:35, 1994.

[64] F. J. Bermejo, M. L. Saboungi, D. L. Price, M. Alvarez, B. Roessli, C. Cabrillo, and A. Ivanov. *Phys. Rev. Lett.*, **85**:106, 2000.

[65] I. Yokoyama. *Materials Transactions*, **42(9)**:2021, 2001.

[66] N. Jakse, J. F. Wax, and A. Pasturel. *J. Chem. Phys.*, **126**:234508, 2007.

[67] S. Blairs. *J. Coll. Inter. Sci.*, **302**:312, 2006.

[68] P. B. Thakor, Y. A. Sonvane, and A. R. Jani. *AIP Conf. Proc.*, **1447**:915, 2012.

[69] M. Dzugutov. *Nature*, **381**:137, 1996.

[70] I. Yokoyama. *Physica B*, **291**:145, 2000.

[71] I. Yokoyama, and T. Arai. *J. Non-Crys. Solids*, **293**:806, 2001.

[72] S. D. Korkmaz, and Ş. Korkmaz. *J. Mole. liquids*, **150**:81, 2009.

[73] G. X. Li, C. S. Liu, and Z. G. Zhu. *J. Non-Crys. Solids*, **351**:946, 2005.

[74] G. X. Li, C. S. Liu, and Z. G. Zhu. *Chin. Phys. Lett.*, **21**:2489, 2004.

[75] Y. Rosenfeld. *Phys. Rev. A*, **15**:2545, 1977.

[76] S. Chapman and T. G. Cowling. *The Mathematical Theory of Non-Uniform Gases*. Cambridge U. P., New York, 1970.

[77] R. C. Gosh, M. R. Amin, and G. M. Bhuiyan. *J. Mole. liquids*, **188**:148, 2013.

[78] J. A. Moriarty. *Phys. Rev. B*, **28**:3199, 1988.

[79] J. A. Moriarty. *Phys. Rev. B*, **42**:1609, 1990.

[80] Y. Arai, Y. Shirakawa, S. Tamaki, M. Saito, and Y. Waseda. *Phys. Chem. Liq.*, **35**:253, 1998.

[81] S. M. M. Rahman, and L. B. Bhuiyan. *Phys. Rev. B*, **33**:7243, 1986.

[82] I. H. Umar, and W. H. Young. *J. Phys. F: Metal Phys.*, **4**:525, 1974.

[83] P. Ascarelli. *Phys. Rev.*, **173**: 271, 1968.

[84] J. Hafner, and G. Kahl. *J. Phys. F: Metal Phys.*, **14**:2259, 1980.

[85] W. Jank, and J. Hafner. *Phys. Rev. B*, **42**: 6926, 1990.

[86] S. K. Lai, W. Li, and M. P. Tosi. *Phys. Rev. A*, **42**:7289, 1990.

[87] D. K. Belashchenko. *High Temperature*, **50**:61, 2011.

[88] D. K. Belashchenko. *High Temperature*, **44**: 675, 2006.

[89] D. K. Belashchenko. *High Temperature*, **51**: 40, 2013.

[90] L. Calderin, L. E. González, and D. J. González. *J. Phys. Condens Matter*, **25**:065102, 2013.

[91] L. Calderin, L. E. González, and D. J. González. *J. Chem. Phys.*, **130**:194505, 2009.

[92] L. Calderin, L. E. González, and D. J. González. *J. Phys. Condens Matter*, **23**:375105, 2011.

[93] L. Calderin, L. E. González, and D. J. González. *Europ. Phys. J.: Special Topics*, **196**:27, 2011.

[94] D. Vanderbilt. *Phys. Rev. B*, **41**: 7892, 1990.

[95] D. M. North, J. E. Enderby, and P. A. Egelstaff. *J. Phys. C*, **1**:1075, 1968.

[96] S. Takeda, Y Kawakita, M. Kanehira, S Tamaki, and Y Waseda. *J. Phys. and Chem. Solids*, **60**:1552, 1999.

[97] P. Bosi, and C. Petrillo. *Nuovo Cim. D*, **8**:285, 1986.

[98] L. E. Bove, F. Sacchetti, C. Petrillo, B. Dorner, F. Formisano, and F. Barocchi. *Phys. Rev. Lett.*, **87**:215504, 2001.

[99] L. E. Bove, F. Sacchetti, C. Petrillo, B. Dorner, F. Formisano, M. Sampoli, and F. Barocchi. *Phil. Mag. B*, **82**:365, 2002.

[100] Y. S. Badyal, U. Bafile, K. Miyazaki, I. M. de Schepper, and W. Montfrooij. *Phys. Rev. E*, **68**: 061208, 2003.

[101] S. Hosokawa, H. Sinn, F. Hensel, A. Alatas, E. E. Alp, and W. C. Pilgrim. *Appl. Phys. A*, **74**: S1648, 2002.

[102] D. Ishikawa, M. Inui, K. Matsuda, K. Tamura, S. Tsutsui, and A. Q. R. Baron. *Phys. Rev. Lett.*, **93**: 097801, 2004.

[103] W. A. Harrison. *Solid State Theory.* McGraw-Hill, New York, 1970.

[104] N. W. Ashcroft, and N. D. Mermin. *Solid State Physics.* W. B. Saunders, Philadelphia, 1976.

[105] R. H. Petrucci, W. S. Harwood, and F. G. Herring. *General Chemistry.* 8th ed., Pearson, Prentice-Hall, 2002.

[106] C. E. Housecroft, and A. G. Sharpe. *Inorganic Chemistry.* 8th ed., Pearson, Prentice-Hall, 2005.

[107] K. A. Gschneider. *Solid State Physics*, **16**:275, 1974.

[108] J. Friedel. *The Physics of Metals 1. Electrons, ed J. M. Ziman.* Cambridge University, UK, 1971.

[109] V. Heine. *The Physics of Metals 1. Electrons, ed J. M. Ziman.* Cambridge University, UK, 1971.

[110] L. I. Schiff. *Quantum Mechanics.* McGraw-Hill, 1968.

[111] L. A. Corathers. *U. S. Geological Survey.* Mineral Commodity Summaries, January, 2009.

[112] L. A. Corathers. *U. S. Geological Survey* . Minerals YearBook, Manganese, 2006.

[113] Xiangliang Pan, Jianlong Wang, and Daoyong Zhang. *Desalination*, **249(2)**:609, 2009.

[114] V. A. Nemilov, and A. A. Rudnitskii. *Izv. Sektora Platini AN SSSR*, **27**, 1952.

[115] D. Marx, and J. Hutter. *Modern Methods and Algorithms of Quantum Chemistry*. J. Grotendorst(Ed.), John von Neumann Institute for Computing, Jülich, NIC series, Vol.1, ISBN 3-00-005618-1, Germany, 2000.

[116] M. E. Tuckerman. *J. Phys. B Condens. Matter*, **14**:R1297, 2002.

[117] R. Iftimie, P. Minary, and M. E. Tuckerman. *Proc. Natl. Acad. Sci. USA*, **102(19)**:6654, 2005.

[118] D. G. Kanhere, and V. Shah. *Ab initio, orbital free molecular dynamics: Technique and applications, in Electronic Structure of Alloys, Surfaces and Clusters*. Chap. 10, Taylor and Francis, eds., Hardcover, 2002.

[119] R. Car, and M. Parrinello. *Phys. Rev. Lett.*, **55**:2471, 1985.

[120] R. Car, and M. Parrinello. *Simple Molecular Systems at Very High Density, in NATO Advanced Study Institute*. Series B: Physics 186, A. Polian, P. Lebouyre and N. Boccaraeds, Plenum, 1989.

[121] H. Chen, and A. Zhou. *Numer. Math. Theor. Meth. Appl.*, **1(1)**:1, 2008.

[122] A. R. Leach. *Molecular Modelling Principles and Applications*. Longman, Edinburg, 1996.

[123] U. Balucani, and M. Zoppi. *Dynamics of the liquid State*. Clarendon Press, Oxford, UK, 1994.

[124] M. P. Allen, and D. J. Tidesley. *Computer Simulation of Liquid*. Clarendon Press, Oxford, 1987.

[125] J. P. Hansen, and I. R. McDonald. *Theory of Simple Liquids*. Academic Press, London, UK, 3rd edition, 2006.

[126] J. P. Mithen. *Molecular dynamics simulations of the equilibrium dynamics of non-ideal plasmas*. PhD Thesis, Trinity College, University of Oxford, 2012.

[127] P. P. Ewald. *Ann. Phys. (Leipzig)*, **64**:253, 1921.

[128] E. Schrödinger. *Phys. Rev.*, **28**:1049, 1926.

[129] D. J. Griffiths. *Introduction to Quantum Mechanics*. Pearson, UK, 2005.

[130] M. Born. *Zeitschrift fuer Physik*, **37**:863, 1926.

[131] Wolfram Koch, and Max C. Holthausen. *A Chemists's Guide to Density Functional Theory*. Wiley-VCH, Germany, 2001.

[132] N. Zettili. *Quantum Mechanic: Concepts and Applications*. Wiley-VCH, 2009.

[133] K. Capelle. *A bird's-eye view of density-functional theory*. arXiv:cond-mat, 0211443v5, 2006.

[134] W. Kohn. *Rev. Mod. Phys.*, **71**:1253, 1999.

[135] W. Kock, and M. C. Holthausen. *A Chemists Guide to Density Functional Theory*. Wiley-VCH, 2001.

[136] M. Born, and J. R. Oppenheimer. *Ann. Phys.*, **84**:457, 1927.

[137] R. G. Parr, and W. Yang. *Density-functional theory of atoms and molecules*. Oxford University Press, New York, 1989.

[138] B. Santra. *Density-Functional Theory Exchange-Correlation Functionals for Hydrogen Bonds in Water*. PhD thesis, der Technischen Universität, Berlin, Germany, August 2010.

[139] H. Hellmann. *Einführung in die Quantenchemie*. Leipzig, Franz Deuticke, 1937.

[140] R. P. Feynman. *Phys. Rev.*, **56 (4)**:340, 1939.

[141] E. Fermi. *Rend. Accad. Naz. Lincei*, **6**:602, 1927.

[142] V. F. Petrenko, and R. W. Whitworth. *Physics of Ice*. Oxford University Press, Inc., New York, 2003.

[143] J. P. Perdew, and Y. Wang. *Phys. Rev. B*, **45**:13244, 1992.

[144] J. P. Perdew, and Y. Wang. *Phys. Rev. B*, **46**:12947, 1992.

[145] A. D. Becke. *J. Chem. Phys.*, **38**:3098, 1998.

[146] P. P. Rushton. *Towards a Non-local Description of Exchnage and Corrlation*. PhD Thesis, University of Durham, 2002.

[147] J. S. Lin, A. Qteish, M. C. Payne, and V. Heine. *Phys. Rev. B*, **47**:4174, 1993.

[148] D. Marx, and J. Hutter. *Ab initio Molecular Dynamics: Basic Theory and Advanced Methods*. Cambridge University Press, UK, 2009.

[149] J. M. Ziman. *Principals of the Theory of Solids*. II ed., Cambridge University Press, London, 1972.

[150] N. Troullier, and J. L. Martins. *Phys. Rev. B*, **43**:1993, 1991.

[151] G. P. Kerker. *J. Phys. C*, **13**:L189, 1980.

[152] D. R. Hamann, M. Schl′uter, and C. Chiang. *Phys. Rev. Lett.*, **43**:1494, 1979.

[153] D. Vanderbilt. *Phys. Rev. B*, **32**:8412, 1985.

[154] S. Goedecker, M. Teter, and J. Hutter. *Phys. Rev. B*, **54**:1703, 1996.

[155] W. E. Pickett. Pseudopotential methods in condensed matter applications. *Comp. Phys. Rep.*, **9**:115, 1989.

[156] L. Calderin, D. J. González, L. E. González, and J. M. López. *J. Chem. Phys.*, **129**:194506, 2008.

[157] L. Calderin, L. E. González, and D. J. González. *Phys. Rev. B*, **80**:115403, 2009.

[158] T Itami, S Munejiri, T Masaki, H. Aoki, Ishil, T. Kamiyama, Y. Senda, F. Shimojo, and K. Hoshino. *Phys. Rev. B*, **67**:064201, 2003.

[159] B. Zhou, V. L. Ligneres, and E. A. Carter. *J. Chem. Phys.*, **122**:044103, 2005.

[160] E. Smargiassi, and P. A. Madden . *Phys. Rev. B*, **49**:5220, 1994.

[161] E. Smargiassi, and P. A. Madden . *Phys. Rev. B*, **51**:117, 1995.

[162] M. Foley, E. Smargiassi, and P. A. Madden . *J. Phys. Condens Matter*, **6**:5231, 1994.

[163] M. Foley. *Developments in the ab initio simulation of metallic systems*. D. Phil. Thesis, Oxford University, UK, 1996.

[164] M. Foley, and P. A. Madden . *Phys. Rev. B*, **53**:10589, 1996.

[165] S. C. Watson. *Structural relaxation at defects by ab initio molecular dynamics*. D. Phil. Thesis, Oxford University, UK, 1996.

[166] Q. Wang, M. D. Gossman, M. P. Iñiguez, and J. A. Alonso. *Phil. Mag. B*, **69**:1045, 1993.

[167] S. C. Watson, and P. A. Madden . *Phys. Chem. Comm.*, **1**:1, 1998.

[168] S. C. Watson, and E. A. carter . *Comput. Phys. Commun.*, **128**:67, 2000.

[169] D. R. Hartree. *Proc. Cambridge Phil. Soc.*, **24**:89, 1928.

[170] V. Fock. *Z. Phys.*, **61**:126, 1930.

[171] C. C. J. Roothaan. *Rev. Mod. Phys.*, **23**:69, 1951.

[172] Y. A. Wang, and E. A. Carter. *Theoritical Methods in Condensed Phase Chemistry.* Kluwer, Dordrecht, 2000.

[173] C. F. von Weizsäcker. *Z. Phys.*, **96**:431, 1935.

[174] R. M. Dreizler, and E. K. U. Gross. *Density Functional Theory.* Springer-Verlag, Berlin, 1990.

[175] R. O. Jones, and O. Gunnarsson. *Rev. Mod. Phys.*, **61**:689, 1989.

[176] F. Perrot. *J. Phys. Condens Matter*, **6**:431, 1993.

[177] E .V. Ludeña, and V. V. Karasiev. *Reviews of Modern Quantum Chemistry: a Celebration of the Contributions of Robert Parr.* World Scientific, Singapore, 2002.

[178] W. Jones. *Phys. Lett. A*, **34**:351, 1971.

[179] W. Jones, and W. H. Young. *J. Phys. C: Solid State Phys.*, **4**:1332, 1971.

[180] J. Lindhard. *K. Dan. Vidensk. Selsk. Mat-Fys. Medd*, **28**:8, 1954.

[181] E. Smargiassi, and P. A. Madden. *Phys. Rev. B*, **49**:5220, 1994.

[182] M. Foley, and P. A. Madden. *J. Phys. Condens Matter*, *ibid* **53**:10589, 1996.

[183] Y. A. Wang, N. Govind, and E. A. Carter. *Phys. Rev. B*, **58**:13 465, 1998.

[184] Y. A. Wang, N. Govind, and E. A. Carter. *Phys. Rev. B*, **60**:16 350, 1999.

[185] E. Chacón, J. E. Alvarellos, and P. Tarazona. *Phys. Rev. B*, **32**:7868, 1985.

[186] P. García-Gonález, J. E. Alvarellos, and E. Chacón. *Phys. Rev. A*, **54**:1897, 1996.

[187] P. García-Gonález, J. E. Alvarellos, and E. Chacón. *Phys. Rev. B*, **53**:9509, 1996.

[188] P. García-Gonález, J. E. Alvarellos, and E. Chacón. *Phys. Rev. B*, **57**:4857, 1998.

[189] S. Gómez, L. E. González, D. J. González, M. J. Stott, S. Dalgic, and M. Silbert. *J. Non-Crys. Solids*, **163**:250, 1999.

[190] S. R. Bickham, O. Pfaffenzeller, L. A. Collins, J. D. Kress, and D. Hohl. *Phys. Rev. B*, **58**:R11813, 1998.

[191] M. Pearson, E. Smargiassi, and P. A. Madden. *J. Phys. Condens Matter*, **5**:3221, 1993.

[192] N. Govind, J. L. Mozos, and H. Guo. *Phys. Rev. B*, **51**:7101, 1995.

[193] P. Blaise, S. A. Blundell, and C. Guet. *Phys. Rev. B*, **55**:15856, 1997.

[194] M. Foley, E. Smargiassi, and P. A. Madden. *J. Phys. Condens Matter*, **6**:5231, 1994.

[195] E. Smargiassi, and P. A. Madden. *Phys. Rev. B*, **51**:117, 1995.

[196] E. Smargiassi, and P. A. Madden. *Phys. Rev. B*, *ibid***51**:129, 1995.

[197] B. J. Jesson, M. Foley, and P. A. Madden. *J. Phys. Condens Matter*, *ibid* **55**:4941, 1997.

[198] M. J. Field. *A practical introduction to the simulation of molecular systems*. Cambridge University Press, UK, 2007.

[199] J. P. Boon, and S. Yip. *Molecular Hydrodynamics*. Dover Publications, Inc., New York, 1991.

[200] R. L. McGreevy, A. Baranyai, and I. Ruff. *Phys. Rev. B*, **16**:47, 1986.

[201] N. E. Cusak. *The Physics of Structurally Disordered Matter*. Adam-Hilger, Bristol, 1987.

[202] R. B. Bird, W. E. Stewart, and E. N. Lightfoot. *Transport phenomena*. 2nd ed., John Wiley and Sons, New York, 2002.

[203] L. Wei-Zhong, C. Cong, and Y. Jian. *Asian Research*, **37(2)**:86, 2008.

[204] L. Van Hove. *Phys. Rev.*, **95**:249, 1954.

[205] M. Shimoji. *Liquid Metals An Introduction to the Physics and Chemistry of Metals in the Liquid States*. Academic Press, London, 1977.

[206] S. J. Blundell, and K. M. Blundell. *Concepts in Thermal Physics*. Oxford University Press, UK, 2006.

[207] D. M. Heyes. *The Liquid state: Application of Molecular Simulations*. Wiley, West Sussex-England, 1998.

[208] B. J. Palmer. *Phys. Rev. E*, **49**:359, 1994.

[209] M. Inui, K. Maruyama, Y. Kajihara, and M. Nakada. *Phys. Rev. B*, **80**:180201, 2009.

[210] T. Schenk, D. Holland-Mority, V. Simonet, R. Bellissent, and D. M. Herlach. *Phys. Rev. Lett.*, **89**: 075507, 2002.

[211] L. E. González, D. J. González, M. R. Molla, A. Z. Z. Ahmed, and G. M. Bhuiyan. Unpublished, Universidad de Valladolid, Valladolid, Spain and University of Dhaka, Dhaka, Bangladesh, 2016.

[212] L. E. González, D. J. González, M. R. Molla, A. Z. Z. Ahmed, and G. M. Bhuiyan. Submitted: *Euro. Phys. J. Web of Conference*, 2016.

[213] R. N. Singh, S. Arafin, and A. K. George. *Physica B-Cond. Matt.*, **387**:344, 2007.

[214] K. Tamura, and S. Hosokawa. *J. Non-Crys. Solids*, **156-158**:646, 1993.

[215] L. E. González, D. J. González, and M. Canales. *J. Phys. B Condens. Matter*, **100**:601, 1996.

[216] M. Walbrühl. *Degree project in Material Science and Engineering*. Second cycle, Stockholm, 2014.

[217] M. Canales, D. J. González, L. E. González, and J. A. Padro. *Phys. Rev. E*, **58**:4747, 1998.

[218] J. Casas, D. J. González, L. E. González, M. M. G. Alemany, and L. J. Gallego. *Phys. Rev. B*, **62**:12095, 2000.

[219] R. P. Chhabra, and T. Sridhar. *Phys. Chem. Liq.*, **13**:37, 1983.

[220] M. J. Assael, I. J. Armyra, J. Brillo, S. V. Stankus, J. Wu, and W. A. Wakeham. *J. Phys. and Chem. Ref. Data*, **41**:033101, 2012.

[221] M. Shimoji, and T. Itami. *Atomic Transport in Liquid Metals*. Trans. Tech. Publications, Switzerland, 1986.

[222] E. A. Brandes, and G. B. Brook. *Smithells Metals Reference Book*. Butterworth-Heinemann, Oxford, 1992.

[223] V. V. M. Lobo, and R. Mills. *Electochim. Acta*, **27**:969, 1982.

[224] D. R. Lide (Ed.). *Handbook of Chemistry and Physics*. 79th ed. CRC Press, Boca Raton, 1998.

[225] U. Balucani, J. P. Brodholt, P. Jedlovszky, and R. Vallauri. *Phys. Rev. E*, **62**:2971, 2000.

[226] M. A. Khaleque, G. M. Bhuiyan, and R. I. M. A. Rashid. *Internal report, ICTP*, **IC/98/6**, 1997.

[227] I. Egry. *Scr. Metall. Mater.*, **28**:1273, 1993.

[228] Y. Sato, K. Sugisawa, D. Aoki, and T. Yamamura. *Meas. Sci. Technol.*, **16**:363, 2005.

[229] Z. Morita, and T. Iida. *Proc. 1st China-Japan symposium on science and technology of iron and steel*. 1986.

[230] G. Kaptay. *Z. Metall.*, **1**:96, 2005.

[231] A. Torcini, U. Balucani, P. H. K. de Jong, and P. Verkerk. *Phys. Rev. E*, **51**:3126, 1995.

[232] S. Kambayashi, and G. Kahl. *Phys. Rev. A*, **46**:3255, 1992.

[233] T. Iida, and R. I. L. Guthrie. *The Thermophysical Properties of Metallic Liquids*. Oxford University Press, Oxford, 1993.

[234] T. Iida, and R. I. L. Guthrie. *The Thermophysical Properties of Metallic Liquids, Vol. 1: Fundamentals*. Oxford University Press, Oxford, 2015.

[235] G. E. LeBlanc, and R. A. Secco. *Geophys. Res. Lett.*, **23**:213, 1996.

[236] Z. Shi, P. G. Debenedetti, and F. H. Stillinger. *J. Chem. Phys.*, **138**:12A526, 2013.

[237] S. Sengupta, S. Karmakar, C. Dasgupta, and S. Sastry. *J. Chem. Phys.*, **138**:12A548, 2013.

[238] L. D. Landau. *Fluid Mechanics*. Pergamon, New York, 1987.